Thionation of Asymmetric Rylene Diimides

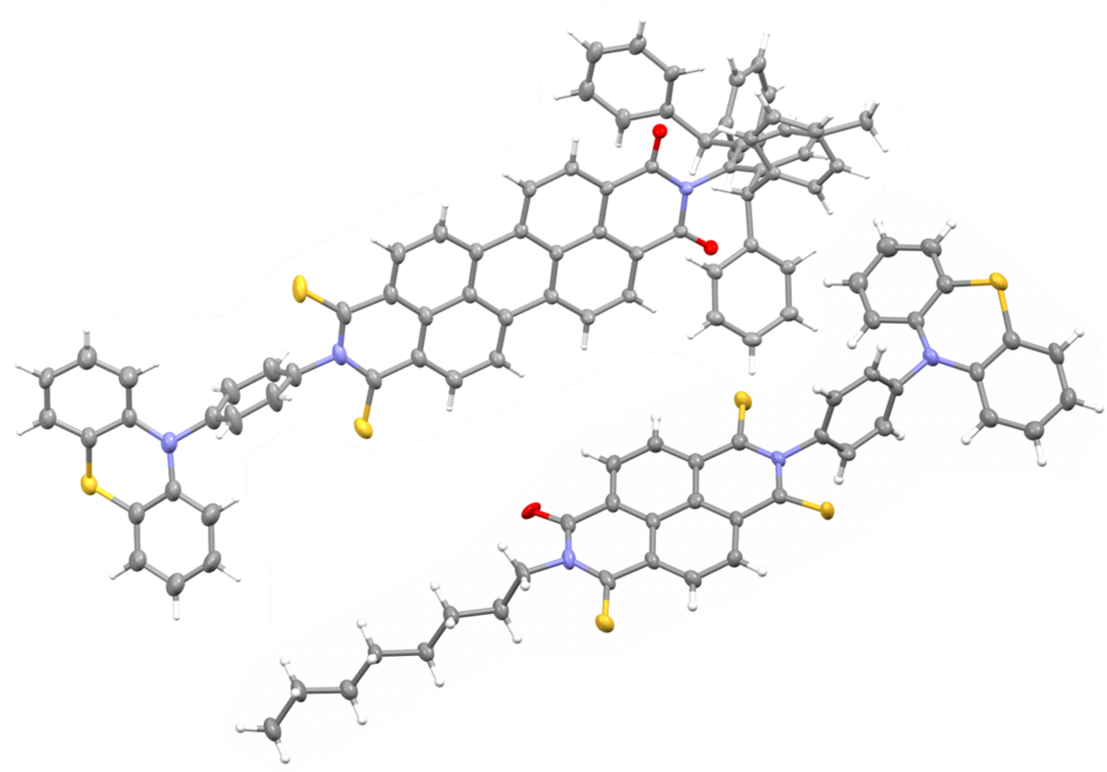

Nicholas Pearce

Thionation of Asymmetric Rylene Diimides

Thesis submitted to the University of Nottingham for the
Degree of Doctor of Philosophy

Nicholas Pearce, MSci

December 2016

Declaration

Except where specific reference is made to other sources, the work presented in this thesis is the original work of the author. It has not been submitted, either in whole or in part, for any other degree.

Signed:

Date:

Abstract

Rylene diimides have attracted much attention for use in optoelectronic devices, with excellent absorption and emission profiles, as well as a tendency to form n-type semiconductors. The absorption and emission properties of rylene diimides can be varied through functionalisation at the imide nitrogens and by substitution to the aromatic core but the effects of alterations to the imide oxygen atoms are less well understood.

A series of thionated naphthalene diimides (NDIs), in which the imide oxygen atoms have been replaced with sulfur has been synthesised in a single reaction using Lawesson's reagent. Electrochemical measurements of the series reveal that the electron affinity increases significantly with sulfur substitution, making the singly and doubly reduced states of the NDI much more accessible. This work is expanded further with the production of asymmetric NDI and naphthalic imide systems. Phenothiazine is employed as an electron donor and thionated derivatives of NDIs and naphthalic imides are implemented as the electron acceptors. Photoinduced charge separation was observed for these dyads using a combination of picosecond time-resolved transient absorbance spectroscopy and infrared spectroscopy, finding that thionation increases the charge separated lifetime of the species by a factor of ten; producing radical pairs with lifetimes greater than 2 ns, sufficient for charge extraction in organic electronic devices.

Perylene diimides (PDIs) are related to NDIs, but with a larger aromatic core. Despite an enhancement of desirable properties relative to NDIs, the practicality of PDIs can be limited by low solubility and demanding syntheses. As the field of supramolecular chemistry expands, the synthesis of more sophisticated molecular arrays has become necessary to build improved nanotechnological components. Herein, the effectiveness of a bulky aromatic solubilising group for PDIs is examined crystallographically and used to synthesise a range of soluble *N*,*N*'-asymmetrically disubstituted PDI compounds. The applications of this new solubilising group were demonstrated in the production of a multichromophoric PDI dimer; in the assessment of binding affinity of a hydrogen-bonding PDI to the nucleobase adenine and finally in the synthesis of a charge transfer complex, again utilising phenothiazine as an electron donor. This charge transfer complex was also thionated, providing a unique perylene monoimide monothiomide with an experimentally determined band gap of approximately 1 eV.

Acknowledgements

The first acknowledgement is for my supervisor: Professor Neil Champness. Thank you so much for encouragement, support and friendly advice throughout the course of both my PhD and MSci projects. It has been a pleasure working in your lab.

A huge thank you as well to Dr. Stephen Davies for all things electrochemistry. He is truly an excellent chemist, with an enthusiasm and keen eye for detail and has helped me to understand a lot of the interesting results presented in this thesis.

Gratitude to all the scientists whose specialist knowledge was invaluable to completing this work: Dr. Raphael Horvath for carrying out transient absorption and TRIR measurements; Dr. William Lewis, Dr. Stephen Argent and Dr. Connie Pfeiffer for help when it came to X-ray crystallography and to Prof. Jonathan McMaster and Dr. Paul Hume for helping me to get started running DFT calculations.

Finally, for all their assistance in the lab during my PhD I would like to thank the expert post-docs of the group: Dr. Stephen Argent, Dr. Anna Slater and Dr. Lixu Yang. I am especially grateful to Dr. Ben Llewellyn and Dr. Simon Harrold, Simon for moulding me into a chemist during my MSci year and Ben for four years' worth of discussions about the ins and outs of perylene diimide chemistry. My greatest appreciation to all the technical staff at Nottingham: Shazad Aslam, Kevin Butler, Mick Cooper, Graham Coxill, and Ben Pointer-Gleadhill. And lastly to all the brilliant scientists I've worked with in the Champness group: Tim, Sarah, Sam, Harry Mack, Charlie, Harry Martin, Phil, Barry, Vic, Tom, Nick and Laura, it was a pleasure to have known you.

List of Symbols and Abbreviations

A_{iso}	Isotropic Hyperfine Coupling Constant
ε	Extinction Coefficient
$E_{1/2}$	Redox potential
E_{pa}	Peak Anodic Potential
Φ_f	Fluorescence Quantum Yield
Fc^+/Fc	Ferrocenium/Ferrocene
g_{iso}	Isotropic *g*-factor
$h\nu$	Photon
K	Association constant
λ	Wavelength
R_f	Retardation Factor
aq	Aqueous
ATR	Attenuated Total Reflectance
BDPA	2,6-Bis(diphenylmethyl)-4-methylaniline
CIF	Crystallographic Information File
CV	Cyclic Voltammetry
DCTB	trans-2-[3-(4-tert-butylphenyl)-2-methyl-2-propenylidene]malonitrile
DFT	Density Functional Theory
DNA	Deoxyribonucleic Acid
EDOT	3,4-Ethylenedioxythiophene
EI	Electron Impact
EPR	Electron Paramagnetic Resonance
eq	Equivalent
ESI	Electrospray Ionisation
FD	Field Desorption
FRET	Fluorescence Resonance Energy Transfer
fwhm	Full Width at Half Maximum
GOF	Goodness Of Fit
HMBC	Heteronuclear Multiple Bond Correlation
HOMO	Highest Occupied Molecular Orbital
HRMS	High Resolution Mass Spectrometry
IR	Infrared
LUMO	Lowest Unoccupied Molecular Orbital
MALDI	Matrix Assisted Laser Desorption Ionisation
MCT	Mercury-Cadmium-Telluride
MS	Mass Spectrometry
NI	Naphthalic Imide
NDI	Naphthalene-1,4,5,8-Tetracarboxylic Diimide
NMI	Naphthalene-1,8-Imide-4,5-anhydride
NMR	Nuclear Magnetic Resonance
OLED	Organic Light Emitting Diode
OFET	Organic Field Effect Transistor
OTFT	Organic Thin Film Transistor
OPA	Optical Parametric Amplifier
OPV	Organic Photovoltaic
PDE	Perylene-3,4-Diester-9,10-Anhydride
PDI	Perylene-3,4,9,10-Tetracarboxylic Diimide
PET	Photoinduced electron transfer

PMI	Perylene-3,4-Imide-9,10-anhydride
PTE	Perylene-3,4,9,10-Tetraester
PTZ	10H-Phenothiazine
PyDI	Pyromellitic Diimide
sat	Saturated
SHJ	Supramolecular n/p-Heterojunction
SOF	Site Occupancy Factor
SOMO	Singly Occupied Molecular Orbital
TA	Transient Absorption
TNCQ	Tetracyanoquinodimethane
TOF	Time of Flight
TRIR	Time Resolved Infrared
TTF	Tetrathiafulvene
UV	Ultraviolet
vis	Visible
vs	Versus
ZnP	Zinc Porphyrin

Contents

Chapter 1

Introduction

1.1. Rylene Diimides

Rylene tetracarboxylic diimides are a family of hydrocarbon molecules, consisting of oligomers of peri-naphthalene connected to two imide groups at the 1 and 8 positions of the terminal naphthalene units. Interest surrounding the rylene diimides built from early observations of their behaviour as electron transport (n-type) materials. Rylene diimides tend to have high electron affinities and mobilities, intense absorbances in the visible spectrum and excellent photochemical and thermal stabilities.[1-3] The ability to modify the optoelectronic properties by variation of substituents to the imide and core regions has established rylene diimides as leading n-type materials for organic electronics.[4] The first three members of the rylene diimide series contain one, two and three naphthalene units and are respectively called naphthalene-1,4,5,8-tetracarboxylic diimide (NDI), perylene-3,4,9,10-tetracarboxylic diimide (PDI) and terrylene-3,4,11,12-tetracarboxylic diimide (Figure 1.1).

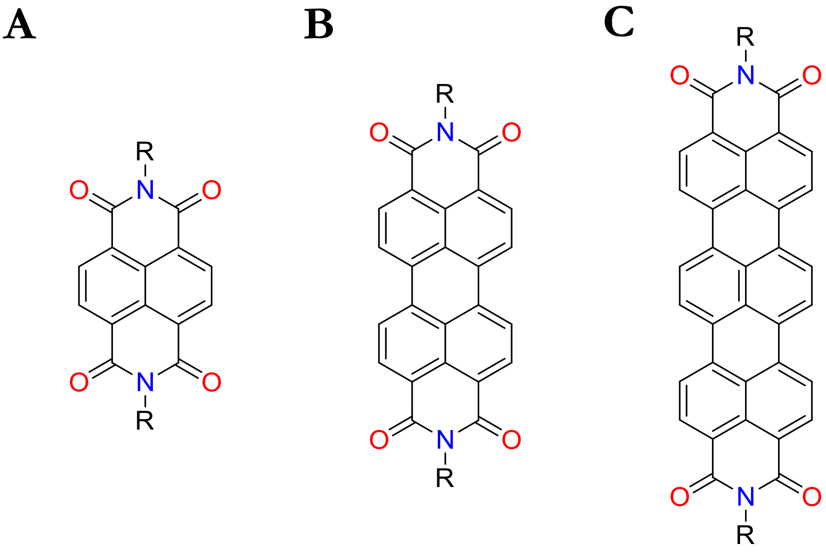

Figure 1.1: General Structure of rylene diimides. A: NDI, B: PDI, C: Terrylene-3,4,11,12-tetracarboxylic diimide.

The attractive electronic and optical properties of rylene diimides has led to their use in devices such as organic light emitting diodes (OLEDs),[5, 6] organic field effect transistors (OFETs),[4, 7-9] laser dyes,[10] fluorescent standards,[11, 12] optical switches and photodetectors.

The corresponding anhydrides of NDI and PDI, the simplest two rylene diimides, are commercially available and serve as a common starting point for the synthesis of these two compounds. The appropriate rylene dianhydride and an excess of the desired alkylamine or aniline are reacted together at moderately high temperature in a condensation reaction to afford the *N*,*N*'-symmetrically substituted rylene diimide product. Higher rylene diimides require a more in-depth synthetic strategy and are usually built up sequentially from smaller aromatic monoimides.[13, 14] For this reason, this thesis will concentrate on the simpler rylene diimides, beginning with NDIs.

1.1.1. Naphthalene Diimides

NDIs are the first member of the rylene diimide family, with a structure consisting of a single naphthyl unit with two six-membered cyclic imide rings connecting the pairs of peri positions (Figure 1.2). There are two main regions on the NDI molecule that lend themselves to functionalisation; the imide region (dark red) and the aromatic core (green).

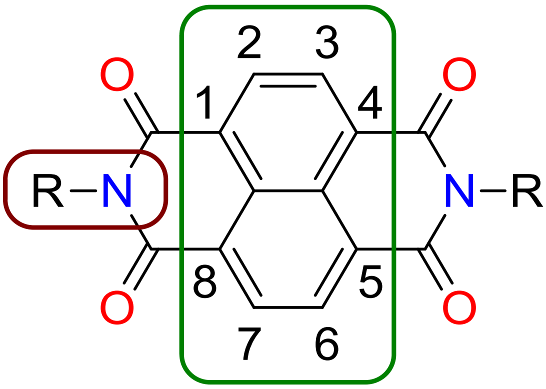

Figure 1.2: Structure and numbering system of NDIs highlighting the imide region (dark red) and the core region (green).

The history of NDI chemistry begins with German chemist Heinrich Vollmann whose experiments with pyrene in the 1930s led to the first synthesis of NDI.[15] Vollmann discovered that with variation of the substituents on the core of the NDI, stable and colourful pigments were produced, thus NDIs became used as vat dyestuffs.[16, 17] Owing their planarity as well as the presence of a large number of hydrogen bond acceptors, the end of the 20th century saw NDIs being incorporated into many supramolecular systems, beginning with work surrounding NDI as a DNA binder; able to intercalate between the base pairs of DNA (Figure 1.3), and form hydrogen bonds with the various nucleobases.[18, 19] The imide region of NDI (and other rylene diimides) resembles the hydrogen bond acceptor-donor-acceptor pattern of nucelobases thymine and uracil.

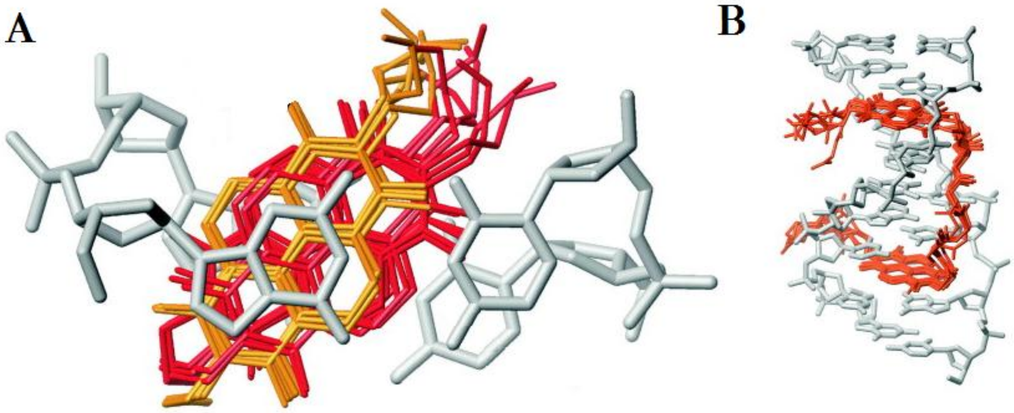

Figure 1.3: Model of NDI-DNA binding showing intercalation between base pairs. Grey: DNA, red and yellow: NDI. A: Close up of intercalation. B: View of a bis-intercalating NDI recognising the major groove of DNA. Adapted from Guelev et al.[19]

The same two annulated electron-withdrawing imide groups that allow NDIs to form such efficient contacts with DNA are reversibly reduced at mild potentials, typically (for non-core substituted NDIs) forming a stable radical anion at -1.1 V (vs. Fc^+/Fc) and a dianion at -1.5 V.[20, 21] The nature of the imide substituents has little effect on the electrochemical properties of NDIs and also has a very limited effect on the optical properties. The absorbance profiles of non-core substituted NDIs show an intense, structured absorbance in the near-ultraviolet region, with prominent peaks from the 0 → 0, 0 → 1 and 0 → 2 vibronic bands.[20] In the case of *N*,*N*'-dialkyl substituted NDIs a mirror image emission can be observed with a 7 nm stokes shift.[22] In contrast to this, functionalisation of the imide nitrogens with an aromatic group will produce either non-fluorescent or weakly fluorescent compounds.

Core-substituted NDIs are blossoming as a distinct class of rylene diimide materials with very different photophysical properties to their unsubstituted NDI counterparts.[23] The aromatic core of NDIs provides four available positions for functionalisation and allows for drastic modification of both the optical and electronic properties. Small structural changes, such as the replacement of the aromatic hydrogens with heteroatoms can vary the frontier molecular orbital energy. A new charge transfer band emerges that can move across the whole visible spectrum as the push-pull character of the NDI is increased (Figure 1.4).[24, 25] The ability of core-substituted NDIs to come in many colours, coupled to their attractive redox properties has led to their use in artificial photosystems.[26-28]

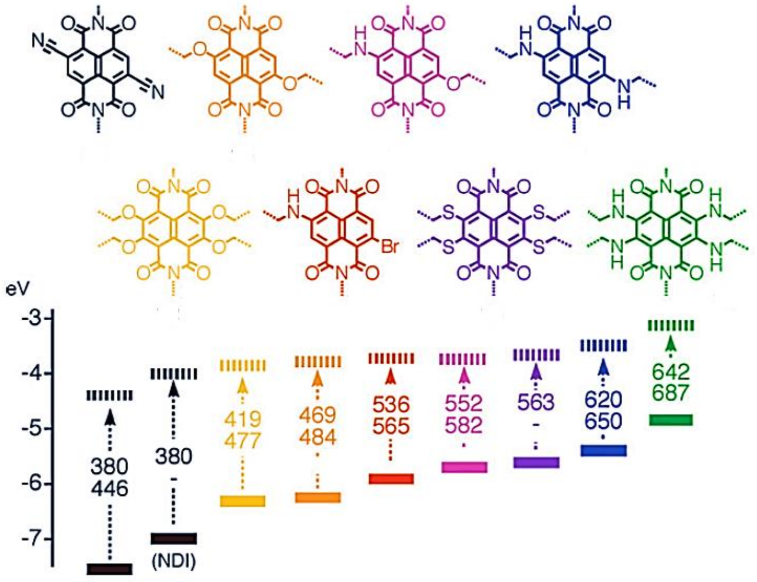

Figure 1.4: A rainbow collection of core-substituted NDIs demonstrating how the optoelectronic properties can be tuned. The HOMO (solid) and LUMO (dashed) energies are shown against vacuum as well as maximal absorption (top) and emission (bottom) wavelengths in nm. Adapted from Sakai et al.[24]

Such artificial photosystems utilise the electron transport properties of NDIs, which have been recognised for some time. Founding research published by Miller and Mann have demonstrated that NDI radical anions exist in π-stacks, permitting electrical conduction along these 'nanowires'.[29] Subsequent work by Katz et al. has identified non-core substituted NDIs that could successfully function as n-type semiconductors even under an atmosphere of air,[30, 31] establishing NDIs as one of just a few known materials that can do this. Since then, the goals of many NDI researchers have been to fabricate systems that can harness the electron transport properties of NDIs, either as devices such as OFETs and OPVs (discussed in Chapter 2) or in charge transfer complexes, where electron donors are coupled to the NDIs, allowing electrons or holes to be moved between the pair (discussed in Chapter 3).

Despite such fascinating properties, as well as the vast potential offered through core-substitution, NDIs have had a slow start with research into them only flourishing after the turn of the millennium. The reason for this (as quoted from a recent NDI review) is that they have been overshadowed somewhat by the higher rylene diimides 'among which perylene diimide is without doubt the most important one'.[21]

1.1.2. Perylene Diimides

PDIs were first reported over 100 years ago, in a patent published by German chemist Kardos[32] and although they possess a more extended structure, were popular as vat dyes and industrial pigments several years before NDIs.[33] The aromatic core of PDIs consists of two naphthalene moieties, joined together by two bonds to create perylene, a polyaromatic structure comprising five fused rings. As for all rylene diimides, two cyclic imide rings are added to the remaining peri positions to create a molecule of PDI (Figure 1.5). The larger aromatic structure means that another set of aromatic core protons is added (compared to NDIs) that are able to be functionalised. In addition to the imide region (dark red), there is the aromatic region closest to the imide groups on each end of the molecule, termed the ortho positions (blue) and the central aromatic region, called the bay positions (green).

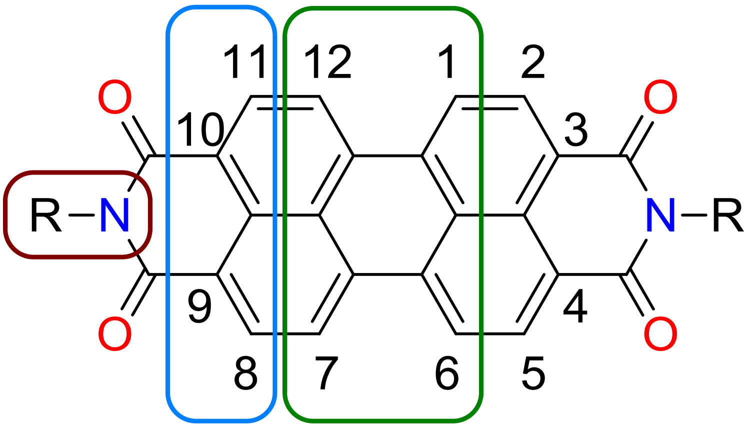

Figure 1.5: Structure and numbering system of PDIs highlighting the imide region (dark red), the ortho region (blue) and the bay region (green).

The extended, planar π-system of PDIs has been long-established crystallographically,[34] and permits intermolecular π-π interactions between the aromatic cores of adjacent PDI molecules. Stacks of parallel molecules form in the solid state, with a separation between the perylene planes ranging from 3.34 to 3.55 Å,[1] similar to the separation between graphene layers in graphite.[35] Owed largely to this stacking and aggregation, PDI molecules exhibit a limited solubility in organic solvents, although the addition of even simple alkyl substituents to the imide position begins to reduce this stacking interaction by causing translational offsets between neighbouring molecules. Among the most frequently used solubilising groups are branched chain 'swallow-tail' alkanes, pioneered by Langhals.[36-39]

The two bonds between the naphthyl rings have more single bond character and thus allow for a twisting of the perylene centre. Substituents to the bay region create torsion of the perylene core as a result of steric clash. This contortion disrupts the π-stacking and further increases solubility.[2] For a tetrachloro bay-substituted PDI, the dihedral angle between the two naphthalene planes is as great as 37°.[40]

PDIs exhibit a broad $S_0 \rightarrow S_1$ absorption band displaying vibrational structure with absorption maxima in the visible region,[41] with extinction coefficients for this absorption typically in the 20,000 to 100,000 $mol^{-1}dm^{3}cm^{-1}$ range.[1, 2] Much like NDIs, substitutions to the imide region do not have a significant effect on the optoelectronic properties of PDIs, due to the frontier orbitals of both systems possessing nodes at these positions.[1, 37] Unlike NDIs, however, PDIs exhibit a much more pronounced fluorescence. The emission profile mirrors the absorbance, with a small Stokes shift and a quantum yield often close to 1.[33, 42] Quenching of this process occurs at high concentration due to aggregation,[43, 44] so is more manifest for PDIs with low solubilities. The solvent environment has little effect on the absorbance and fluorescence profiles of PDIs and the long-term photostability of PDIs makes them especially attractive for applications as light collectors[45] and as biological markers (Figure 1.6).[46, 47]

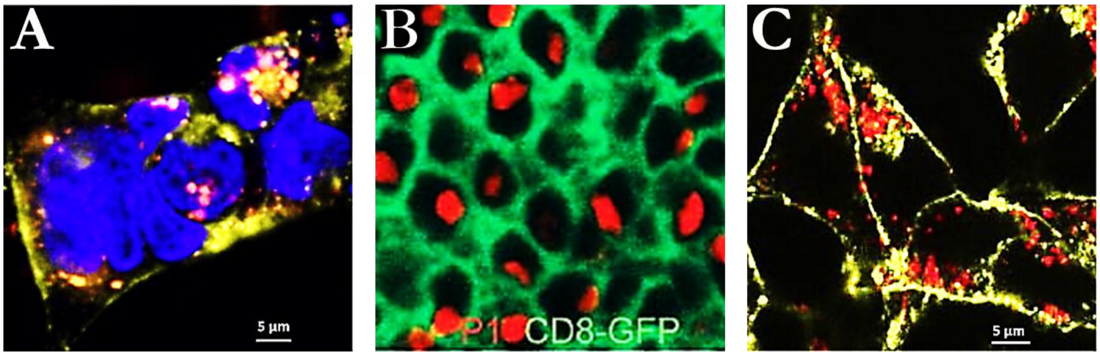

Figure 1.6: Various fluorescent PDIs (red) used as biological markers in tandem with other fluorescent dyes. A and C adapted from Ribeiro et al,[47] B adapted from Ahrens et al.[46]

Two electrons can be added to the core of PDIs at even milder potentials than NDIs, with reversible reductions occurring at -1.0 and -1.2 V (vs. Fc^+/Fc). The electron affinity of the PDI core can be tuned with substitutions to the bay area: electron withdrawing groups such as cyano- and chloro- substantially increase the electron affinity,[48] whereas electron donating groups such as pyrrolidino- or phenoxy- decrease the electron affinity.[1] The electron deficient nature of PDIs accounts for their photostability, limiting destructive photooxidation. The PDI scaffold had also been used to conjugate redox active groups across the perylene core, allowing communication between the centres.[49-51]

The vast majority of substitution to the aromatic core of PDIs is focussed on the bay region, with established synthesis and purification of bay-halogenated PDIs leading to a variety of interesting and useful materials.[52-54] Recently, a route to substitution of the ortho positions has also been demonstrated[55, 56] expanding the library of PDI modifications and allowing new properties to be explored.[57, 58] Furthermore, substitution to the aromatic core has culminated in the synthesis of a fully substituted octachloro-PDI.[41, 59] The Würthner group have investigated some of the properties of such octachloro-PDIs, noting a substantial lowering the LUMO level alongside a highly contorted aromatic backbone, facilitating electron transport.[60]

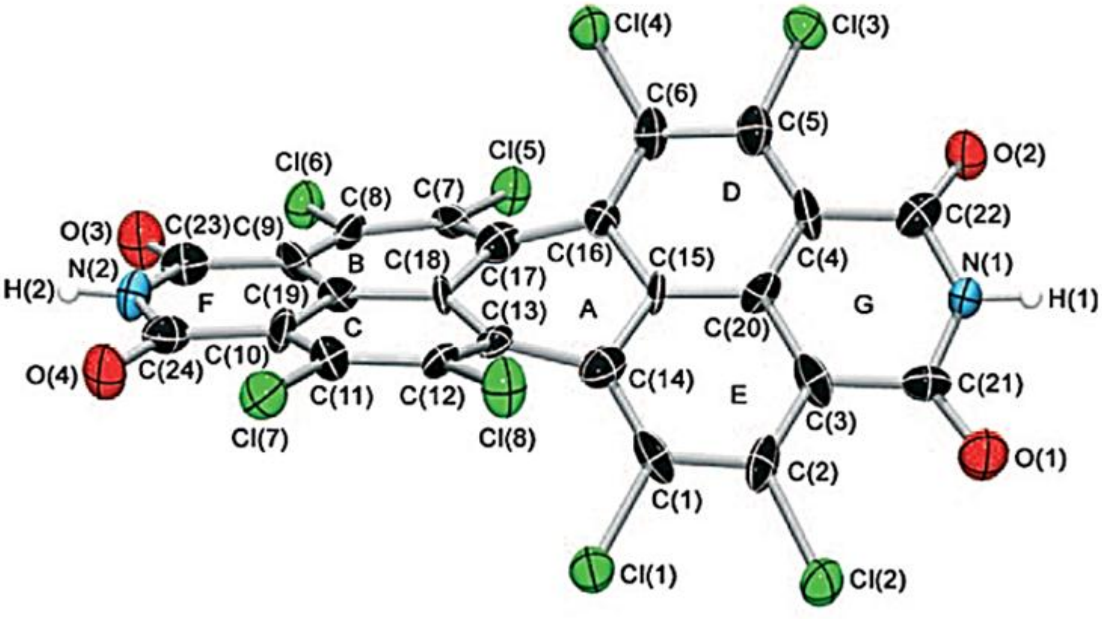

Figure 1.7: Crystal structure of 1,2,5,6,7,8,11,12-octachloroperylene-3,4,9,10-diimide. Reproduced from Gsänger et al.[60]

In spite of a rich history of substitutions to the imide region of rylene diimides, and a mounting interest surrounding modifications to the aromatic cores of NDIs and PDIs, there are presently only very few examples where changes to the carbonyl groups are made in order to alter their properties.

1.2. Thionation of Rylene Diimides

Substitution of molecules with chalcogen elements is a convenient method of altering the optical and electronic properties of a molecule without having to cause large-scale changes in the molecular structure.[61-63] In particular, substitution with sulfur, known as thionation, has been used to convert carbonyl groups into thiocarbonyls. Carbonyl thionation is common in biological applications (where carbonyl groups are prevalent), though has also been used in the imide- and amide- containing molecules phthalimides[64, 65] and diketopyrrolopyrolles.[66-68] As opposed to other thiocarbonyl systems, thioimide compounds tend to be stable.[64]

The first example of successful thionation of rylene diimides was reported in a patent by the Facchetti group in 2011,[69] whereby commercially available thionating reagents were used to achieve sulfur atom substitution of the carboxylic oxygens. NDIs bearing aliphatic imide cyclohexyl and 2-ethylhexyl substituents were reacted with Davy reagent at high temperature to afford a mixture of monothionated and dithionated NDIs (Scheme 1.1). No tetrathionated products were reported, but the 2-ethylhexyl substituted NDI also gave trithionated NDI in a low yield of 0.5 %. The dithionated NDIs formed as a pair of cis- and trans- regioisomers that could be separated by flash chromatography on a silica gel stationary phase.

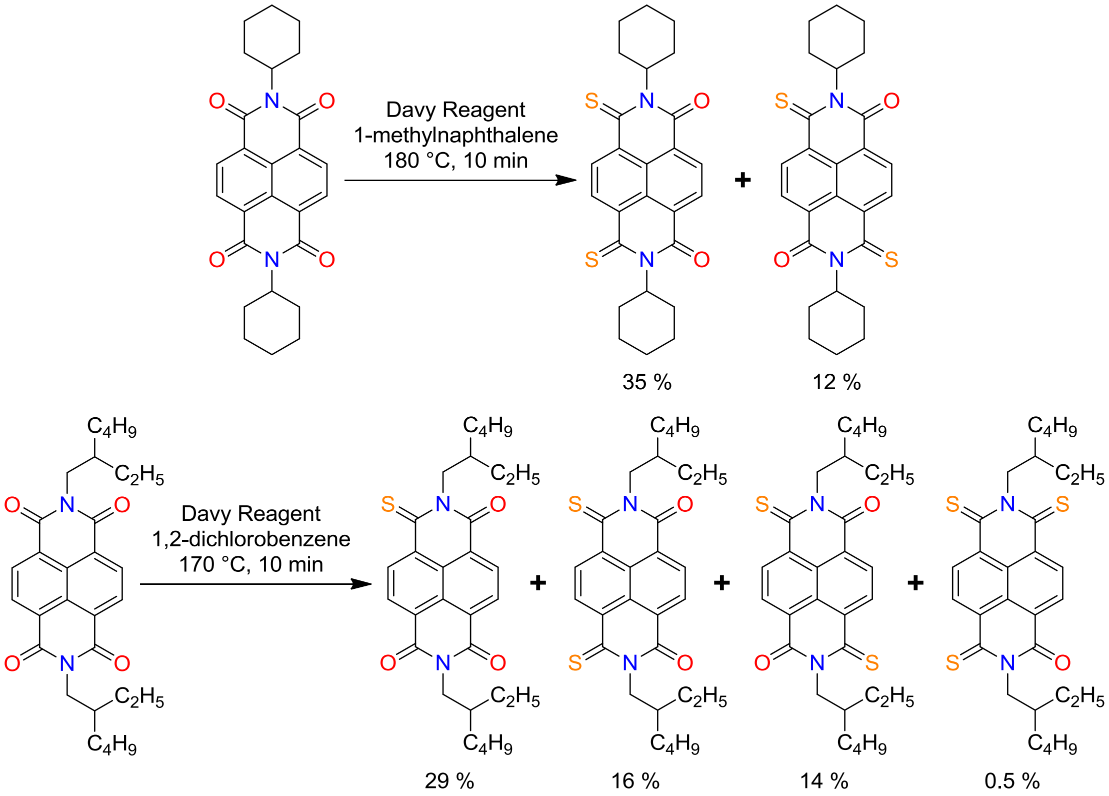

Scheme 1.1: Synthesis of thionated NDIs by Facchetti and co-workers.[69]

The patent also covers thionation of PDIs bearing a variety of aliphatic imide substituents. Once again predominately mono- and dithionated products were obtained, with only trace amounts of the tri- and tetrathionated PDIs isolated. Rudimentary optical absorbance data for the thionated NDI series (0 to 3 sulfur atom substitutions) and PDI series (0 to 4 sulfur atom substitutions) show a distinct bathochromic shift in absorption maxima as the level of thionation increases for both classes of rylene compound. For NDIs, this means moving the absorbance maximum out of the ultraviolet range and into visible wavelengths as the first sulfur atom is substituted.

In 2014, the Seferos group[70] were able to synthesise a complete series of thionated PDIs in significant quantity for photophysical characterisation. Thionation of their 3-hexylundecyl substituted PDI caused a colour change from the deep red of the parent PDI to intense purple blue colours. Optical absorbance spectroscopy revealed that successive sulfur substitution causes a regular bathochromic shift in the absorption maximum from 526 nm (0 sulfurs) to 706 nm (4 sulfurs). Electrochemical measurements combined with theoretical calculations demonstrated that this was due to an increased electron affinity; with reduction potentials becoming less negative as the sulfur content of the PDI was increased. Finally, whereas the nonthionated PDI was strongly fluorescent, with a quantum yield of 0.97, unusually, no fluorescence could be detected for any of the thionated derivatives. Ultrafast transient absorption spectroscopy established that fluorescence quenching occurred due to a highly efficient intersystem crossing to a triplet state irrespective of the level of thionation, attributed to a reordering of the molecular electronic structure (Figure 1.8).

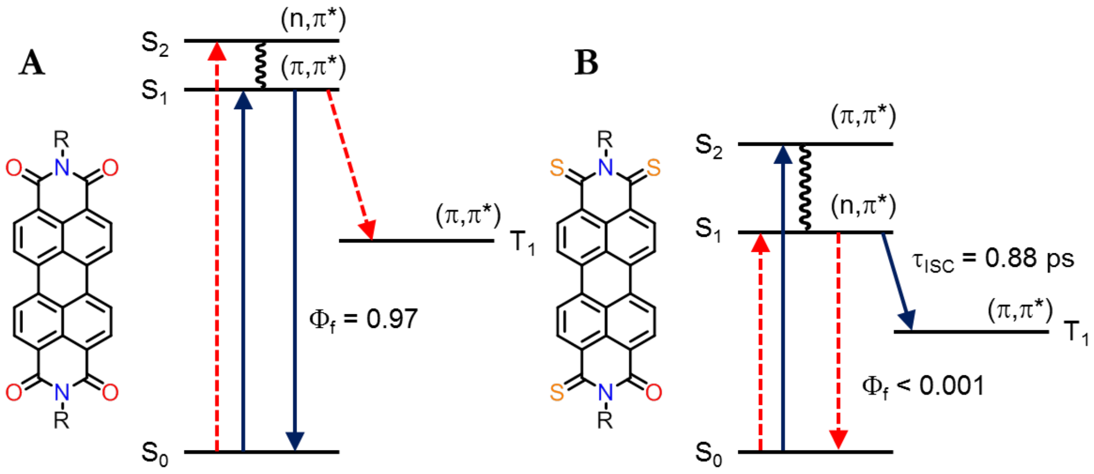

Figure 1.8: Energy level schematic proposed by Tilley et al.[70] of nonthionated PDI (A) and trithionated PDI (B). Blue arrows represent the most likely electronic transitions, red arrows represent less likely transitions. R = 3-hexylundecyl.

The property of forming a triplet exciton is especially promising for a variety of applications, including organic light-emitting diodes,[71, 72] photon upconversion[73, 74] and spintronics.[75, 76] Organic photovoltaic devices can benefit from triplet excited states as their greater diffusion lengths can increase the probability of charge separation occurring at a donor-acceptor boundary, improving photocurrent.

Following on from this, Seferos and co-workers fabricated OFET devices incorporating their thionated PDIs, finding that electron mobility increased with thionation to an average mobility of 0.16 $cm^2V^{-1}s^{-1}$ for the tetrathionated PDI.[77] The average electron mobility for devices constructed using the nonthionated PDI was 0.00069 $cm^2V^{-1}s^{-1}$, over 200 times lower. The rationale for the improved performance resulting from the oxygen-sulfur substitution was attributed to stronger π-π interactions, amongst other solid state properties, that facilitate charge transport.

The first example of NDI thionation followed shortly afterwards from Etheridge et al,[78] who examined the effects of thionation upon core-substituted NDIs. The reaction between a 2,6-dialkylamino substituted NDI and Lawesson's reagent resulted in selective thionation of the carbonyls distal to the core alkylamino substituents; the selectivity attributed to steric hindrance by the alkylamino group at the closer carbonyl.[65] In addition to the trans- regioisomer, the monothionated product from a partial reaction was also isolated and characterised crystallographically (Figure 1.9). Solution phase absorption measurements of their thionated NDI products demonstrated that a 50 nm shift in absorption maximum occurs with each sulfur atom substitution. An anodic shift in reduction potential also followed thionation, but little effect on the oxidation potentials were noted suggesting a reduction in LUMO energy, which was supported by DFT calculations. These effects combined to diminish the optical gap of the dithionated NDI molecule to 1.59 eV, especially low for an NDI.

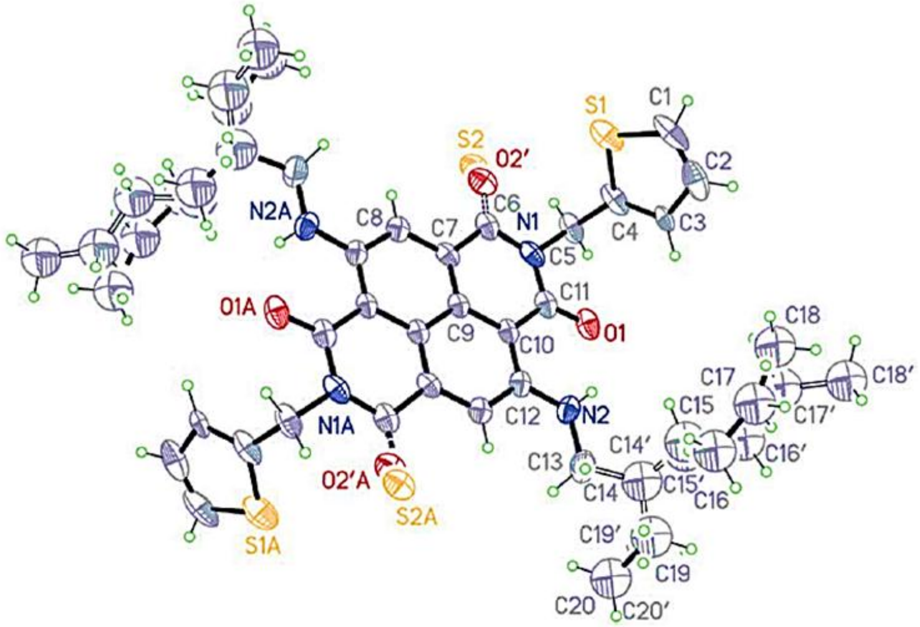

Figure 1.9: Crystal structure of a monothionated NDI reported by Etheridge et al.[78] Sulfur S2 and Oxygen O2’ atoms were found to have structural occupancy factors of 50 %, such that a complete molecule contains just one sulfur atom.

Published shortly afterwards by the Zhang group, organic thin film transistors (OTFTs) were fabricated using a thionated series of NDIs (0 to 3 sulfur atom substitutions) bearing an aliphatic 2-ethylhexyl imide group.[79] The OTFT devices constructed from the thionated NDIs performed significantly better than the nonthionated precursor NDI, with electron mobilities (under ambient conditions) ranging from undetectable, for the nonthionated NDI to 0.01 cm^{2}V^{-1}cm^{-1}, for the trans- isomer of the dithionated NDI. Transistor performance of the lesser thionated NDIs was found to degrade quickly following exposure to air, however, for the trithionated NDI, transistor performance could be maintained after as many as ten operations. The group rationalised that the lower LUMO energy of the trithionated NDI reduces sensitivity to oxygen and moisture. The same month saw another group of researchers report a very similar result for thionated pyromellitic diimides (PyDIs), a related class of aromatic diimide.[80] Thionation improved the air stability and performance of n-type PyDI devices, seeing electron mobilities as high as 0.62 cm^{2}V^{-1}cm^{-1} for one such transistor.

In addition to their work on PDI thionation, the Seferos group have also reported the first example of a tetrathionated NDI, bearing a linear n-dodecyl imide chain.[81] In spite of such a large aliphatic imide group, the solubility of the tetrathionated NDI derivative was found to be too poor for most analytical measurements, and hence only the UV/vis absorption properties are presented; the tetrathionated NDI red-shifted ~40 nm with respect to its trithionated counterpart. For comparison to Zhang's branched alkyl chain NDIs,[79] OTFT devices were constructed for the other members of their thionated NDI series. Whilst electron mobilities were three orders of magnitude greater for the thionated NDIs than the nonthionated parent molecule, no difference in performance was noted with respect to the level of thionation, in contrast to their earlier reports for PDIs.[77] This is perhaps due to the favourable solid state packing permitted by their choice of imide group.

Lastly and from within my own research group, a combination of thionation and secondary amine substitution to the bay region has been used to manufacture PDIs with absorbances in the near infrared.[82] Absorption maxima of 864 and 838 nm are reported for tetrathionated PDIs bearing two morpholine groups in the 1,7- and 1,6- positions respectively. Particularly noteworthy is the tetrathionated 1,6-substituted PDI isomer, which is an unprecedented black colour in solution (Figure 1.10). This is due to the possession of a large molar extinction coefficient across the entire visible spectrum and therefore has excellent potential for use in light harvesting devices.

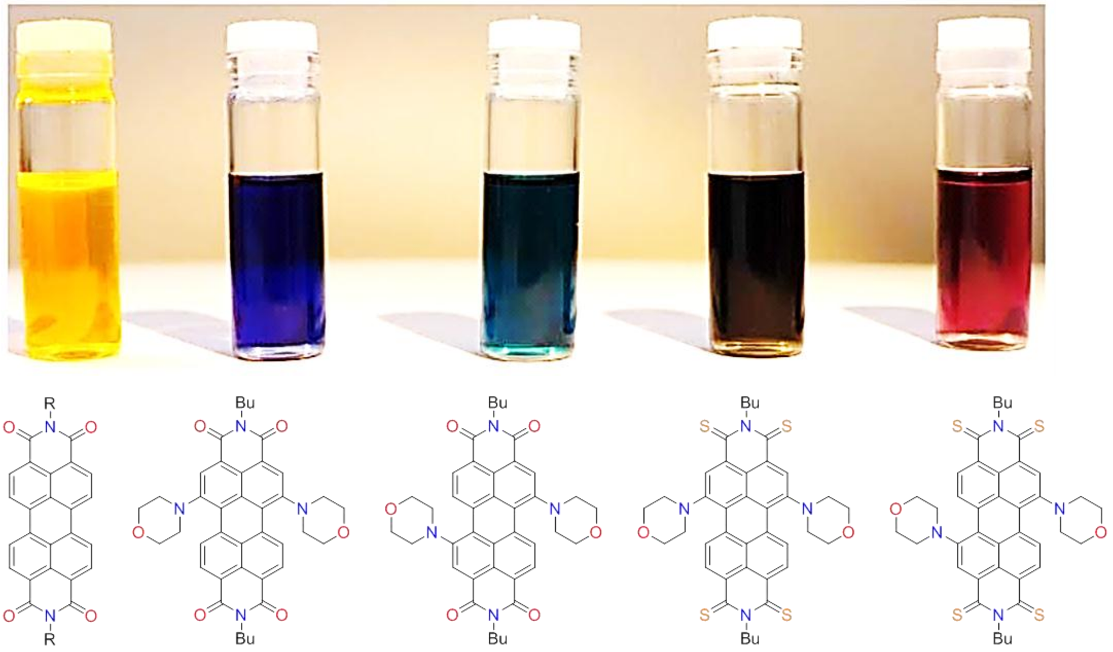

Figure 1.10: Structures and colours of thionated PDIs synthesised by Llewellyn et al.[82]

Overall, early investigations into the thionation of rylene diimides have been extremely promising, establishing thionation as an efficient method of altering the frontier orbital energies significantly. Much of the preliminary work has been limited in scope, usually with only the optical properties for neutral molecules reported, especially in the case of NDIs. The synthesis of more functional molecules is a valuable pursuit.

1.3. Thesis Overview

This thesis focuses on the synthesis and thionation of *N*,*N*'-asymmetrically substituted rylene diimides, in particular, NDIs and PDIs, whose anhydrides are readily available from commercial sources. No modifications to the aromatic core of either the NDIs or PDIs have been made, instead relying on the thionation as the method of altering the energies of the frontier orbitals. Substituting the imide region of rylene diimides with two different groups presents a challenge in itself, as this is not straightforward, although allows for functionality to be imparted on the molecules without having to devote both imide regions to improving solubility.

Chapter 2 explores the electrochemical and optical properties of a thionated NDI series in depth. The thionation of related naphthalic imide (NI) molecules is also investigated.

Chapter 3 examines the synthesis and properties of donor-acceptor systems, where an imide-coupled phenothiazine donor is used alongside NDI and NI acceptors. Ultrafast transient absorption spectroscopy is used to determine charge separation in the molecules.

Chapter 4 looks at the synthesis and characterisation of a variety of *N*,*N*'-asymmetrically imide-substituted perylene diimide molecules. 2,6-(Bisdiphenylmethyl)-4-methylphenyl has been employed as one of the imide groups to great effect; preventing aggregation between perylene cores even in the perylene-3,4-imide-9,10-anhydride form. The properties of thionated donor-acceptor systems of phenothiazine and PDI have also been probed.

Chapter 5 summarises the results of this thesis, highlighting the impact of the results and the scope for further study.

1.4. References

1. F. Wurthner, *Chem. Commun.*, 2004, 1564-1579.
2. Z. Chen, U. Baumeister, C. Tschierske and F. Würthner, *Chem. Eur. J.*, 2007, **13**, 450-465.
3. G. Seybold and G. Wagenblast, *Dyes Pigm.*, 1989, **11**, 303-317.
4. X. Zhan, A. Facchetti, S. Barlow, T. J. Marks, M. A. Ratner, M. R. Wasielewski and S. R. Marder, *Adv. Mater.*, 2011, **23**, 268-284.
5. S.-H. Hwang, C. N. Moorefield and G. R. Newkome, *Chem. Soc. Rev.*, 2008, **37**, 2543-2557.
6. S. Erten, F. Meghdadi, S. Gunes, R. Koeppe, N. S. Sariciftci and S. Icli, *Eur. Phys. J. Appl. Phys.*, 2006, **36**, 225-229.
7. J. G. Laquindanum, H. E. Katz, A. Dodabalapur and A. J. Lovinger, *J. Am. Chem. Soc.*, 1996, **118**, 11331-11332.
8. D. Shukla, S. F. Nelson, D. C. Freeman, M. Rajeswaran, W. G. Ahearn, D. M. Meyer and J. T. Carey, *Chem. Mater.*, 2008, **20**, 7486-7491.
9. M. Sommer, *J. Mater. Chem. C*, 2014, **2**, 3088-3098.
10. H. Langhals, H. Jaschke, U. Ring and P. von Unold, *Angew. Chem. Int. Ed.*, 1999, **38**, 201-203.
11. S. Kalinin, M. Speckbacher, H. Langhals and L. B. A. Johansson, *Phys. Chem. Chem. Phys.*, 2001, **3**, 172-174.
12. A. M. Brouwer, *Pure Appl. Chem.*, 2011, **83**, 2213-2228.
13. Y. Avlasevich, C. Li and K. Mullen, *J. Mater. Chem.*, 2010, **20**, 3814-3826.
14. L. Chen, C. Li and K. Mullen, *J. Mater. Chem. C*, 2014, **2**, 1938-1956.
15. G. Kranzlein and H. Vollmann, *Patent US1920406 A*, 1933.
16. H. Vollmann, *Patent 2087133*, 1937.
17. H. Vollmann, H. Becker, M. Corell and H. Streeck, *Liebigs Ann. Chem.*, 1937, **531**, 1-159.
18. S. Takenaka, M. Mamabe, M. Yokoyama, M. Nishi, J. Tanaka and H. Kondo, *Chem. Commun.*, 1996, 379-380.
19. V. Guelev, J. Lee, J. Ward, S. Sorey, D. W. Hoffman and B. L. Iverson, *Chem. Biol.*, 2001, **8**, 415-425.
20. S. V. Bhosale, C. H. Jani and S. J. Langford, *Chem. Soc. Rev*, 2008, **37**, 331-342.
21. S.-L. Suraru and F. Würthner, *Angew. Chem. Int. Ed.*, 2014, **53**, 7428-7448.
22. G. Andric, J. F. Boas, A. M. Bond, G. D. Fallon, K. P. Ghiggino, C. F. Hogan, J. A. Hutchison, M. A. Lee, S. J. Langford, J. R. Pilbrow, G. J. Troup and C. P. Woodward, *Aust. J. Chem.*, 2004, **57**, 1011-1019.
23. F. Würthner, S. Ahmed, C. Thalacker and T. Debaerdemaeker, *Chem. Eur. J.*, 2002, **8**, 4742-4750.
24. N. Sakai, J. Mareda, E. Vauthey and S. Matile, *Chem. Commun.*, 2010, **46**, 4225-4237.
25. S. V. Bhosale, S. V. Bhosale and S. K. Bhargava, *Org. Biomol. Chem.*, 2012, **10**, 6455-6468.
26. N. Sakai, R. Bhosale, D. Emery, J. Mareda and S. Matile, *J. Am. Chem. Soc.*, 2010, **132**, 6923-6925.
27. V. L. Gunderson, A. L. Smeigh, C. H. Kim, D. T. Co and M. R. Wasielewski, *J. Am. Chem. Soc.*, 2012, **134**, 4363-4372.
28. R. Bhosale, J. Misek, N. Sakai and S. Matile, *Chem. Soc. Rev.*, 2010, **39**, 138-149.
29. L. L. Miller and K. R. Mann, *Acc. Chem. Res.*, 1996, **29**, 417-423.

30. H. E. Katz, A. J. Lovinger, J. Johnson, C. Kloc, T. Siegrist, W. Li, Y. Y. Lin and A. Dodabalapur, *Nature*, 2000, **404**, 478-481.
31. H. E. Katz, J. Johnson, A. J. Lovinger and W. Li, *J. Am. Chem. Soc.*, 2000, **122**, 7787-7792.
32. M. Kardos, *Patent 276357*, 1913.
33. H. Zollinger, *Color Chemistry: Syntheses, Properties, and Applications of Organic Dyes and Pigments*, Wiley-VCH, Germany, 3rd edn., 1991.
34. D. M. Donaldson, J. M. Robertson and J. G. White, *Proc. R. Soc. Lond. Series A.*, 1953, **220**, 311-321.
35. P. Delhaès, *Graphite and precursors*, Gordon and Breach Science Publishers, 1st edn., 2001.
36. H. Langhals, *Heterocycles*, 1995, **40**, 477-500.
37. H. Langhals, S. Demmig and H. Huber, *Spectrochim. Acta A*, 1988, **44**, 1189-1193.
38. H. Langhals, R. Ismael and O. Yürük, *Tetrahedron*, 2000, **56**, 5435-5441.
39. A. Wicklein, A. Lang, M. Muth and M. Thelakkat, *J. Am. Chem. Soc.*, 2009, **131**, 14442-14453.
40. Z. Chen, M. G. Debije, T. Debaerdemaeker, P. Osswald and F. Würthner, *ChemPhysChem*, 2004, **5**, 137-140.
41. M. Sadrai, L. Hadel, R. R. Sauers, S. Husain, K. Krogh-Jespersen, J. D. Westbrook and G. R. Bird, *J. Phys. Chem.*, 1992, **96**, 7988-7996.
42. A. Miasojedovas, K. Kazlauskas, G. Armonaite, V. Sivamurugan, S. Valiyaveettil, J. V. Grazulevicius and S. Jursenas, *Dyes Pigm.*, 2012, **92**, 1285-1291.
43. W. E. Ford and P. V. Kamat, *J. Phys. Chem.*, 1987, **91**, 6373-6380.
44. E. Z. M. Ebeid, S. A. El-Daly and H. Langhals, *J. Phys. Chem.*, 1988, **92**, 4565-4568.
45. K. Balakrishnan, *Self-assembly of Organic Semiconducting Molecules Into One-dimensional Nanostructures*, Southern Illinois University at Carbondale, 2008.
46. M. Yin, J. Shen, R. Gropeanu, G. O. Pflugfelder, T. Weil and K. Müllen, *Small*, 2008, **4**, 894-898.
47. T. Ribeiro, S. Raja, A. S. Rodrigues, F. Fernandes, C. Baleizão and J. P. S. Farinha, *Dyes Pigm.*, 2014, **110**, 227-234.
48. M. J. Ahrens, M. J. Fuller and M. R. Wasielewski, *Chem. Mater.*, 2003, **15**, 2684-2686.
49. B. A. Llewellyn, A. G. Slater, G. Goretzki, T. L. Easun, X.-Z. Sun, E. S. Davies, S. P. Argent, W. Lewis, A. Beeby, M. W. George and N. R. Champness, *Dalton Trans.*, 2014, **43**, 85-94.
50. T. W. Chamberlain, E. S. Davies, A. N. Khlobystov and N. R. Champness, *Chem. Eur. J.*, 2011, **17**, 3759-3767.
51. G. Goretzki, E. S. Davies, S. P. Argent, J. E. Warren, A. J. Blake and N. R. Champness, *Inorg. Chem.*, 2009, **48**, 10264-10274.
52. A. Boehm, H. Arms, G. Henning and P. Blaschka, *German Patent DE 19547209 A1*, 1997, **BASF**.
53. F. Würthner, V. Stepanenko, Z. Chen, C. R. Saha-Möller, N. Kocher and D. Stalke, *J. Org. Chem.*, 2004, **69**, 7933-7939.
54. P. Rajasingh, R. Cohen, E. Shirman, L. J. W. Shimon and B. Rybtchinski, *J. Org. Chem.*, 2007, **72**, 5973-5979.
55. S. Nakazono, S. Easwaramoorthi, D. Kim, H. Shinokubo and A. Osuka, *Org. Lett.*, 2009, **11**, 5426-5429.
56. S. Nakazono, Y. Imazaki, H. Yoo, J. Yang, T. Sasamori, N. Tokitoh, T. Cédric, H. Kageyama, D. Kim, H. Shinokubo and A. Osuka, *Chem. Eur. J.*, 2009, **15**, 7530-7533.

57. D. Dasgupta, A. M. Kendhale, M. G. Debije, J. ter Schiphorst, I. K. Shishmanova, G. Portale and A. P. H. J. Schenning, *ChemistryOpen*, 2014, **3**, 138-141.
58. T. T. Clikeman, E. V. Bukovsky, X.-B. Wang, Y.-S. Chen, G. Rumbles, S. H. Strauss and O. V. Boltalina, *Euro. J. Org. Chem.*, 2015, **2015**, 6641-6654.
59. M. Sadrai, G. R. Bird, J. A. Potenza and H. J. Schugar, *Acta Cryst. C*, 1990, **46**, 637-640.
60. M. Gsänger, J. H. Oh, M. Könemann, H. W. Höffken, A.-M. Krause, Z. Bao and F. Würthner, *Angew. Chem. Int. Ed.*, 2010, **49**, 740-743.
61. R. D. Pensack, Y. Song, T. M. McCormick, A. A. Jahnke, J. Hollinger, D. S. Seferos and G. D. Scholes, *J. Phys. Chem. B*, 2014, **118**, 2589-2597.
62. G. L. Gibson, T. M. McCormick and D. S. Seferos, *J. Phys. Chem. C*, 2013, **117**, 16606-16615.
63. M. Chattopadhyaya, S. Sen, M. M. Alam and S. Chakrabarti, *J. Chem. Phys.*, 2012, **136**, 094904.
64. D. Melon-Ksyta, A. Orzeszko, W. Borys and K. Czuprynski, *J. Mater. Chem.*, 2002, **12**, 1311-1315.
65. A. Orzeszko, J. K. Maurin and D. Melon-Ksyta, *Z. Naturforsch B*, 2001, **56**, 1035-1040.
66. J. Mizuguchi, A. C. Rochat and G. Rihs, *Ber. Bunsenges. Phys. Chem.*, 1992, **96**, 607-619.
67. J. Mizuguchi, *J. Phys. Chem. A*, 2001, **105**, 1125-1130.
68. S. Lévesque, D. Gendron, N. Bérubé, F. Grenier, M. Leclerc and M. Côté, *J. Phys. Chem. C*, 2014, **118**, 3953-3959.
69. J. Quinn, Y. Zheng, Z. Chen, H. Usta, C. Newman, H. Yan and A. Facchetti, *US Patent 0155247 A1*, 2011.
70. A. J. Tilley, R. D. Pensack, T. S. Lee, B. Djukic, G. D. Scholes and D. S. Seferos, *J. Phys. Chem. C*, 2014, **118**, 9996-10004.
71. A. van Dijken, J. J. A. M. Bastiaansen, N. M. M. Kiggen, B. M. W. Langeveld, C. Rothe, A. Monkman, I. Bach, P. Stössel and K. Brunner, *J. Am. Chem. Soc.*, 2004, **126**, 7718-7727.
72. H. Yersin, in *Transition Metal and Rare Earth Compounds*, Springer Berlin Heidelberg, 2004, vol. 241, pp. 1-26.
73. T. N. Singh-Rachford and F. N. Castellano, *Coord. Chem. Rev.*, 2010, **254**, 2560-2573.
74. T. N. Singh-Rachford and F. N. Castellano, *J. Phys. Chem. Lett.*, 2010, **1**, 195-200.
75. V. A. Dediu, L. E. Hueso, I. Bergenti and C. Taliani, *Nat. Mater.*, 2009, **8**, 707-716.
76. A. Monkman and R. H. Friend, *Phil. Trans. R. Soc. A*, 2015, **373**.
77. A. J. Tilley, C. Guo, M. B. Miltenburg, T. B. Schon, H. Yan, Y. Li and D. S. Seferos, *Adv. Funct. Mater.*, 2015, **25**, 3321-3329.
78. F. S. Etheridge, R. Fernando, J. A. Golen, A. L. Rheingold and G. Sauve, *RSC Adv.*, 2015, **5**, 46534-46539.
79. W. Chen, J. Zhang, G. Long, Y. Liu and Q. Zhang, *J. Mater. Chem. C*, 2015, **3**, 8219-8224.
80. T.-F. Yang, S.-H. Huang, Y.-P. Chiu, B.-H. Chen, Y.-W. Shih, Y.-C. Chang, J.-Y. Yao, Y.-J. Lee and M.-Y. Kuo, *Chem. Commun.*, 2015, **51**, 13772-13775.
81. L. M. Kozycz, C. Guo, J. G. Manion, A. J. Tilley, A. J. Lough, Y. Li and D. S. Seferos, *J. Mater. Chem. C*, 2015, **3**, 11505-11515.
82. B. A. Llewellyn, E. S. Davies, C. R. Pfeiffer, M. Cooper, W. Lewis and N. R. Champness, *Chem. Commun.*, 2016, **52**, 2099-2102.

Chapter 2

Electrochemistry of Thionated Naphthalene Diimides

2.1. Introduction

NDIs are a versatile class of electron-transporting materials with excellent thermal, chemical and photochemical stabilities. NDIs possess both high electron affinities and mobilities, making them ideal candidate materials for organic electronic applications. These applications include photovoltaic cells, field-effect transistors (Figure 2.1), logic gates and organic n/p junctions, materials that form the foundation of the current computing climate. As such, research into organic electronics is increasingly vital.

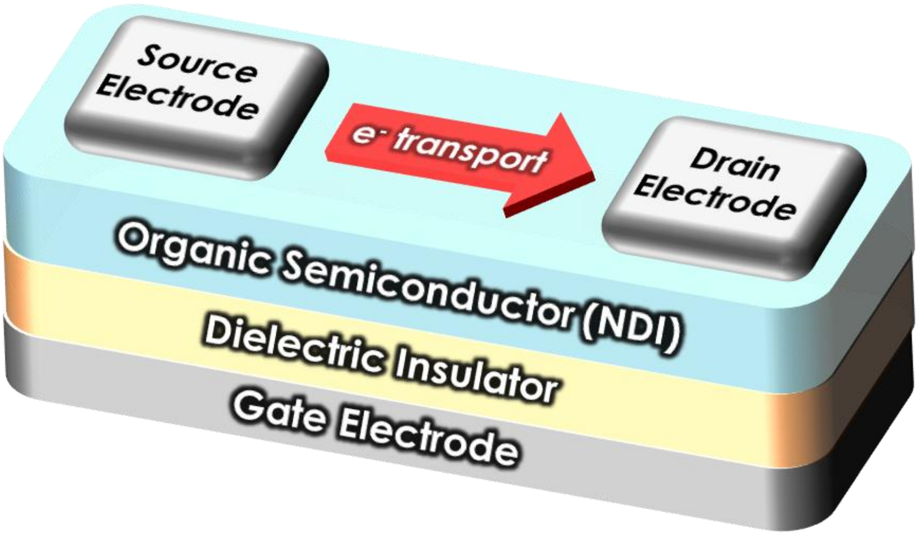

Figure 2.1: Schematic diagram of a typical n-type OFET device using NDI as the organic semiconductor.

2.1.1. Organic Electronics

Organic materials with useful charge-transport properties are either small molecule or polymeric π-conjugated compounds that allow charge carriers to travel under an electric field. Electrons can be removed either from filled molecular orbitals (hole-transporting), or from the addition of electrons to empty orbitals (electron-transporting).[1] In contrast to classical inorganic n- and p-type semiconductors, organic charge-transporting materials are undoped, with fewer charge carriers present unless under an applied electric field.

Carriers can be introduced to the system via injection from electrodes, from nearby organic compounds or by photoexcitation (see Chapter 3).[2]

The electron mobility of an organic compound is a physical property that characterises the ability of charge carriers to migrate under the influence of an electric field. Charge transport is the successive transfer of electrons between neutral and charged molecular units, either as repeating monomers in a polymer or as discrete molecular entities. Hole transporters utilise localised cationic species, whereas electron transporters require anions and the charge is passed to a corresponding neutral moiety.[3] Generally, the development of electron-transporting materials has lagged behind that of hole-transporters, despite importance in the applications listed above.

For ideal performance in photovoltaic cells and field-effect transistors, an electron transporting material should have an electron affinity between 3 and 5 eV, good intermolecular orbital overlap and air stability (ideally for both neutral and anionic species).[2] A solution phase electrochemical reduction potential greater than -1.16 V vs. Fc^+/Fc is considered necessary to stabilise the charge carriers in electron-transporting materials with respect to water reduction, equating to a LUMO energy of ~3.7 eV.[2, 4] NDIs are one of a limited number of materials that satisfy these requirements.

2.1.2. NDIs in Organic Electronics

The first attempt to manufacture an organic field-effect transistor (OFET) from an NDI (**2a**) was published in 1996 by Katz and co-workers.[5] An electron mobility of 10^{-4} $cm^2V^{-1}s^{-1}$ under vacuum was achieved for their device at room temperature, but diminished significantly under an air atmosphere. Substituting the hydrogen functionalised imide group (**2a**) enhanced both the performance and air stability of their transistors. An imide octyl group (**2b**) increased mobility to 0.16 $cm^2V^{-1}s^{-1}$ under vacuum, and a perfluorocarbon chain (**2c**) granted the device superior air stability.[6] The fluorocarbon chain promotes closer packing in the solid state which acts as an atmospheric barrier. Various other changes to the imide substituents have been explored affecting intermolecular packing, yielding NDI based OFETs with electron mobilities as high as 6.2 cm^{2}V^{-1}s^{-1} (under vacuum) for a cyclohexyl NDI (**2d**).[7] These non-core substituted diimides have negligible absorption in the visible region permitting their use in optically transparent devices.[8]

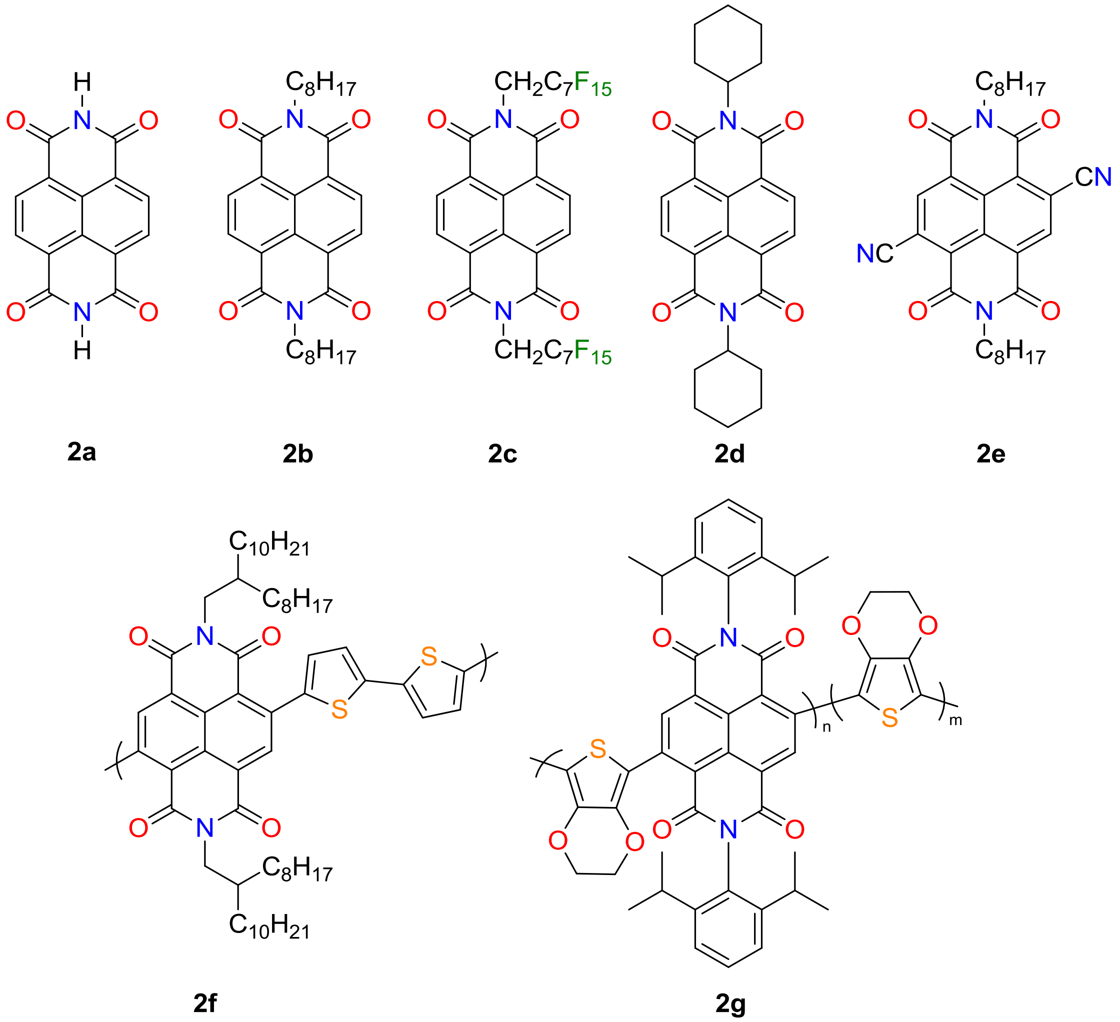

Figure 2.2: Structures of NDI compounds used in organic electronic devices.

Additional electron withdrawing groups attached to the NDI core (such as cyano and fluoro) improve electron affinity even further, and decrease LUMO energy significantly thereby improving air stability. Cyano-substituted NDI (**2e**) OFET devices could operate in air with mobilities as large as 0.11 $cm^2V^{-1}s^{-1}$.[9] Thin film transistors constructed from an NDI polymer (**2f**), of repeating monomer units linked at the NDI core with thiophenes could maintain electron mobilities in the 10^{-2} $cm^2V^{-1}s^{-1}$ range after three months without diminishing substantially.[10] An organic solar cell has even been fabricated from an NDI-EDOT polymer (**2g**) with an efficiency of ~0.15 %,[11] establishing the importance of NDIs in the field of organic electronics.

Chapter 1 discusses some of the early research into OFET and OTFT devices fabricated from rylene diimides that have had their imide oxygen atoms exchanged with sulfur. Improvements in both air stability[12] and electron mobility[12, 13] have been noted for these thionated analogues and are especially promising results, however a full electrochemical characterisation of thionated NDI compounds has not yet been reported.

2.2. Results and Discussion

2.2.1. Synthesis of a Series of Thionated NDIs

For comparison of the properties of nonthionated and thionated NDIs, a nonthionated control NDI (**NDIS$_0$**) was synthesised using a typical imidization procedure.[14] Commercially available naphthalene-1,4,5,8-tetracarboxylic dianhydride and 3-aminopentane were condensed in DMF to afford **NDIS$_0$** in acceptable yield (Scheme 2.1). The solid product was a pale pink colour, unusual for an NDI lacking core substituents, which are typically colourless or beige.[15] 3-aminopentane was selected since imide-substitution of NDIs with branched chain alkanes is a simple method of providing solubility by disrupting π-stacking between the naphthalene cores.[16] Furthermore, unlike the more commonly used 2-ethylhexyl- chain, 1-ethylpropyl- (from 3-aminopentane) facilitates crystallographic characterisation by lacking both a chiral centre and conformational entropy.

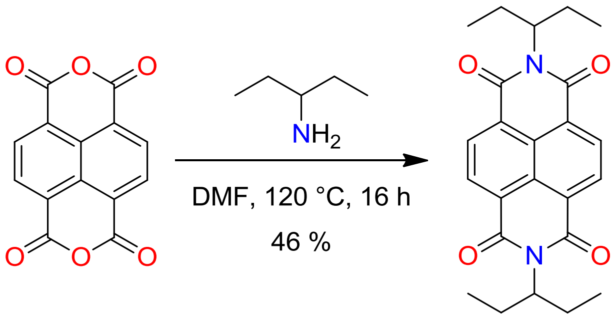

NDIS$_0$

Scheme 2.1: Synthesis of NDIS$_0$.

The thionated NDIs were prepared by the treatment of **NDIS$_0$** with Lawesson's reagent, which is able to convert the NDI carbonyls into thiocarbonyls, in toluene (Scheme 2.2). During the course of the reaction, the initially colourless mixture turned a dark brown. Analysis of the crude reaction mixture with mass spectrometry indicated the presence of molecular ions with masses corresponding to mono- and dithionated products. Thin layer chromatography of the crude mixture revealed three distinct spots; combined with the information from mass spectrometry and results from Tilley et al.,[17] it was presumed that cis and trans isomers of the dithionated products were obtained.

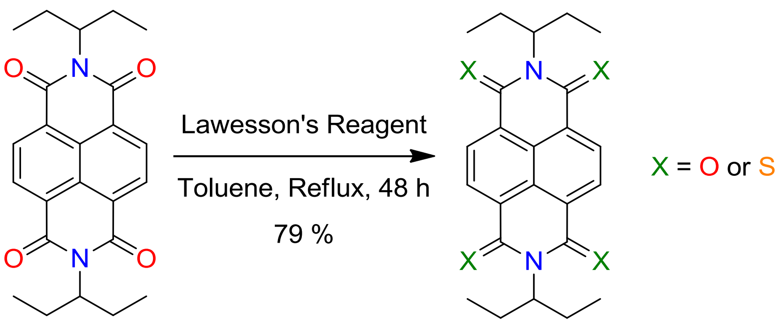

$NDIS_0$

Scheme 2.2: Synthesis of thionated NDIs.

The three thionated products of this reaction (Figure 2.3) could be separated with silica gel column chromatography, using a gradient elution from 1:1 pentane: dichloromethane to pure dichloromethane. ^{1}H NMR spectroscopy of these products provided structural assignments of **$NDIS_1$**, **$NDIS_2$ cis** and **$NDIS_2$ trans**. The cis isomer possesses a C_2 symmetry axis perpendicular to the length of the molecule, such that the hydrogen atoms on the same side of the aromatic core are chemically equivalent and do not couple to each other, resulting in singlet peaks in the aromatic region. The trans isomer lacks this symmetry axis, and so doublets were observed for the aromatic hydrogen atoms. A third dithionated isomer is also possible: **$NDIS_2$ gem**, with the sulfur atoms in geminate positions, on the same imide group, however this was not observed. The trans and gem isomers would be distinguishable by 1D ^{1}H NMR spectroscopy because the alkyl chains at the imide positions would be inequivalent for the gem isomer, but not the trans, so an additional set of peaks would be present in the aliphatic region of the NMR spectrum.

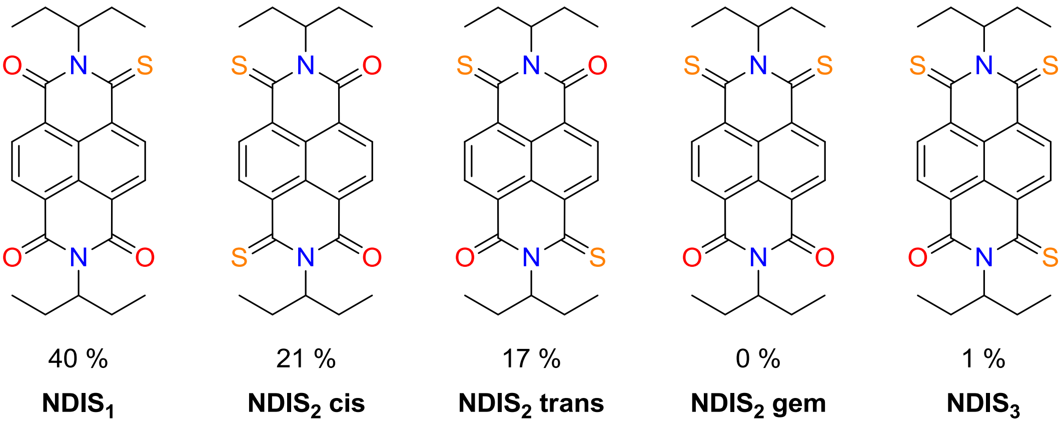

Figure 2.3: Structures and nomenclature of thionated NDI products. Yields of products according to synthesis described in Scheme 2.2 are shown.

In addition to the products already mentioned, **NDIS$_3$** was also present in small quantity. The trithionated product was short lived, decomposing after ~24 hours. Tilley et al.[17] propose 'it is likely that it is unfavourable for thionation to occur at two adjacent carbonyl positions', explaining their own absence of a geminate PDI isomer, equivalent to **NDIS$_2$ gem** above. This result could explain why so little **NDIS$_3$** was obtained: to substitute three (or more) sulfur atoms requires that substitution occurs on adjacent carbonyls. Overcoming this barrier might be too difficult in the case of these NDIs and additionally the higher thionated species appear to decompose, suggesting why so little trithionated and no tetrathionated NDI were attained. Zhang and coworkers were also unable to synthesise tetrathionated NDI with a branched aliphatic imide group, considering 'the reactivity of [Lawesson's reagent] is not strong enough to replace the fourth oxygen'.[12]

To investigate substitution on adjacent carbonyls, naphthalic imide **NIS$_0$** was used as a model system, possessing only a single imide group. Under similar thionation conditions, if any dithionated **NIS$_2$** was produced, then thionation on adjacent carbonyls should be possible. Despite a long reaction time and increased Lawesson's reagent stoichiometry, no significant quantity of **NIS$_2$** was obtained, implying the existence of a barrier to full sulfur substitution across the 1-ethylpropyl substituted imide (Scheme 2.3).

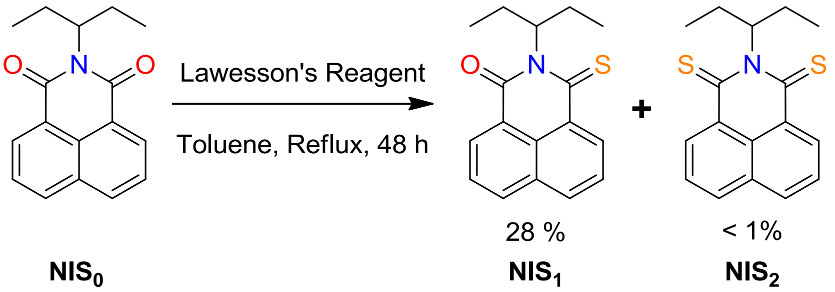

Scheme 2.3: Synthesis of thionated NIs.

Regardless of the impairment to thionation of both sides of a carbonyl, attempts to synthesise trithionated and tetrathionated NDI were undertaken. A mixture of the dithionated NDIs were treated with more Lawesson's reagent in refluxing toluene (Scheme 2.4). If any thionation reaction occurred, it could be guaranteed that at least trithionated NDI would be obtained. This approach proved more successful, affording **NDIS$_3$** in 6 % yield, sufficient for electrochemical analysis.

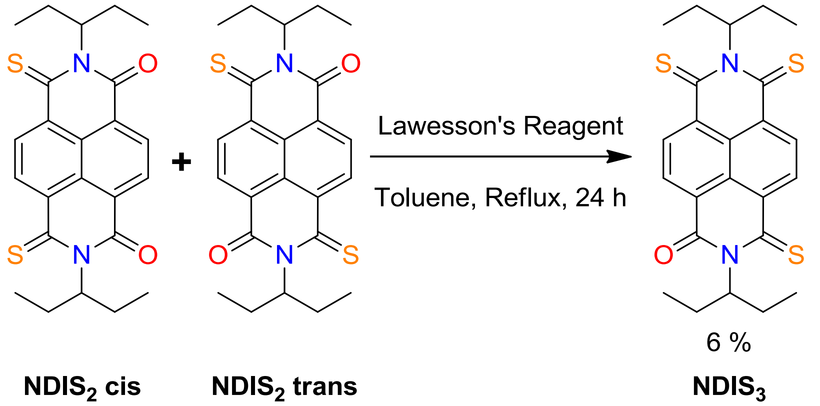

Scheme 2.4: Synthesis of NDIS$_3$.

Typically for NDIs, **NDIS$_0$** forms colourless solutions in organic solvents, only absorbing light with wavelengths below 400 nm. The thionated NDIs, however, form coloured solutions in dichloromethane: **NDIS$_1$** is green, the **NDIS$_2$** isomers are a similar shade of brown and **NDIS$_3$** has a reddish colour (Figure 2.4). The optical properties are discussed in more detail below.

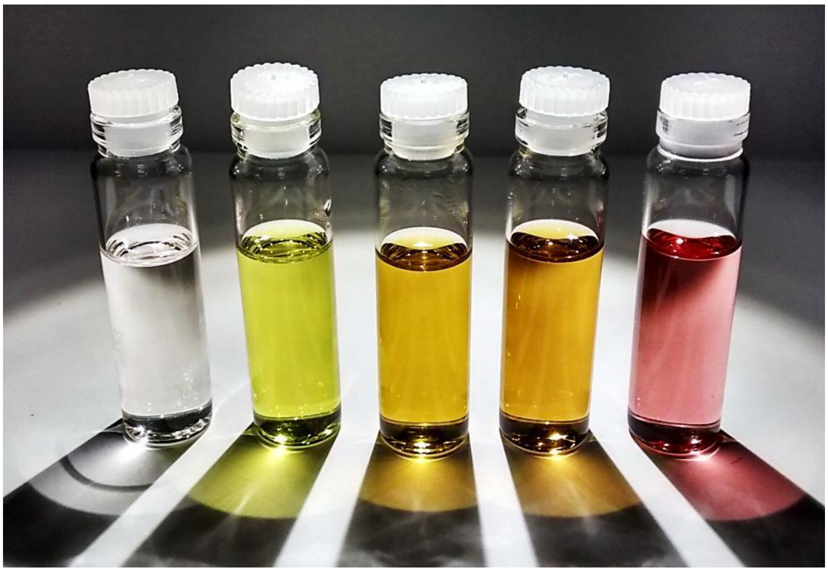

Figure 2.4: Colours of thionated NDIs as dichloromethane solutions. Left to right: NDIS$_0$, NDIS$_1$, NDIS$_2$ cis, NDIS$_2$ trans and NDIS$_3$.

2.2.2. X-ray Crystallography

Single crystals suitable for X-ray diffraction were obtained for **NDIS$_0$**, **NDIS$_1$** and **NDIS$_2$ trans** (Figure 2.5) by slow evaporation of chloroform solutions of the compounds. All structures are very similar; with planar aromatic cores and the aliphatic 1-ethylpropyl chain perpendicular to this plane. Additionally, molecules of each NDI species pack in a similar manner, with a herringbone arrangement of adjacent molecules. Instead of the aromatic cores of neighbouring molecules π-π stacking, as is common for NDIs, the aliphatic imide chain actually interacts with the naphthalene core of a nearby molecule, with an average separation between the hydrogen atoms of this imide alkyl chain and the plane of the naphthalene core of ~3.0 Å (Figure 2.6). Both thionated NDIs crystallise in the monoclinic space group $P2_1/c$, with half a molecule in the asymmetric unit. **NDIS$_0$** is slightly different, crystallising in the $P2_1/n$ space group and thus having a complete molecule in the asymmetric unit.

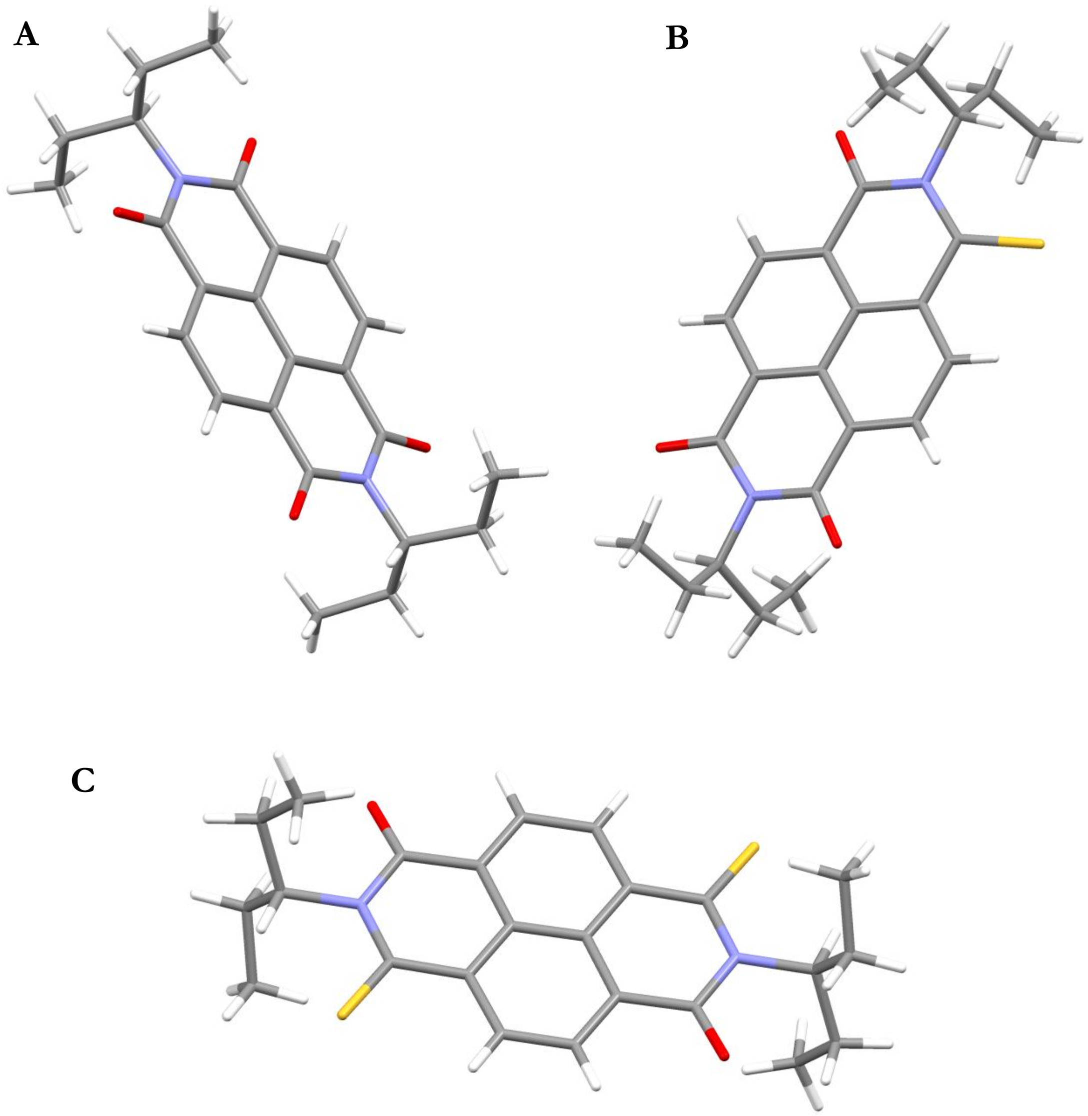

Figure 2.5: X-ray crystal structures of thionated NDIs. A: NDIS$_0$, B: NDIS$_1$, C: NDIS$_2$ trans. Atom colours - C: grey, O: red, N: blue, H: white and S: yellow.

The crystal structure of compound **NDIS$_1$** exhibits a substitutional replacement of its oxygen and sulfur atoms. The oxygen atom has a non-integral site occupancy factor (SOF) of 0.75 and the sulfur's SOF is 0.25, such that across the four possible carbonyl positions there is an average of 3 oxygen atoms and 1 sulfur atom, consistent with the molecule's empirical formula. No substitutional replacement of oxygen and sulfur is observed for **NDIS$_2$ trans** which would indicate that during crystal growth of **NDIS$_1$**, nucleating molecules align randomly with respect to each neighbour, but for **NDIS$_2$ trans**, molecules arrange in a fixed relative orientation, so no fractional SOFs arise.

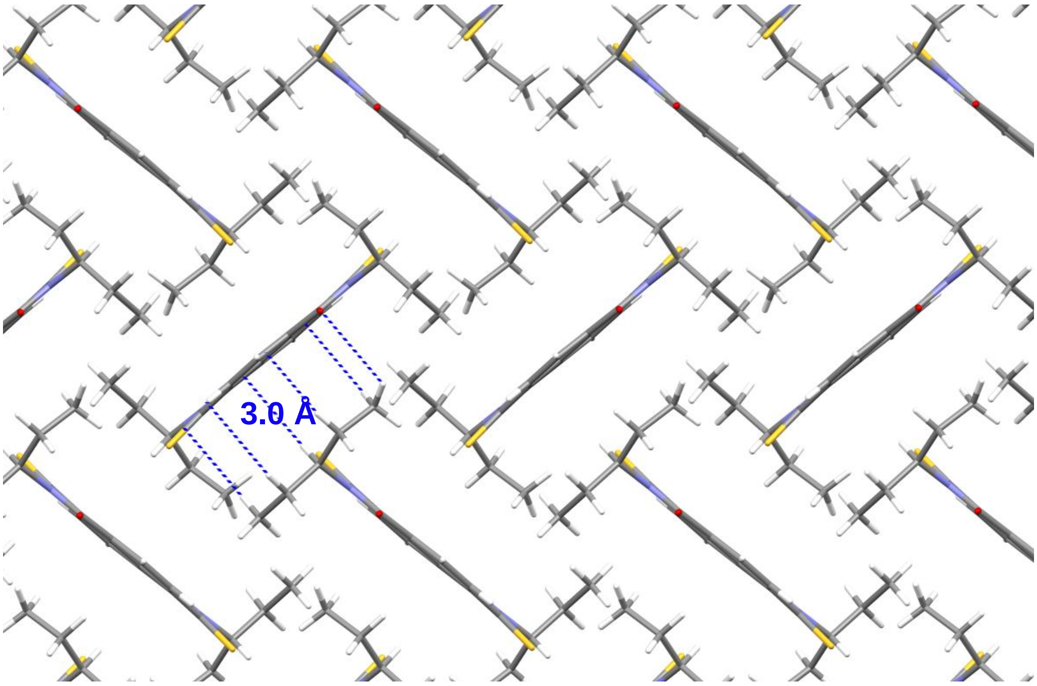

Figure 2.6: Packing motif of $NDIS_2$ trans molecules in a single crystal, displaying a herringbone arrangement. Atom colours - C: grey, O: red, N: blue, H: white and S: yellow. Blue dashed lines: shortest contacts between NDI plane and imide chain hydrogen atoms.

2.2.3. Electrochemistry

The electrochemical properties of the thionated NDI series were fully examined using a combination of electroanalytical techniques. Cyclic voltammetry was initially used to determine the number and nature of redox processes for each molecule of the thionated series. If a reversible process was observed, spectroelectrochemistry was employed to probe the chemical stability and UV/vis absorbance profiles of the resultant species. Finally, when appropriate, bulk electrolysis in tandem with electron paramagnetic resonance spectroscopy was used to provide information about the location of unpaired electrons on electrochemically generated radicals.

2.2.3.1. Cyclic Voltammetry

Cyclic voltammograms for each member of the thionated NDI series exhibit two redox couples (Figure 2.7). Each couple was studied in detail at five different potential sweep rates: 300, 200, 100, 50 and 20 mVs^{-1}. Both the overall shape of the voltammogram as well as the potential at the peak anodic and cathodic currents were found to be independent of the scan rate, signifying that each couple is reversible. Moreover, the peak currents were directly proportional to the square root of the scan rate, verifying this reversibility. Without exception, each process was stable to multiple scans. Coulometry measurements during bulk electrolysis revealed each redox process to be a one-electron reduction.

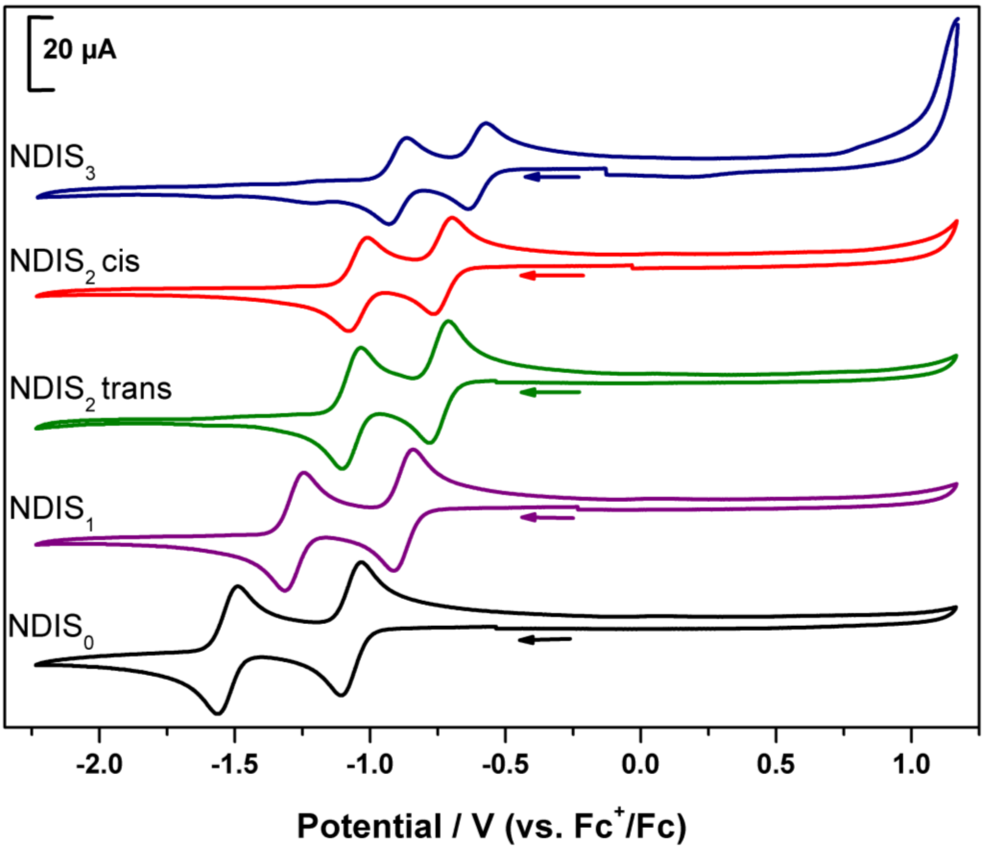

Figure 2.7: Cyclic voltammograms of the thionated NDI series in dichloromethane containing 0.4 M [^{n}Bu$_4$N][BF$_4$] as the supporting electrolyte, with a scan rate of 100 mVs^{-1}. Black: NDIS$_0$, purple: NDIS$_1$, green: NDIS$_2$ trans, red NDIS$_2$ cis, blue: NDIS$_3$.

The first reduction potential for the nonthionated **NDIS$_0$** occurs at -1.07 V (vs. Fc$^+$/Fc), representative for this type of compound. As the level of thionation increases, the first reduction potentials become less negative by ~150 mV per sulfur substitution. The observed increase in electron affinity of NDIs with thionation is most likely due to a decrease in LUMO energy; the addition of an electron into the LUMO of the molecule becomes easier, so occurs at a less extreme potential. A similar trend is displayed more prominently (~200 mV per sulfur substitution) for the second reduction potentials of each compound, such that the difference between first and second reduction potentials decreases with thionation. This data is summarised below (Table 2.1). Slight peaks are noted in the cyclic voltammogram of **NDIS$_3$** at potentials of -1.54 and -1.24 V (vs. Fc$^+$/Fc). These peaks correspond to the second reductions of **NDIS$_0$** and **NDIS$_1$**, and suggesting that the trithionated compound is perhaps decomposing into these lower thionated products.

Table 2.1: Reduction potentials of a thionated NDI compound series.

Compound	1st Reduction $E_{1/2}$ / V	2nd Reduction $E_{1/2}$ / V	Difference Between Reduction Potentials / V	Change from NDIS$_0$ 1st Reduction / V	Change from NDIS$_0$ 2nd Reduction / V
NDIS$_0$	-1.07	-1.53	0.46	0.00	0.00
NDIS$_1$	-0.88	-1.29	0.41	0.19	0.24
NDIS$_2$ trans	-0.75	-1.08	0.33	0.32	0.45
NDIS$_2$ cis	-0.73	-1.05	0.32	0.34	0.48
NDIS$_3$	-0.61	-0.91	0.30	0.46	0.62

Potentials quoted against $E_{1/2}$ Fc$^+$/Fc at 100 mVs^{-1} used as the internal standard. Recorded in dichloromethane at ambient temperature containing [^{n}Bu$_4$N][BF$_4$] (0.4 M) as the supporting electrolyte.

Cyclic voltammetry experiments of the thionated and nonthionated naphthalic imide (NI) compounds **NIS$_0$** and **NIS$_1$** produced similar results to those of the NDI series (Figure 2.8). Both NIs displayed a single, reversible one-electron reduction process, occurring at -1.82 V (vs. Fc$^+$/Fc) for **NIS$_0$** and -1.44 V for **NIS$_1$**. The effect of thionation upon the electron affinity of the NIs is even more pronounced than for the NDIs, with the reduction potential becoming 380 mV less negative for just a single sulfur substitution. In spite of this increase in affinity, the reduction process is still less accessible than for nonthionated NDIs.

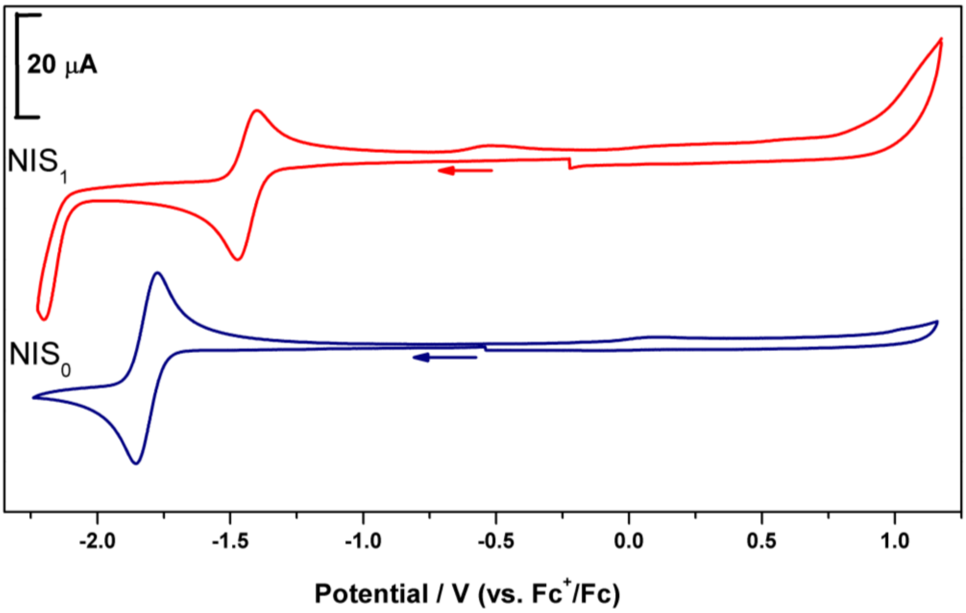

Figure 2.8: Cyclic voltammograms of the thionated NI compounds in dichloromethane containing 0.4 M [^{n}Bu$_4$N][BF$_4$] as the supporting electrolyte, with a scan rate of 100 mVs^{-1}. Blue: NIS$_0$, red NIS$_1$.

2.2.3.2. Spectroelectrochemistry and Optical Properties

Optical absorption spectra for the neutral series of thionated NDI compounds were recorded in dichloromethane (Figure 2.9). Again, **NDIS$_0$** exhibits an absorbance profile typical for a non-core substituted NDI, with an absorbance maximum of 382 nm and a molar extinction coefficient of 33,600 mol^{-1}dm^{3}cm^{-1}. The absorbance profile for **NDIS$_0$** is highly structured, featuring prominent peaks from the 0 → 0, 0 → 1 and 0 → 2 vibronic bands. Upon thionation, a steady bathochromic shift occurs in absorbance maximum from 382 nm for **NDIS$_0$** to 502 nm for **NDIS$_3$**. This redshift implies that the optical band gap decreases in energy with increasing thionation, consistent with the electrochemical measurements obtained, where it was demonstrated that the LUMO energy decreases with each sulfur substitution. The vibrational structure of the spectra changes for the thionated NDI molecules, with the vibronic bands merging into a single, broader band.

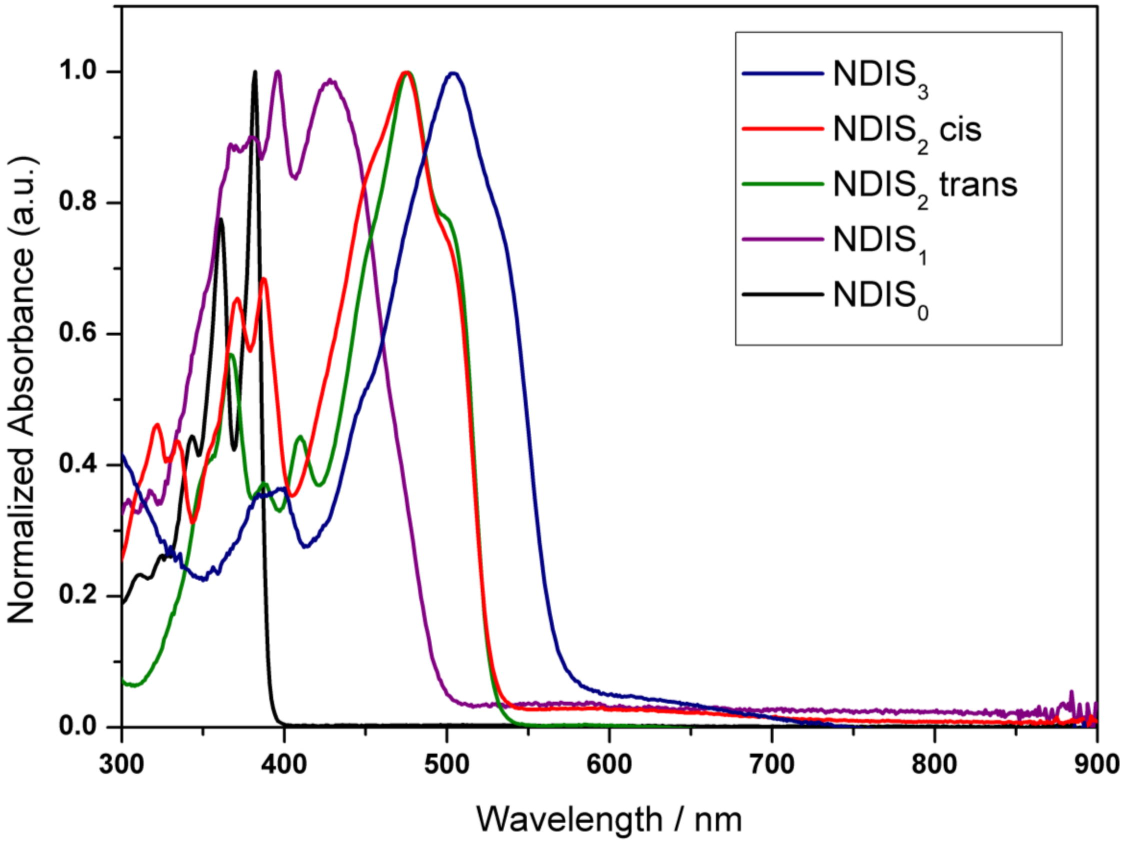

Figure 2.9: Normalised UV/vis absorption spectra for the thionated NDI series in dichloromethane containing [^{n}Bu$_4$N][BF$_4$] (0.4 M) at 273 K.

The mono-reduced radical species generated during the spectroelectrochemical measurements follow a similar pattern for the NDI series. Briefly, upon reduction at the appropriate potential, a depletion of the major bands for the neutral species occurs which are replaced by a set of intense bands spanning the visible wavelengths and into the near infrared region of the spectrum. The most intense of these bands is redshifted roughly 100 nm relative to the λ_{max} for the neutral species, with less intense bands at still longer wavelengths (Figure 2.10).

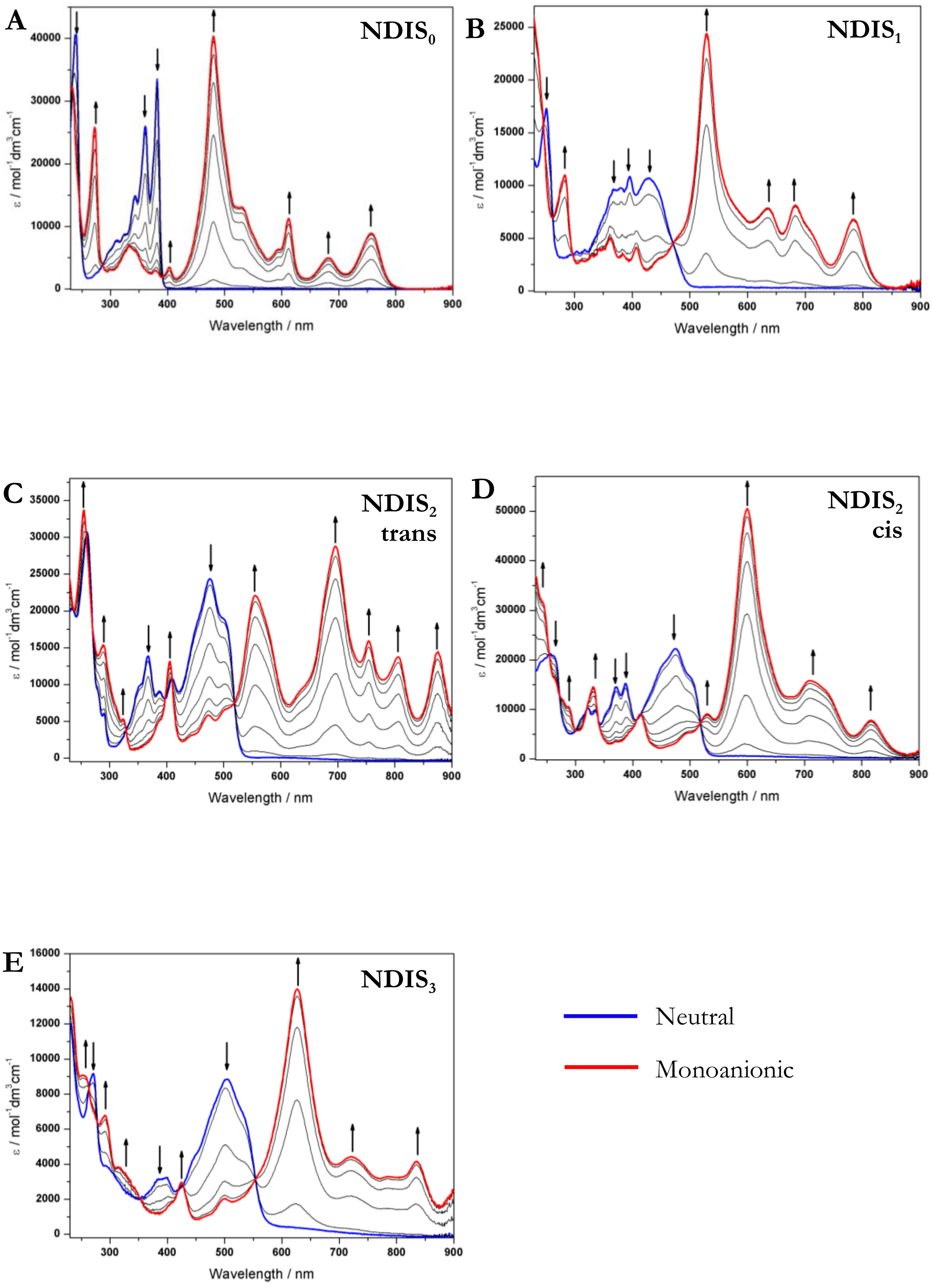

Figure 2.10: UV/vis absorption spectra showing the inter-conversion from neutral (blue) to monoanionic (red) species for a thionated NDI series, arrows indicate the progress of the reduction. Spectra were recorded in dichloromethane containing [^{n}Bu$_4$N][BF$_4$] (0.4 M) as the supporting electrolyte at 273 K. A: NDIS$_0$, B: NDIS$_1$, C: NDIS$_2$ trans, D: NDIS$_2$ cis and E: NDIS$_3$.

Comparison of the five members of the series shows that the sequential spectral redshift associated with thionation is preserved for the monoanionic forms of the molecules, with fairly similar optical profiles for each NDI (Figure 2.11). One exception to the general trend is the dithionated **$NDIS_2$ trans** isomer, with a λ_{max} of 696 nm, greater than that of the more thionated **$NDIS_3$** (λ_{max} = 627 nm). This difference is discussed in more detail below.

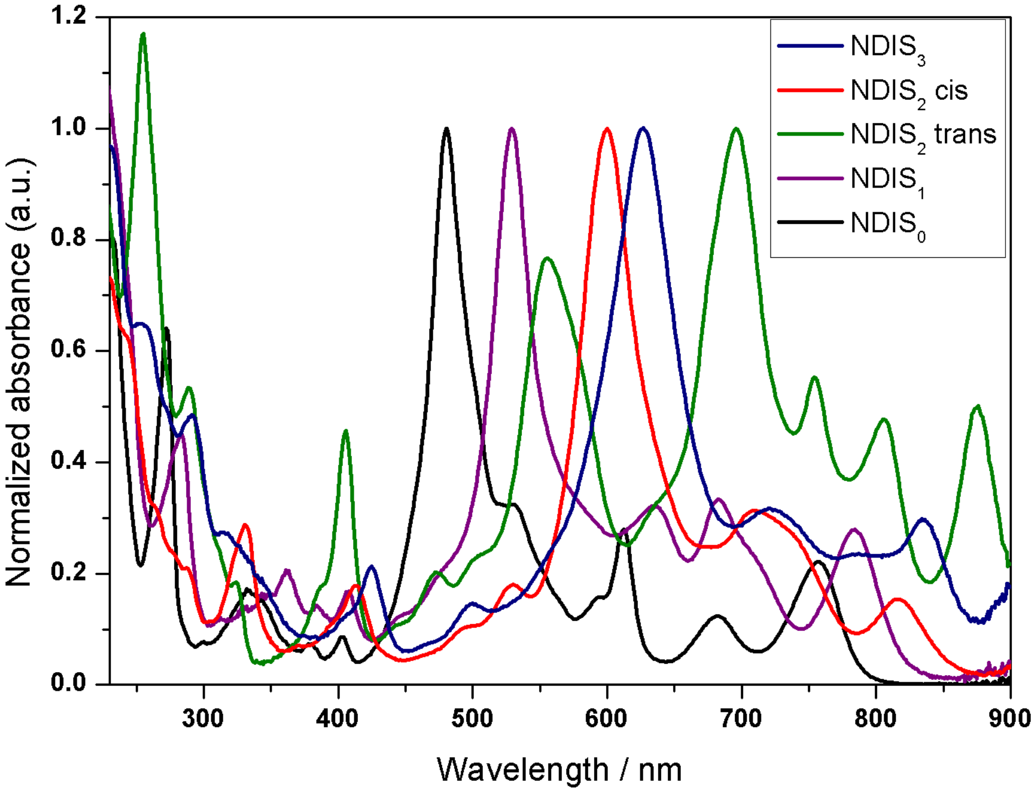

Figure 2.11: Normalised UV/vis absorption spectra for the monoanionic forms of the thionated NDI series. Recorded in dichloromethane containing $[^nBu_4N][BF_4]$ (0.4 M) at 273 K.

Spectroelectrochemical reduction of **$NDIS_0$** to dianonic **$[NDIS_0]^{2-}$** generated a chromophore with similar absorbance properties to the neutral form. Intense, well-structured bands formed at higher energy wavelengths, with similar shape to those of the neutral molecule and an additional set of bands at lower intensity was also present at the lower energy end of the visible region. The spectral profiles for all other members of the thionated series fit the description above, although in the case of **NDIS$_2$ trans**, it was the lower energy bands that had greater molar extinction coefficients (Figure 2.12).

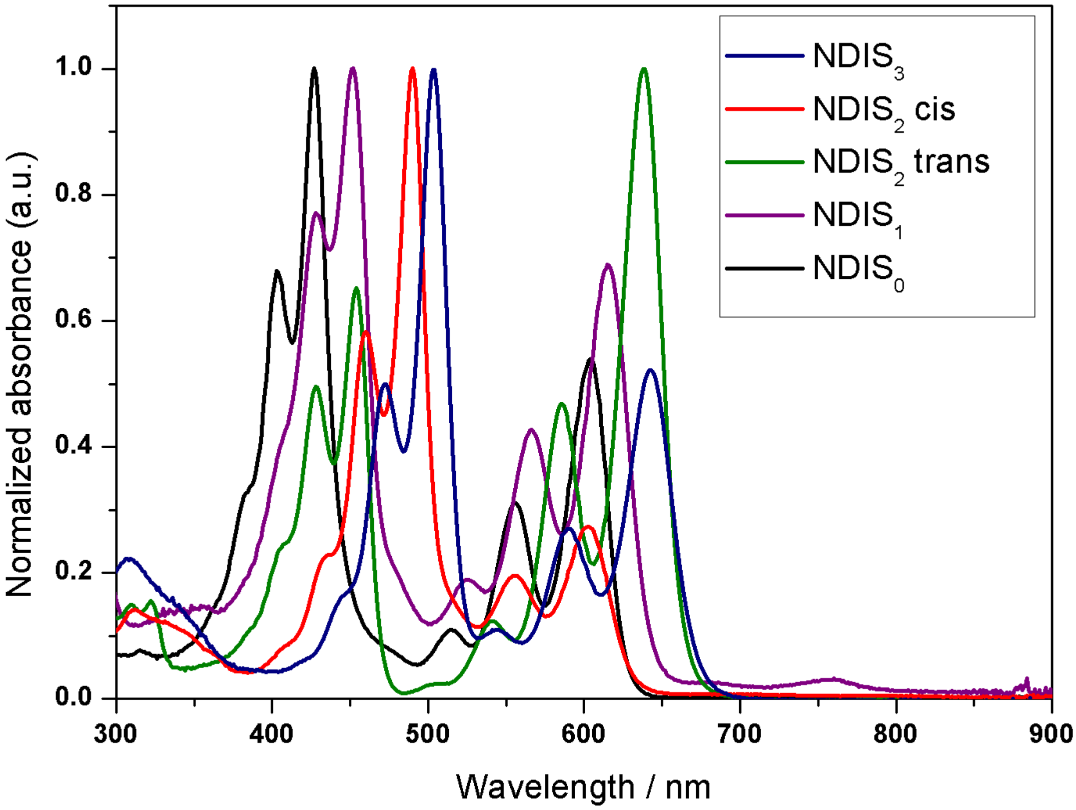

Figure 2.12: Normalised UV/vis absorption spectra for the dianionic forms of the thionated NDI series. Recorded in dichloromethane containing [^{n}Bu$_4$N][BF$_4$] (0.4 M) at 273 K.

The spectroelectrochemical inter-conversion between monoanionic and dianionic forms of the thionated NDI series are shown below (Figure 2.13).

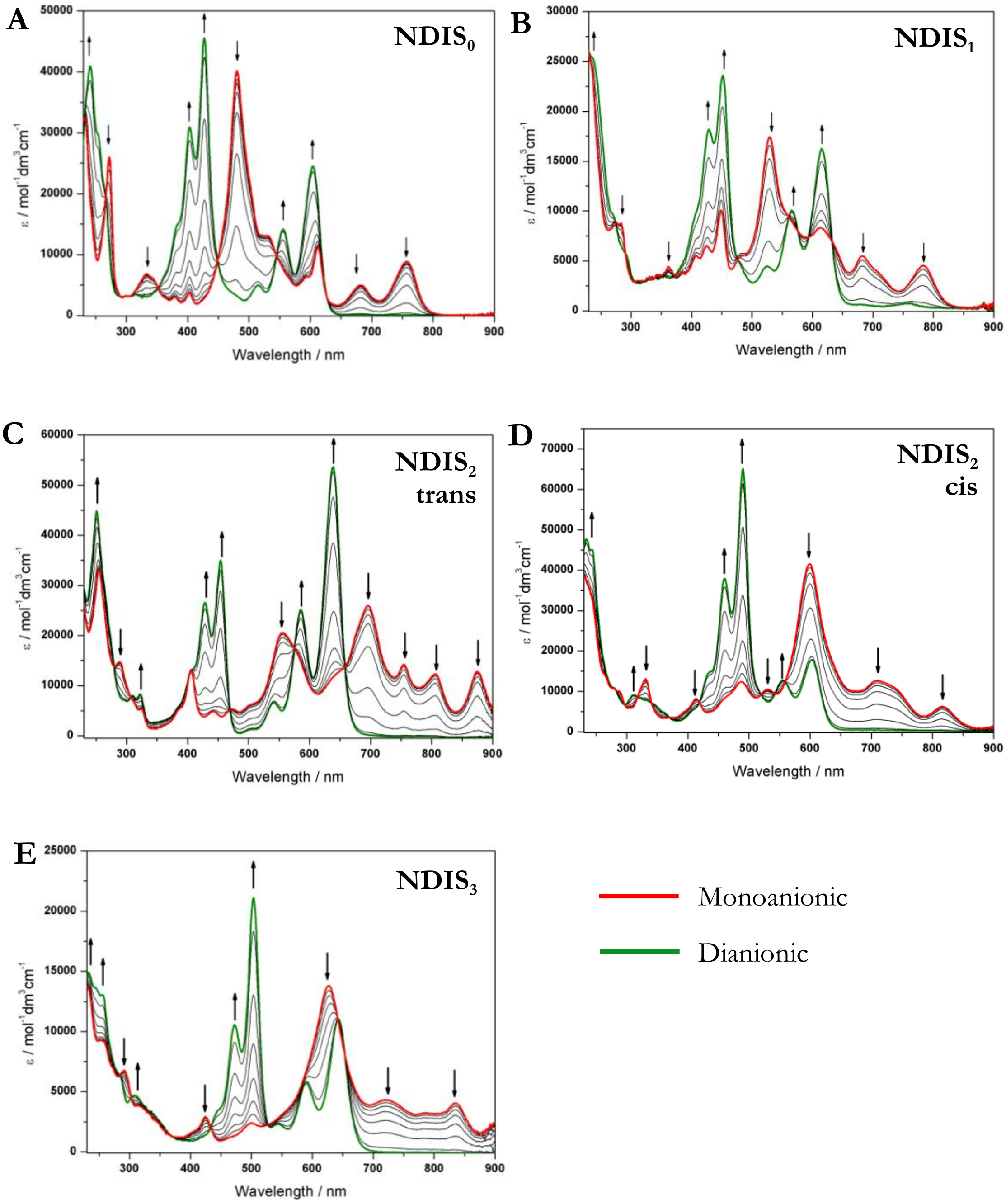

Figure 2.13: UV/vis absorption spectra showing the inter-conversion from monoanionic (red) to dianionic (green) species for a thionated NDI series, arrows indicate the progress of the reduction. Spectra were recorded in dichloromethane containing [^{n}Bu$_4$N][BF$_4$] (0.4 M) as the supporting electrolyte at 273 K. A: NDIS$_0$, B: NDIS$_1$, C: NDIS$_2$ trans, D: NDIS$_2$ cis and E: NDIS$_3$.

The first reduction processes for all members of the thionated NDI series are completely reversible under spectroelectrochemical conditions: the absorbance spectra for the neutral compounds could be returned to after formation of the corresponding monoanions without any loss of intensity of appearance of superfluous bands. For the second reduction process, the monoanionic forms of **NDIS$_1$** and the **NDIS$_2$** isomers could not be fully regenerated following the second reduction. Whilst this result suggests that these processes might not be completely reversible (at 273 K), there was no loss of isosbestic points and no new spectral bands appeared, indicating no decomposition of the compound had occurred. Since this did not occur for **NDIS$_0$** or **NDIS$_3$**, which were fully reversible under the spectroelectrochemical conditions, it is conceivable that the irreversibility for the other NDIs was due an extraneous factor such as equipment malfunction, or perhaps an unexpected concentration dependent effect, rather than a chemical one. The other thionated rylenes later examined (see Chapters 3 and 4) were all fully reversible in spectroelectrochemical experiments further suggesting that this might be the case.

Reduced forms of **NDIS$_2$ trans** behave differently to the other thionated NDIs. The chromophore for [**NDIS$_2$ trans**]$^{\bullet-}$ possesses sharp absorbances at 555 nm (ε = 22,100 $\mathrm{mol^{-1}dm^{3}cm^{-1}}$) and 696 nm ($\varepsilon$ = 28,800 $\mathrm{mol^{-1}dm^{3}cm^{-1}}$), vastly different from that of the isomeric counterpart [**NDIS$_2$ cis**]$^{\bullet-}$ which only exhibits one strong absorption peak at 600 nm (ε = 50,500 $\mathrm{mol^{-1}dm^{3}cm^{-1}}$), despite a resemblance in the spectra of both molecules' neutral forms. Interestingly, if the two sharp absorbance peaks of [**NDIS$_2$ trans**]$^{\bullet-}$ were combined, the result would much more closely mimic that of [**NDIS$_2$ cis**]$^{\bullet-}$ with $\lambda_{max} \approx$ 629 nm and a molar extinction coefficient of 50,900 $\mathrm{mol^{-1}dm^{3}cm^{-1}}$. [**NDIS$_2$ trans**]$^{2-}$ strongly absorbs red light: at 639 nm, ε = 53,700 $\mathrm{mol^{-1}dm^{3}cm^{-1}}$ with a weaker violet absorbance at 454 nm, ε = 35,000 $\mathrm{mol^{-1}dm^{3}cm^{-1}}$. An opposite scenario is the case for [**NDIS$_2$ cis**]$^{2-}$: a strong violet absorbance (ε = 65,100 $\mathrm{mol^{-1}dm^{3}cm^{-1}}$ at 490 nm) and a weak red absorbance (ε = 17,800 $\mathrm{mol^{-1}dm^{3}cm^{-1}}$ at 603 nm). Together, these data imply that a different chromophore exists for the reduced forms of **NDIS$_2$ trans**, potentially owing to a different conjugation across the molecule's core (Figure 2.14).

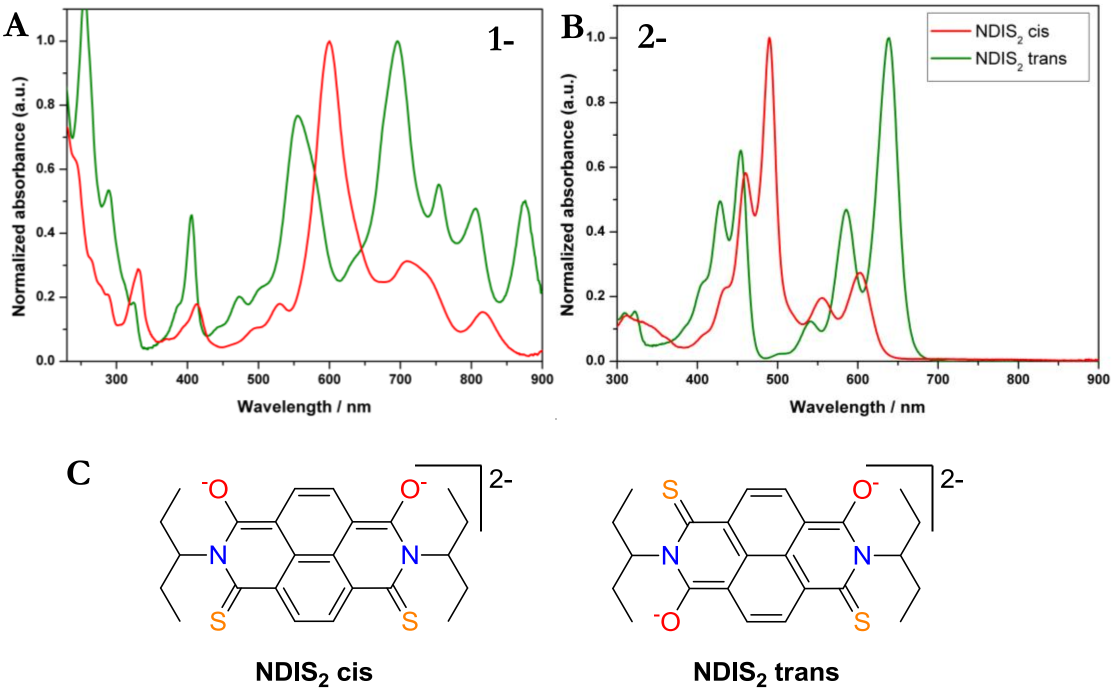

Figure 2.14: Differences in UV/vis absorbance spectra of reduced dithionated NDIs. A: Monoanionic, B: dianionic. NDIS$_2$ cis (red), NDIS$_2$ trans (green). C: Hypothetical structures of dithionated NDI dianions, showing differences in conjugation across cis and trans isomers.

Spectroelectrochemistry was also used to probe the optical properties of the NI molecules to compare the differences caused by thionation. Much like for **NDIS$_0$**, **NIS$_0$** exhibits a structured absorbance of near-ultraviolet wavelengths; the lowest energy absorbance is at 350 nm, with nothing in the visible range. Reduction diminishes these bands and a sharper, more intense band forms at 422 nm, along with some broad bands at longer wavelengths (Figure 2.15A). Thionation has a very similar effect to that described for the NDI series, with the absorbance maximum of **NIS$_1$** redshifted 54 nm to 404 nm for the neutral molecule and 40 nm to 444 nm for [**NIS$_1$**]$^{\cdot-}$ (Figure 2.15B). The absorption redshift for these NI molecules is on a similar magnitude to the NDI series, suggesting the effect of the thionation on the absorbance properties is largely similar.

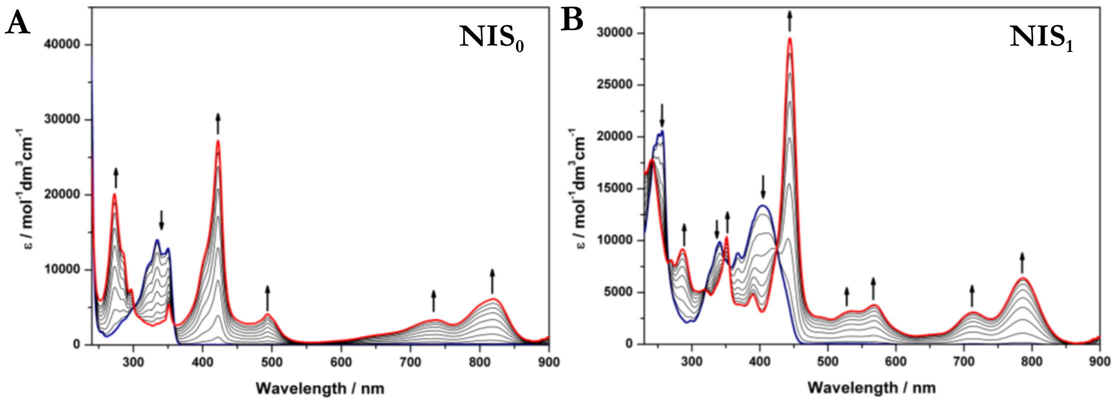

Figure 2.15: UV/vis absorption spectra showing the inter-conversion from neutral (blue) to monoanionic (red) species of a thionated NI series, arrows indicate the progress of the reduction. Spectra were recorded in dichloromethane containing [^{n}Bu$_4$N][BF$_4$] (0.4 M) as the supporting electrolyte at 273 K. A: NIS$_0$, B: NIS$_1$.

The optical absorbance data recorded for the complete thionated NDI series are summarised below (Table 2.2). Also included are data for the NI molecules **NIS$_0$** and **NIS$_1$**.

Table 2.2: Summary of optical spectroscopy for the thionated NDI and NI series.

Compound	λ_{abs} / nm (ε / 10^3 mol^{-1}dm^{3}cm^{-1})		
	Neutral	**Monoanionic**	**Dianionic**
NDIS$_0$	382 (33.6), 361 (26.0), 343 (14.9), 312 (7.8), 238 (40.6)	756 (8.9), 682 (5.0), 612 (11.3), 594 (6.4), 530 (13.1), 480 (40.4), 403 (3.5), 378 (3.0), 332 (7.0), 272 (25.9), 233 (32.3)	604 (24.5), 556 (14.2), 514 (5.0), 427 (45.5), 403 (30.9), 242 (41.0)
NDIS$_1$	428 (10.7), 396 (10.9), 379 (9.8), 367 (9.6), 317 (3.9), 304 (3.8), 252 (17.3)	784 (6.8), 682 (8.1), 635 (7.9), 529 (24.4), 408 (4.1), 383 (3.5), 361 (5.0), 283 (11.0)	760 (0.8), 615 (16.2), 566 (10.1), 525 (4.5), 452 (23.6), 428 (18.2)
NDIS$_2$ (trans)	585 (0.1), 476 (24.4), 410 (10.8), 387 (9.1), 367 (13.9), 290 (6.1), 261 (30.7), 233 (20.2)	876 (14.5), 806 (13.8), 696 (28.8), 555 (22.1), 473 (5.8), 406 (13.2), 324 (5.3), 289 (15.4), 255 (33.7)	639 (53.7), 586 (25.2), 541 (6.6), 454 (35.0), 428 (26.6), 322 (8.3), 309 (8.0), 251 (44.9)
NDIS$_2$ (cis)	475 (22.2), 387 (15.2), 371 (14.6), 334 (9.7), 322 (10.3), 255 (21.2)	816 (7.8), 708 (15.8), 600 (50.5), 530 (9.1), 414 (9.0), 330 (14.6), 287 (10.6)	603 (17.8), 555 (12.8), 490 (65.1), 460 (37.9), 312 (9.2), 243 (45.1), 234 (47.7)
NDIS$_3$	502 (8.9), 400 (3.2), 384 (3.2), 271 (9.2)	836 (4.2), 787 (4.4), 627 (14.0), 500 (2.0), 425 (3.0), 314 (3.8), 291 (6.8), 252 (9.1)	643 (11.0), 589 (5.7), 544 (2.3), 504 (21.1), 472 (10.6), 309 (4.7), 255 (13.1), 233 (14.9)
NIS$_0$	335 (14.0), 350 (12.9)	237 (27.9), 273 (20.2), 267 (7.4), 351 (5.4), 422 (27.3), 494 (4.1), 736 (3.3), 819 (6.1)	
NIS$_1$	251 (20.3), 256 (20.6), 341 (9.9), 368 (8.8), 404 (13.4), 527 (0.1)	241 (17.9), 269 (8.2), 286 (9.2), 318 (5.3), 351 (10.4), 390 (4.8), 444 (29.5), 536 (3.2), 568 (3.8), 714 (3.1), 786 (6.4)	

Obtained at an optically transparent electrode cell in dichloromethane, containing [^{n}Bu$_4$N][BF$_4$] (0.4 M) at 273 K, spectral range: 230 - 900 nm.

2.2.3.3. Electron Paramagnetic Resonance Spectroscopy

In order to learn more about the location of the radical electron in the monoanionic NDI systems, EPR spectroscopy was employed. Electrolyte solutions of the radical species were generated by bulk electrolysis, affording the corresponding monoanionic NDI in good yield. Once again **NDIS$_0$** functions as an appropriate control molecule; the EPR spectrum recorded displays habitual structure, distinctive of coupling of the radical electron with the hydrogen atoms on the naphthalene core and with the two imide nitrogens (Figure 2.16). It can be deduced from the EPR spectrum that upon reduction to [**NDIS$_0$**]$^{\cdot-}$, the radical electron occupies a π-orbital based around that NDI core, consistent with the LUMO structure (below).

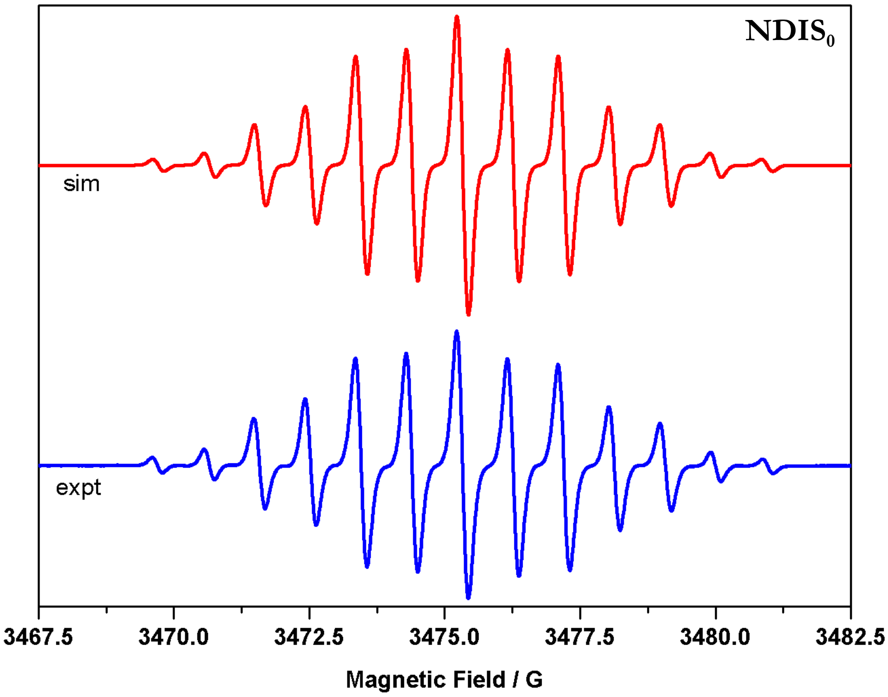

Figure 2.16: EPR spectrum of NDIS$_0$. Experimental data (blue), simulated data (red).

^{1}H NMR spectra of both dithionated NDI derivatives confirms that each isomer contains two pairs of chemically equivalent hydrogen environments in the aromatic region. The EPR spectra recorded for each mono-reduced isomer (Figure 2.17) agree with this, and could be accurately simulated using three parameters: two sets of two equivalent hydrogen atoms, and a pair of equivalent nitrogen atoms. Even though the resulting EPR spectra do not closely resemble one another, the values of the hyperfine coupling constants to each spin-active nucleus are not drastically different (Table 2.3). Of the assigned coupling values, the lowest is allocated to the nitrogen atoms, expected as the frontier orbitals possess nodes at this position.

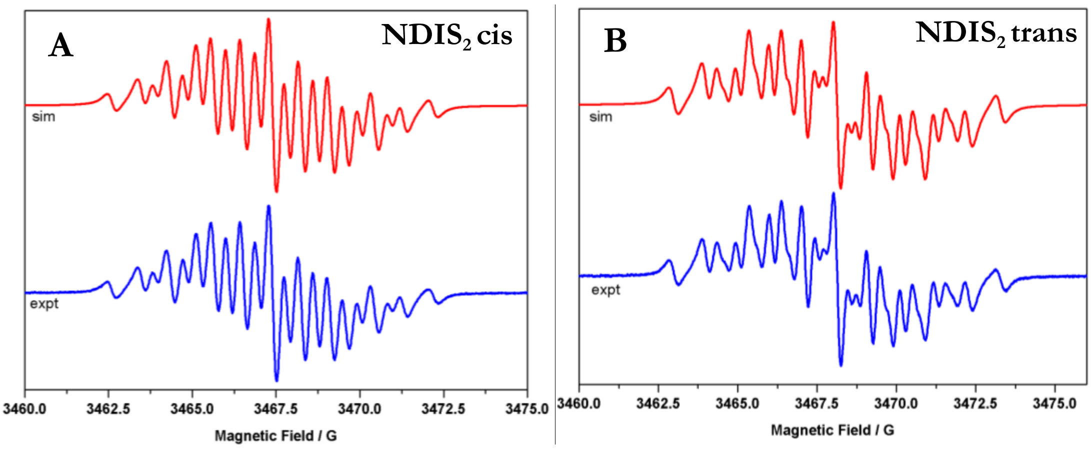

Figure 2.17: EPR spectra of dithionated NDIs. A: NDIS$_2$ cis, B: NDIS$_2$ trans. Experimental data (blue), simulated data (red).

For **[NDIS$_1$]**$^{\cdot-}$, and **[NDIS$_3$]**$^{\cdot-}$ the hydrogen and nitrogen environments are expected to be inequivalent, the molecules belonging to the C_s point group. Simulation of these spectra to determine coupling constants requires the fitting of six interdependent parameters and it was not possible to overcome this difficulty, consequently, only g_{iso} values are reported for these spectra (Table 2.3). Experimentally recorded EPR spectra for these radicals support this argument; the EPR spectrum of **[NDIS$_1$]**$^{\cdot-}$ is especially complicated, **[NDIS$_3$]**$^{\cdot-}$ is simpler likely due to overlap of lines (Figure 2.18).

Table 2.3: EPR measurements for the reduced thionated NDI series.

Compound	g_{iso}	A_{iso} / 10^{-4} cm^{-1}	Linewidth / G	Lineshape
NDIS$_0$	2.0037	1.740 (4H) 0.889 (2N)	0.21	0.8
NDIS$_1$	2.0058	-	-	-
NDIS$_2$ trans	2.0078	1.569 (2H) 1.346 (2H) 0.956 (2N)	0.31	Lorentzian
NDIS$_2$ cis	2.0085	1.603 (2H) 1.219 (2H) 0.835 (2N)	0.30	Lorentzian
NDIS$_3$	2.0105	-	-	-

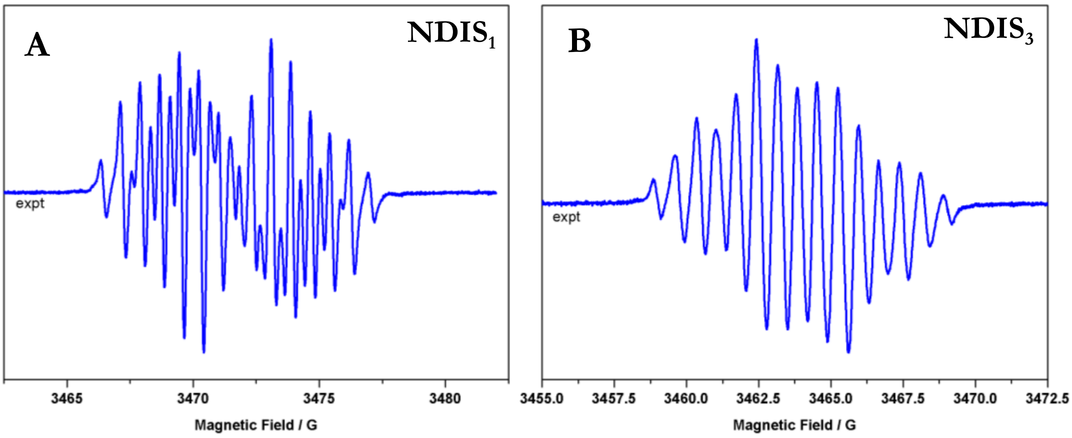

Figure 2.18: Experimentally obtained EPR spectra of thionated NDIs. A: NDIS$_1$, B: NDIS$_3$.

A general trend is seen in the g_{iso} values obtained for the series. Experimentally determined g_{iso} values are 2.0037 (**NDIS$_0$**), 2.0058 (**NDIS$_1$**), 2.00815 (**NDIS$_2$** average for both isomers) and 2.0105 (**NDIS$_3$**), representing a steady increase of 0.0023 per additional sulfur atom. This shift results from progressively larger π-spin population across the series due to an increase in spin-orbit coupling, an effect promoted by the presence of increasing numbers of heavier sulfur atoms.

The colours of the radical species in the electrolyte solution produced by bulk reduction resemble the trend revealed by spectroelectrochemistry. [**NDIS$_0$**]$^{\cdot -}$ gave a purple solution; [**NDIS$_1$**]$^{\cdot -}$ was blue-purple; [**NDIS$_2$ trans**]$^{\cdot -}$ was purple-blue; [**NDIS$_2$ cis**]$^{\cdot -}$ was blue and [**NDIS$_3$**]$^{\cdot -}$ was blue-green in solution, moving through the colour spectrum as the absorption maximum redshifts.

The presence of additional hydrogen atoms in the 4 and 5 positions for the NI molecules increased complexity of the EPR spectra for **NIS$_0$** and **NIS$_1$** due to the additional coupling to these hydrogen atoms (Figure 2.19). It was possible to simulate the data obtained for **NIS$_0$**, providing hyperfine coupling values of 5.265 (2H), 4.564 (2H), 0.720 (2H) and 1.328 (1N) x 10^{-4} cm^{-1}. From this information, the location of the radical electron is expected to lie in an orbital over the aromatic core of the NI, enabling interaction of the electron to the three pairs of hydrogen atoms as well as the imide nitrogen. Simulation of the data for **NIS$_1$** was not possible: the symmetry breaking caused by the sulfur atom creates six hydrogen environments, complicating the spectrum too much for adequate simulation.

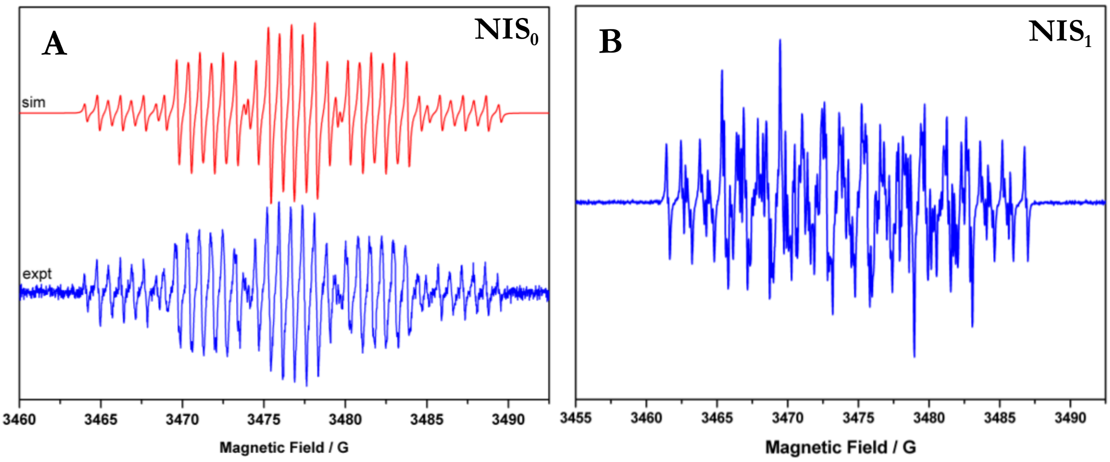

Figure 2.19: EPR spectra of NI compounds. A: NIS$_0$, B: NIS$_1$. Experimental data (blue), simulated data (red).

The g_{iso} values for **NIS$_0$** and **NIS$_1$** are 2.0032 and 2.0046 respectively. There is an increase in value as a result of the heavy atom effect due to the presence of the sulfur atom, as for the NDI compounds. The difference (0.0014) is less pronounced for these NIs than for the NDIs, perhaps because the hyperfine coupling to the hydrogen atoms is stronger for the NI molecules, so changes to the imide group have a lesser effect.

2.2.4. DFT Calculated Molecular Orbitals

Density functional theory (DFT) was used to calculate the energies of the molecular orbitals for the entire thionated NDI series to compare the experimentally observed trend in LUMO energies with theoretically obtained values. Orbital energies could also be calculated for the two possible thionated NDIs not obtained; tetrathionated **NDIS$_4$**, and the geminately dithionated isomer **NDIS$_2$ gem** (Table 2.4). Additional calculations were performed for the monoanionic forms of the thionated NDI series to generate SOMO orbital diagrams for the singly reduced radicals.

Table 2.4: Calculated molecular orbital diagrams for the thionated NDI series.

	HOMO	LUMO	Anion SOMO
NDIS$_0$	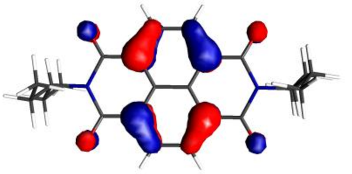 -6.95 eV	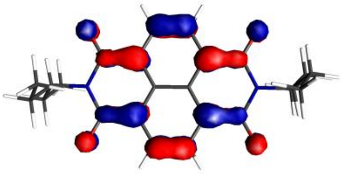 -3.33 eV	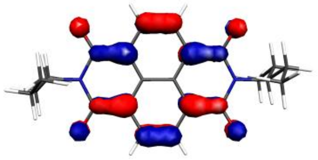
NDIS$_1$	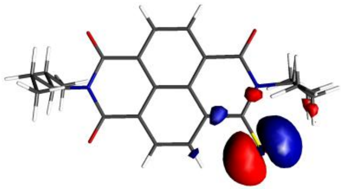 -6.20 eV	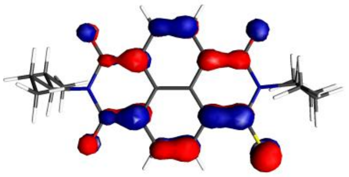 -3.55 eV	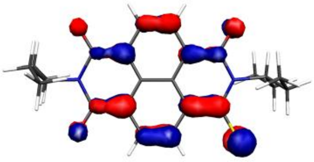
NDIS$_2$ cis	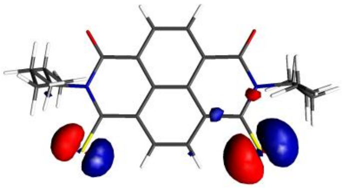 -6.21 eV	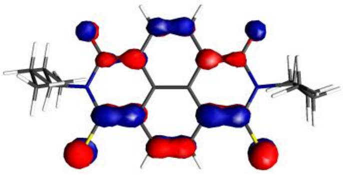 -3.73 eV	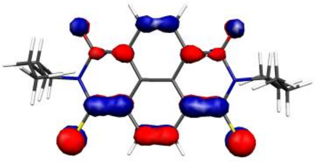
NDIS$_2$ gem	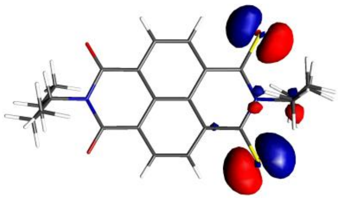 -6.27 eV	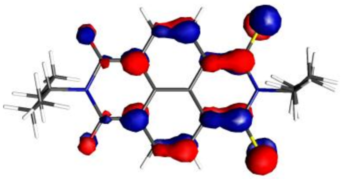 -3.76 eV	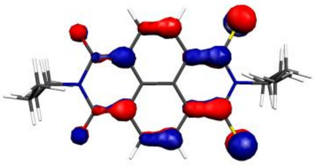
NDIS$_2$ trans	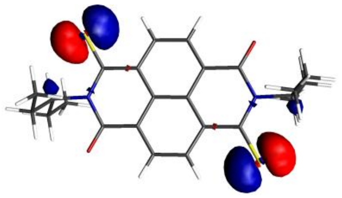 -6.24 eV	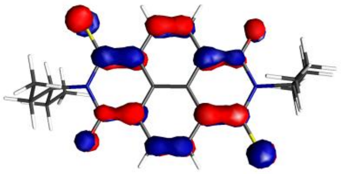 -3.74 eV	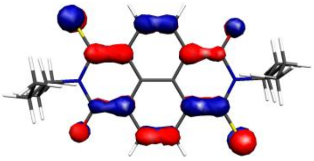
NDIS$_3$	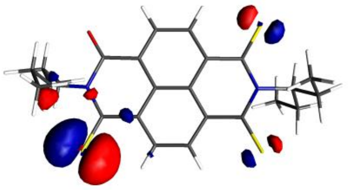 -6.24 eV	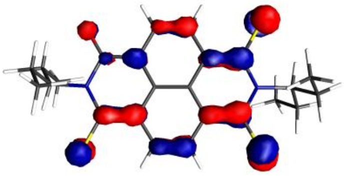 -3.90 eV	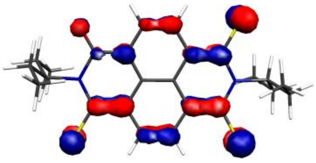
NDIS$_4$	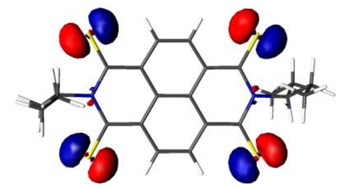 -6.25 eV	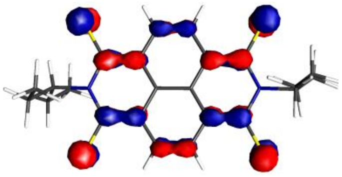 -4.05 eV	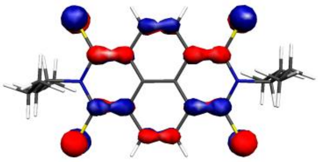

The calculated LUMO values were found to steadily decrease with increasing thionation, consistent with the experimentally observed trend in reduction potential, hence electron affinity increases upon thionation (Figure 2.20). This decrease is approximately 0.15 eV per additional sulfur substitution, strongly in agreement with the first reduction potentials experimentally determined using cyclic voltammetry: as discussed above the first reduction potential increases by 0.15 V as each oxygen is replaced by a sulfur atom. The calculated HOMO energies for the thionated NDIs are all very similar, within 0.07 eV of each other, whereas the nonthionated **NDIS$_0$** HOMO lies at a much lower energy of -6.95 eV. This can be explained through the shape of the orbital diagrams: the HOMO of **NDIS$_0$** is a π-type orbital, with a node along the long central axis of the molecule, but the thionated NDIs all possess HOMOs primarily on their sulfur atoms. Since the thionated NDI HOMOs all lay exclusively on one type of atom, the energy is likely to be similar for all these cases.

For most of the thionated molecules the HOMO orbital lobes on the sulfur atoms are all roughly equal in size. **NDIS$_3$** is an exception: the majority of the HOMO lies over the sulfur atom that shares an imide group with the remaining oxygen atom, and only small orbital lobes are calculated over the other two sulfur atoms. Also of note is that for the three dithionated isomers, the lowest calculated HOMO and LUMO energies were obtained for **NDIS$_2$ gem**. These lower frontier orbital energies could account for why the geminate substitution pattern is not seen in the reaction products, acting as a barrier to the reaction with Lawesson's reagent.

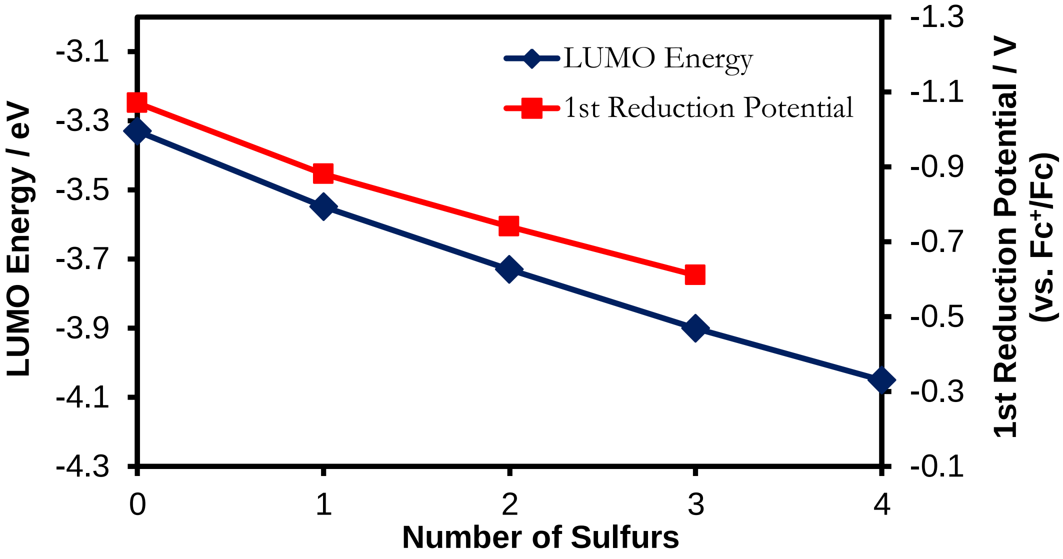

Figure 2.20: Comparison of LUMO energies and first reduction potential values for the thionated NDI series.

The LUMO geometry is steady throughout the series, with slightly more orbital character on the sulfur atoms than oxygen atoms. Calculated SOMO diagrams for the monoanionic forms of the NDI series produce orbital diagrams identical to those of the corresponding LUMOs, forming a consistent orbital picture. The calculated HOMO-LUMO gap gradually decreases from 3.61 eV for **NDIS$_0$** to 2.20 eV for **NDIS$_4$**; the decreasing gap energy corresponds to an increase in wavelength of the absorption maximum in the UV/vis spectrum, in agreement with the experimentally determined trend from the optical absorbance data (Table 2.5). A large initial decrease in HOMO-LUMO gap occurs on thionation, of almost 1 eV as a consequence of **NDIS$_0$** possessing a lower lying HOMO than the thionated NDIs. After this, the gap decreases in size by about 0.15 eV per additional sulfur substitution, as the LUMO energy incrementally decreases whilst the HOMO energy remains roughly constant.

Table 2.5: Calculated HOMO-LUMO gaps for the thionated NDI series.

Compound	HOMO/ eV	LUMO/ eV	Gap/ eV	Change from $NDIS_0$ / eV
$NDIS_0$	-6.95	-3.33	3.61	0.00
$NDIS_1$	-6.20	-3.55	2.66	0.95
$NDIS_2$ cis	-6.21	-3.73	2.48	1.13
$NDIS_2$ gem	-6.27	-3.76	2.51	1.10
$NDIS_2$ trans	-6.24	-3.74	2.50	1.11
$NDIS_3$	-6.24	-3.90	2.34	1.27
$NDIS_4$	-6.25	-4.05	2.20	1.41

2.2.5. Photophysics of Thionated NDIs

The photophysical properties of the thionated NDI series were examined using a combination of transient absorption (TA) spectroscopy and time-resolved infrared (TRIR) spectroscopy. Following excitation at 355 nm of nonthionated **$NDIS_0$**, two transient absorption bands form at 465 and 610 nm, with a shoulder at 574 nm (Figure 2.21A). These transients decays over the first few picoseconds to produce bands at 460 and 490 nm in agreement with TA data published by Ganesan et al. for a similar di(2-ethylhexyl) substituted NDI.[18] These emergent peaks at 460 and 490 nm, are attributed to a triplet ππ* excited state.[18-20] Ganesan et al. propose that the rapidly formed transient is 'most likely the singlet excited state of NDI' and the triplet state is populated directly from this via intersystem crossing.[18] The final excited state persists into the microsecond timescale, decaying after a lifetime of 11 ± 1 μs. This extended lifetime is highly concentration dependant (a 2.3 $mmoldm^{-3}$ concentration provided this lifetime), which indicates the presence of self-quenching interactions.

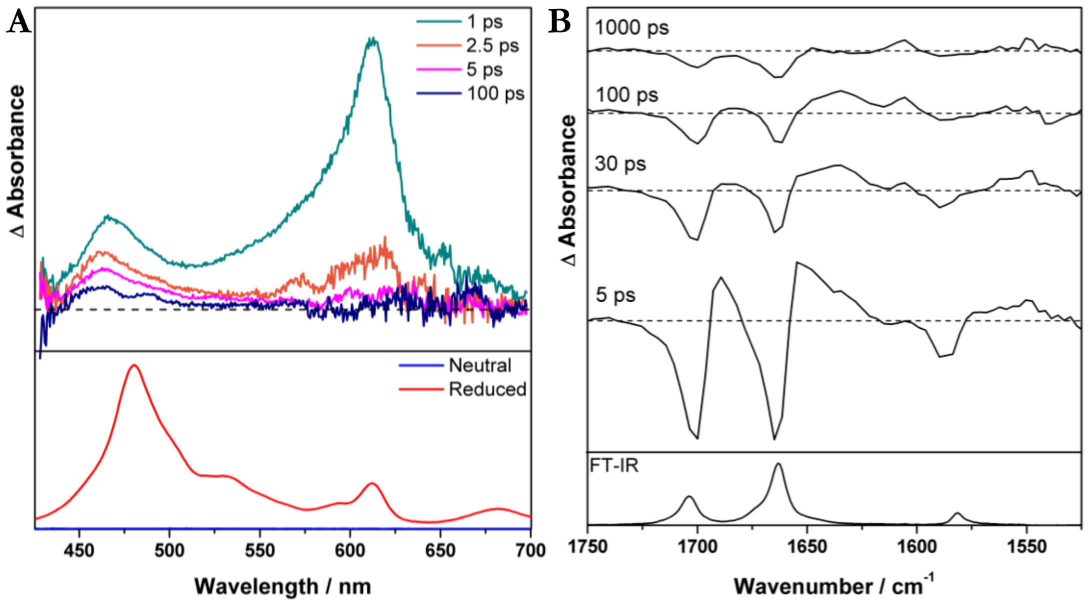

Figure 2.21: Time resolved photochemistry of $\mathbf{NDIS_0}$ after excitation at 355 nm in dichloromethane. A: Picosecond TA spectra, B: TRIR spectra.

TRIR spectroscopy of $\mathbf{NDIS_0}$ shows a rapid bleaching of the ground state carbonyl C=O bands at 1693 and 1703 cm^{-1} following excitation (Figure 2.21B). New bands emerge at lower energies which quickly decay to form final peaks at 1642 and 1605 cm^{-1}, also assigned to the triplet manifold of NDI, which persist until the end of the picosecond experiment.

The TA and TRIR spectra of $\mathbf{NDIS_1}$ appear to tell a similar story: transients emerge at 561 and 608 nm, decaying after 4 ± 3 ps giving rise to another longer-lasting band at 470 nm which persists for 490 ± 80 ps (Figure 2.22A). From the previous data it can be inferred that a singlet excited state quickly forms and decays into a triplet excited state. Comparing to $\mathbf{NDIS_0}$ it appears that these transitions occur marginally more quickly for the thionated NDI than the nonthionated one. Thionation of the NDI appears to promote both the formation of the triplet state and its relaxation back to the ground state. The kinetic data for the transient bands observed in the TRIR measurements of $\mathbf{NDIS_1}$ corroborate the lifetimes obtained from TA measurements (Figure 2.22B). The TRIR spectrum shows major bands at 1675, 1654 and 1632 cm^{-1} at early times. Over 9 ±

6 ps an increase in intesnsity at 1704, 1675 and 1578 cm^{-1} occurs, corresponding to recover of the parent bands, whilst bands at 1652 and 1624 cm^{-1} diminish. A return to ground state is observed after 530 ± 30 ps in the TRIR data.

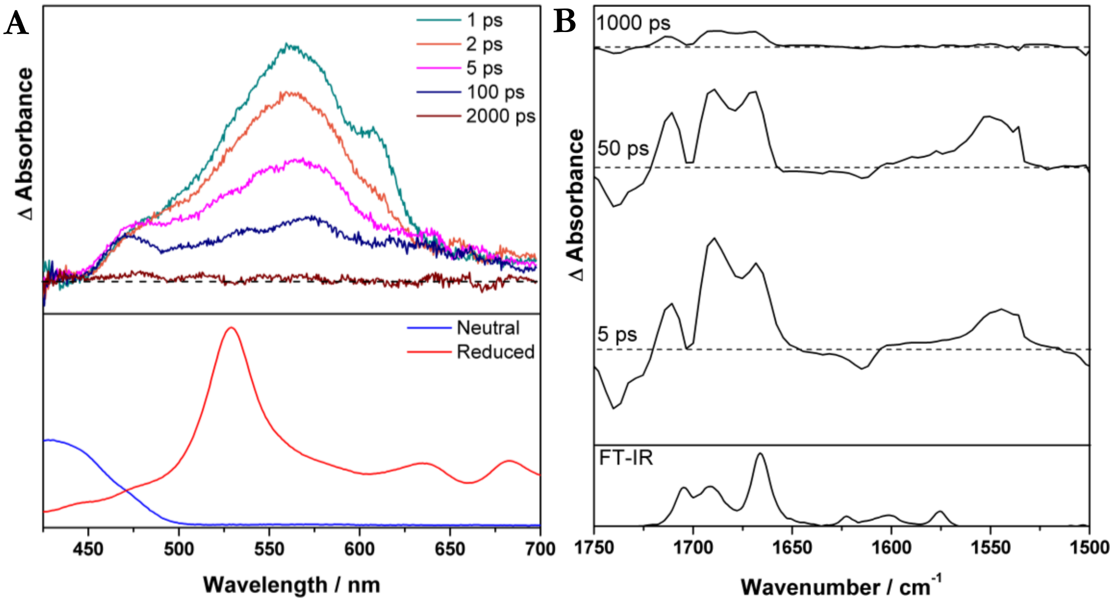

Figure 2.22: Time resolved photochemistry of NDIS$_1$ after excitation at 355 nm in dichloromethane. A: Picosecond TA spectra, B: TRIR spectra.

The TA spectra of the dithionated NDI isomers also appear to develop from a singlet excited state to a triplet excited state (Figure 2.23). The initial spectrum recorded for both compounds at 1 ps (teal lines) decay into new spectra with absorbance peaks in the 450 to 500 nm range. For **NDIS$_2$ cis** the singlet to triplet conversion takes 9 ± 3 ps, and the triplet excited state decays after 2500 ± 500 ps. **NDIS$_2$ trans** experiences a quicker intersystem crossing to the triplet excited state at 3 ± 1 ps, relaxing back to ground state after a similar time. The TRIR data match these observations, which show processes on a 10 ps timeline, accompanied by a subsequent return to ground state.

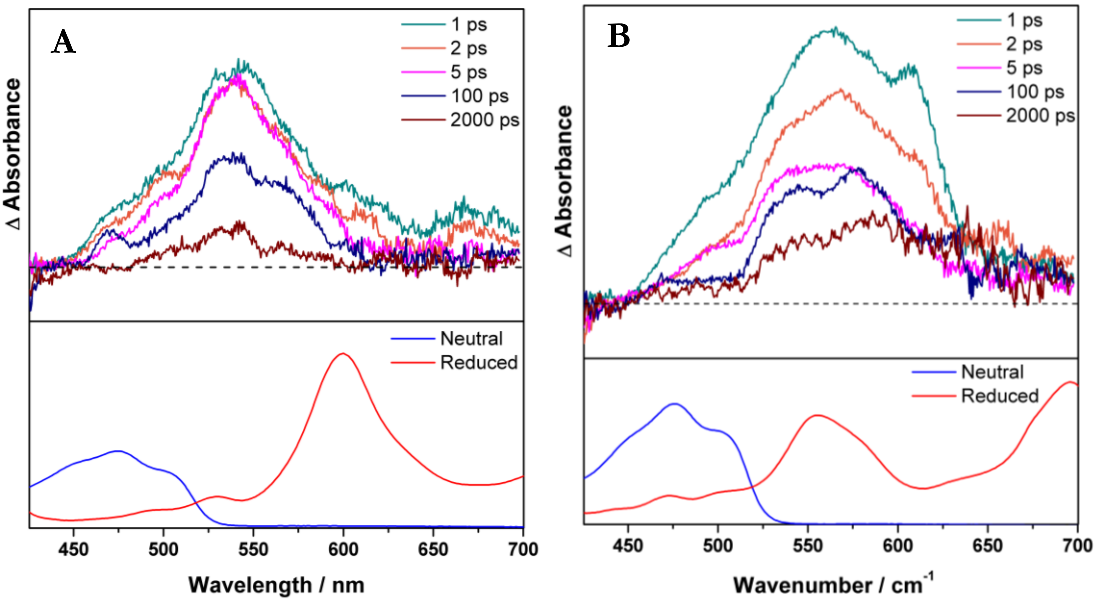

Figure 2.23: Picosecond TA spectra recorded after excitation at 355 nm in dichloromethane for dithionated NDIs. A: NDIS$_2$ cis, B: NDIS$_2$ trans.

Considering the NDI series as a group the transient data show that a singlet state is initially formed, which converts rapidly to a triplet state before a return to the ground state. Overall, these data suggest that thionation helps improve intersystem crossing from a singlet excited state to a triplet excited state, with shorter timescales for the transition from singlet to triplet manifolds observed for the thionated compounds over the nonthionated ones. The presence of sulfur decreases the excited state lifetime of the compounds by 4 orders of magnitude. The increase in spin-orbit coupling for the thionated NDIs may facilitate a more efficient return to ground state. For their thionated PDI series Seferos and co-workers conclude their own TA observations by stating 'the reordering of the molecular electronic structure is the primary cause of the rapid [intersystem crossing] in thionated PDIs',[17] agreeing with these results for the related NDI series.

2.3. Conclusions

The most complete electrochemical characterisation to date of a series of thionated NDIs has been completed revealing that thionation of NDIs is a straightforward method of adjusting the energy levels of the frontier orbitals. Synthetic strategies utilising naphthalic imide suggest there is a barrier to the synthesis of higher thionated products containing three and four sulfur atoms, explaining why there are few reports of these compounds in current literature.

Each successive sulfur substitution causes a spectral redshift of ~45 nm representing a decrease in the HOMO-LUMO gap. Cyclic voltammetry measurements indicate each thionation causes an anodic shift in the reduction potentials by approximately 150 mV, with DFT data confirming that this increased electron affinity is due to a decrease in LUMO energy. As chromophores, the thionated NDIs behave very similarly to their parent NDI; the bathochromic shifts caused by thionation are preserved both upon one-electron reduction to stable radical species and also when reduced again to form stable dianions.

A difference between the dithionated NDI cis and trans isomers becomes apparent in the spectroscopy of their electrochemically reduced chromophores, perhaps due to a difference in conjugation across the molecules. Simulations of the EPR spectra for these reduced isomers are in good agreement with the experimental data, thus are able to provide reasonable approximations of the hyperfine coupling constants between the radical electrons and the spin active H and N nuclei, finding subtle differences between the two isomers.

Picosecond time-resolved transient absorption measurements were able to identify the singlet and triplet excited stated of the parent nonthionated NDI compound and comparisons with this data allowed for tentative assignment of singlet and triplet spectral features in the mono- and dithionated NDI analogues. Decay kinetics of these data entail a faster conversion from singlet to triplet excited states, implying that intersystem crossing is improved as a result of thionation, and in agreement with current data for other thionated rylene diimides. Similarly, the excited state relaxes faster for the thionated NDI compounds, with lifetimes roughly four orders of magnitude smaller for the thionated NDIs than for the nonthionated parent.

2.4. Materials and Methods

2.4.1. Synthesis

*2.4.1.1. Synthesis of N,N'-di(1-ethylpropyl)-naphthalene-1,4,5,8-tetracarboxylic acid diimide (**NDIS$_0$**)*

A mixture of naphthalene-1,4,5,8-tetracarboxylic dianhydride (3.00 g, 11.2 mmol) and 3-aminopentane (4.5 mL, 38.6 mmol) in *N*,*N*-dimethylformamide (30 mL) was stirred at 120 °C for 16 h. After 16 h, the solution was allowed to cool and the solvent removed under reduced pressure to give a brown solid which was dissolved in chloroform (100 mL) and washed with H_2O (2 x 250 mL) and sat. aq. NaCl (250 mL), dried over $MgSO_4$, filtered and concentrated. The brown solid was purified by column chromatography (silica, chloroform) to afford the title compound as a pale orange-pink solid (2.21 g, 46 %). A suitable crystal for X-ray diffraction was grown by slow evaporation of a chloroform solution of the compound. λ_{max} (abs) = 382 nm. ^{1}H NMR (500 MHz, $CDCl_3$) δ ppm 8.73 (s, 4 H), 4.98 - 5.11 (m, 2 H), 2.23 (ddd, *J* = 14.03, 9.38, 7.49 Hz, 4 H), 1.93 (dt, *J* = 13.87, 6.78 Hz, 4 H), 0.90 (t, *J* = 7.49 Hz, 12 H). ^{13}C NMR (500 MHz, $CDCl_3$) δ ppm 163.72, 130.94, 126.79, 126.60, 77.00, 58.09, 24.92, 11.23. FT-IR (neat, cm^{-1}) 1698 (ν C=O), 1653 (ν C=O). HRMS (EI)$^+$ m/z 406.1893 ($C_{24}H_{26}N_2O_4$ $[M]^+$ requires 406.1891).

*2.4.1.2. Synthesis of **NDIS$_{1\text{-}2}$***

NDIS$_0$ (1.00 g, 2.46 mmol) and Lawesson's reagent (5.97 g, 14.76 mmol) were dissolved in anhydrous toluene (100 mL) and heated to reflux for 42 h. The solution was cooled to room temperature and concentrated under reduced pressure. The resulting brown residue was dissolved in chloroform (100 mL) and washed with NaOH (250 mL, 100 mM), sat. aq. $NaHCO_3$ (250 mL) and sat. aq. NaCl (250 mL), dried over $MgSO_4$, filtered and concentrated to give a crude mixture of NDIS$_{1\text{-}2}$. This mixture was purified by column chromatography (silica, gradient elution from 1:1 pentane: dichloromethane to dichloromethane) to give NDIS$_{1\text{-}2}$ in the following yields.

NDIS$_1$ as a pale green powder (414 mg, 40 %). Suitable crystals for X-ray diffraction were grown by evaporation of a pentane/dichloromethane solution of the compound. λ_{max} (abs) = 429 nm. ^{1}H NMR (400 MHz, CDCl$_3$) δ ppm 9.07 (d, *J* = 8.04 Hz, 1 H), 8.71 (s, 2 H), 8.63 (d, *J* = 8.04 Hz, 1 H), 6.08 - 6.31 (m, 1 H), 5.04 (tt, *J* = 9.61, 5.88 Hz, 1 H), 2.16 - 2.37 (m, 4 H), 1.99 - 2.11 (m, 2 H), 1.87 - 1.98 (m, 2 H), 0.88 - 0.95 (m, 12 H). ^{13}C NMR (500 MHz, CDCl$_3$) δ ppm 196.56, 160.03, 137.15, 130.96, 130.51, 130.27, 127.29, 126.94, 126.21, 125.24, 124.84, 65.70, 58.07, 25.36, 24.93, 11.24, 11.16. FT-IR (neat, cm^{-1}) 1700 (sym. ν C=O), 1682 (sym. ν C=O), 1660 (antisym. ν C=O), 1153 (ν C=S). HRMS (EI)$^+$ m/z 422.1660 ($C_{24}H_{26}N_2O_3S_1$ [M]$^+$ requires 422.1664).

NDIS$_2$ cis as a dark brown solid (225 mg, 21 %). λ_{max} (abs) = 474 nm. ^{1}H NMR (400 MHz, CDCl$_3$) δ ppm 8.96 (s, 2 H), 8.69 (s, 2 H), 6.20 (t, *J* = 6.87 Hz, 2 H), 2.17 - 2.40 (m, 4 H), 2.04 (dquin, *J* = 14.11, 7.14, 7.14, 7.14, 7.14 Hz, 4 H), 0.92 (t, *J* = 7.45 Hz, 12 H). ^{13}C NMR (500 MHz, CDCl$_3$) δ ppm 196.60, 160.32, 136.69, 130.92, 128.87, 126.97, 124.91, 65.61, 25.35, 11.17. FT-IR (neat, cm^{-1}) 1682 (ν C=O), 1152 (ν C=S). HRMS (EI)$^+$ m/z 438.1427 ($C_{24}H_{26}N_2O_2S_2$ [M]$^+$ requires 438.1436).

NDIS$_2$ trans as deep green crystals (178 mg, 17 %). Suitable crystals for X-ray diffraction were grown by evaporation of a dichloromethane solution of the compound. λ_{max} (abs) = 476 nm. ^{1}H NMR (400 MHz, CDCl$_3$) δ ppm 9.06 (m, *J* = 8.03 Hz, 2 H), 8.61 (m, *J* = 8.03 Hz, 2 H), 6.04 - 6.32 (m, 2 H), 2.17 - 2.42 (m, 4 H), 2.04 (dquin, *J* = 14.12, 7.13, 7.13, 7.13, 7.13 Hz, 4 H), 0.93 (t, *J* = 7.53 Hz, 12 H). ^{13}C NMR (500 MHz, CDCl$_3$) δ ppm 196.77, 160.37, 137.15, 130.46, 129.85, 125.97, 124.99, 77.00, 65.75, 25.37, 11.17. FT-IR (neat, cm^{-1}) 1674 (ν C=O), 1149 (ν C=S). HRMS (EI)$^+$ m/z 438.1445 ($C_{24}H_{26}N_2O_2S_2$ [M]$^+$ requires 438.1436).

*2.4.1.3. Synthesis of **NDIS$_3$***

A mixture of **NDIS$_2$ cis** (50 mg, 114 μmol), **NDIS$_2$ trans** (50 mg, 114 μmol) and Lawesson's reagent (138 mg, 342 μmol) were dissolved in anhydrous toluene (25 mL) and heated to reflux for 24 h. The solution was cooled to room temperature and concentrated under reduced pressure. The resulting brown residue was dissolved in chloroform (50 mL) and washed with NaOH (250 mL, 100 mM), sat. aq. $NaHCO_3$ (250 mL) and sat. aq. NaCl (250 mL), dried over $MgSO_4$, filtered and concentrated. This residue was purified by column chromatography (silica, gradient elution from pentane to 1:1 pentane: dichloromethane to dichloromethane) to give **NDIS$_3$** as a red solid (6.5 mg, 6 %). λ_{max} (abs) = 502 nm. MS (MALDI)$^-$ m/z 454.1 ($C_{24}H_{26}N_2O_1S_3$ [M]$^-$ requires 454.12).

*2.4.1.4. Synthesis of N-(1-ethylpropyl)-1,8-naphthalic imide (**NIS$_0$**)*

1,8-naphthalic anhydride (3.00 g, 15.14 mmol) and 3-aminopentane (2.64 mL, 22.71 mmol) were dissolved in *N*,*N*-dimethylformamide (30 mL) and heated to 120 °C for 6 h. The reaction mixture was concentrated on a rotary evaporator and extracted with chloroform (50 mL), washed with water (100 mL) and brine (100 mL). The solution was dried over $MgSO_4$, filtered and the crude product purified by column chromatography (silica, chloroform) to yield the product as a white solid (2.93 g, 72.2 %). λ_{max} (abs) = 335 nm. ^{1}H NMR (400 MHz, $CDCl_3$) δ ppm 8.59 (d, *J* = 7.15 Hz, 2 H), 8.21 (d, *J* = 8.28 Hz, 2 H), 7.76 (t, *J* = 7.78 Hz, 2 H), 4.99 - 5.12 (m, 1 H), 2.26 (spt, *J* = 7.40 Hz, 2 H), 1.92 (spt, *J* = 6.90 Hz, 2 H), 0.91 (t, *J* = 7.47 Hz, 6 H). ^{13}C NMR (100 MHz, $CDCl_3$) δ ppm 159.84, 133.51, 131.44, 131.13, 128.33, 126.90, 122.94, 57.33, 25.00, 11.29. HRMS (EI)$^+$ m/z 267.1263 ($C_{17}H_{17}N_1O_2$ [M]$^+$ requires 267.1259).

2.4.1.5. Synthesis of ***NIS$_1$***

NIS$_0$ (500 mg, 1.85 mmol) and Lawesson's reagent (2.25 g, 5.57 mmol) were dissolved in anhydrous toluene (50 mL) and heated to reflux for 24 h. The reaction mixture was cooled, filtered and concentrated under reduced pressure. The crude mixture was purified by column chromatography (silica, gradient elution from 2:1 hexane: chloroform to 1:1 hexane: chloroform) to give **NIS$_1$** as a bronze powder (146 mg, 27.7 %). λ_{max} (abs) = 404 nm. ^{1}H NMR (400 MHz, CDCl$_3$) δ ppm 9.04 (d, *J* = 7.53 Hz, 1 H), 8.57 (d, *J* = 7.28 Hz, 1 H), 8.10 - 8.23 (m, 1 H), 7.69 (t, *J* = 7.91 Hz, 1 H), 7.73 (t, *J* = 7.78 Hz, 1 H), 6.33 (quin, *J* = 6.90 Hz, 1 H), 2.30 (spt, *J* = 7.50 Hz, 2 H), 2.03 (spt, *J* = 7.15 Hz, 2 H), 0.94 (t, *J*=7.47 Hz, 6 H). ^{13}C NMR (400 MHz, CDCl$_3$) δ ppm 198.54, 161.40, 138.12, 133.55, 133.12, 131.61, 131.44, 128.21, 127.18, 126.99, 126.43, 123.48, 65.12, 25.41, 11.21. HRMS (EI)$^+$ m/z 283.1037 ($C_{17}H_{17}N_1O_1S_1$ [M]$^+$ requires 283.1031).

2.5. References

1. A. Facchetti, *Mater. Today*, 2007, **10**, 28-37.
2. X. Zhan, A. Facchetti, S. Barlow, T. J. Marks, M. A. Ratner, M. R. Wasielewski and S. R. Marder, *Adv. Mater.*, 2011, **23**, 268-284.
3. A. Nitzan, *Ann. Rev. Phys. Chem.*, 2001, **52**, 681-750.
4. R. G. Pearson, *J. Am. Chem. Soc.*, 1986, **108**, 6109-6114.
5. J. G. Laquindanum, H. E. Katz, A. Dodabalapur and A. J. Lovinger, *J. Am. Chem. Soc.*, 1996, **118**, 11331-11332.
6. H. E. Katz, J. Johnson, A. J. Lovinger and W. Li, *J. Am. Chem. Soc.*, 2000, **122**, 7787-7792.
7. D. Shukla, S. F. Nelson, D. C. Freeman, M. Rajeswaran, W. G. Ahearn, D. M. Meyer and J. T. Carey, *Chem. Mater.*, 2008, **20**, 7486-7491.
8. B. J. Jung, J. Sun, T. Lee, A. Sarjeant and H. E. Katz, *Chem. Mater.*, 2009, **21**, 94-101.
9. B. A. Jones, A. Facchetti, T. J. Marks and M. R. Wasielewski, *Chem. Mater.*, 2007, **19**, 2703-2705.
10. Z. Chen, Y. Zheng, H. Yan and A. Facchetti, *J. Am. Chem. Soc.*, 2009, **131**, 8-9.
11. Y. Wei, Q. Zhang, Y. Jiang and J. Yu, *Macromol. Chem. Phys.*, 2009, **210**, 769-775.
12. W. Chen, J. Zhang, G. Long, Y. Liu and Q. Zhang, *J. Mater. Chem. C*, 2015, **3**, 8219-8224.
13. L. M. Kozycz, C. Guo, J. G. Manion, A. J. Tilley, A. J. Lough, Y. Li and D. S. Seferos, *J. Mater. Chem. C*, 2015, **3**, 11505-11515.
14. S. V. Bhosale, C. H. Jani and S. J. Langford, *Chem. Soc. Rev*, 2008, **37**, 331-342.
15. S.-L. Suraru and F. Würthner, *Angew. Chem. Int. Ed.*, 2014, **53**, 7428-7448.
16. H. Langhals, *Heterocycles*, 1995, **40**, 477-500.
17. A. J. Tilley, R. D. Pensack, T. S. Lee, B. Djukic, G. D. Scholes and D. S. Seferos, *J. Phys. Chem. C*, 2014, **118**, 9996-10004.
18. P. Ganesan, J. Baggerman, H. Zhang, E. J. R. Sudhölter and H. Zuilhof, *J. Phys. Chem. A*, 2007, **111**, 6151-6156.
19. P. Ganesan, X. Yang, J. Loos, T. J. Savenije, R. D. Abellon, H. Zuilhof and E. J. R. Sudhölter, *J. Am. Chem. Soc.*, 2005, **127**, 14530-14531.
20. S. Green and M. A. Fox, *J. Phys. Chem.*, 1995, **99**, 14752-14757.

Chapter 3

Naphthalene Diimide Donor-Acceptor Systems

3.1. Introduction

Following on from the encouraging electrochemical results described for model NDIs in Chapter 2, the thionation of more functional NDI systems was explored. Inspired by nature's photosynthesis, the construction of defined molecular architectures that are able to undergo charge-delocalisation or charge hopping between units is a goal of many chemical researchers.[1-5] Such charge hopping, either as electrons or holes, is necessary for organic electronic applications and for OPVs.[6] One method of promoting charge sharing or separation is with donor-acceptor dyads.

3.1.1. Electron Donor-Acceptor Systems

An electron donor-acceptor complex or charge transfer complex is formed from an association of molecules that are capable of transferring a fraction of electronic charge from one part (the donor) to another (the acceptor). The donor and acceptor can be separate molecular entities or attached to each other as two parts of a larger molecule. Nomenclature of charge transfer complexes is such that dyads refer to donor-acceptor systems with one of each component; triads to systems with either two donors and one acceptor, or one donor and two acceptors; and tetrads contain a mixture of up to four donor and acceptor moieties etc. There is substantial interest in these charge transfer systems as solar energy convertors, in optoelectronic devices and as ambipolar semiconductors.[7, 8] The first donor-acceptor complex reported was constructed in 1973 from tetrathiafulvene (TTF) and tetracyanoquinodimethane (TCNQ).[9] The TTF-TCNQ system displayed an impressive conductivity, comparable to metals and could function as a current rectifier.[10]

Photoinduced electron transfer (PET) can occur when an electron is passed from a donor orbital to an acceptor orbital. A photon of light is first required to excite an electron and create an electron-hole pair in either the donor or acceptor, allowing the electron from to the donor to be transferred. In photoinduced oxidation, the photon excites an electron from a ground state orbital in the acceptor, creating an electron-hole pair in the ground state orbital. An electron from the ground state of the donor molecule can then transfer an electron to this newly vacated hole. In photoinduced reduction it is the donor molecule that is excited by the photon, promoting an electron to an excited state orbital that is then transferred to the LUMO of the acceptor (Figure 3.1).

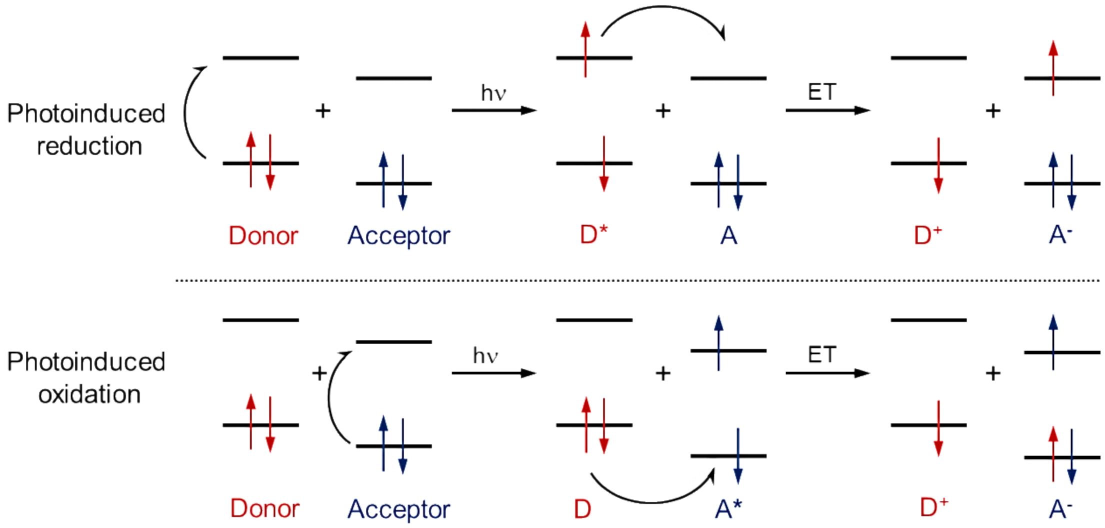

Figure 3.1: Schematic describing the electronic transitions in two types of photoinduced electron transfer.

The transfer of an electron results in a charge separated pair, with a positively charged hole on the donor and a negatively charged electron on the acceptor (Figure 3.2). The efficiency of this process depends on the orbital energies of the donor and acceptor, as well as the distance between them. In single molecule dyad systems a bridge may be used to separate the donor and acceptor segments and separate their orbitals. The length of this bridge can affect the rate and nature of electron transport, with longer bridges even serving as 'wires' through which the electron can be transported.[11-13] The ground state starting material can be regenerated by passing the electron back from the acceptor to the donor. This process is known as charge recombination, and the photon's energy is released again as heat. Alternatively the energy of a charge separated species can be used by organic photovoltaic systems or for artificial photosynthesis. The generation of charge separated states is 'fundamental to the production of renewable solar electricity using molecular photovoltaics'.[14]

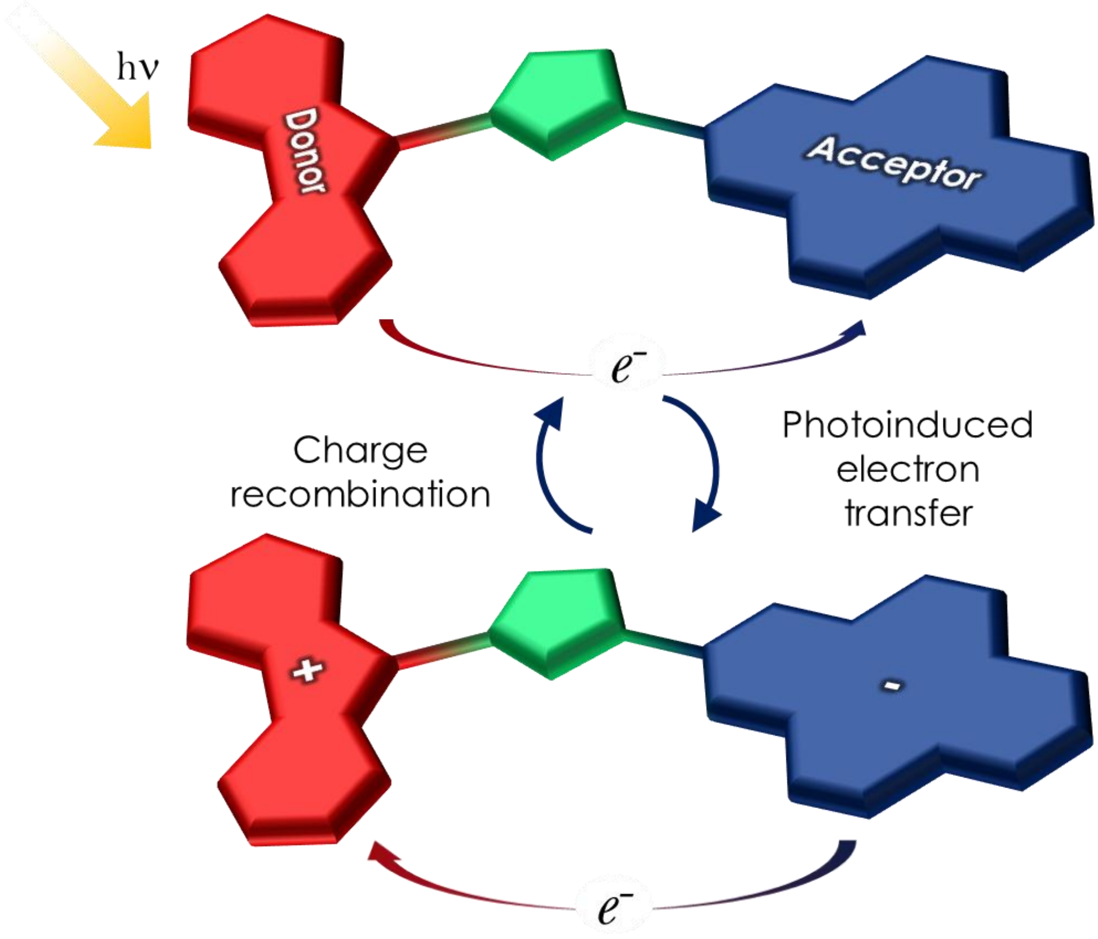

Figure 3.2: Schematic of photoinduced charge separation and charge recombination in a bridged donor-acceptor dyad.

3.1.2. Electron Donor-Acceptor Systems Using NDIs

NDIs began to be seen as an attractive choice of electron acceptor due to their chemical and physical robustness, ease of synthesis from commercially available materials and electronic complementarity to ubiquinones, biology's choice acceptor in photosynthetic reaction centres. Unsubstituted NDIs can be reversibly reduced chemically or electrochemically at the fairly mild potential of -1.1 V vs. Fc^+/Fc, forming stable radicals.[7] For reference, trimethylbenzoquinone is reduced at -1.2 V vs. Fc^+/Fc.[15]

Osuka et al.[16] synthesised a series of linear triads containing an NDI tethered to a free-base porphyrin and a metallated zinc-porphyrin. Photoexcitiation of these systems resulted in long-lived charge separated states on the microsecond timescale. Modification to the length of the bridge spacing between the two porphyrin units affected the charge separated lifetimes and efficiencies of the triads. The same team also produced switchable electron transfer complexes utilising an NDI-Zinc porphyrin-pyromellitic diimide triad, where preferential charge transfer to either the NDI or PyDI acceptors could be controlled by the addition of fluoride (Figure 3.3).[17] Following photoexcitation, a charge separated state preferentially forms with an anionic NDI unit, as a result of the better electron accepting properties of the NDI versus the PyDI. The addition of fluoride ions can switch off this PET pathway by coupling to a boron centre that lies between the porphyrin and NDI units, causing electron transport to occur completely in the direction of the PyDI.

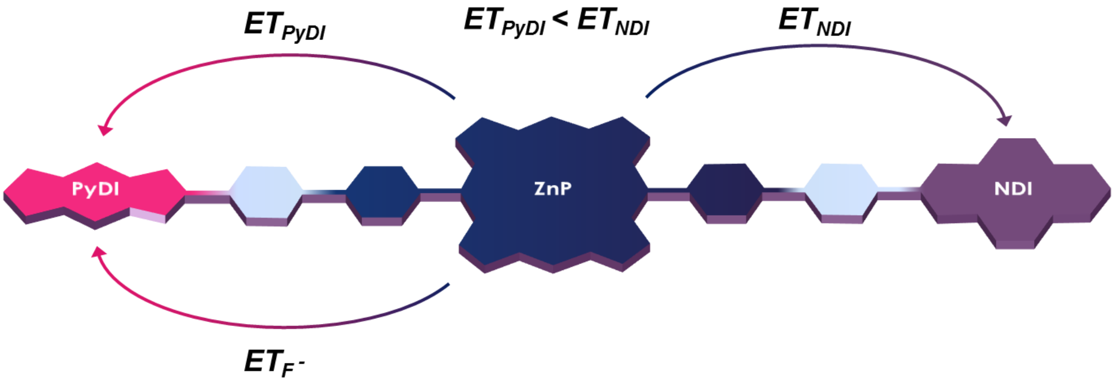

Figure 3.3: Electron transfer pathways in an NDI-Zinc Porphyrin (ZnP)-PyDI triad.

Further, increasingly complicated NDI-porphyrin electron transport systems, exploring hydrogen bonding between the NDI and porphyrin and even coordination of the NDI unit to a metallated porphyrin have been investigated, and are the subject of a review article published by Langford et al.[18]

NDI was employed as the terminal electron acceptor in a series of triads extensively investigated by the Wasielewski group in 1996.[19-21] One triad comprising anisidine-aminonaphthlalic imide-NDI subunits was capable of storing ~2 eV for over 300 ns following photoexcitiation.[19] Recombination of the charges yielded a radical pair triplet state, characterised by electron paramagnetic resonance spectroscopy.[21] The group have also reported mixtures of triplet radical pairs and correlated radical pairs for artificial NDI photosystems.[22] More recently, a pentad comprising a central silicon-phthalocyanine ligated to two NDI-fullerene units exhibited fast charge separation through the singlet excited state of NDI and subsequent recombination into triplet states of the fullerene and phthalocyanine (Figure 3.4).[23] As described in Chapter 2, NDI-thiophene oligomers function admirably in OFETs, providing encouragement for Kondratenko et al. to fabricate dyads of NDI and bis-3,4-ethylenedioxythiophene (EDOT) in pursuit of exceptionally stable dyads.[24]

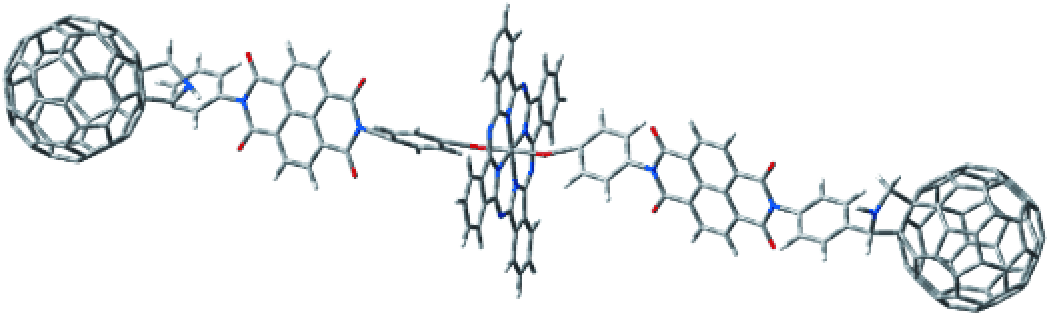

Figure 3.4: Structure of the silicon-phthalocyanine-NDI-fullerene pentad reported by Fukuzumi and co-workers.[23]

The examples described above solely cover NDI donor-acceptor systems utilising non-core substituted NDIs, though the literature also contains plethora of core-substituted NDI electron transport structures. One inspiring example and the most advanced photosystem to date is a zipper assembly synthesised within the research group of Matile (Figure 3.5).[5, 25] Short *p*-oligophenyl and *p*-oligophenylethinyl scaffolds are furnished with red and yellow core-substituted NDI acceptors that 'zip up' (organise) into columns of electron transporting NDI stacks and hole transporting *p*-oligophenyl rods, driven by hydrogen bonding and ion pairing between adjacent NDIs in the stacks. The arrangement is grown from an initiator NDI column tethered to a gold surface. The resulting coaxial arrangement of electron and hole transporting channels is termed a supramolecular n/p-heterojunction (SHJ). As soon as photoexcitation generates electron-hole pairs they are funnelled in opposite directions, generating efficient photocurrent.

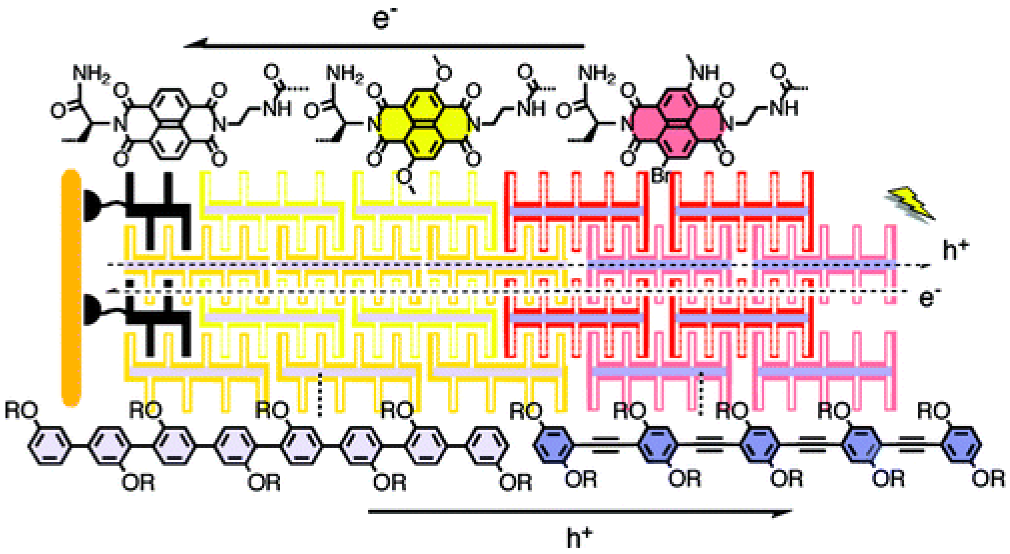

Figure 3.5: Artificial photosystem SHJ zipper assembly of coloured NDIs. Adapted from Sakai et al.[5]

In summary, NDI based charge transfer complexes have been extensively examined, taking advantage of the NDI moiety as one of the few air-stable n-type materials. In a review article published by Matile and co-workers,[26] it is stated that 'the decreasing LUMO with electron-withdrawing substituents in the core suggests that [core-substituted] NDIs should afford even better n-semiconductors'. Since then, however, the use of thionation as a synthetically convenient method of adjusting the LUMO of NDIs is becoming popular and could lead to more versatile charge separated complexes.

3.2. Results and Discussion

3.2.1. Molecular Design and Synthesis

Following on from the encouraging results obtained for the simple thionated NDI and NI systems, more complicated, functional molecular targets were pursued. Owing to the significant increase in reduction potential upon thionation, it was decided that naphthalic imide and naphthalene diimide would be excellent candidates for electron acceptors in a donor-acceptor dyad system. Phenothiazine was selected as the electron donor, inspired by promising results obtained by Weiss et al.[11] for a similar phenothiazine-perylene diimide system.

In order to couple the phenothiazine to the selected electron acceptors, it was necessary to furnish the phenothiazine with an amine group, capable of reaction with the anhydride functionalities of the NI and NDI precursors. A phenylene spacer was used to separate the phenothiazine and amine over an aliphatic alternative, as this would allow for a conformationally defined architecture and facilitate crystallographic characterisation. Thus, **PTZ-NO$_2$** was synthesised from 4-iodonitrobenzene and phenothiazine using a palladium catalysed Buchwald–Hartwig amination, before reduction to **PTZ-NH$_2$** with tin chloride under acidic conditions (Scheme 3.1).

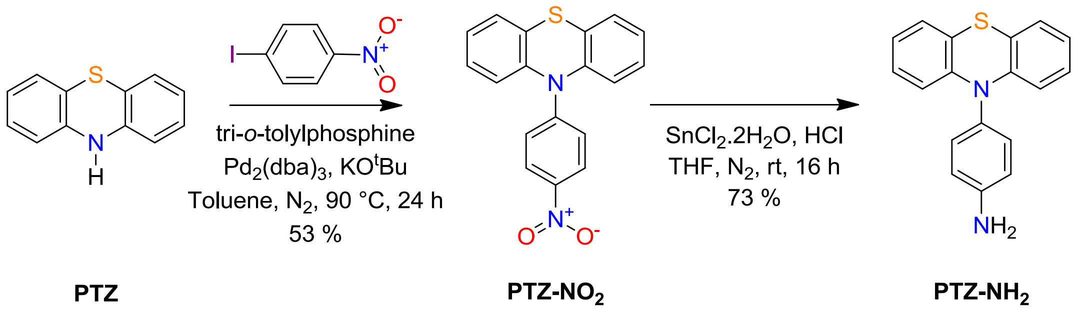

Scheme 3.1: Synthesis of PTZ-NH$_2$.

1,8-Naphthalic anhydride and **PTZ-NH$_2$** were then coupled in molten imidazole to afford the first donor-acceptor system, **NIS$_0$-PTZ**, before being thionated with Lawesson's reagent to generate **NIS$_2$-PTZ** (Scheme 3.2). Interestingly, unlike when the aliphatic imide chain was used, as in the case of **NIS$_0$** (see Chapter 2), full thionation was possible. Moreover, no monothionated product was present in the crude reaction mixture, leading to a high overall yield (44 %) of the final dyad product. The presence of the aromatic imide group perhaps increases the nucleophilicity of the imide oxygen atoms by electron donation from the phenylene ring, improving reactivity towards Lawesson's reagent, and permitting the geminate dithionation pattern.

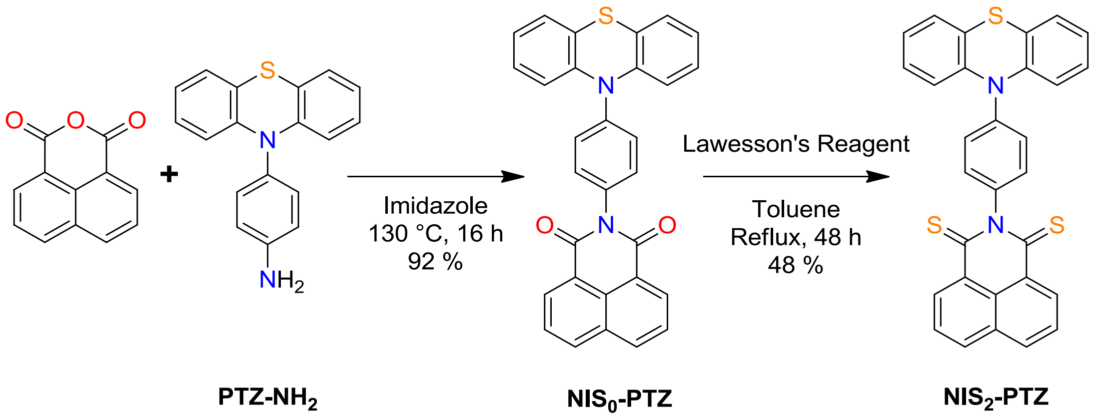

Scheme 3.2: Synthesis of naphthalic imide based donor-acceptor dyads NIS$_0$-PTZ and NIS$_2$-PTZ.

Phenothiazine dyads based around an NDI electron acceptor were also synthesised. Initially, a symmetrically substituted diphenothiazine-NDI was created, although due to issues with solubility, was discarded in favour of an *N*,*N*'-asymmetrically substituted NDI. Such a diimide would allow for a one acceptor-one donor dyad and leave an N-terminus of the NDI free to include a solubilising group. Following a preparation reported by Shavaleev et al.[27] a suitable naphthalene monoimide monoanhydride (**NMI**) was produced (Scheme 3.3).

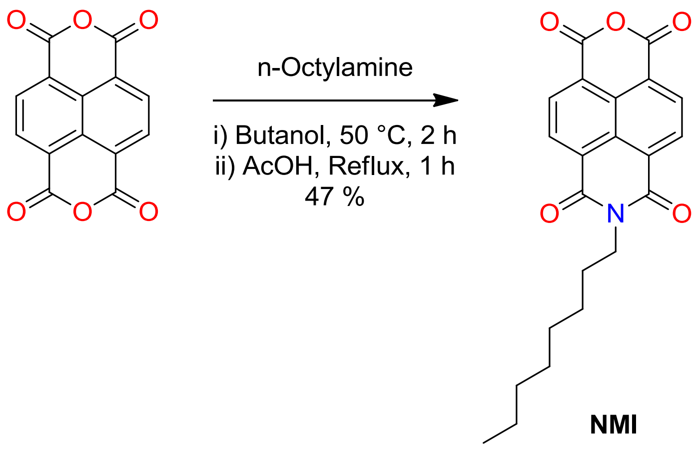

Scheme 3.3: Synthesis of NMI.

Under commonly utilised imidization conditions, **NMI** was able to react with **PTZ-NH$_2$**, affording another dyad system **NDIS$_0$-PTZ** (Scheme 3.4). The NDI dyad was isolated as a blue powder, an unexpected result; core substitution to the NDI is usually required to absorb visible wavelengths.[26] This absorbance does not extend to solution phase: the UV/vis absorption spectrum of **NDIS$_0$-PTZ** in dichloromethane is typical of an NDI, though extra peaks due to the phenothiazine chromophore are present (see below).

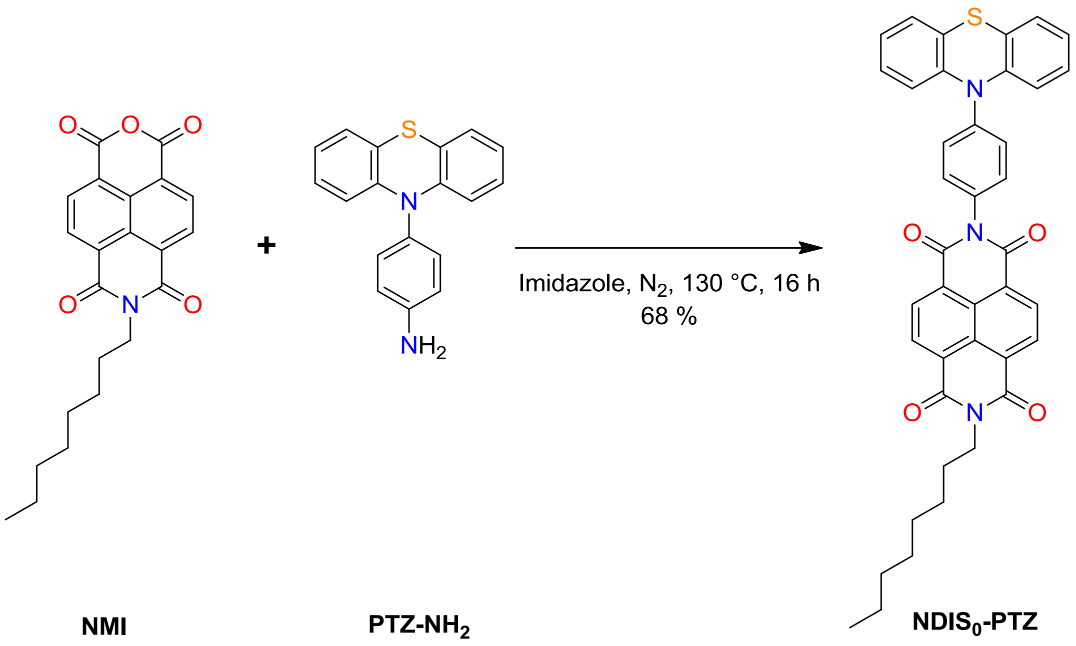

Scheme 3.4: Synthesis of NDIS$_0$-PTZ.

Thionation of **NDIS$_0$-PTZ** was straightforward (Scheme 3.5). Two thionated products were isolated through column chromatography of the crude reaction mixture, which mass spectrometry revealed to be tri- and di-thionated derivatives. Additionally, a fraction was isolated from column chromatography with a mass consistent with a dithionated product. ^{1}H NMR spectroscopy of this fraction could not assist with structural assignment, so it was concluded that this fraction contained a mixture of possible dithionated isomers (see below). Further column chromatography could not separate these isomers.

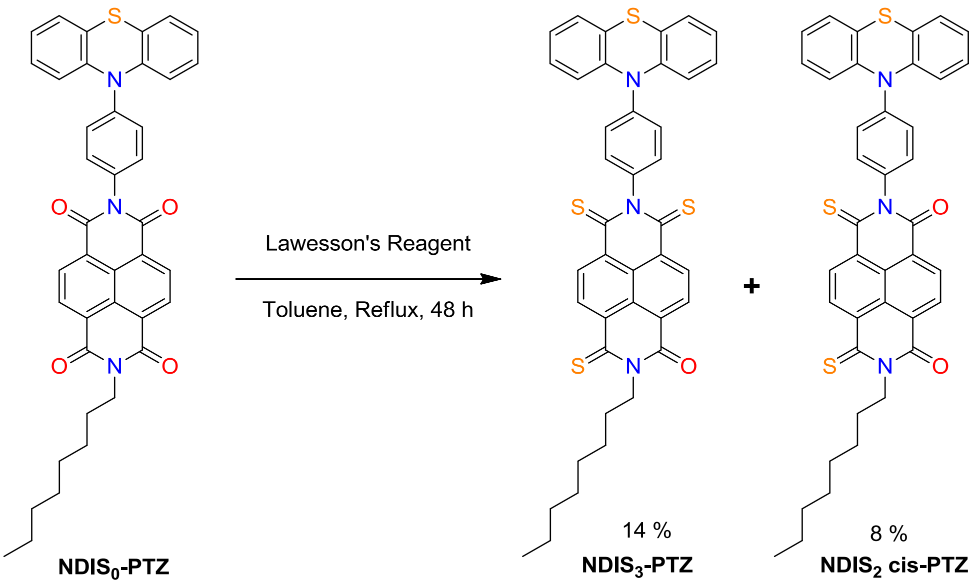

Scheme 3.5: Synthesis of thionated NDI-PTZ systems.

3.2.1.1. Structural assignment of ***NDIS$_2$ cis-PTZ*** *and* ***NDIS$_3$-PTZ***

Because the two imide terminals are not equivalent, structural assignment of the thionated products was more difficult: there are two possible **NDIS$_3$-PTZ** isomers and four for **NDIS$_2$-PTZ** (Figure 3.6). Since it proved possible to fully exchange the imide oxygens for sulfur in the naphthalic imide system, it seemed more likely that this would also occur in the NDI case. A single crystal was grown of **NDIS$_3$-PTZ**, allowing X-ray crystallography to confirm this structure (see below). A combination of 1D and 2D NMR experiments allowed for structural assignment of the dithionated product. ^{1}H NMR signals were observed at 9.02 and 8.80 ppm, attributed to the aromatic protons on the naphthalene core. The shape of the peaks in this region allowed both geminate isomers to be discounted, which would have resulted in clear doublets, whereas the observed peaks had a more complicated shape. These peaks represented shifts of +0.18 and -0.04 ppm relative to the nonthionated **NDIS$_0$-PTZ** (at 8.84 ppm), more consistent with results originally obtained for the **NDIS$_2$ cis** isomer than the trans. In an HMBC experiment, the trans isomer should show four cross-peaks; each set of core-protons can couple to C=S and C=O carbon nuclei, the cis isomer would only display coupling between the core-protons and either a C=O or C=S carbon nucleus. This is the case, with cross peaks at (9.04, 192.88 ppm) and (9.02, 194.22 ppm) showing that the set of naphthalene ring protons at 9.02 ppm only couple to carbons that are attached to sulfur atoms (at 192.88 and 194.22 ppm); and a cross peak at (8.82, 160.48 ppm) showing coupling between the other naphthalene ring protons and the carbonyl carbons (at 160.88 and 160.32 ppm). Finally, since different chromophores are generated upon reduction of the cis and trans isomers, spectroelectrochemical measurements allowed for unambiguous characterisation of the dithionated product as **NDIS$_2$ cis-PTZ**.

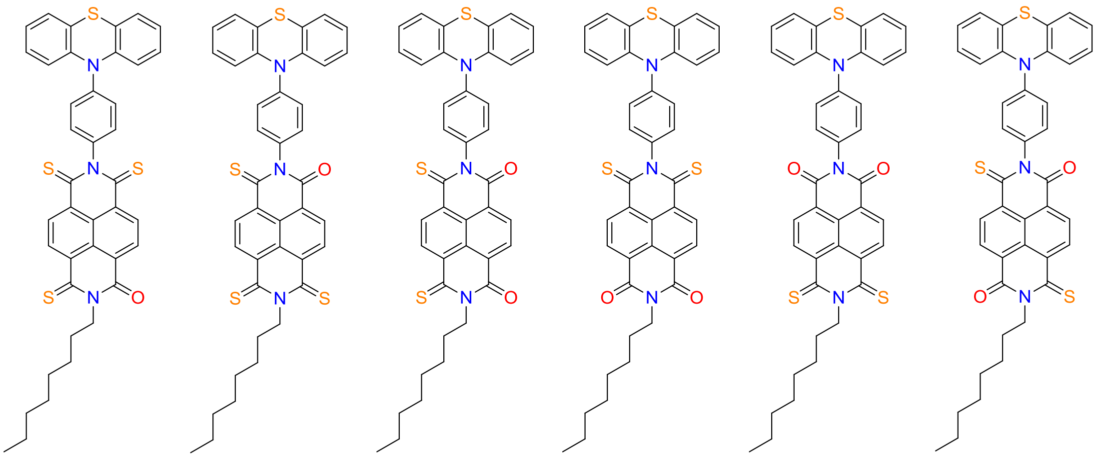

NDIS$_3$-PTZ **NDIS$_3$-PTZ 2** **NDIS$_2$ cis-PTZ** **NDIS$_2$ gem-PTZ 1** **NDIS$_2$ gem-PTZ 2** **NDIS$_2$ trans-PTZ**

Figure 3.6: Possible structures of tri- and di-thionated NDI-PTZ isomers.

3.2.2. X-ray Crystallography

Single crystals of both naphthalic imide-phenothiazine compounds were obtained from vapour diffusion of pentane into chloroform solutions of the compound, and their structures determined by X-ray crystallography (Figure 3.7). Both NI structures are very similar: the greatest difference between the molecules are the C=O and C=S bond lengths. **NIS$_0$-PTZ** has an average C=O length of 1.22 Å, the average C=S bond length in **NIS$_2$-PTZ** is 1.65 Å. The phenylene spacer separating the phenothiazine and naphthalic imide groups lies perpendicular to the NI plane in both molecules, preventing any conjugation between the donor and acceptor.

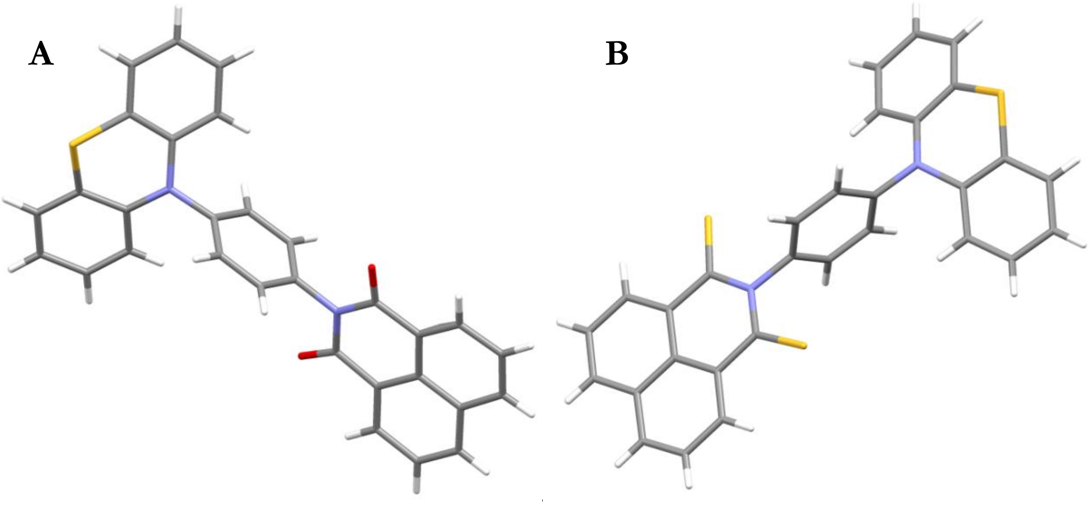

Figure 3.7: X-ray crystal structures of naphthalic imide-phenothiazine dyads. A: NIS$_0$-PTZ, B: NIS$_2$-PTZ. Atom colours - C: grey, O: red, N: blue, H: white and S: yellow.

Crystal structures were also determined for **NDIS$_0$-PTZ** and **NDIS$_3$-PTZ** (Figure 3.8). In the case of the latter molecule, structure determination allowed for unambiguous structural assignment because there was no disorder in the occupancy of the remaining oxygen atom. Two crystallographically distinct molecules of **NDIS$_3$-PTZ** appear in the asymmetric unit, adopting a head-to-tail configuration. The angle between the planes of the two naphthalene cores was measured at 17.06°, the two C=O groups pointing in opposite directions.

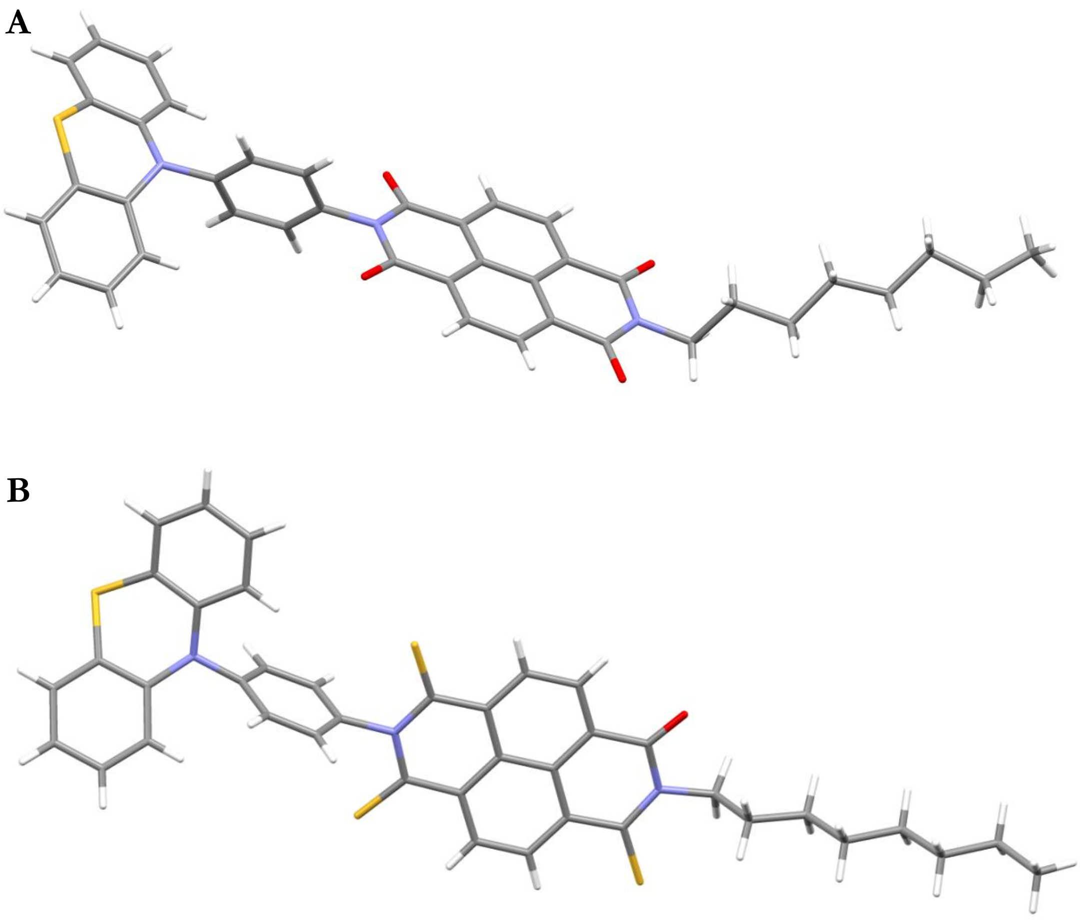

Figure 3.8: X-ray crystal structures of NDI-phenothiazine dyads. A: NDIS$_0$-PTZ, B: NDIS$_3$-PTZ. Atom colours - C: grey, O: red, N: blue, H: white and S: yellow.

Single crystals of the dithionated NDI fraction obtained in addition to the isolated cis isomer could also be grown. Structure solution and refinement revealed that this fraction contained a mixture of the dithionated isomers **NDIS$_2$ trans-PTZ** and **NDIS$_2$ gem-PTZ 1** (see above) as a cocrystal. The asymmetric unit contained two crystallographically distinct molecules of dithionated NDIs, in a head to tail configuration, analogous to **NDIS$_3$-PTZ** (Figure 3.9). On one side of each molecule (with respect to the imide axis) are fixed occupancy sulfur and oxygen atoms, ruling out both **NDIS$_2$ cis-PTZ** and **NDIS$_2$ gem-PTZ 2** isomers. The other side of the molecules contain a mixture of sulfur and oxygen atoms with fractional SOFs signifying the bulk crystal comprises a mixture of both **NDIS$_2$ trans-PTZ** and **NDIS$_2$ gem-PTZ 1**. The remaining possible dithionated isomer (**NDIS$_2$ gem-PTZ 2**) was not observed, reinforcing the observation discussed in

Chapter 2 that thionation on both sides of the aliphatic-substituted imide group is unfavourable, and explaining why only one trithionated product was obtained, despite the possibility of two isomers.

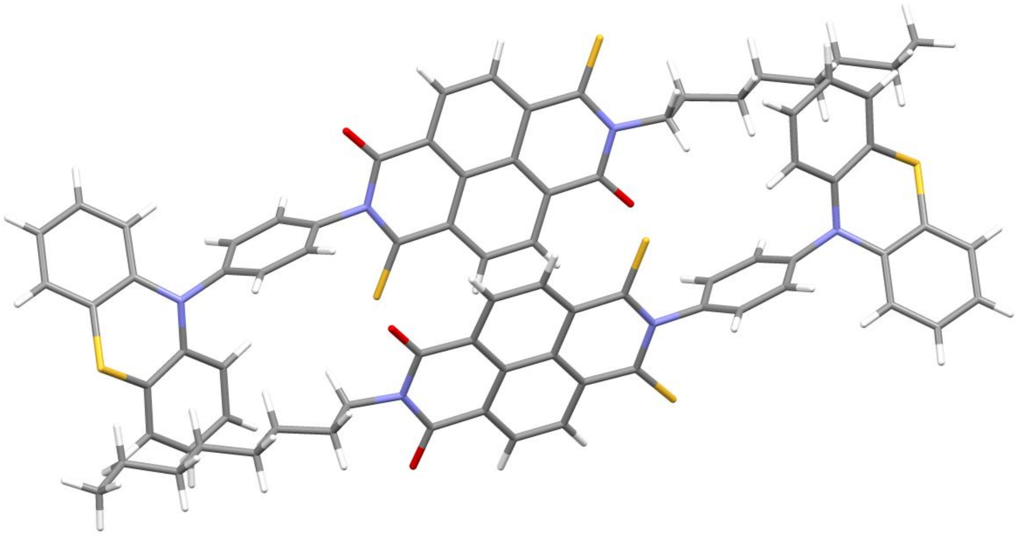

Figure 3.9: X-ray crystal structure of the dithionated NDIS$_2$-PTZ cocrystal, sulfur and oxygen atoms with partial SOFs are omitted to showcomplete molecules of NDIS$_2$ trans-PTZ and NDIS$_2$ gem-PTZ 1. Atom colours - C: grey, O: red, N: blue, H: white and S: yellow.

3.2.3. Electrochemistry

The phenothiazine dyads were studied using cyclic voltammetry and coulometry (Figure 3.10). As expected, all the NI dyads possessed a single reversible one-electron reduction and NDI compounds displayed two reversible one-electron reductions. Additionally, all the dyads were shown to exhibit two oxidation processes, one of which was reversible, resulting from the phenothiazine donor orbitals. A cyclic voltammogram was also recorded for **PTZ-NH$_2$** which revealed two reversible one-electron oxidations.

Across all the dyads, the oxidation processes were found to occur at almost identical potentials, with a reversible oxidation at 0.33 V (vs. Fc$^+$/Fc) and the irreversible oxidation (no return wave was detected under the experimental conditions) at ~1 V. The thionation of the carbonyls had no effect on the phenothiazine portion of the dyads, suggesting there is no communication between the frontier orbitals of the dyad systems. The free phenothiazine amine could be oxidised more readily, at a lower potential of 0.21 V; the second oxidation was also more facile at 0.63 V and was shown to be reversible.

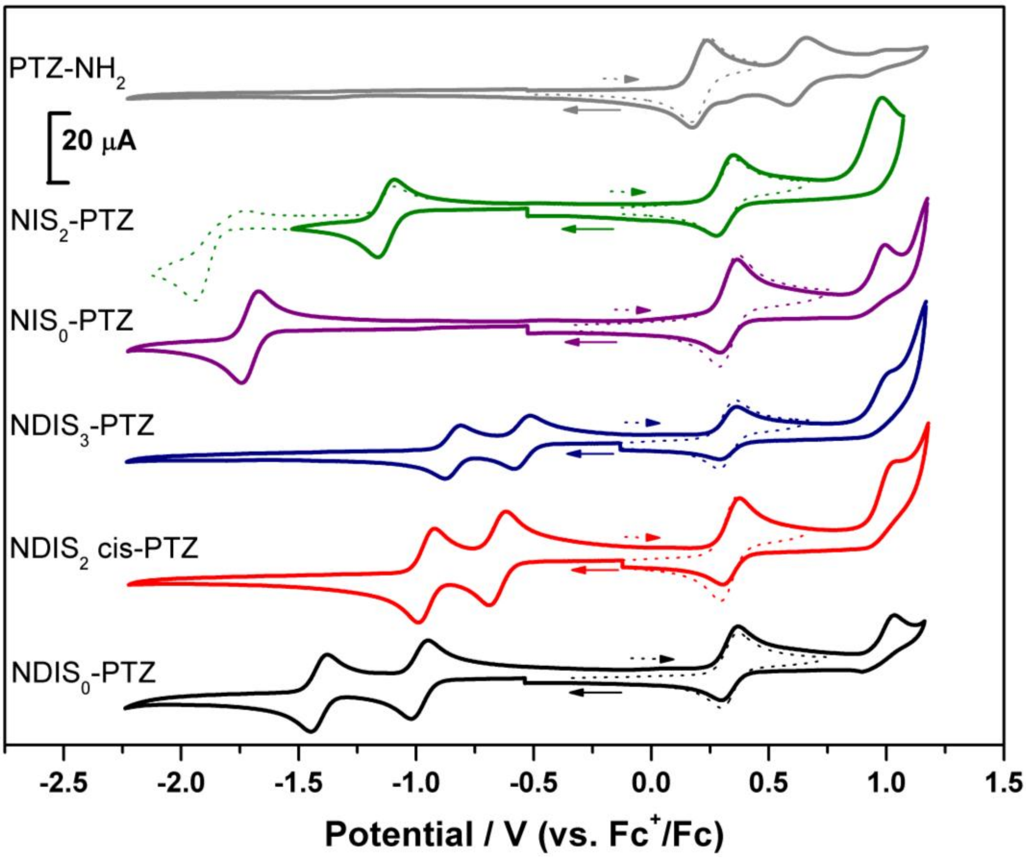

Figure 3.10: Cyclic Voltammograms of thionated NI and NDI dyads in dichloromethane containing 0.4 M [^{n}Bu$_4$N][BF$_4$] as the supporting electrolyte, with a scan rate of 100 mVs^{-1}. Black: NDIS$_0$-PTZ, red NDIS$_2$ cis-PTZ, blue: NDIS$_3$-PTZ, purple: NIS$_0$-PTZ, green: NIS$_2$-PTZ, grey: PTZ-NH$_2$.

The increase in reduction potential that occurs upon thionation of the molecules is almost identical in size for the dyads and the basic NDI systems. Relative to the nonthionated molecule **NDIS$_0$**, the reduction potentials for **NDIS$_2$ cis** are 0.34 V and 0.48 V. For **NDIS$_2$ cis-PTZ**, relative to its nonthionated precursor, the reduction potentials are 0.36 V and 0.45 V, indicating the effect of thionation is just as prominent for the dyads as for the simpler NDIs. Comparison of the two trithionated NDIs synthesised further support this observation.

The most dramatic increase in reduction potential occurs for the naphthalic imide systems. **NIS_2-PTZ** has a first reduction potential at -1.13 V (vs. Fc^+/Fc), 580 mV higher that of its precursor, **NIS_0-PTZ**. Typical NDIs such as **$NDIS_0$** have first reduction potentials of ~-1.1 V, hence the effect of full sulfur substitution to the naphthalic imide molecule has an influence on the electron affinity as pronounced as the addition of a second imide group to form an NDI (though does not add a second reduction process). This shift in reduction potential is significant since NIs are more synthetically accessible than NDIs and lend themselves to further functionalization (e.g. by halogenation of the 2, 3 or 4 positions of the naphthalene ring) for incorporation into devices or other supramolecular systems. The cyclic voltammetry data for the full series of dyad molecules is summarised in Table 3.1.

Table 3.1: Redox potentials of phenothiazine-NDI and –NI dyads.

Compound	1st Reduction $E_{1/2}$ / V	2nd Reduction $E_{1/2}$ / V	1st Oxidation $E_{1/2}$ / V	2nd Oxidation E_{pa} / V
$NDIS_0$-PTZ	-0.99	-1.41	0.33	0.98
$NDIS_2$ cis-PTZ	-0.63	-0.96	0.33	1.02
$NDIS_3$-PTZ	-0.55	-0.85	0.32	1.00
NIS_0-PTZ	-1.71		0.33	0.99
NIS_2-PTZ	-1.13		0.32	0.99
PTZ-NH_2			0.21	0.63*

Potentials quoted against $E_{1/2}$ Fc^+/Fc at 100 mVs^{-1} used as the internal standard. Recorded in dichloromethane at ambient temperature containing $[^nBu_4N][BF_4]$ (0.4 M) as the supporting electrolyte. * $E_{1/2}$ value given.

3.2.3.1. Spectroelectrochemistry and Optical Measurements

The optical absorbance properties of the dyad compounds were probed using spectroelectrochemical techniques to investigate changes to the absorbance profiles upon reduction and oxidation of the compounds. All fully reversible processes were examined, which included the first oxidation and reduction for all dyads and the second reduction for the NDI compounds. Furthermore, the free amine phenothiazine **PTZ-NH$_2$** was also investigated spectroelectrochemically, to examine the spectral changes to the isolated phenothiazine chromophore.

The addition of the phenothiazine chromophore supplied each compound with a strong, sharp absorbance in the ultraviolet region at 257 nm (ε > 40,000 mol^{-1}dm^{3}cm^{-1}), which upon oxidation was replaced with a band at 276 nm of roughly equal intensity. The free neutral phenothiazine **PTZ-NH$_2$** does not absorb any visible light, though the development of a broad, lower intensity (ε = ~10,000 mol^{-1}dm^{3}cm^{-1}) band is observed at 515 nm following oxidation (Figure 3.11). Oxidation of the dyads does not appear to have any effect on the neutral acceptor absorption bands: for molecules **NDIS$_0$-PTZ** and **NIS$_0$-PTZ**, very little perturbation of the bands between 300 and 400 nm (attributed to the naphthalene-imide rings of the acceptors) occurs following oxidation of the compounds. Some change does occur for the thionated molecules **NDIS$_2$ cis-PTZ**, **NDIS$_3$-PTZ** and **NIS$_2$-PTZ** whose absorptions are redshifted so that they are observed close to 500 nm, and thus overlap with the emerging band at 515 nm from the oxidised phenothiazine. A lack of communication between the chromophores reinforces that separation of the frontier orbitals has occurred, and suggests that viable candidates for charge transfer devices have been synthesised.

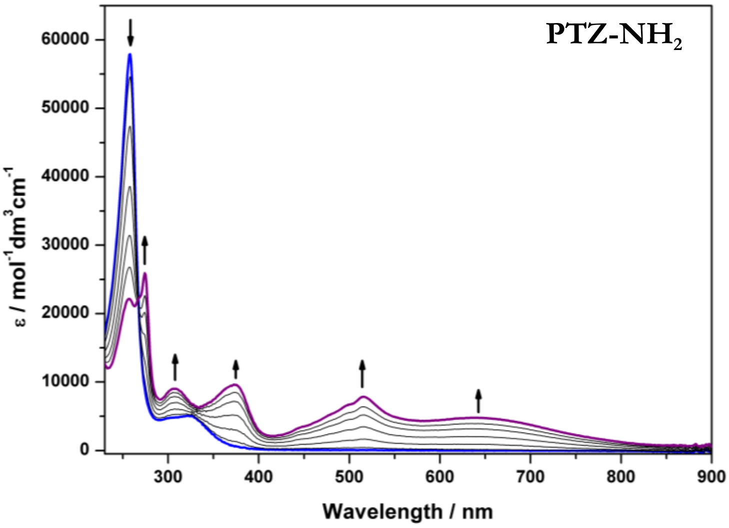

Figure 3.11: UV/vis absorption spectra showing the inter-conversion from neutral (blue) to monocationic (purple) species for PTZ-NH$_2$, arrows indicate the progress of the oxidation. Spectra were recorded in dichloromethane containing [^{n}Bu$_4$N][BF$_4$] (0.4 M) as the supporting electrolyte at 243 K.

Reduction of the NDI compounds proceeded as described in Chapter 2 for the simple, symmetric thionated systems, with spectra for the monoanionic and dianionic phenothiazine-NDI compounds almost exactly resembling those of the corresponding symmetric NDIs. This result was expected since the NDI chromophore is considered closed at the imide nitrogen atoms and substitutions to these positions will not affect the frontier orbitals. Thionation caused a redshift of the NDI bands, which is preserved upon reduction. As discussed above, the absorption spectra for the various redox states of **NDIS$_2$ cis-PTZ** proved to be a useful tool for the characterisation of the compound. The spectrum for [**NDIS$_2$ cis-PTZ**]$^{\cdot-}$ strongly resembled that of [**NDIS$_2$ cis**]$^{\cdot-}$, with one intense peak at λ = 596 nm. The trans isomer, however, could be expected to possess two lower intensity peaks at 696 and 555 nm, allowing for unambiguous characterisation of the compound as the cis isomer.

The spectroelectrochemical interconversions between neutral, monocationic, monoanionic and dianionic forms of the NDI-phenothiazine compounds are shown below (Figure 3.12: **NDIS$_0$-PTZ**, Figure 3.13: **NDIS$_2$ cis-PTZ**, Figure 3.14: **NDIS$_3$-PTZ**). All processes were found to be fully reversible.

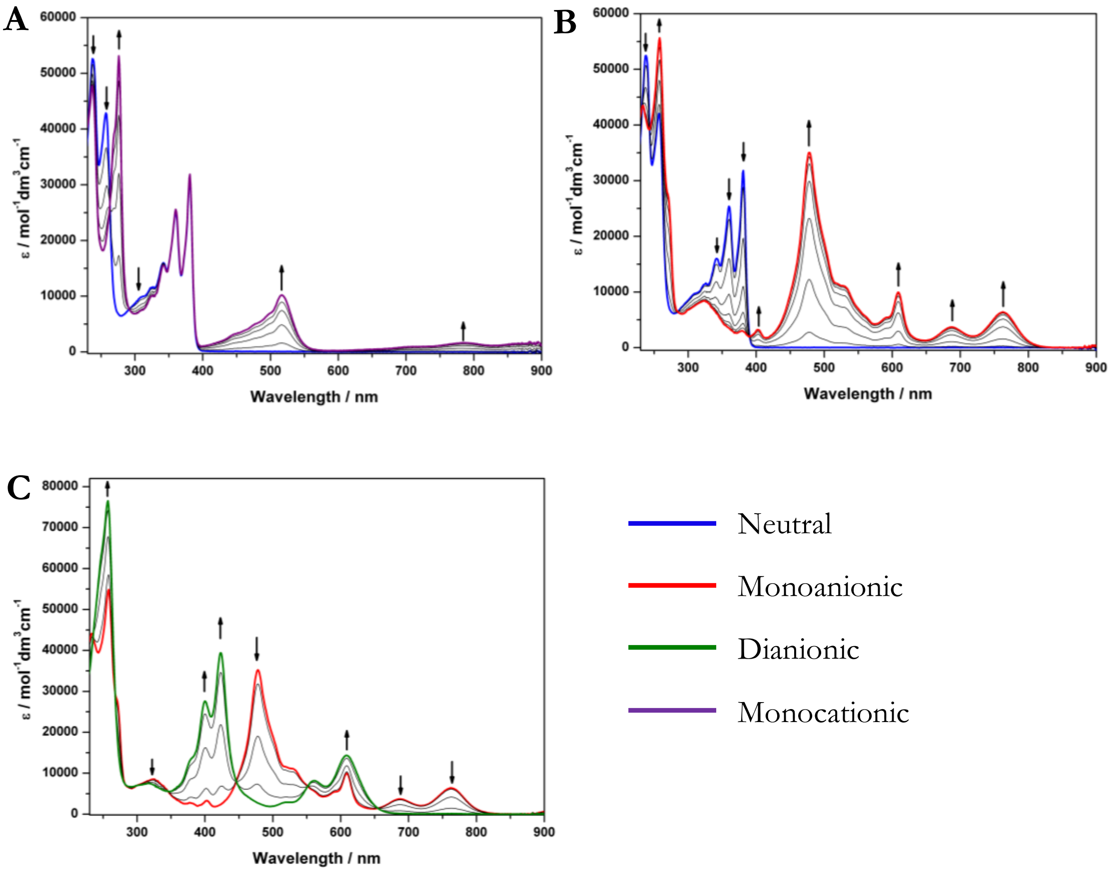
NDIS$_0$-PTZ

Figure 3.12: UV/vis absorption spectra showing the inter-conversion between the various charge states of NDIS$_0$-PTZ, arrows indicate the progress of the oxidation/reduction. A: from neutral (blue) to monocationic (purple), B: from neutral (blue) to monoanionic (red), C: from monoanionic (red) to dianionic (green) species. Spectra were recorded in dichloromethane containing [^{n}Bu$_4$N][BF$_4$] (0.4 M) as the supporting electrolyte at 243 K.

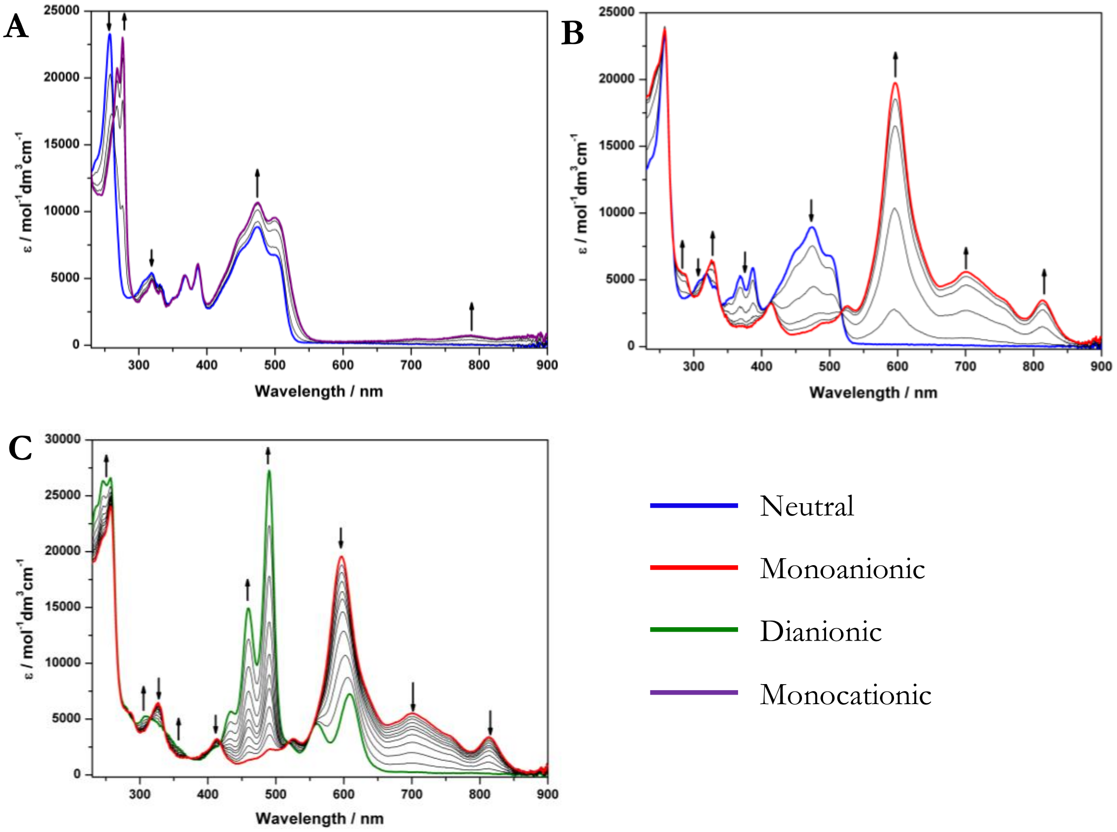

NDIS$_2$ cis-PTZ

Figure 3.13: UV/vis absorption spectra showing the inter-conversion between the various charge states of NDIS$_2$ cis-PTZ, arrows indicate the progress of the oxidation/reduction. A: from neutral (blue) to monocationic (purple), B: from neutral (blue) to monoanionic (red), C: from monoanionic (red) to dianionic (green) species. Spectra were recorded in dichloromethane containing [^{n}Bu$_4$N][BF$_4$] (0.4 M) as the supporting electrolyte at 243 K.

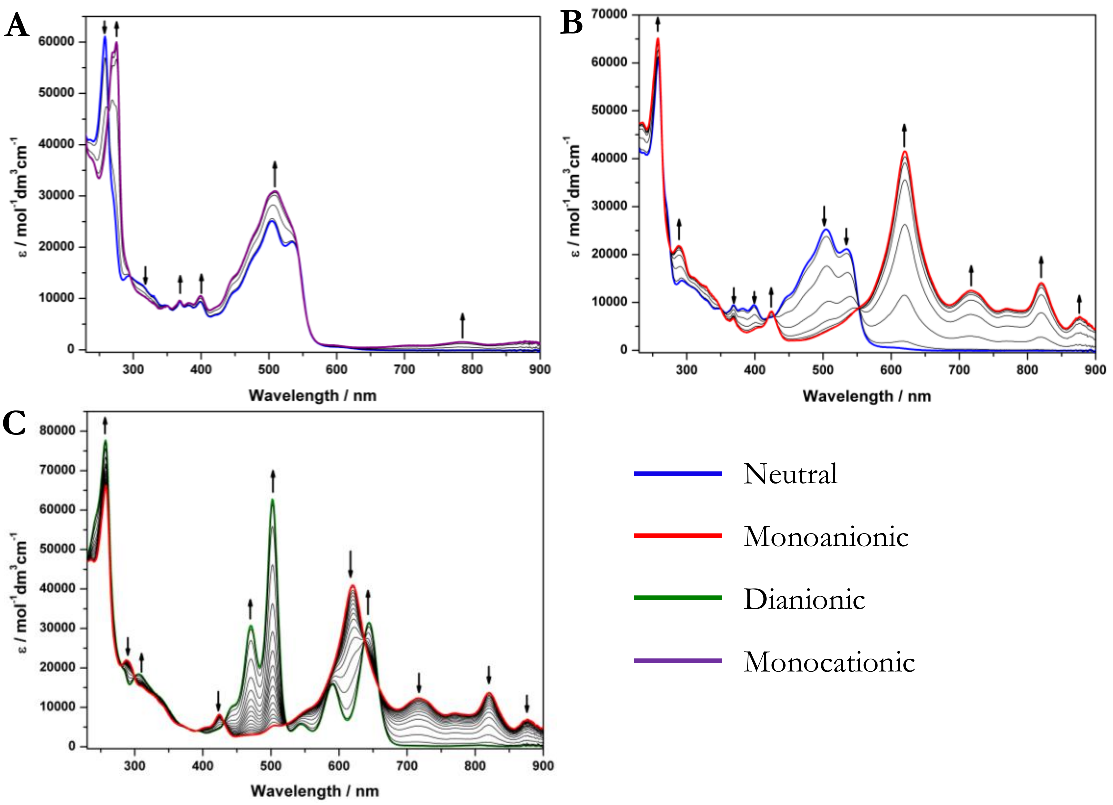

NDIS$_3$-PTZ

Figure 3.14: UV/vis absorption spectra showing the inter-conversion between the various charge states of NDIS$_3$-PTZ, arrows indicate the progress of the oxidation/reduction. A: from neutral (blue) to monocationic (purple), B: from neutral (blue) to monoanionic (red), C: from monoanionic (red) to dianionic (green) species. Spectra were recorded in dichloromethane containing [^{n}Bu$_4$N][BF$_4$] (0.4 M) as the supporting electrolyte at 243 K.

Thionation of the naphthalic imide also causes a bathochromic shift to the absorption maximum. **NIS$_0$-PTZ** does not absorb any visible light and forms colourless solutions (λ_{max} = 337 nm). The absorption maximum for **NIS$_2$-PTZ** occurs at 442 nm, representing a redshift of 105 nm as a result of the dithionation. This effect is marginally more pronounced than that of the NDI systems: as mentioned in Chapter 2 each sulfur atom substitution causes a redshift of ~45 nm, so for two sulfur replacements, one would expect a 90 nm shift. Reduction of the two NI-phenothiazine compounds saw the emergence of new, lower energy bands at 419 nm for **NIS$_0$-PTZ** and 458 nm for **NIS$_2$-PTZ**. Whilst this also occurs for the related NDI compounds, the effect of the thionation is significantly diminished for the NIs. The emergent intense absorption band for the monoanionic form of **NIS$_2$-PTZ** is shifted by a mere 16 nm relative to the neutral species, even though the same emergent band for [**NIS$_0$-PTZ**]$^{\cdot-}$ is redshifted by 82 nm. This means that the 105 nm difference in absorption maxima for the neutral NI dyads has decreased to only 39 nm for the monoanionic NIs. Additional, lower intensity bands (ε < 10,000 mol^{-1}dm^{3}cm^{-1}) develop in the near infrared region at 833 and 748 nm for both NI dyads.

The spectroelectrochemical interconversion between neutral, monocationic and monoanionic forms of the NDI-phenothiazine compounds are shown below (Figure 3.15: **NIS$_0$-PTZ**, Figure 3.16: **NIS$_2$-PTZ**). All processes were found to be fully reversible.

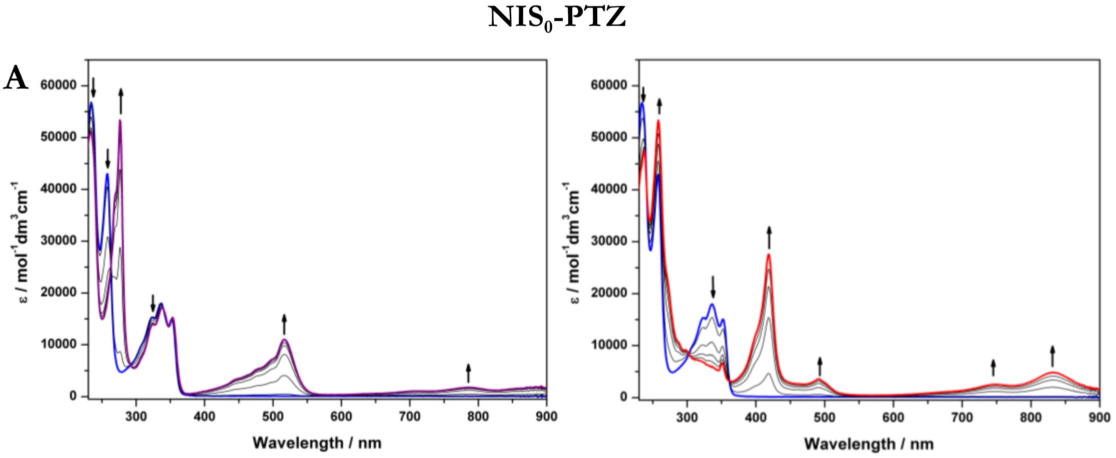

Figure 3.15: UV/vis absorption spectra showing the inter-conversion between the various charge states of NIS$_0$-PTZ, arrows indicate the progress of the oxidation/reduction. A: from neutral (blue) to monocationic (purple), B: from neutral (blue) to monoanionic (red) species. Spectra were recorded in dichloromethane containing [^{n}Bu$_4$N][BF$_4$] (0.4 M) as the supporting electrolyte at 243 K.

NIS_2-PTZ

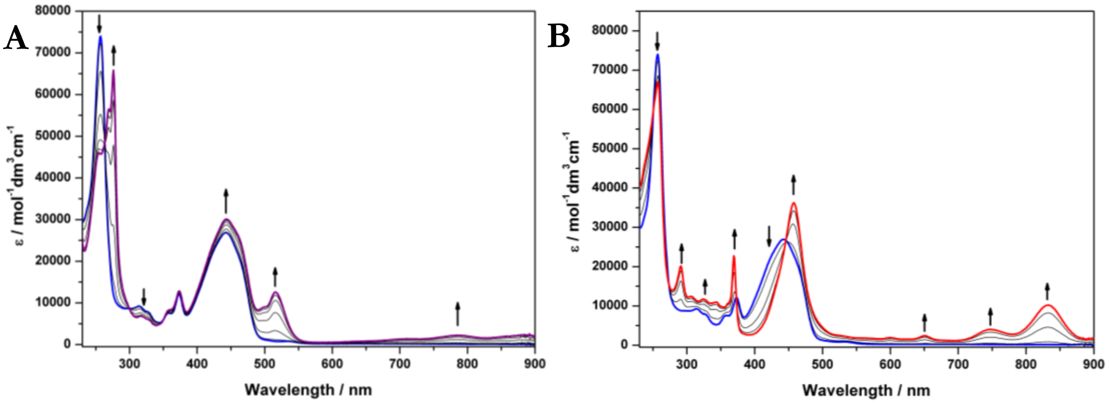

Figure 3.16: UV/vis absorption spectra showing the inter-conversion between the various charge states of NIS_2-PTZ, arrows indicate the progress of the oxidation/reduction. A: from neutral (blue) to monocationic (purple), B: from neutral (blue) to monoanionic (red) species. Spectra were recorded in dichloromethane containing $[^nBu_4N][BF_4]$ (0.4 M) as the supporting electrolyte at 243 K.

The optical absorbance data for the NDI- and NI-phenothiazine dyads are summarised below (Table 3.2). Also included are the data for **$PTZ-NH_2$**.

Table 3.2: Summary of optical spectroscopy for phenothiazine-NDI and -NI compounds.

Compound	λ_{abs} / nm (ε / 10^3 mol^{-1}dm^{3}cm^{-1})			
	Neutral	**Monocationic**	**Monoanionic**	**Dianionic**
NDIS$_0$-PTZ	381 (31.9), 360 (25.4), 342 (16.0), 326 (11.6), 257 (42.1), 237 (52.5)	784 (1.6), 517 (10.2), 381 (31.9), 360 (25.6), 342 (15.5), 326 (10.2), 276 (53.2), 237 (47.8)	762 (6.4), 688 (3.7), 609 (10.0), 478 (35.1), 402 (3.2), 379 (3.0), 325 (8.4), 258 (55.7), 234 (43.6)	608 (14.4), 561 (8.2), 423 (39.5), 400 (27.6), 316 (7.5), 257 (76.6)
NDIS$_2$ cis-PTZ	473 (8.9), 387 (5.8), 368 (5.2), 319 (5.4), 257 (23.3)	788 (0.8), 500 (9.6), 475 (10.7), 387 (6.1), 367 (5.2), 352 (3.6), 331 (4.1), 319 (4.8), 276 (23.0), 268 (20.8)	812 (3.5), 702 (5.6), 596 (19.8), 526, (3.0), 414 (3.2), 326 (6.5), 257 (23.8)	609 (7.2), 560 (4.6), 490 (27.3), 459 (15.0), 434 (5.7), 309 (5.3), 257 (26.6), 245 (46.2)
NDIS$_3$-PTZ	534 (21.1), 505 (25.1), 398 (9.4), 383 (8.7), 369 (9.4), 293 (14.4), 258 (61.1)	784 (1.5), 509 (31.0), 399 (10.5), 381 (9.1), 368 (9.7), 350 (8.6), 275 (60.0)	877 (7.0), 820 (14.1), 770 (8.7), 716 (12.5), 620 (41.6), 424 (8.1), 368 (6.7), 288 (21.8), 258 (65.3)	644 (31.5), 590 (15.9), 543 (5.7), 502 (62.8), 471 (30.7), 306 (18.4), 257 (77.7)
NIS$_0$-PTZ	352 (15.0), 337 (18.0), 325 (15.3), 258 (43.1), 234 (56.8)	784 (1.8), 714 (1.1), 517 (11.0), 353 (15.3), 338 (17.2), 325 (14.1), 276 (53.7), 234 (51.1)	832 (4.8), 749 (2.5), 490 (3.6), 419 (27.6), 351 (6.7), 298 (9.2), 258 (53.4), 237 (47.6)	
NIS$_2$-PHZ	442 (26.9), 373 (12.1), 357 (7.6), 313 (8.5), 257 (74.1)	783 (2.2), 516 (12.6), 442 (30.1), 373 (12.9), 317 (6.9), 276 (65.9), 269 (56.6), 254 (46.0)	833 (10.2), 748 (4.0), 650 (2.4), 400 (1.9), 458 (36.3), 369 (22.9), 344 (11.0), 325 (11.7), 307 (12.4), 291 (20.2), 257 (67.1)	
PTZ-NH$_2$	322 (5.1), 258 (58.0)	642 (4.8), 515 (7.9), 373 (9.6), 309 (9.0), 274 (26.0), 257 (22.2)		

Obtained at an optically transparent electrode cell in dichloromethane, containing [^{n}Bu$_4$N][BF$_4$] (0.4 M) at 243 K, spectral range: 230 - 900 nm.

3.2.3.2. Electron Paramagnetic Resonance Spectroscopy

EPR experiments were conducted to determine any differences in the location of the radical electron in the oxidised monocationic and reduced monoanionic forms of the dyad molecules. NIs and NDIs are known to function as electron acceptors, so one would expect that reduction of these compounds would be achieved through the addition of an electron into a LUMO orbital located on the NI or NDI unit. Similarly, with phenothiazine as an electron donor, oxidation should cause the loss of an electron from a HOMO orbital located on the phenothiazine chromophore.

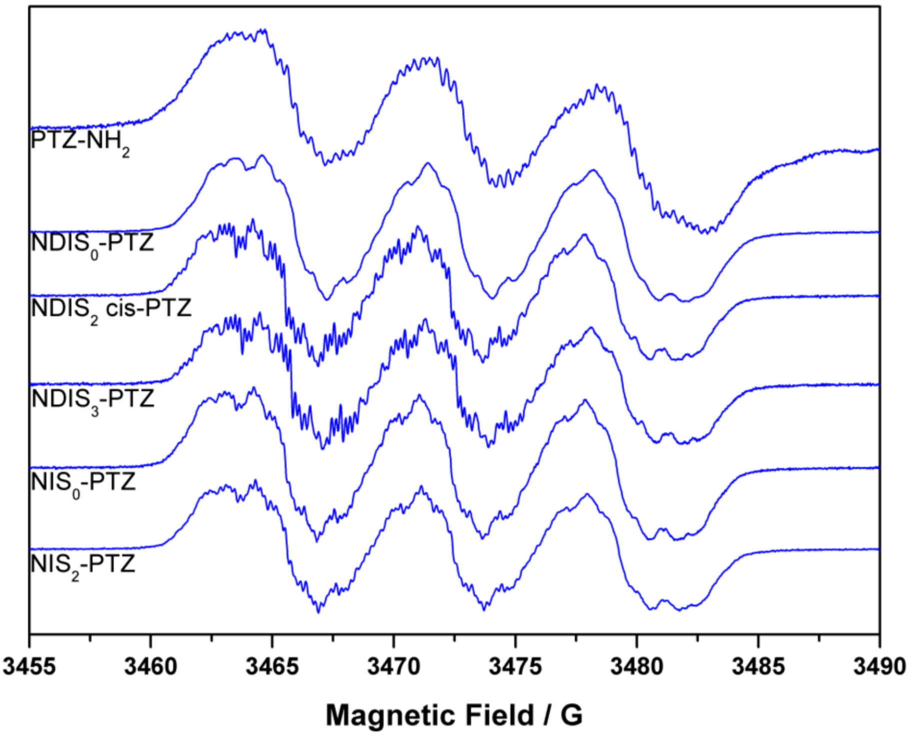

Figure 3.17: Experimentally obtained EPR Spectra of oxidised NDI- and NI-phenothiazine dyads.

The EPR data obtained agree with this picture: different spectra are produced for oxidised and reduced forms of the same molecule, implying the locations of the radical electrons for the monocationic and monoanionic species are different. Moreover, a change in the acceptor between NDI and NI (as well as thionation), affects the EPR spectrum of the reduced compound, however, since all dyads contain the same phenothiazine electron donor, the EPR spectra for the oxidised molecules are largely consistent (Figure 3.17).

The overall shape of the EPR spectra of the oxidised free phenothiazine [**PTZ-NH$_2$**]$^{\cdot+}$ consists of 3 lines of equal intensity, deformed slightly by additional, weak hyperfine coupling. Coupling of the radical electron to a nitrogen atom would result in an EPR spectrum with 3 lines (Nitrogen-14 has a magnetic spin of 1), perhaps implying the radical electron lies within an orbital largely located on the nitrogen atom of the phenothiazine group. As discussed, the EPR spectra recorded for all dyad molecules following bulk oxidation was consistent with that of the free phenothiazine compound, thus it can be deduced that the HOMO of all the dyads lies on the phenothiazine portion of the molecules. The g_{iso} values are identical for all the oxidised dyad molecules and only marginally different for **PTZ-NH$_2$** signifying the radical electron is located within a HOMO on the phenothiazine unit, as predicted (Table 3.3).

Table 3.3: Experimentally determined g_{iso} values for oxidised phenothiazine species.

Compound	g_{iso}
PTZ-NH$_2$	2.0053
NDIS$_0$-PTZ	2.0055
NDIS$_2$ cis-PTZ	2.0055
NDIS$_3$-PTZ	2.0055
NIS$_0$-PTZ	2.0055
NIS$_2$-PTZ	2.0055

The EPR spectrum of [**NDIS$_0$-PTZ**]$^{\cdot-}$ showed more complexity than that of the simpler symmetric **NDIS$_0$** (Figure 3.18). Because **NDIS$_0$-PTZ** is *N*,*N*'-asymmetrically disubstituted, the hydrogen atoms located on the aromatic core of the NDI exist in two pairs of equivalent environments, instead of all four hydrogens belonging to the same environment, increasing the complexity of the spectrum and resulting in more lines. Simulation of the experimental data to obtain values for hyperfine coupling constants was possible, although also required coupling to an additional set of two equivalent protons; revealing that a weak coupling of the radical electron to the alkyl chain at one imide end also takes place. The general shape of 13 lines (the case for **NDIS$_0$**) is present, though each of these is split further by the extra interaction. Extension of the delocalisation of the radical electron into the first carbon of the imide position is occasionally observed for hydrocarbon chains.[7] The two imide nitrogen atoms lie in chemically distinct environments; one bears an alkyl substitution, the other aryl, though a difference in their hyperfine contribution to the EPR spectrum is negligible and simulation of the recorded data did not require the fitting of two independent nitrogen parameters.

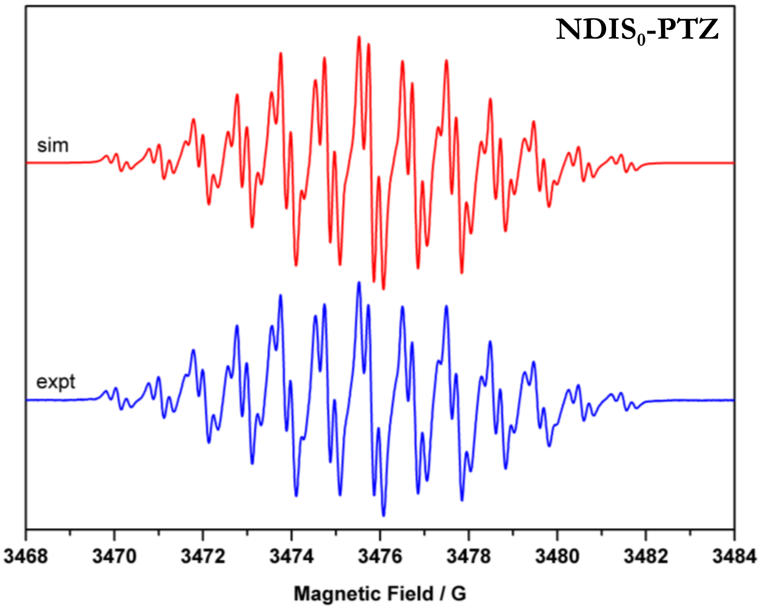

Figure 3.18: EPR spectra of reduced NDIS$_0$-PTZ. Blue line experimental data, red line simulated data.

Despite the differences in spectra, both nonthionated NDI radicals have virtually identical g_{iso} values at 2.0037 for **NDIS$_0$** and 2.0038 for **NDIS$_0$-PTZ**.

Simulation of the EPR data for the thionated NDI dyads **NDIS$_2$ cis-PTZ** and **NDIS$_3$-PTZ** to obtain values for the hyperfine coupling constants was not possible because the molecules are significantly more complex and hence require the fitting of a large number of inter-dependent parameters in order to accurately simulate the spectra. The experimentally obtained spectra are shown below (Figure 3.19). The g_{iso} value of **$NDIS_2$ cis-PTZ** was found to be 2.0085, identical to that recorded for **$NDIS_2$ cis**, reinforcing the structural assignment as cis, since the trans isomer has a lower g_{iso} value of 2.0078.

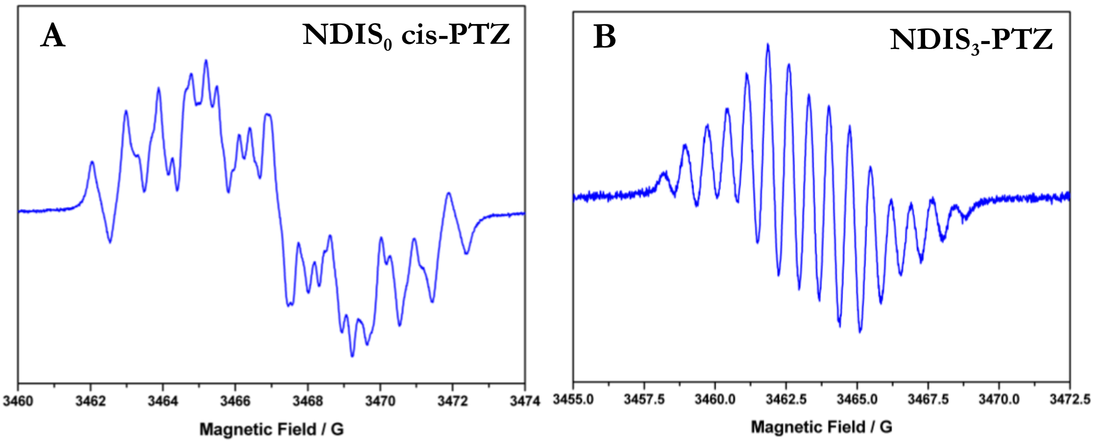

Figure 3.19: EPR Spectra of reduced NDI-phenothiazine dyads. A: $NDIS_2$ cis-PTZ, B: $NDIS_3$-PTZ.

Simulation of the EPR data for the two NI dyads was possible (Figure 3.20), with 3 pairs of hydrogen atoms and one nitrogen atom contributing hyperfine coupling to the overall shape of the spectra. Significantly more coupling to the nitrogen atom is observed for the thionated molecule, with an $A_{iso} = 2.285 \times 10^{-4}$ cm^{-1} for **NIS_2-PTZ** and $A_{iso} = 1.324 \times 10^{-4}$ cm^{-1} for **NIS_0-PTZ**. Differences in the hydrogen hyperfine coupling constants are also apparent (Table 3.4), with larger values for the nonthionated compound. DFT computed orbital structures (see below) place a larger LUMO contribution on the thiocarbonyl carbons of **NIS_2-PTZ**, than on the carbonyl carbon atoms of **NIS_0-PTZ**, with nodes at carbons 3 and 6 on the naphthyl ring. These data combined suggest that the radical electron density is greater close to the imide group of the thionated molecule, and greater on the naphthyl ring of the nonthionated counterpart.

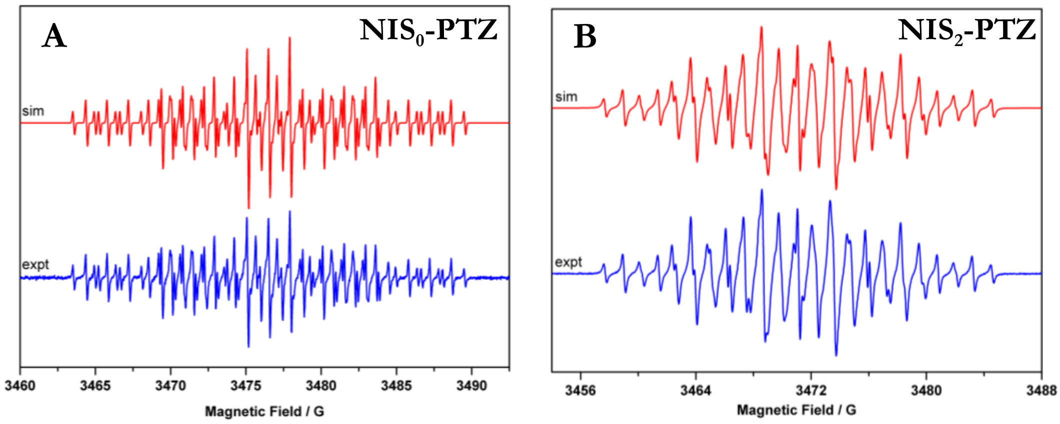

Figure 3.20: EPR Spectra of reduced NI-phenothiazine dyads. A: NIS$_0$-PTZ, B: NIS$_2$-PTZ. Experimental data (blue), simulated data (red).

Table 3.4: EPR parameters for reduced phenothiazine dyad species.

Compound	g_{iso}	A_{iso} / 10^{-4} cm^{-1}	Linewidth / G	Lineshape
NDIS$_0$-PTZ	2.0038	1.872 (2H), 1.656 (2H), 0.206 (2H), 0.903 (2N)	0.13	Lorentzian
NDIS$_2$ cis-PTZ	2.0085			
NDIS$_3$-PTZ	2.0110			
NIS$_0$-PTZ	2.0032	5.331 (2H), 4.695 (2H), 0.797 (2H), 1.324 (1N)	0.11	Gaussian
NIS$_2$-PTZ	2.0062	4.674 (2H), 4.402 (2H), 1.227 (2H), 2.285 (1N)	0.20	Lorentzian

3.2.4. DFT Calculated Molecular Orbitals

To supplement the electrochemical data discussed above, density functional theory was employed to generate molecular orbital geometries and associated energies. Cyclic voltammetry, spectroelectrochemistry and EPR spectroscopy indicate that separate orbitals are involved in the oxidation and reduction processes of the dyads, with a phenothiazine-based HOMO and an NDI- or NI-based LUMO. The calculated orbital geometries support the electrochemical data: the HOMO for each of the dyads is a π-type orbital located solely on the phenothiazine unit, without extending beyond the nitrogen atom into the phenylene spacer; the LUMOs for the NDI and NI units do not extend past the imide nitrogens and lie entirely on the naphthalene and imide rings without including the imide nitrogen atom (NDIs: Table 3.5, NIs: Table 3.6). Separate calculations were also undertaken for the monoanionic molecules, to compare the SOMO and LUMO structures.

Table 3.5: Calculated molecular orbital diagrams for the thionated NDI-phenothiazine dyads.

Compound	HOMO	LUMO	Anion SOMO
NDIS$_0$-PTZ	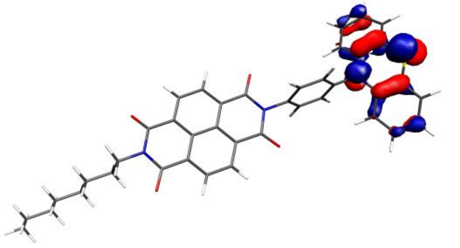 -4.97 eV	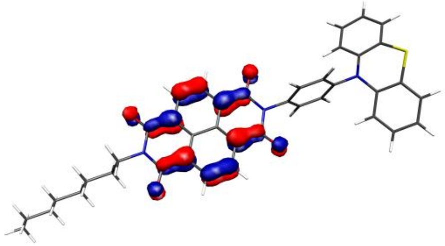 -3.47 eV	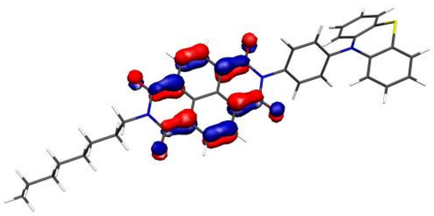
NDIS$_2$ cis-PTZ	 -4.98 eV	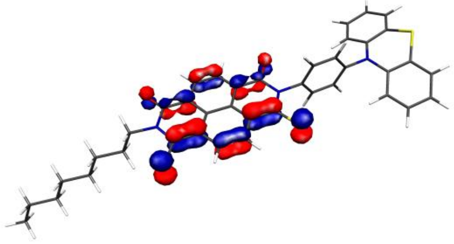 -3.86 eV	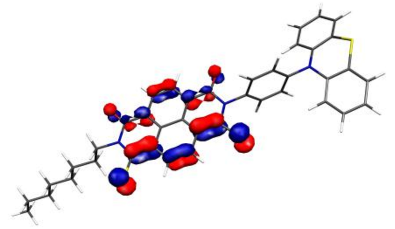
NDIS$_3$-PTZ	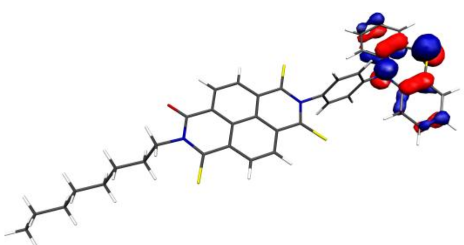 -4.99 eV	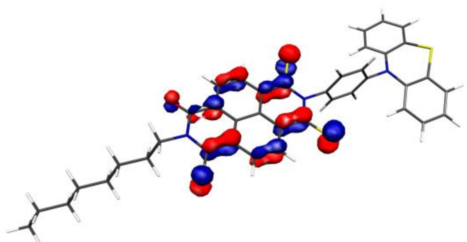 -4.03 eV	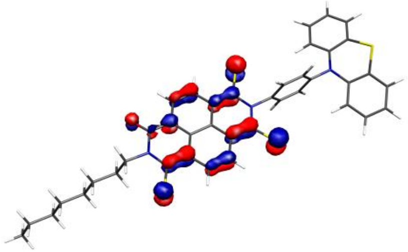

Table 3.6: Calculated molecular orbital diagrams for the thionated NI-phenothiazine dyads.

Compound	HOMO	LUMO	Anion SOMO
NIS$_0$-PTZ	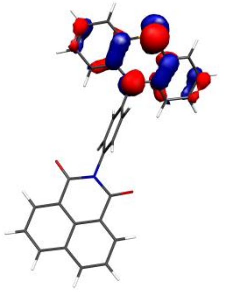 -4.85 eV	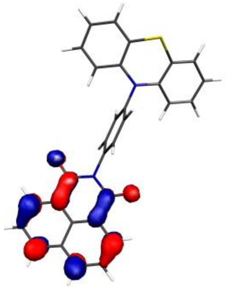 -2.54 eV	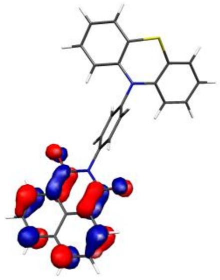
NIS$_2$-PTZ	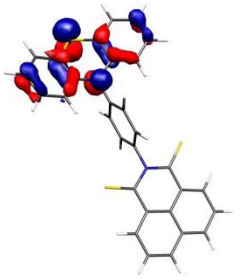 -4.85 eV	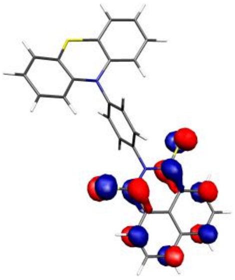 -3.22 eV	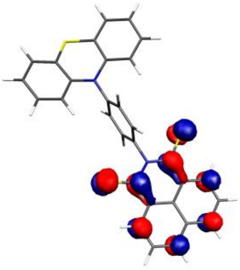

The LUMO structure of the NDI dyads is similar to the corresponding symmetrical NDIs: a node runs down the central long axis of the molecules and the lobes of the orbitals are slightly larger over the sulfur atoms than the oxygen atoms. As expected, the SOMO of the monoanionic NDIs greatly resembles the LUMO of the neutral molecule. Thionation reduces the LUMO energy of the dyads by the same amount as it does for the simpler NDIs. The energy difference between the LUMOs of **NDIS$_0$** and **NDIS$_2$ cis** is 0.40 eV; the difference in energy between the LUMOs of **NDIS$_0$-PTZ** and **NDIS$_2$ cis-PTZ** is 0.39 eV. A similar case is observed for the trithionated NDIs, with the difference for the model NDIs at 0.57 eV and for the phenothiazine-NDIs at 0.56 eV. These data suggest that the effect of thionation to the NDI system is just as prominent, regardless of imide substituents. The addition of phenothiazine moves the HOMO from the NDI core, separating the HOMO and LUMO. The HOMO for all NDI-phenothiazine systems is identical in nature, with only trivial differences in the calculated energies (the greatest energy difference is 0.02 eV). This means that the HOMO-LUMO energy gap decreases in energy progressively with the level of thionation, becoming about 0.2 eV smaller with each sulfur substitution, allowing for tunability of the gap across a broad range of values (Table 3.7).

The LUMO shape of **NIS_0-PTZ** resembles that of the nonthionated NDIs, with a node at the imide nitrogen atom and at the centre of the naphthyl ring. Thionation to **NIS_2-PTZ** increases the extent of the orbital on the thiocarbonyl carbons, drawing it away from the carbon atoms at positions 3 and 6 of the naphthalene ring. Thionation considerably reduces the LUMO energy from -2.54 eV to -3.22 eV, a change of 0.68 eV, the experimentally obtained data gave an energy difference of 0.58 V for comparison. The SOMO diagrams are consistent with the LUMO pictures and the calculated HOMO energies are identical for both NI systems at -4.85 eV.

Table 3.7: Calculated HOMO-LUMO gaps for NDI- and NI-phenothiazine dyads.

Compound	HOMO/ eV	LUMO/ eV	Gap/ eV
$NDIS_0$-PTZ	-4.97	-3.47	1.51
$NDIS_2$ cis-PTZ	-4.98	-3.86	1.12
$NDIS_3$-PTZ	-4.99	-4.03	0.96
NIS_0-PTZ	-4.85	-2.54	2.31
NIS_2-PTZ	-4.85	-3.22	1.62

3.2.5. Infrared Electrochemistry

The infrared spectra of **$NDIS_0$-PTZ**, **NIS_0-PTZ** and **NIS_2-PTZ** were recorded in the solution phase. The reduced forms of each of these the molecules were electrogenerated (as for EPR spectroscopy) and the infrared spectra measured for these reduced species to monitor changes in the carbonyl region of the infrared spectra (Figure 3.21). For **NDIS$_0$-PTZ** and **NIS$_2$-PTZ**, infrared spectra for the oxidised species were also recorded.

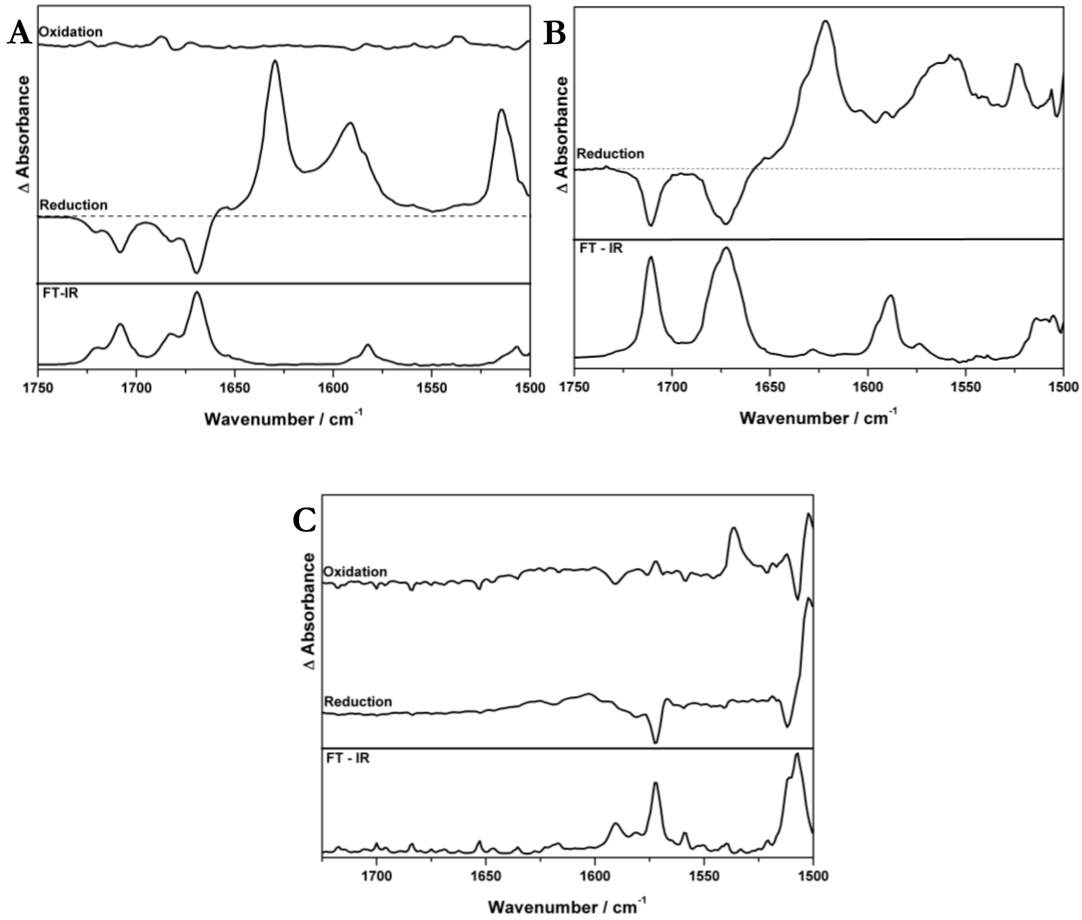

Figure 3.21: Infrared spectra showing the change in absorbance that occurs upon reduction or oxidation for NDI- and NI-dyads. A: NDIS$_0$-PTZ, B: NIS$_0$-PTZ, C: NIS$_2$-PTZ.

Reduction of the carbonyl containing compounds **NDIS$_0$-PTZ** and **NIS$_0$-PTZ** saw a disappearance of the bands corresponding to the C=O stretches (at 1708 and 1669 cm^{-1} for **NDIS$_0$-PTZ** and 1710 and 1672 cm^{-1} for **NIS$_0$-PTZ**) and the emergence of a new set of bands at lower wavenumber. These new bands are assigned to the carbonyl stretches of the reduced molecules, but are at lower wavenumber because the bond strength (and bond order) is reduced through the addition of an electron into an antibonding orbital. A similar change is not detected for **NIS$_2$-PTZ** in the same spectral region because there aren't any C=O bonds. Oxidation of the compounds had little effect on the carbonyl stretches of **NDIS$_0$-PTZ** because the electron is lost from the HOMO located on the phenothiazine portion of the molecule, unable to affect the bond strength or structure of the imide-carbonyl bands.

3.2.6. Photoinduced Electron Transfer

A combination of transient absorption (TA) spectroscopy and time resolved infrared spectroscopy (TRIR) was used to investigate photoinduced electron transfer processes of the NDI- and NI-dyads. For each compound of **NDIS$_0$-PTZ**, **NDIS$_3$-PTZ**, **NIS$_0$-PTZ** and **NIS$_2$-PTZ** both TA and TRIR measurements were recorded in dichloromethane solutions and were excited at 355 nm.

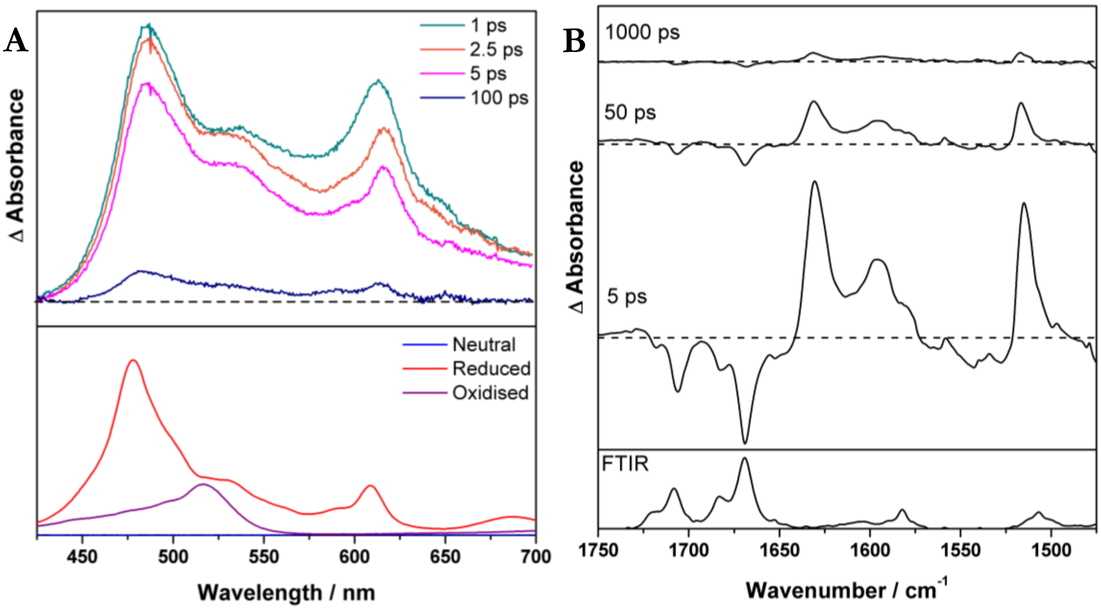

Figure 3.22: Time-resolved photochemistry of NDIS$_0$-PTZ after excitation at 355 nm in dichloromethane. A: Picosecond TA spectra, B: TRIR Spectra.

Upon excitation of **NDIS$_0$-PTZ**, three transient absorption bands are observed around 485, 520 and 608 nm (Figure 3.22A). Combined with the spectroelectrochemical data (above), these bands can be assigned to NDI$^{\cdot -}$ (485 and 608 nm) and PTZ$^{\cdot +}$ (520 nm), hence the TA spectra appears similar to a superposition of the electrochemically oxidised and reduced states. Additional TRIR (Figure 3.22B) data show ground state bleaching of the carbonyl bands at 1708 and 1669 cm^{-1} coupled with the development of three new bands at lower wavenumber, conforming strongly to the IR spectrum recorded for the reduced compound (Figure 3.21A) and further supporting the generation of $NDI^{\cdot -}$ following photoexcitation. This charge separation occurs rapidly, with a time constraint of <1 ps. Recombination to the ground state also occurs quickly, with a charge-separated lifetime of 130 ± 60 ps.

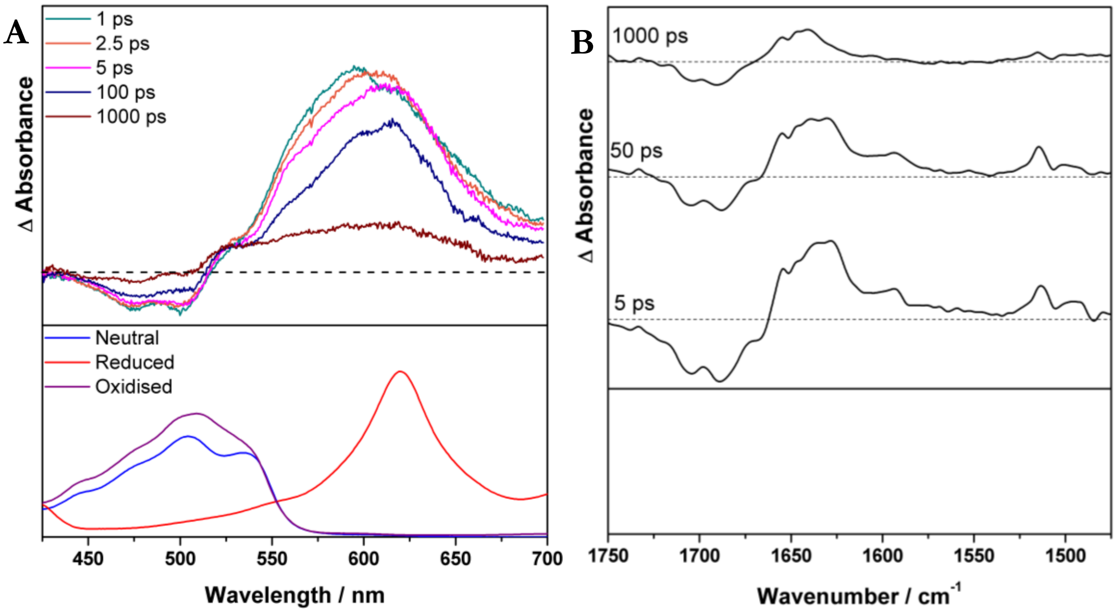

Figure 3.23: Time-resolved photochemistry of NDIS$_3$-PTZ after excitation at 355 nm in dichloromethane. A: Picosecond TA spectra, B: TRIR Spectra.

The thionated analogue **NDIS$_3$-PTZ** was investigated in a similar manner (Figure 3.23). The picosecond TA data reveal that charge separation occurs on a slower timescale than the nonthionated **NDIS$_0$-PTZ**, forming a radical pair after 9 ± 4 ps. This charge separated pair recombined after ~2 to 3 ns, roughly eight times longer than **NDIS$_0$-PTZ**. This is a desirable result: 'a lifetime approaching 2 ns is a significant improvement toward the regime desired for charge transport'.[28] A charge separated lifetime of 340 ps has been previously demonstrated to be sufficient for a 30 % yield of free charge carriers.[29]

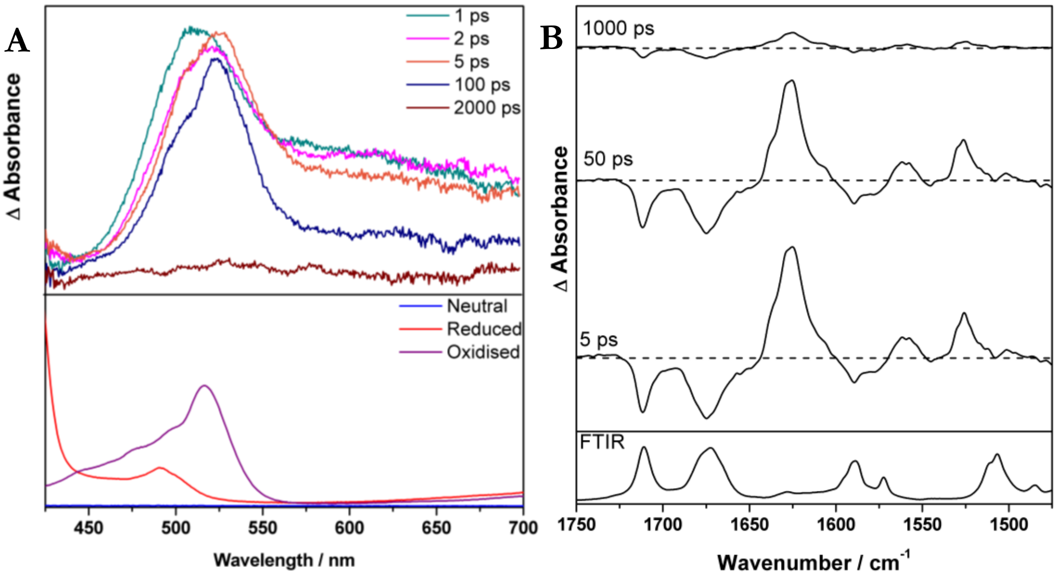

Figure 3.24: Time-resolved photochemistry of NIS$_0$-PTZ after excitation at 355 nm in dichloromethane. A: Picosecond TA spectra, B: TRIR Spectra.

Transient absorption bands assigned to PTZ$^{\cdot+}$ are readily observable at 520 nm following excitation of **NIS$_0$-PTZ** (Figure 3.24A). The NI$^{\cdot-}$ band (at 419 nm) could not be detected as it develops outside of the scan range, though TRIR data allow for the detection of NI$^{\cdot-}$: the carbonyl bands at 1710 and 1672 cm^{-1} are bleached, accompanied by the development of a new band at 1626 cm^{-1} (Figure 3.24B). The infrared data are directly comparible to that obtained for a solution of [**NIS$_0$-PTZ**]$^{\cdot-}$ (Figure 3.21B), and together with the TA data, fully establish the formation of a charge separated **NIS$_0^-$-PTZ$^+$** species. Charge separation occurs on a timescale of 23 ± 8 ps, followed by a return to ground state within a lifetime of 260 ± 60 ps. PET has been observed in NI-phenothiazine dyads connected by aliphatic and oligo(ethyl ether) linkers, with slower kinetics due to an increased donor-acceptor distance.[30]

NIS$_2$-PTZ behaves slightly differently to its nonthionated counterpart. Rapid ground state bleaching at 450 nm occurs from 1 to 5 ps, before a second process shows a decrease in the bands at 504 and 558 nm, accompanied by an arrival of bands at 458 and 520 nm (Figure 3.25). These new bands match well as a superposition of the UV/vis spectra of oxidised and reduced states, again signifying that charge transfer is taking place. Kinetics of the transient absorption band at 450 nm show that charge separation occurs after 30 ± 10 ps. The radical pair persists for a similar timescale to the thionated NDI compound (**NDIS$_3$-PTZ**), with a lifetime of 2 to 5 ns. This result concurs with that of the NDI dyads: thionation delays the onset of formation of a charge separated state, however also increases the charge separated lifetime by rougly one order of magnitude. The delay in the onset of charge separation could be due to competition between charge transfer and the NI triplet state. This possibility is discussed by Cho and et al.[30] for NI-phenothiazine dyads. In acetonitrile, charge transfer occurred much slower than fluorescence decay of the singlet excited state, although in toluene, a transient absorption band assigned to the triplet state of NI was detected; the triplet state did not compete with charge separation in less polar media.

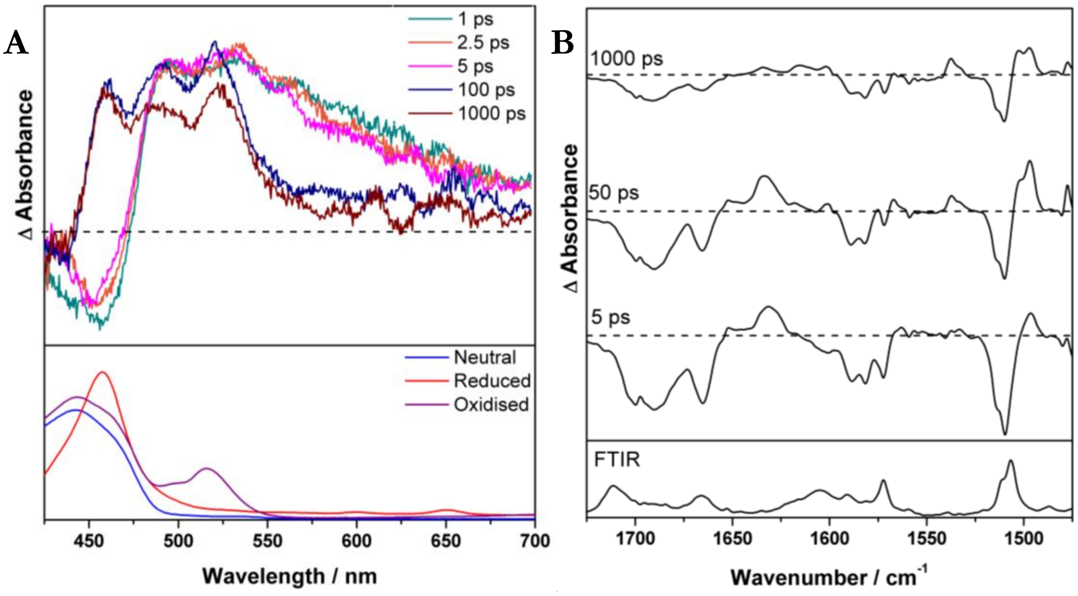

Figure 3.25: Time-resolved photochemistry of NIS$_2$-PTZ after excitation at 355 nm in dichloromethane. A: Picosecond TA spectra, B: TRIR Spectra.

A bimolecular charge transfer reaction between radical pairs and neutral dyads forming donor$^+$-acceptor and donor-acceptor$^-$ species is one possible cause of the apparent extended charge separated lifetimes of the thionated systems over the nonthionated systems.[30] A summary of the kinetics of the formation of charge separated states and the lifetimes of the radical pairs using the TA and TRIR data is given below (Table 3.8).

Table 3.8: Summary of charge separated lifetimes of NDI- ad NI-phenothiazine dyads

Compound	Time of formation / ps **Charge Separation**	 **Charge Recombination**
NDIS$_0$-PTZ	0.7 ± 0.5	130 ± 60
NDIS$_3$-PTZ	9 ± 4	2000 - 3000
NIS$_0$-PTZ	23 ± 8	260 ± 60
NIS$_2$-PTZ	30 ± 10	2000 - 5000

In order to fully realise to potential of the thionated systems in optoelectronic devices more experimental work is required to assess their solid state properties and behaviour under device-like conditions. Examination of the crystal structures does not reveal any especially beneficial solid-state properties: the electron donor and acceptor portions of any of the dyad molecules are not aligned in such a fashion as to facilitate charge transport. The non-phenothiazine imide functionality of the NDI dyads could be replaced with a group able to arrange the molecules optimally for bulk chage-transport, e.g. by tethering to a surface to align donor and acceptor fragments, thus forming a wire capable of shuttling electrons and holes in antiparallel directions. Furthermore, both NDI and NI molecular structures allow for the possibility of further functionalisation or substitution with several substitutable positions on the aromatic naphthalene cores. As such, these compounds show great promise for application in photoactive materials.

3.3. Conclusions

A variety of donor-acceptor dyads have been synthesised employing phenothiazine as an electron donor and either naphthalene diimide (NDI) or naphthalic imide (NI) as the acceptor. The dyads were subsequently thionated using Lawesson's reagent, finding that thionation is favourable next to the aromatic imide group, unlike the behaviour observed for aliphatic substituted NDI and NIs. Full thionation of naphthalic imide proved possible, and in good yield, proving the viability of these systems for use in optoelectronic applications. The dyads were fully electrochemically characterised finding that sulfur substitution increases acceptor electron affinity without affecting the ability of phenothiazine to serve as an electron donor, allowing for precise control of the HOMO-LUMO separation.

Density functional theory calculated molecular orbitals in tandem with X-ray crystallography, spectroelectrochemistry and electron paramagnetic resonance spectroscopy confirm that coupling of phenothiazine to NDIs and NIs forms donor-acceptor complexes, separated by a non-conjugated phenylene bridge. Thionation results in a pronounced effect on the electron acceptance characteristics of the NI unit: an anodic shift in reduction potential alongside a 90 nm bathochromic shift in absorption maximum into the visible spectrum greatly improves the capacity of NI materials for use in organic electronic applications. For **NIS_2-PTZ**, the reduction potential is increased by 580 mV to -1.13 V (vs. Fc^+/Fc), comparable to that of nonthionated NDIs. For **$NDIS_3$-PTZ**, the experimentally determined HOMO-LUMO gap is decreased to 0.87 eV, unprecedentedly low for this type of compound.

Lastly, a combination of transient absorption spectroscopy and time resolved infrared spectroscopy demonstrate that photoinduced charge separation occurs for these NDI and NI dyads, supported by data obtained from the infrared spectra of the reduced compounds and spectroelectrochemistry. Thionation enhances the charge separated lifetimes of these dyads by an order of magnitude; producing radical pairs that persist long enough for charge extraction in organic electronic devices.

3.4. Materials and Methods

3.4.1. Synthesis

3.4.1.1. Synthesis of 10-(4-nitrophenyl)-10H-phenothiazine (**PTZ-NO$_2$**)

This compound was synthesised according to a literature procedure.[11] 4-nitro-iodobenzene (1.255 g, 5.04 mmol), phenothiazine (1.012 g, 5.08 mmol), tris(dibenzylideneacetone)palladium(0) (255 mg, 0.28 mmol), tri-*o*-tolylphosphine (744 mg, 0.24 mmol) and potassium *tert*-butoxide (568 mg, 5.06 mmol) were dissolved in toluene (150 mL) and N_2 was bubbled through for 15 min. The mixture was heated to 90 °C for 24 h, cooled and washed with water (100 mL). The solvent was removed on a rotary evaporator and the crude product purified by column chromatography (silica, 5:1 hexane: chloroform) to afford 10-(4-nitrophenyl)-10H-phenothiazine as a yellow solid (854 mg, 52.9 %). ^{1}H NMR (400 MHz, $CDCl_3$): δ ppm 8.03 - 8.10 (m, 2 H), 7.52 (dd, *J* = 7.72, 1.19 Hz, 2 H), 7.47 (dd, *J* = 8.03, 2.50 Hz, 2 H), 7.40 (td, *J* = 7.65, 1.38 Hz, 2 H), 7.28 (td, *J* = 7.56, 1.32 Hz, 2 H), 7.00 - 7.05 (m, 2 H). HRMS $(EI)^+$ m/z 320.0623 ($C_{18}H_{12}N_2O_2S_1$: $[M]^+$ requires 320.0619).

3.4.1.2. Synthesis of 10-(4-aminophenyl)-10H-phenothiazine (**PTZ-NH$_2$**)

This compound was synthesised according to a literature procedure.[11] 10-(4-nitrophenyl)-10H-phenothiazine (532 mg, 1.67 mmol) and tin chloride dihydrate (5.855 g, 25.9 mmol) were added to tetrahydrofuran (45 mL), acidified with hydrochloric acid (50 drops, 33 %). N_2 was bubbled through the mixture for 10 min and the reaction was stirred at room temperature. After 16 h, the reaction mixture was extracted with chloroform (150 mL) and washed once with sodium bicarbonate (100 mM, 100 mL) and with water (4 x 200 mL) to remove any tin salts. The solvent was removed on a rotary evaporator and the crude product purified by column chromatography (silica, chloroform) to yield 10-(4-

aminophenyl)-10H-phenothiazine as a pale green powder (350 mg, 72.6 %). λ_{max} (abs) = 258 nm. ^{1}H NMR (400 MHz, $CDCl_3$): δ ppm 7.12 - 7.19 (m, 2 H), 6.98 (dd, *J* = 7.40, 1.63 Hz, 2 H), 6.86 - 6.91 (m, 2 H), 6.84 (td, *J* = 7.75, 1.69 Hz, 2 H), 6.78 (td, *J* = 7.40, 1.30 Hz, 2 H), 6.25 (dd, *J* = 8.09, 1.07 Hz, 2 H), 3.87 (br. s., 2 H). ^{13}C NMR (100 MHz, $CDCl_3$): δ ppm 146.03, 144.80, 132.00, 131.32, 126.76, 126.51, 122.06, 119.52, 116.85, 115.63. HRMS (ESI)$^+$ m/z 291.0946 ($C_{18}H_{15}N_2S_1$ $[M+H]^+$ requires 291.0950).

*3.4.1.3. Synthesis of N-(10-phenyl-10H-phenothiazine)-1,8-naphthalic imide (**NIS$_0$-PTZ**)*

1,8-Naphthalic anhydride (200 mg, 1.01 mmol), **PTZ-NH$_2$** (322 mg, 1.11 mmol) and imidazole (3 g) were heated to 130 °C under N_2 for 7 h. The mixture was cooled to 100 °C, hydrochloric acid (50 mL, 2 M) was added and the suspension stirred for 10 min. After cooling to room temperature, the mixture was extracted with chloroform (100 mL) and washed with hydrochloric acid (2 x 100 mL, 2 M), water (100 mL) and brine (100 mL). The solution was concentrated using a rotary evaporator and purified by column chromatography (silica, chloroform) to afford the title compound as a bright yellow powder (438 mg, 92 %). Suitable crystals for X-ray diffraction were grown by vapour diffusion of hexane into a chloroform solution of the compound. λ_{max} (abs) = 337 nm. ^{1}H NMR (400 MHz, $CDCl_3$): δ ppm 8.70 (d, *J* = 7.28 Hz, 2 H), 8.33 (d, *J* = 7.65 Hz, 2 H), 7.85 (t, *J* = 7.78 Hz, 2 H), 7.55 (s, 4 H), 7.08 (dd, *J* = 7.53, 1.38 Hz, 2 H), 6.96 (td, *J* = 7.91, 1.63 Hz, 2 H), 6.88 (td, *J* = 7.40, 1.00 Hz, 2 H), 6.47 (dd, *J* = 8.03, 1.00 Hz, 2 H). ^{13}C NMR (100 MHz, $CDCl_3$): δ ppm 164.33, 143.84, 141.51, 134.49, 131.80, 131.73, 131.10, 130.41, 128.57, 127.15, 127.03, 126.89, 122.89, 122.70, 121.36, 117.23. HRMS (EI)$^+$ m/z 470.1102 ($C_{30}H_{18}N_2O_2S_1$ $[M]^+$ requires 470.1089).

3.4.1.4. Synthesis of ***NIS$_2$-PTZ***

NIS$_0$-PTZ (200 mg, 425 μmol) and Lawesson's reagent (344 mg, 850 μmol) were dissolved in anhydrous toluene (25 mL) and heated to reflux for 24 h under N_2. The mixture was cooled and washed with sat. sodium carbonate (100 mL) and water (2 x 200 mL), dried over $MgSO_4$ and filtered. The solvent was removed on a rotary evaporator and the crude product purified by column chromatography (silica, 1:1 hexane: chloroform) to afford the product as a brown solid (103 mg, 48 %). Suitable crystals for X-ray diffraction were grown by vapour diffusion of pentane into a chloroform solution of compound. λ_{max} (abs) = 442 nm. ^1H NMR (400 MHz, $CDCl_3$): δ ppm 8.95 (dd, *J* = 7.60, 1.02 Hz, 2 H), 8.26 (dd, *J* = 8.26, 0.95 Hz, 2 H), 7.72 (t, *J* = 7.89 Hz, 2 H), 7.47 - 7.54 (m, 2 H), 7.34 - 7.40 (m, 2 H), 7.09 (dd, *J* = 7.60, 1.61 Hz, 2 H), 7.00 (td, *J* = 7.78, 1.53 Hz, 2 H), 6.89 (td, *J* = 7.45, 0.88 Hz, 2 H), 6.54 (dd, *J* = 8.18, 1.02 Hz, 2 H). ^{13}C NMR (100 MHz, $CDCl_3$): δ ppm 192.30, 144.82, 137.66, 133.94, 131.86, 130.80, 130.58, 129.75, 127.54, 127.08, 126.91, 124.02, 122.90, 121.45, 117.28. HRMS $(EI)^+$ m/z 502.0649 ($C_{30}H_{18}N_2S_3$ $[M]^+$ requires 502.0632).

*3.4.1.5. Synthesis of N-(octyl)-naphthalene-1,8-dicarboximide-4,5-anhydride (**NMI**)*

This compound was synthesised following a literature procedure.[27] n-Octylamine (4.0 mL, 24.2 mmol) was added to a suspension of 1,4,5,8-naphthalene tetracarboxylic dianhydride (1.00 g, 3.73 mmol) in a 1:1 water: n-propanol mixture (20 mL) under N_2. The mixture was sonicated and heated to 50 °C for 24 h, after which time a white precipitate had formed. After cooling to room temperature, the mixture was acidified with hydrochloric acid to pH 1 and further stirred for 1 h. The solid was filtered off, added to glacial acetic acid (100 mL) and heated to reflux for 1 h until a clear yellow solution had formed. After cooling to room temperature, the solution was diluted with dichloromethane (200 mL) and washed with water (200 mL). The organic layer was dried over $MgSO_4$ and concentrated *in vacuo*. Ethanol (50 mL) was added and the remaining dichloromethane removed with a rotary evaporator. The resulting suspension was filtered and washed with ethanol (5 mL), hexane (5 mL) and diethyl ether (1 mL) to afford a 5:2 mixture of **NMI**: *N,N'*-di(octyl)-naphthalene-1,4,5,8-tetracarboxylic diimide as a white powder (ratio determined by ^1H NMR). This mixture was used without further purification, as the diimide impurity is inert to the conditions used in further reactions and can be easily removed. Crude yield: 1.85 g, containing **NMI** (1.32 g, 47 %). MS $(MALDI)^-$ m/z 379.1 ($C_{22}H_{21}N_1O_5$ $[M]^-$ requires 379.14).

*3.4.1.6. Synthesis of N,N'-(octyl)-(10-phenyl-10H-phenothiazine)-1,4,5,8-naphthalenetetracarboxylic diimide (**NDIS$_0$-PTZ**)*

A mixture of *N*-(octyl)-1,4,5,8-naphthalenetetracarboxylic monoimide monoanhydride (379 mg, 1 mmol), 10-(4-aminophenyl)-10H-phenothiazine (290 mg, 1 mmol) and imidazole (5 g) were heated to 130 °C for 16 h. The reaction mixture was cooled to 100 °C and hydrochloric acid (50 mL, 2 M) was added and the mixture stirred for 15 min. The product was extracted into chloroform (100 mL) and washed once with hydrochloric acid (100 mL, 2 M), water (100 mL) and brine (100 mL), then dried over $MgSO_4$, filtered and the solvent removed on a rotary evaporator. The crude product was purified by column chromatography (silica, chloroform) to give the title product as a blue solid (330 mg, 67.6 %). Suitable crystals for X-ray diffraction were grown by vapour diffusion of pentane into a chloroform solution of the compound. λ_{max} (abs) = 381 nm. ^1H NMR (400 MHz, $CDCl_3$): δ ppm 8.84 (s, 4 H), 7.45 - 7.61 (m, 4 H), 7.13 (dd, *J* = 7.53, 1.38 Hz, 2 H), 7.01 (td, *J* = 7.90, 1.40 Hz, 2 H), 6.92 (td, *J* = 7.40, 1.00 Hz, 2 H), 6.56 (d, *J* = 8.16 Hz, 2 H), 4.12 - 4.33 (m, 2 H), 1.78 (quin, *J* = 7.53 Hz, 2 H), 1.27 - 1.50 (m, 10 H), 0.89 (t, *J* = 6.40 Hz, 3 H). ^{13}C NMR (125 MHz, $CDCl_3$): δ ppm 163.02, 162.71, 143.56, 142.44, 132.95, 131.46, 131.08, 130.74, 129.25, 127.16, 127.12, 127.09, 127.06, 126.88, 126.57, 123.30, 122.75, 118.12, 41.11, 31.80, 29.28, 29.19, 28.09, 27.09, 22.63, 14.08. MS (MALDI)$^-$ m/z 651.1 ($C_{40}H_{33}N_3O_4S_1$ [M]$^-$ requires 651.22). Elemental Analysis: 73.44 %C, 5.83 %H, 6.29 %N ($C_{40}H_{33}N_3O_4S_1$ requires 73.71 %C, 5.10 %H, 6.45 %N).

*3.4.1.7. Synthesis of thionated NDI-PTZ molecules: (**NDIS$_3$-PTZ** and **NDIS$_2$ cis-PTZ**)*

NDIS$_0$-PTZ (100 mg, 154 μmol) and Lawesson's reagent (300 mg, 741 μmol) were dissolved in anhydrous toluene (25 mL) and heated to reflux for 24 h. The solution was cooled to room temperature and washed with NaOH (50 mL, 100 mM), sat. aq. $NaHCO_3$ (50 mL) and sat. aq. NaCl (50 mL), dried over $MgSO_4$, filtered and concentrated to give a crude mixture of thionated NDI-PTZ molecules. This mixture was purified by column chromatography (silica, gradient elution from hexane to 1:1 hexane: chloroform to chloroform) to give **NDIS$_3$-PTZ** and **NDIS$_2$ cis-PTZ** in the following isolated yields.

NDIS$_2$ cis-PTZ as a brown powder (8 mg, 8 %). λ_{max} (abs) = 473 nm. ^{1}H NMR (400 MHz, $CDCl_3$): δ ppm 9.02 (m, *J* = 8.30 Hz, 2 H), 8.76 - 8.83 (m, 2 H), 7.50 - 7.57 (m, 2 H), 7.39 - 7.45 (m, 2 H), 7.13 (dd, *J* = 7.53, 1.53 Hz, 2 H), 7.00 - 7.05 (m, 2 H), 6.93 (td, *J* = 7.45, 1.17 Hz, 2 H), 6.58 (dd, *J* = 8.18, 1.17 Hz, 2 H), 4.70 - 4.78 (m, 2 H), 1.85 (quin, *J* = 7.60 Hz, 2 H), 1.37 - 1.29 (m, 10 H)), 0.91 (t, *J* = 6.90 Hz, 3 H). ^{13}C NMR (125 MHz, $CDCl_3$): δ ppm 194.23, 192.80, 160.88, 160.32, 143.54, 142.18, 138.21, 135.51, 135.36, 131.55, 131.49, 130.58, 129.43, 129.19, 128.98, 127.16, 127.08, 126.87, 126.62, 125.61, 125.33, 123.29, 122.75, 118.12, 47.78, 31.81, 29.22, 29.21, 27.01, 26.62, 22.65, 14.10. HRMS (FD)$^+$ m/z 683.1738 ($C_{40}H_{33}N_3O_2S_3$ [M]$^+$ requires 683.1729).

NDIS$_3$-PTZ as a dark red powder (15 mg, 14 %). Suitable crystals for X-ray diffraction were grown by vapour diffusion of pentane into a chloroform solution of the compound). λ_{max} (abs) = 505 nm. ^{1}H NMR (400 MHz, $CDCl_3$): δ ppm 8.98 (d, *J* = 8.04

Hz, 1 H), 9.02 (d, *J* = 8.33 Hz, 1 H), 8.88 (d, *J* = 8.33 Hz, 1 H), 8.68 (d, *J* = 8.04 Hz, 1 H), 7.47 - 7.54 (m, 2 H), 7.40 - 7.70 (m, 1 H), 7.31 - 7.37 (m, 2 H), 7.13 (dd, *J* = 7.53, 1.53 Hz, 2 H), 7.00 - 7.06 (m, 2 H), 6.92 (td, *J* = 7.49, 1.24 Hz, 2 H), 6.57 (dd, *J* = 8.11, 1.10 Hz, 2 H), 4.69 - 4.77 (m, 2 H), 1.85 (quin, *J* = 7.56 Hz, 2 H), 1.28 - 1.49 (m, 10 H), 0.91 (t, *J* = 6.70 Hz, 3 H). ^{13}C NMR (125 MHz, $CDCl_3$): δ ppm 193.01, 190.27, 190.19, 160.71, 143.74, 143.56, 141.60, 136.47, 135.85, 135.55, 131.29, 131.00, 130.54, 130.46, 129.91, 128.52, 127.10, 127.07, 125.43, 123.20, 122.48, 122.39, 117.83, 47.78, 31.81, 29.21, 29.21, 27.01, 26.59, 22.65, 14.10. HRMS (FD)$^+$ m/z 699.1510 ($C_{40}H_{33}N_3O_1S_4$ [M]$^+$ requires 699.1501).

3.5. References

1. M. R. Wasielewski, *Acc. Chem. Res.*, 2009, **42**, 1910-1921.
2. K. Susumu, P. R. Frail, P. J. Angiolillo and M. J. Therien, *J. Am. Chem. Soc.*, 2006, **128**, 8380-8381.
3. V. Lloveras, J. Vidal-Gancedo, T. M. Figueira-Duarte, J.-F. Nierengarten, J. J. Novoa, F. Mota, N. Ventosa, C. Rovira and J. Veciana, *J. Am. Chem. Soc.*, 2011, **133**, 5818-5833.
4. M. Gilbert Gatty, A. Kahnt, L. J. Esdaile, M. Hutin, H. L. Anderson and B. Albinsson, *J. Phys. Chem. B*, 2015, **119**, 7598-7611.
5. N. Sakai, R. Bhosale, D. Emery, J. Mareda and S. Matile, *J. Am. Chem. Soc.*, 2010, **132**, 6923-6925.
6. X. Guo, A. Facchetti and T. J. Marks, *Chem. Rev.*, 2014, **114**, 8943-9021.
7. S. V. Bhosale, C. H. Jani and S. J. Langford, *Chem. Soc. Rev*, 2008, **37**, 331-342.
8. K. P. Goetz, D. Vermeulen, M. E. Payne, C. Kloc, L. E. McNeil and O. D. Jurchescu, *J. Mater. Chem. C*, 2014, **2**, 3065-3076.
9. P. W. Anderson, P. A. Lee and M. Saitoh, *Solid State Commun.*, 1973, **13**, 595-598.
10. A. Aviram and M. A. Ratner, *Chem. Phys. Lett.*, 1974, **29**, 277-283.
11. E. A. Weiss, M. J. Ahrens, L. E. Sinks, A. V. Gusev, M. A. Ratner and M. R. Wasielewski, *J. Am. Chem. Soc.*, 2004, **126**, 5577-5584.
12. C. E. Smith, S. O. Odoh, S. Ghosh, L. Gagliardi, C. J. Cramer and C. D. Frisbie, *J. Am. Chem. Soc.*, 2015, **137**, 15732-15741.
13. M. Kuss-Petermann and O. S. Wenger, *J. Am. Chem. Soc.*, 2016, **138**, 1349-1358.
14. Y. Wu, R. M. Young, M. Frasconi, S. T. Schneebeli, P. Spenst, D. M. Gardner, K. E. Brown, F. Würthner, J. F. Stoddart and M. R. Wasielewski, *J. Am. Chem. Soc.*, 2015, **137**, 13236-13239.
15. M. Bauscher and W. Maentele, *J. Phys. Chem.*, 1992, **96**, 11101-11108.
16. A. Osuka, R.-P. Zhang, K. Maruyama, T. Ohno and K. Nozaki, *Bull. Chem. Soc. Japan*, 1993, **66**, 3773-3782.
17. H. Shiratori, T. Ohno, K. Nozaki, I. Yamazaki, Y. Nishimura and A. Osuka, *J. Org. Chem.*, 2000, **65**, 8747-8757.
18. S. J. Langford, M. J. Latter and C. P. Woodward, *Photochem. Photobiol.*, 2006, **82**, 1530-1540.
19. S. R. Greenfield, W. A. Svec, D. Gosztola and M. R. Wasielewski, *J. Am. Chem. Soc.*, 1996, **118**, 6767-6777.
20. M. P. Debreczeny, W. A. Svec, E. M. Marsh and M. R. Wasielewski, *J. Am. Chem. Soc.*, 1996, **118**, 8174-8175.
21. K. Hasharoni, H. Levanon, S. R. Greenfield, D. J. Gosztola, W. A. Svec and M. R. Wasielewski, *J. Am. Chem. Soc.*, 1996, **118**, 10228-10235.
22. H. Levanon, T. Galili, A. Regev, G. P. Wiederrecht, W. A. Svec and M. R. Wasielewski, *J. Am. Chem. Soc.*, 1998, **120**, 6366-6373.
23. M. E. El-Khouly, J. H. Kim, K.-Y. Kay, C. S. Choi, O. Ito and S. Fukuzumi, *Chem. Eur. J.*, 2009, **15**, 5301-5310.
24. M. Kondratenko, A. G. Moiseev and D. F. Perepichka, *J. Mater. Chem.*, 2011, **21**, 1470-1478.
25. R. Bhosale, J. Misek, N. Sakai and S. Matile, *Chem. Soc. Rev.*, 2010, **39**, 138-149.
26. N. Sakai, J. Mareda, E. Vauthey and S. Matile, *Chem. Commun.*, 2010, **46**, 4225-4237.
27. N. M. Shavaleev, E. S. Davies, H. Adams, J. Best and J. A. Weinstein, *Inorg. Chem.*, 2008, **47**, 1532-1547.

28. L. E. Shoer, S. W. Eaton, E. A. Margulies and M. R. Wasielewski, *J. Phys. Chem. B*, 2015, **119**, 7635-7643.
29. P. E. Hartnett, S. M. Dyar, E. A. Margulies, L. E. Shoer, A. W. Cook, S. W. Eaton, T. J. Marks and M. R. Wasielewski, *Chem. Sci.*, 2015, **6**, 402-411.
30. D. W. Cho, M. Fujitsuka, A. Sugimoto, U. C. Yoon, P. S. Mariano and T. Majima, *J. Phys. Chem. B*, 2006, **110**, 11062-11068.

Chapter 4

Asymmetric Perylene Diimides

4.1. Introduction

As discussed in Chapter 1, modification of the aromatic core of perylene-3,4,9,10-diimides (PDIs) can modify their properties, but the nature of the imide substituents has little effect on their optoelectronic properties.[1] Consequently, imide groups are usually selected to regulate the solubility of PDIs, either by disruption of aggregation caused by π-stacking,[2] or as a means of conferring solubility in aqueous media (e.g. imide-polyethylene glycol chains have been used to this end).[3] For these reasons, the vast majority of examples in the literature use PDIs with the same group at both imide termini of the molecule.

4.1.1. Synthesis of Asymmetric PDIs

The most common route to the synthesis of PDIs is the condensation reaction between perylene-3,4,9,10-dianhydride and the selected aliphatic amine or aniline, yielding an *N,N'*-symmetrically substituted PDI. In order to construct more structurally intricate systems from PDIs for crystal or molecular engineering purposes, it may be desired to synthesise a PDI bearing two different imide groups.

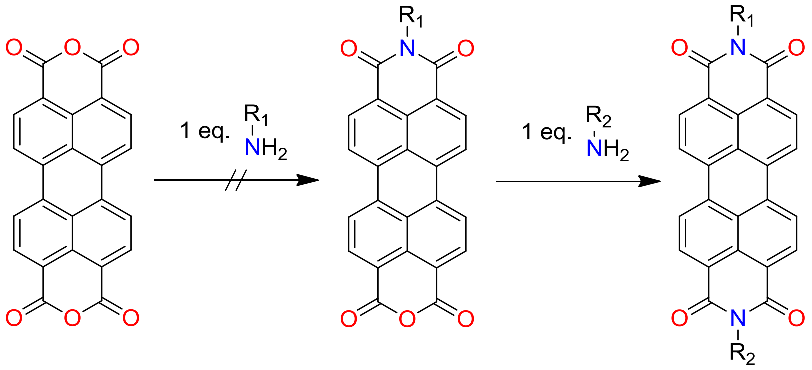

Scheme 4.1: Synthesis of N,N'-asymmetrically substituted PDIs using a stepwise approach is unsuccessful.

The stepwise condensation of the dianhydride with two different amines in stoichiometric equivalents does not provide a suitable route (Scheme 4.1).[4-7] Generally the reaction with the first quantity of amine will produce a symmetric PDI, and leave behind unreacted perylene dianhydride.[8] Moreover, the one-pot statistical approach of simultaneous condensation with two amines requires that each has similar reactivity, and is often unsuccessful. If traces of the asymmetrical product are formed, the subsequent purification of the desired reaction product from the unwanted symmetrically substituted PDIs is usually difficult. Notwithstanding, efficient routes to asymmetrically *N,N'*-disubstituted PDIs have been found.[6-12]

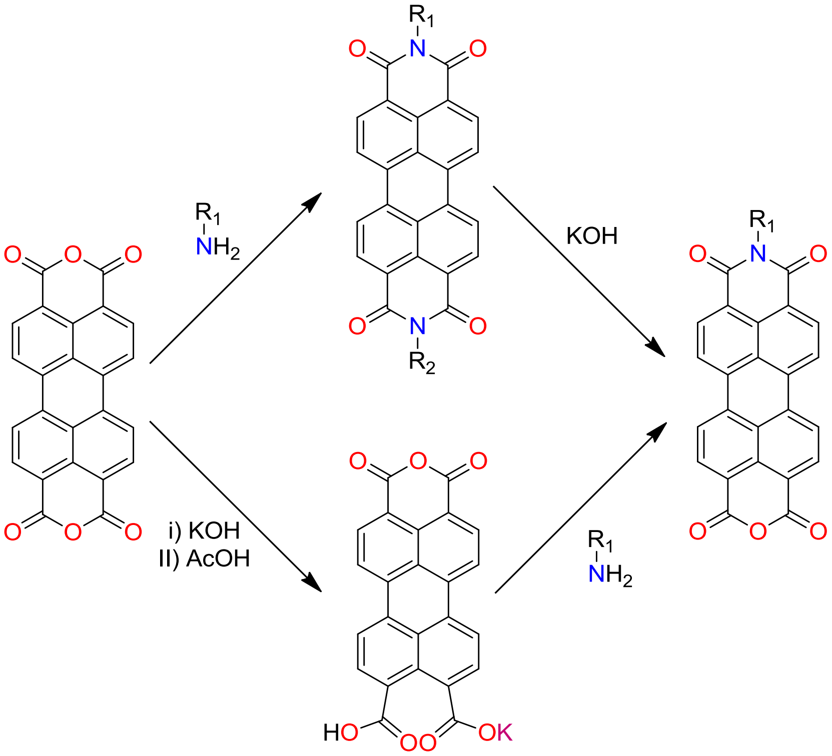

Scheme 4.2: Possible synthetic routes to PMI. Top: PDI hydrolysis with potassium hydroxide, bottom: potassium-salt route.

A thesis published by Huang[7] describes two methods of producing asymmetrically substituted PDIs using a multi-step synthetic approach that generates a perylene-3,4-imide-9,10-anhydride (PMI) intermediate (Scheme 4.2).[13] This PMI can then be reacted with another different amine or aniline to form the asymmetric PDI. The first method is the partial hydrolysis of a symmetrically substituted PDI under basic conditions to remove one of the imide substituents. The second route, initially published by Tröster,[9] forms the mono-potassium salt of perylene-3,4,9,10-dianhydride by selective protonation of tetrapotassium perylene-3,4,9,10-tetracarboxylate under careful control of pH. This salt can be reacted with the first amine, forming a PMI.

In 2009, a new high-yielding synthesis of a perylene monoanhydride diester was reported by Xue et al. (Scheme 4.3).[14] The synthesis begins with the familiar dianhydride and forms a perylene tetra-ester species (PTE) by the addition of n-decyl chains to each carbonyl. An acid catalysed hydrolysis of PTE is able to selectively form a perylene monoanhydride diester (PDE) under carefully chosen conditions.

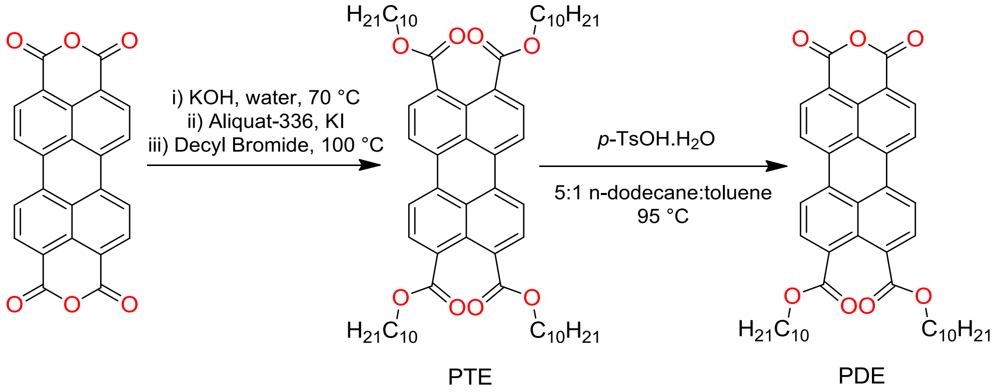

Scheme 4.3: Synthesis of perylene esters PTE and PDE by Xue et al.[14]

In the ester-hydrolysis reaction equilibrium, when two of the ester chains are removed from adjacent positions, a rapid intramolecular cyclisation reaction occurs to form a six-membered anhydride ring. The solvent system (5:1 n-dodecane: toluene) will readily dissolve PTE but not PDE, removing PDE from the reaction equilibrium thus preventing further hydrolysis of the ester groups. Unless two of the ester chains are removed from adjacent carbonyl groups, the cyclisation reaction can't occur, allowing the hydrolysis-equilibrium to 'correct' itself, improving the yield of PDE. One equivalent of *p*-toluenesulfonic acid monoanhydride is sufficient to serve as both the acid catalyst and the water source for the saponification reaction. The published yield for this reaction is

74 %, in excess of yields established for the hydrolysis route (<50 %),[7] and requiring far less precise pH control than the potassium-salt method.

Xue highlighted the applicability of PDE for the synthesis of asymmetric PDIs through the synthesis of several perylene imide diesters by performing condensation reactions with various amines under familiar conditions. Finally, the remaining two ester chains could be cleaved form the monoimide diester compounds to leave a PMI in a high yielding reaction.

4.1.2. Self-Assembly of Asymmetric PDIs

In addition to affecting the solubilities, the self-assembly properties of PDIs can also be influenced by the imide chains, with linear n-alkyl chains forming one dimensional nanobelt morphologies and branched 'swallow-tail' chains forming nanoparticle structures.[15] Recently, molecular engineers have taken advantage of this self-assembly by synthesising amphipathic asymmetric PDIs that self-assemble into ribbon[16-18] or coil[19-21] structures. A systematic screening of a variety of methoxyphenyl imide-groups on one end of an aliphatic-PDI published by Zhao and co-workers identified that morphology control between monolayer and bilayer nanocoils could be achieved.[19] In general, two methoxy- substituents on the phenyl ring gave bilayered coils, whereas monolayered coils were produced if only one methoxy- substituent was used, with specific positions providing more emissive structures (Figure 4.1). Other such PDI nanostructures have been demonstrated to serve as efficient sensors of both nitro [17] and amine compounds,[18, 20] utilising the photoconductivity and emission properties of PDIs in these ordered structures to respond to the presence of specific molecular vapours. A recent review article published by Chen et al.[22] discusses the self-assembly and applications of both symmetric and asymmetric one-dimensional PDI nanostructures.

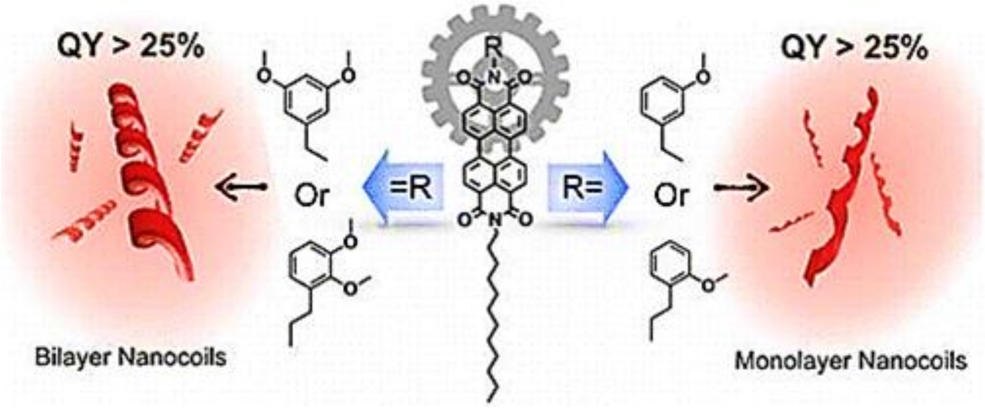

Figure 4.1: Schematic depicting the self-assembly of asymmetric PDIs into fluorescent mono- or bi-layered nanocoils by control of a methoxyaryl imide group. Adapted from Liu et al.[19]

4.1.3. Arrays of PDIs

The use of asymmetric PDIs allows for greater control of synthesis at the imide region, allowing discrete PDI oligomers or architectures to be formed. The development of compounds comprising more than one PDI subunit to study the effects of interactions between PDI chromophores has applications in light-harvesting systems and in the production of semiconducting devices. Such compounds are often rationally designed to enhance π-orbital overlap between neighbouring orbitals to increase carrier mobility by either furnishing the semiconducting molecule with functional groups to enhance π-π stacking or by using rigid spacers to hold the molecules in position relative to each other.

There have been several reported interactions between subunits in a multi-chromophoric PDI system. For instance in 1998, Langhals and Ismael[23] synthesised a macrocycle containing two PDI units connected by long alkyl chains that exhibited an H-type stacking interaction in its absorption spectrum and slipped to a J-type aggregate after excitation, maintaining a quantum yield of 40 %. In contrast to this, the absorption spectra of xanthene spaced dimers synthesised by Li and co-workers[24] indicated J-type aggregates formed, with excimer-like excited states. Similarly spaced trimers reduced interaction between PDI units due to steric hindrance provided by bay-substitution of the

PDI subunit. The same xanthene spacer is able to provide charge separation between two halves of a green PDI-dimer, representing the first instance of charge-separation between identical chromophores in a low-polarity medium.[25] A significant improvement in organic field-effect transistor (OFET) performance was noted for another dimer, using a triazine linker to bridge the imide regions of two asymmetric PDIs[26] illuminating the potential of PDI arrays in optoelectronic applications. A similar, symmetric, cyclophane comprising two triazine-linked PDIs was also reported,[27] with substantial changes in absorbance, fluorescence and electrochemistry as the torsion angle between PDI planes was tuned by means of minor structural changes.

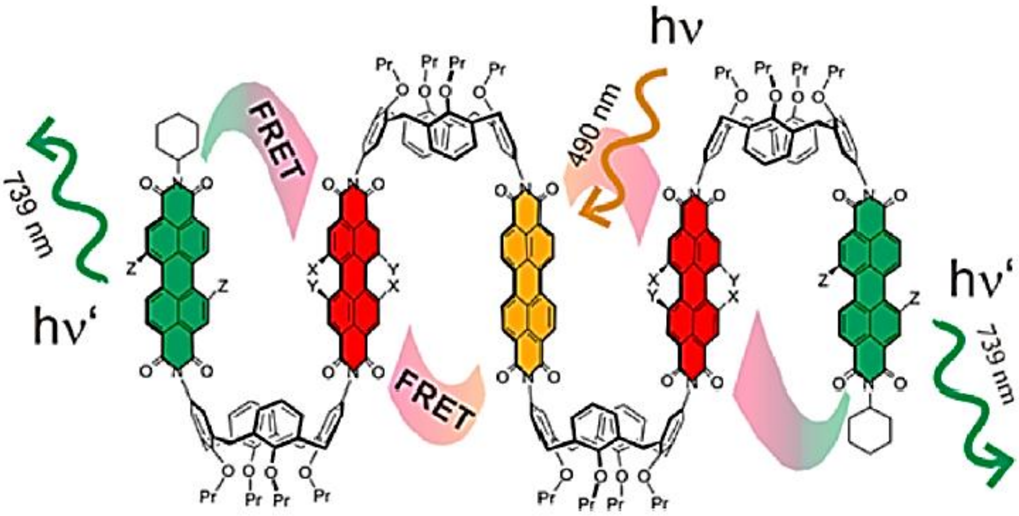

Figure 4.2: Schematic of a multichromophoric PDI assembly in which asymmetrically substituted PDIs are linked, allowing energy transfer between subunits. Reproduced from Hippius et al.[28]

Furthermore, PDI arrays have been extended beyond dimers: in 2002, the Wasielewski group published a porphyrin structure symmetrically furnished with four PDI moieties.[29] Van der Waal’s interactions between PDI units triggered self-assembly into nanoparticles of up to 20 molecules capable of quantitative charge separation to form porphyrin$^{\cdot+}$-PDI$^{\cdot-}$ radical ion pairs. A linearly organised tetramer of PDI units, separated by phenyl linkers can transfer excitation energy as far as 4.7 nm to an acceptor PDI without any loss in efficiency.[30] A pentamer assembly of multi-coloured PDIs was described by the Würthner group in 2006,[28] in which energy transfer between the cofacially oriented PDI subunits occurs, allowing the inner, yellow PDI to be excited, resulting in emission from the outermost, green PDI (Figure 4.2). Finally, several assemblies of six asymmetric PDIs have been synthesised: with subunits associated by hexaazaphenylene,[31] the hexamer functioning as an electron accepting antenna; hexaphenylbenzene[32] and even hexabenzocoronene.[33]

4.2. Results and Discussion

4.2.1. Design and Synthesis of a Non-aggregating PDI

Described above, the extended aromatic core of PDIs drives the molecules to form intermolecular π-π contacts, self-aggregating into stacks. PDIs are often very insoluble in most organic solvents, which can't break up these collective π-type intermolecular interactions. Whilst controlled aggregation of PDI dyes is useful for some light-harvesting applications, including charge conduits[34, 35] and J-aggregates,[36] prohibition of aggregation is also desirable for promoting fluorescent properties,[37] even in the solid state,[2, 38] constructing light-harvesting antennae[39] and also aides charge separation in donor-acceptor films.[40] Discounting bay substitution as a means of preventing aggregation, which twists the perylene core causing a broadening of the vibronic bands in the visible spectrum and alters the redox chemistry,[41] sterically encumbering imide groups must be used to minimise aggregation.

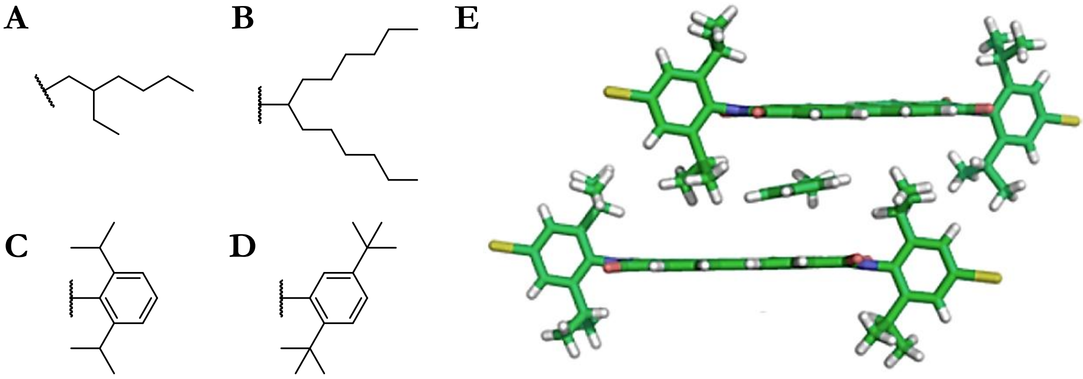

Figure 4.3: A to D: Structures of imide groups of PDIs with limited aggregation. E: Crystal structure of a 2,6-diisopropylphenyl substituted PDI highlighting how stacking is disrupted. Adapted from Frischmann and Würthner.[42]

Among the most common PDI imide groups used to improve solubility (Figure 4.3A to D) are branched 'swallowtail' alkanes[2, 4, 8, 43] and bulky aromatics such as 2,6-diisopropylphenyl,[42, 44] that contain ortho-position substituents designed to clash with the carbonyl oxygen atoms of PDIs and twist the phenyl ring perpendicular to the perylene plane (Figure 4.3E). The latter has become the choice group for PDI chemists more recently; its conformational rigidity allowing for crystallisation that the aliphatic alternatives do not facilitate. Initially for this work, a 2-ethylhexyl ‘swallowtail’ alkyl group was used, although at the later stages of synthesis the asymmetric PDI solubility was found to be too poor. 2,6-Diisopropylphenyl substituted PDI derivatives were also tested, though the improvement in solubility was still insufficient for full electrochemical characterisation of the downstream PDI targets.

In this study an even more sterically hindered imide-group was targeted to gain an adequate increase in solubility of the target PDIs to allow for full characterisation. Based on the structure of 2,6-diisopropylphenyl, a bulkier tecton was designed by replacement of the diisopropyl groups with diphenylmethyl groups. This tecton also requires a free amine group to react with the anhydride ring of PDIs and as such, 2,6-bis(diphenylmethyl)-4-methylaniline (**BDPA**) was synthesised from diphenylmethanol and *p*-toludidine in solvent-free conditions using a zinc chloride catalyst (Scheme 4.4). The methyl group para to the amine blocks substitution at that position, improving atom economy of the reaction. Further functionalisation of **BDPA** as an imide group is also conceivable, especially if the methyl group is replaced with a halogen atom to permit various cross-coupling reactions.

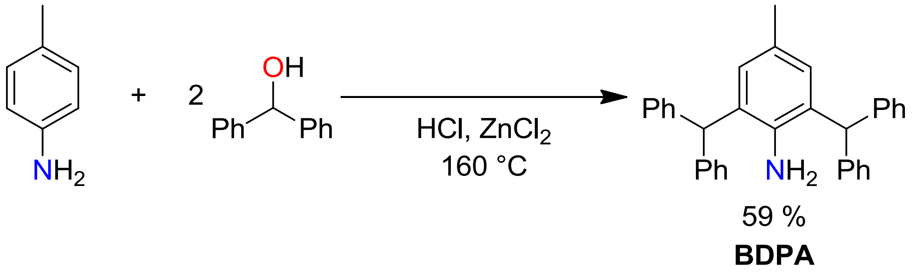

Scheme 4.4: Synthesis of BDPA.

A symmetric PDI (**PDI-(BDPA)$_2$**) was prepared from a one-step reaction between perylene-3,4,9,10-dianhydride and **BDPA** under the commonly used imidization conditions (Scheme 4.5). At less than 10 %, the yield for this reaction was low, however, only one reaction step is needed and both starting reagents can be obtained in large quantity. It is likely that due to the size of this group, steric effects might limit the rate of reaction, resulting in such a low yield.

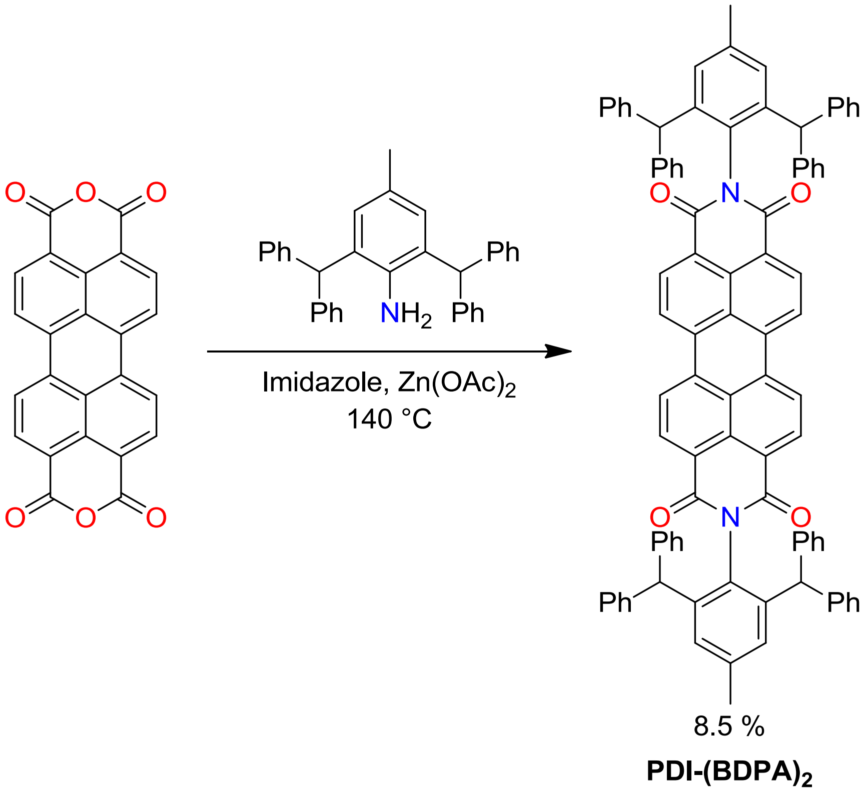

Scheme 4.5: Synthesis of PDI-(BDPA)$_2$.

To analyse the effect upon aggregation, the solid state packing of **PDI-(BDPA)$_2$** was elucidated by single-crystal X-ray diffractometry. Suitable crystals were grown by vapour diffusion of hexane into a chloroform solution of the compound, which crystallised in the *I*2/*a* space group (Figure 4.4). The asymmetric unit contained half a molecule of **PDI-(BDPA)$_2$** and two chloroform molecules. The phenyl ring at the imide nitrogen is almost perpendicular to the perylene plane, with a dihedral angle between them of 81.1°, pushing the diphenylmethyl substituents away from the aromatic backbone of the molecule, thereby blocking any potential π- π interactions.

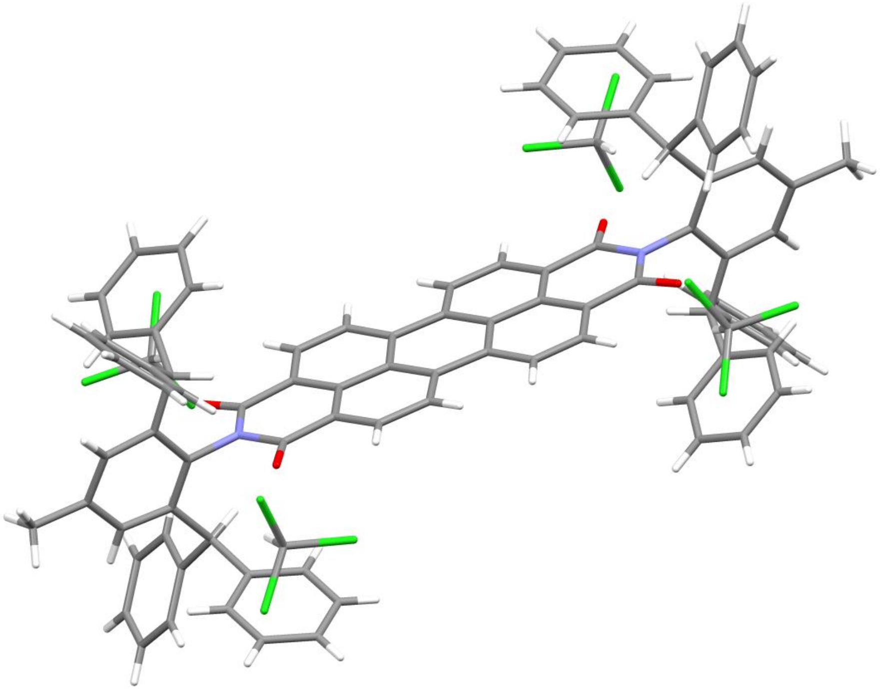

Figure 4.4: Crystal structure of PDI-(BDPA)$_2$ including crystallographically resolved chloroform molecules. Atom colours - C: grey, O: red, N: blue, H: white and Cl: green.

Examination of the intermolecular packing reveals that any π-stacking between perylene cores is completely avoided: the angle between the perylene planes of adjacent molecules is 67.2° and the distance between the centres of these planes is 11.47 Å (Figure 4.5). This distance is over three times greater than the typical separation of 3.40 Å,[1] representing a huge translational offset and allows solvent chloroform molecules to comfortably fit between adjacent PDI molecules. In the solid state, **PDI-(BDPA)$_2$** is a bright orange colour, more-closely resembling the solution phase colouring of PDIs, than the typical red tone of other solid PDIs. It is hypothesised that this is due to the elimination of fluorescence-quenching aggregation, which would usually occur for solid phase PDIs. **PDI-(BDPA)$_2$** is strongly fluorescent in the solution phase and the quantum yield for this fluorescence was determined to be 1.00.

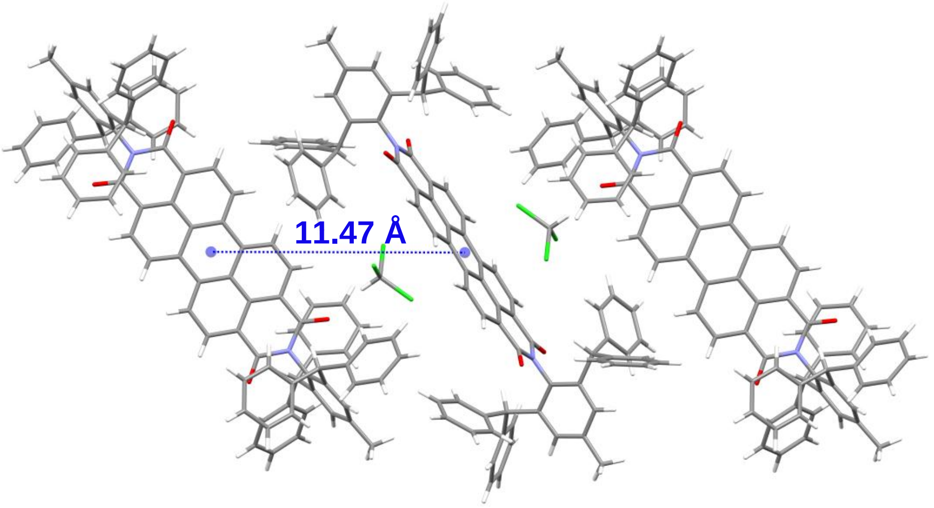

Figure 4.5: Packing motif of PDI-(BDPA)$_2$ molecules in a single crystal. Atom colours - C: grey, O: red, N: blue, H: white and Cl: green. Blue dashed line: distance between centres of neighbouring molecules' perylene planes.

Additionally, the NDI equivalent, **NDI-(BDPA)$_2$** was assembled utilising the same reaction conditions as for the PDI (Scheme 4.6). Single crystals of **NDI-(BDPA)$_2$** could be grown from vapour diffusion of hexane into a chloroform solution and were analysed by single crystal X-ray diffractometry, crystallising in the *P*-1 space group. The asymmetric unit contained half of each of two crystallographically distinct NDI molecules and one chloroform molecule (Figure 4.6).

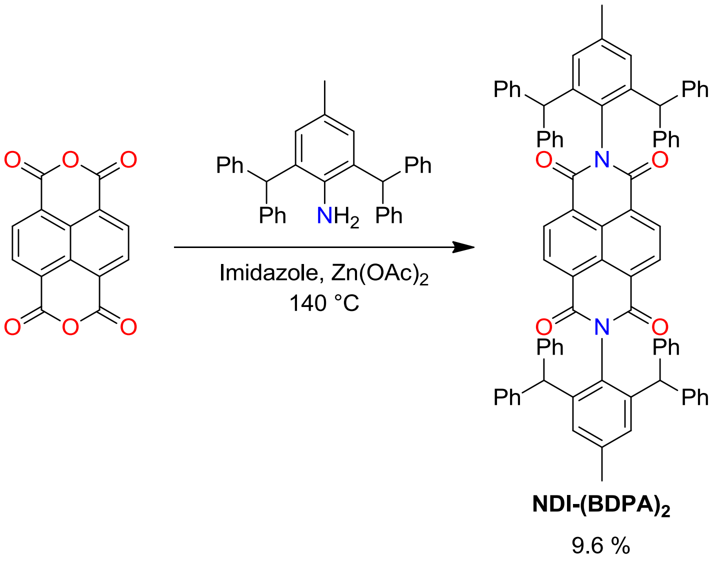

Scheme 4.6: Synthesis of NDI-(BDPA)$_2$.

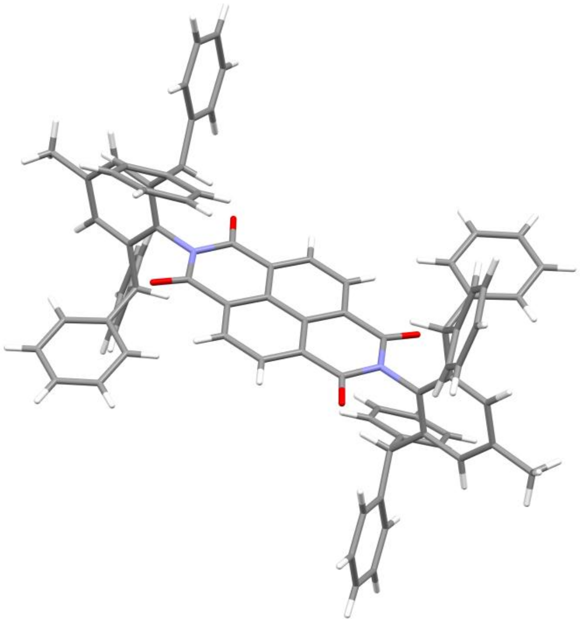

Figure 4.6: Crystal structure of NDI-(BDPA)$_2$. Atom colours - C: grey, O: red, N: blue and H: white.

The NDI molecules pack in a similar manner to those of the PDI, with adjacent molecules rotated almost perpendicular to their neighbour (Figure 4.7). The angle between NDI planes of adjacent molecules is 70.0° and the separation between the centres of neighbouring molecules 11.03 Å.

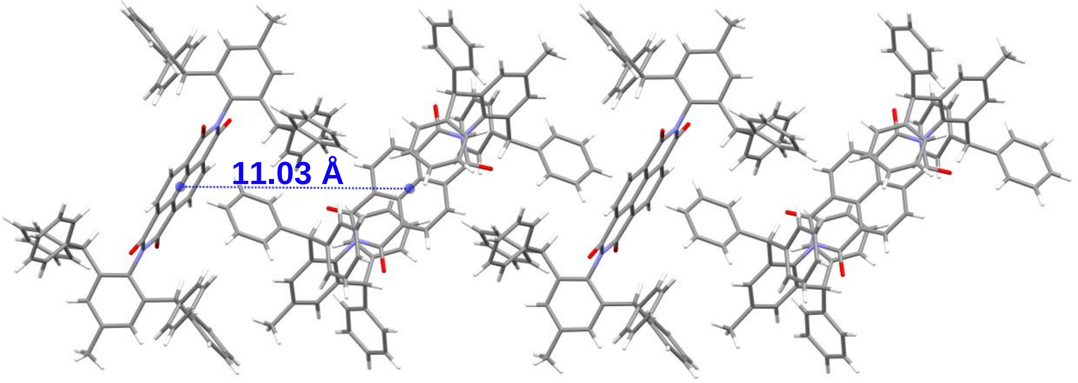

Figure 4.7: Packing motif of NDI-(BDPA)$_2$ molecules in a single crystal. Atom colours - C: grey, O: red, N: blue and H: white. Blue dashed line: distance between centres of neighbouring molecules' naphthalene planes.

This crystallographic study demonstrates the effectiveness of the **BDPA** tecton as a solubilising group for rylene-type molecules. The large phenyl substituents coupled with the rigid conformation ensure that molecules cannot approach each other closely enough to form π-contacts, thereby eliminating stacking and aggregation. Additionally, the conformational rigidity of the **BDPA** group facilitates characterisation by crystallographic methods, an advantage over 'swallow-tail' type imide groups whose flexibility (and chirality) can be prohibitive to crystal growth. Due to these advantageous properties, the **BDPA** moiety was employed as one of the imide groups in asymmetric PDI synthesis.

4.2.2. Synthesis of an Asymmetric Perylene Monoimide Monoanhydride

The asymmetric perylene monoanhydride diester **PDE** was prepared according to the synthetic procedure described in the introduction to this chapter, published by Xue et al.[14] **PDE** was synthesised on a gram-scale, with a 67 % yield across two steps, illustrating the utility of **PDE** as a precursor to asymmetric PDI synthesis. The first step is the esterification of each carbonyl group of perylene-3,4,9,10-dianhydride with ten-carbon aliphatic esters to form the tetra-ester species **PTE**. Unlike PDIs, which tend to form bright orange solutions and red solids, **PTE** is a very bright yellow in solution and a deeper yellow-orange in the solid state. The effect upon the optical properties and electrochemistry of the perylene core caused by the difference in the electron-withdrawing properties of the four ester groups compared to the usual two imide groups is examined below.

The first imide group added was **BDPA**, to effectively boost solubility of the downstream products (discussed in detail above). The addition of this imide group to produce a perylene monoimide diester (**PMIDE**), proved to be the limiting step in the overall synthetic pathway. The steric bulk that contributes so well to the improvement in solubility of the perylene species impedes the imidization reaction, reducing the yield to 30 %, although this is much greater than the 9 % yield achieved for the symmetric **PDI-(BDPA)$_2$**, likely due to only having to add one such group. The final step required to synthesise an asymmetric perylene monoimide monoanhydride (**PMI**) is the removal of the last two ester groups, reforming the anhydride ring. Conditions similar to the first saponification reaction were recycled: excess *p*-toluenesulfonic acid in refluxing toluene could remove the ester groups in almost quantitative yield (Scheme 4.7).

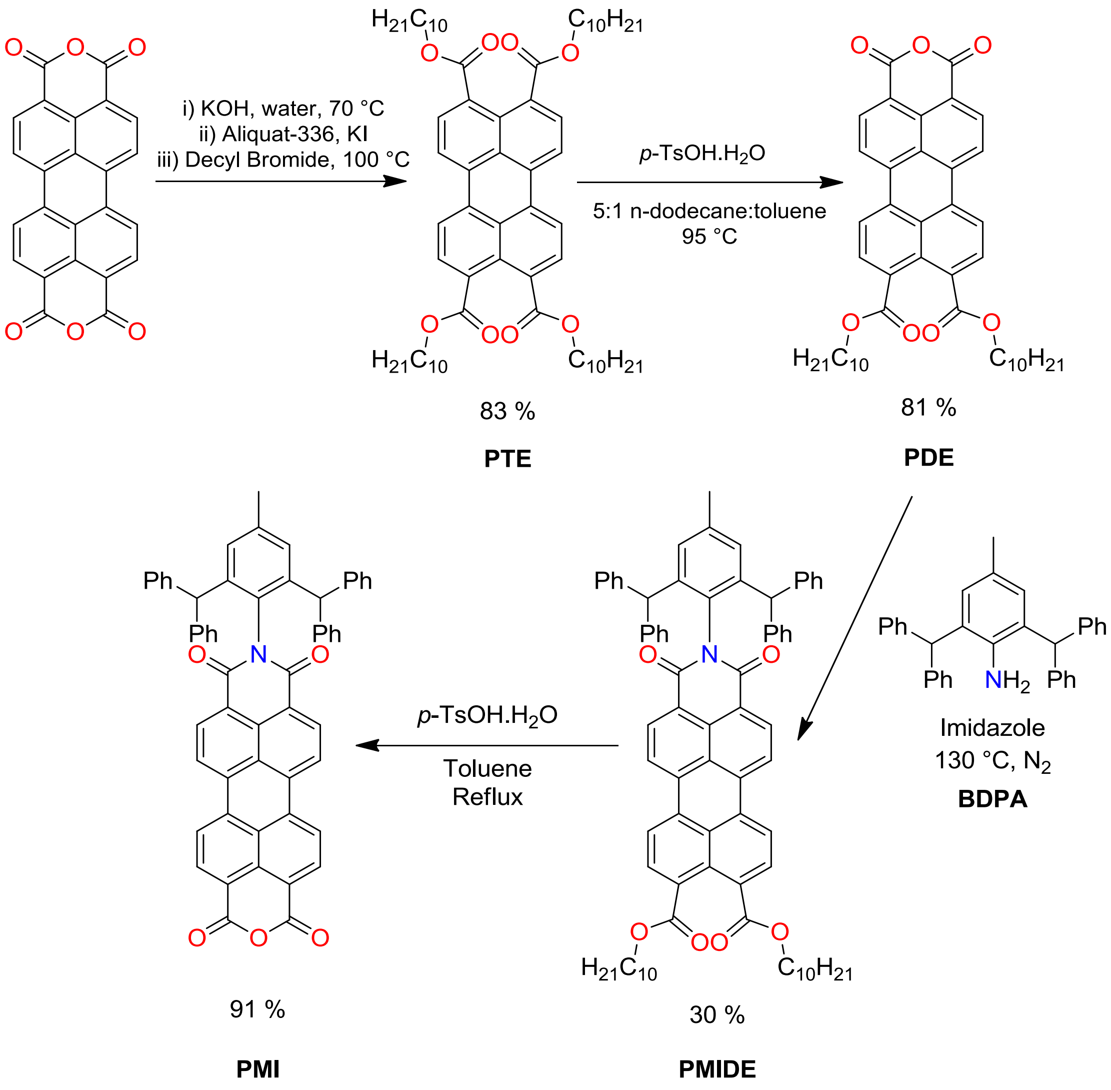

Scheme 4.7: Synthesis of PMI via the esterification route.

Each of the synthetic intermediates was purified using silica gel column chromatography, allowing for electrochemical characterisation (see below). Importantly, **PMI** proved to be amply soluble for cyclic voltammetry and ^{13}C NMR experiments. It should be noted that isolation of **PMIDE** can be circumvented; after work up of the **PDE→PMIDE** reaction, the crude reaction mixture can be effectively used in the next stage of reaction, simplifying the chromatography procedure (isolating **PMIDE** requires the most delicate column chromatographic step). Also of note is that **PDE** and **PMI** have very similar R_f values and will co-elute during chromatography. This can be avoided by using an excess of *p*-toluenesulfonic acid when synthesising **PMI**: any **PDE** still present will also be hydrolysed back to the insoluble dianhydride and is removed by filtration.

Single crystals of **PMI** were grown from an evaporating chloroform solution of the compound, forming rhomboid plates. X-ray diffraction studies determined that **PMI** crystallised in the *P*-1 space group, the asymmetric unit containing one molecule of **PMI** and one chloroform molecule (Figure 4.8).

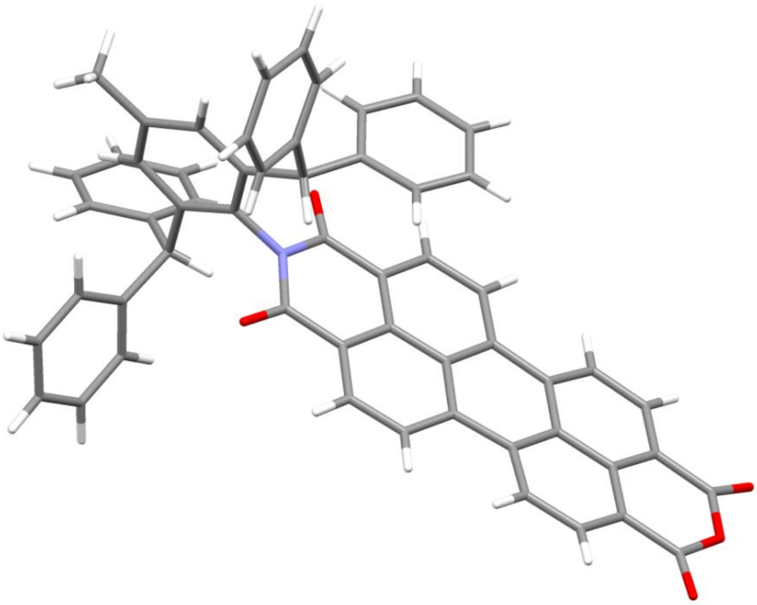

Figure 4.8: Single crystal structure of PMI. Atom colours - C: grey, O: red, N: blue and H: white.

In contrast to **PDI-(BDPA)$_2$**, π-stacking is present, but limited to pairs of molecules. Neighbouring molecules of **PMI** stack in an antiparallel fashion, with the imide groups pointing in opposite directions (Figure 4.9). The perylene planes of these pairs are separated by a characteristic 3.36 Å, extending to a substantial 6.84 Å between the perylene planes of non-stacking adjacent molecules. Also noteworthy is the puckering of the imide group, such that it is not in line with the perylene backbone. A slight twisting of the perylene plane is also observable: the torsion angle between the two naphthalene rings that comprise a single perylene core is 7.2°.

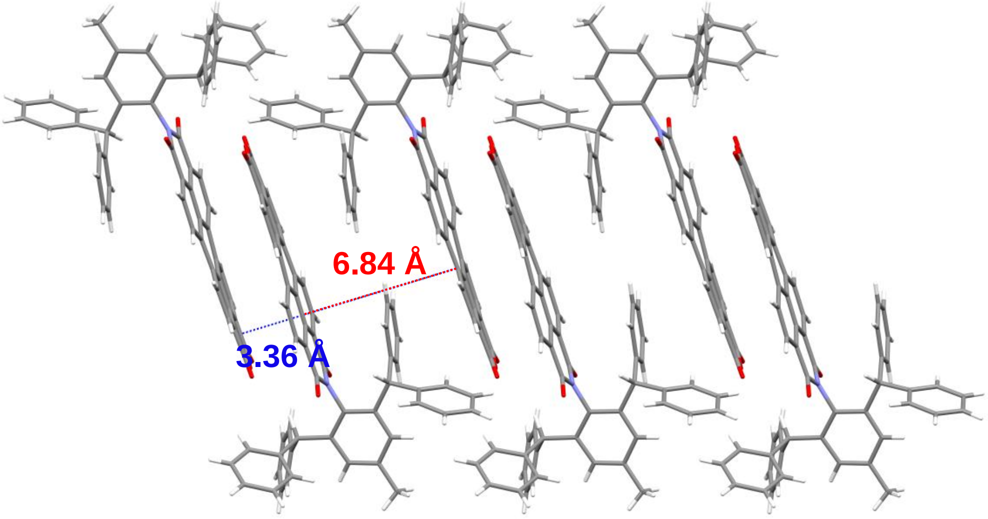

Figure 4.9: Packing motif of PMI molecules in a single crystal, displaying cofacial pairing. Atom colours - C: grey, O: red, N: blue and H: white. Blue dashed line: distance between perylene planes in a stacked pair. Red dashed line: distance between adjacent perylene planes in a non-stacking pair.

4.2.3. Electrochemistry of Perylene Tetracarboxylic Compounds

A series of perylene compounds with electron withdrawing carboxylic groups attached at the four peri- positions have been synthesised, with perylene cores furnished with combinations of ester, anhydride and imide groups. Each of these carboxylic groups possesses different electron withdrawing powers, which affect the electron density of the perylene core and alter the electron affinity of the molecule. Cyclic voltammetry and spectroelectrochemistry were used to analyse this effect on perylene compounds with four ester groups (**PTE**), two ester groups and an anhydride (**PDE**), two ester groups and an imide (**PMIDE**), an imide and an anhydride (**PMI**) and two imide groups (**PDI-**

(BDPA)$_2$). **NDI-(BDPA)$_2$** was also included in this study to compare the analogous perylene and naphthalene diimide compounds.

4.2.3.1. *Cyclic Voltammetry*

The cyclic voltammograms for each of the tetracarboxylic perylene compounds and the NDI display two reversible reduction processes (Figure 4.10). These processes were stable to multiple scans and peak anodic and cathodic potentials were independent of the scan rate. Additionally, it was found that **PTE** and **PMIDE** each showed a reversible oxidation process within the scan range of dichloromethane.

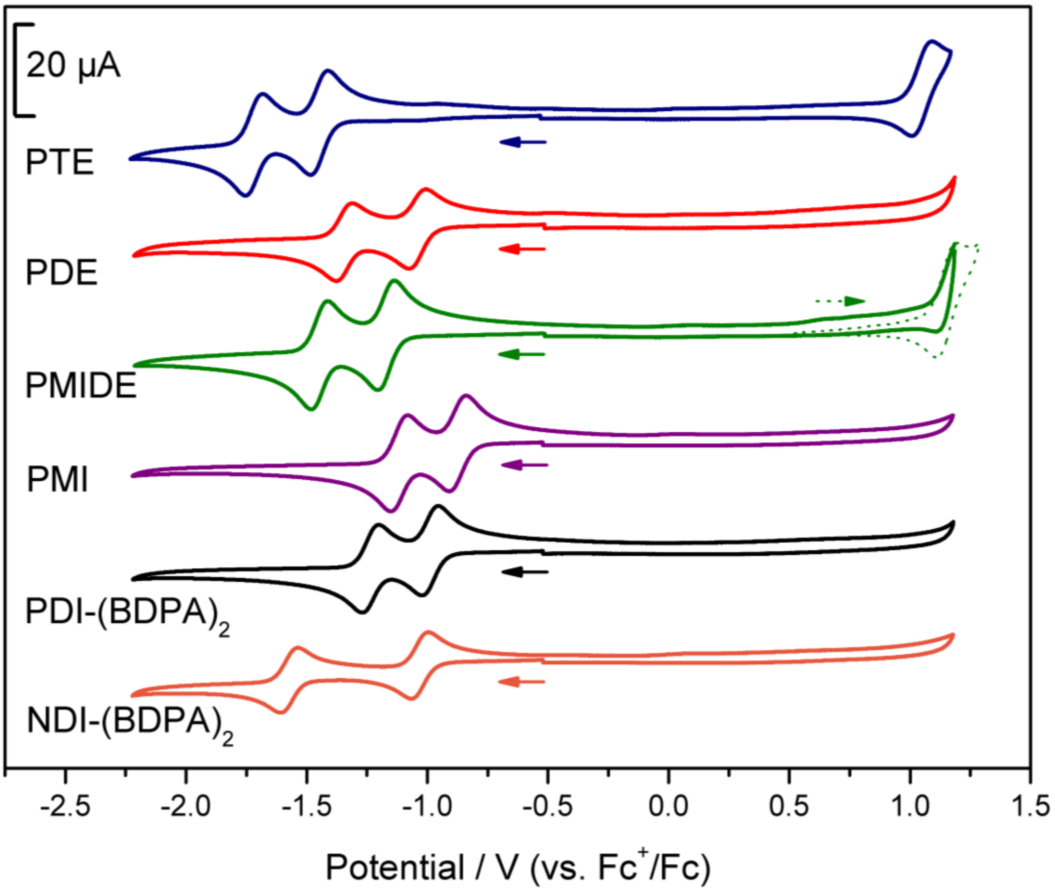

Figure 4.10: Cyclic voltammograms of a series of tetracarboxylic rylene compounds in dichloromethane containing 0.4 M [^{n}Bu$_4$N][BF$_4$] as the supporting electrolyte, with a scan rate of 100 mVs^{-1}. Blue: PTE, red: PDE, green: PMIDE, purple PMI, black: PDI-(BDPA)$_2$, orange NDI-(BDPA)$_2$.

These data show that the most electron deficient perylene core is that of **PMI**, with a first reduction potential of -0.87 V (vs. Fc^+/Fc) and the least electron deficient perylene core is observed for **PTE** at -1.45 V. These results are as expected, since the more powerful electron withdrawing group is the anhydride, followed by imide and finally the esters. In agreement with this, **PMIDE** is reduced at an intermediate potential between the diester anhydride **PDE** and tetraester **PTE** perylene molecules and the first reduction potential of the diimide **PDI-(BDPA)$_2$** lies between that of the monoimide monoanhydride **PMI** and the monoimide diester **PMIDE**. The ability to tune the electron acceptor affinity is valuable to OPVs, allowing energy loss during electron transfer from the donor to the acceptor to be minimised.[45]

PTE and **PMIDE** can also lose an electron, becoming oxidised at the fairly extreme potentials of +1.05 and +1.15 V (vs Fc^+/Fc) respectively. It is likely that the other perylene compounds can also be oxidised and that this oxidation was not observed because the required potential is so great it lies outside of the electrochemical window of the solvent. As the least electron deficient perylene derivatives, **PTE** and **PMIDE** have mild enough oxidation potentials to be detected in dichloromethane.

The difference between the first and second reduction potentials is reasonably consistent for the tetracarboxylic perylene compounds, ranging from 240 mV for **PMI** to 300 mV for **PDE**. This would imply the electron withdrawing effect of the various carboxylate groups is maintained evenly between the first and second reductions. For **NDI-(BDPA)$_2$** this difference is 540 mV, suggesting a significant decrease in the electron accepting ability of the NDI core versus the PDI core after one electron has been supplied. Interestingly for the aliphatic **NDIS$_0$** (see Chapter 2) the difference between reduction potentials is only 460 mV, much lower than for **NDI-(BDPA)$_2$**. The large aromatic bis(diphenylmethyl-4-methylphenyl) imide substituent of **NDI-(BDPA)$_2$** appears to stabilise the molecule slightly to the first reduction (-1.03 V compared to -1.07 (vs Fc^+/Fc) for **$NDIS_0$**) and destabilise it slightly to the second (-1.57 V compared to -1.53 (vs Fc^+/Fc) for **$NDIS_0$**), increasing the gap between reductions. The first reduction of **$PDI\text{-}(BDPA)_2$** lies at -0.99 V, a very similar potential to **$NDI\text{-}(BDPA)_2$**, which would suggest very similar LUMO energies for both compounds. The electrochemical data obtained for the tetracarboxylic perylene series including **$NDI\text{-}(BDPA)_2$** is summarised below (Table 4.1).

Table 4.1: Redox potentials for a range of tetracarboxylic perylene compounds and $NDI\text{-}(BDPA)_2$.

Compound	1st Reduction $E_{1/2}$ / V	2nd Reduction $E_{1/2}$ / V	1st Oxidation $E_{1/2}$ / V	Difference Between Reduction Potentials / V
PTE	-1.45	-1.72	+1.05	0.27
PDE	-1.04	-1.34	-	0.30
PMIDE	-1.14	-1.45	+1.15	0.28
PMI	-0.87	-1.12	-	0.24
$PDI\text{-}(BDPA)_2$	-0.99	-1.24	-	0.25
$NDI\text{-}(BDPA)_2$	-1.03	-1.57	-	0.54

Potentials quoted against $E_{1/2}$ Fc^+/Fc at 100 mVs^{-1} used as the internal standard. Recorded in dichloromethane at ambient temperature containing $[^nBu_4N][BF_4]$ (0.4 M) as the supporting electrolyte.

4.2.3.2. *Spectroelectrochemistry and Optical Properties*

Spectroelectrochemical techniques were used to record the optical absorption spectra for the neutral, monoanionic, dianionic and when appropriate, the monocationic tetracarboxylic perylene compounds. In general, the perylene compounds present a strong, structured absorbance, with the strongest absorbance arising from the 0→0 vibronic band, and an additional prominent peak for the 0→1 band. An additional peak corresponding to the 0→2 vibronic band is observed for **PMI** and **$PDI\text{-}(BDPA)_2$**, that is only seen as a 'shoulder' band for the other perylene species. The various electron withdrawing carbonyl groups manifest themselves in the absorbance spectra; the least electron withdrawing tetraester species **PTE** has an absorption maximum at 471 nm and **PMI** with its imide and anhydride groups has an absorbance maximum of 527 nm. The presence of imide groups appears to redshift the absorption maximum relative to anhydride groups, such that imides **PDI-(BDPA)$_2$** (λ_{max} = 533 nm) and **PMIDE** (λ_{max} = 509 nm) had slightly lower energy absorption maxima than when one of their imide groups was replaced with an anhydride ring: **PMI** (λ_{max} = 527 nm) and **PDE** (λ_{max} = 507 nm). The absorption maxima occupy a range of 62 nm, representing considerable tuning of the optical properties of these perylene molecules with the assorted carbonyl groups. In spite of this, the solution-phase colours of the compounds were all typically orange, with the exception of **PTE**, which was a bright yellow. The molar extinction coefficients for the 0→0 transitions were considerably lower for the perylene ester compounds than those without ester chains. **PTE** and **PDE** had molar extinction coefficients below 40,000 $mol^{-1}dm^{3}cm^{-1}$, whereas those of **PMI** and **PDI-(BDPA)$_2$** were greater than 85,000 $mol^{-1}dm^{3}cm^{-1}$. **PMIDE** had an intermediate value of 59,300 $mol^{-1}dm^{3}cm^{-1}$.

Following reduction, a sharp band arises at lower energy, with a similar extinction coefficient to the neutral molecules' 0→0 vibronic band, which is entirely diminished by the reduction for all the perylene species (Figure 4.11). The absorption maximum tends to be redshifted ~160 nm for the monoanionic molecule compared to its neutral counterpart. The range of absorption maxima for the monoanionic tetracarboxylic perylene series was 88 nm. Additional bands at longer wavelengths and lower intensity are also seen in the near infrared region. Formation of the dianionic perylene species by further reduction saw replacement of the intense lower energy band with one at slightly higher energy and roughly equal intensity (Figure 4.12). The position of the absorption maxima of the dianionic tetracarboxylic perylene series lies within a 25 nm range, (a lower series range than for neutral and monoanionic perylene tetraesters) with absorption maxima for the dianionic molecules ranging from 553 nm (for **PTE**) to 578 nm (for **PDI-(BDPA)$_2$**). Overall, the change in absorbance properties upon reduction of the perylene tetracarboxylic compounds is largely similar, though tuneable with the choice of electron withdrawing group; esters are more blueshifted and less intense, imides are more redshifted and more intense.

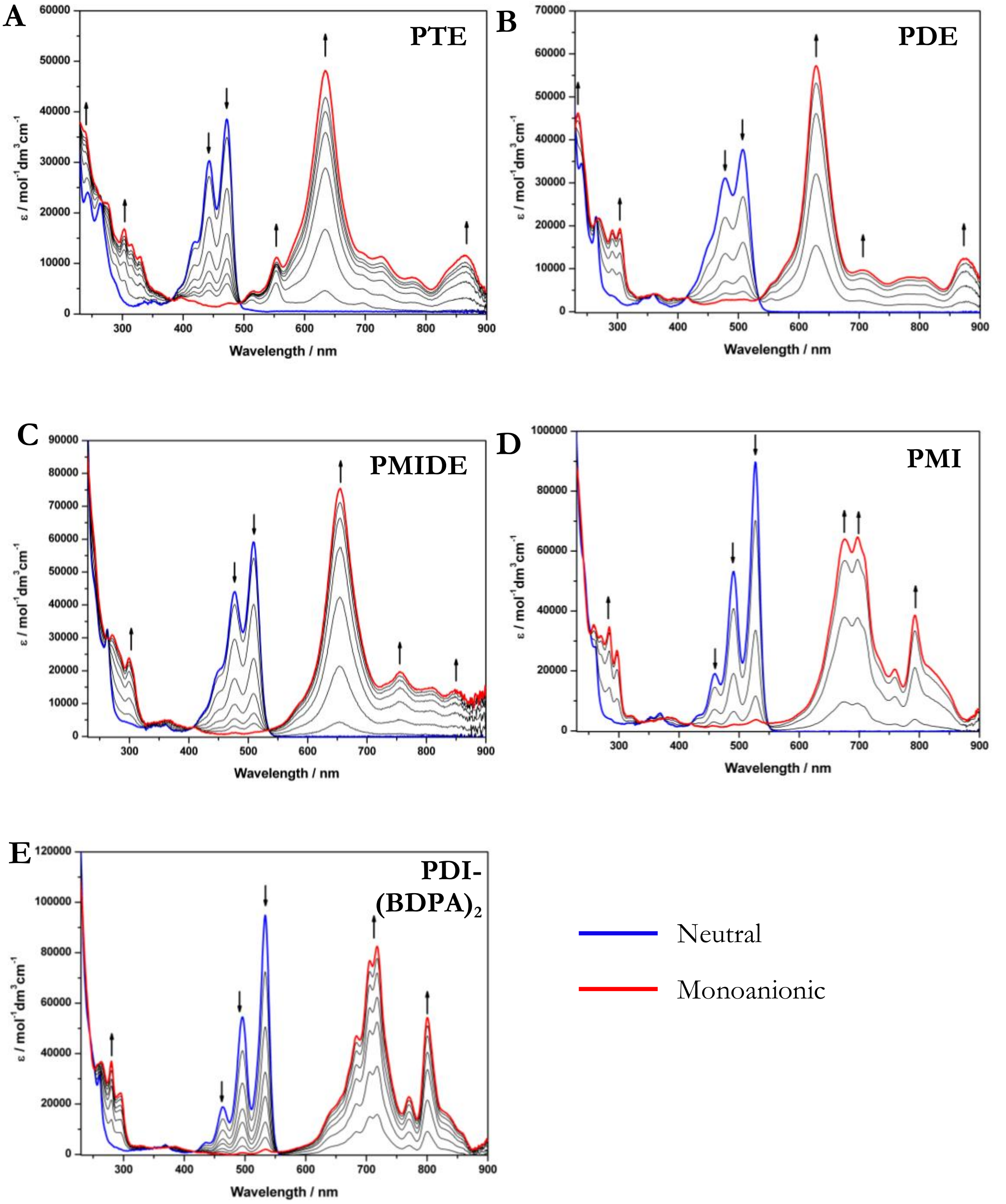

Figure 4.11: UV/vis absorption spectra showing the interconversion from neutral (blue) to monoanionic (red) species for a series of perylene tetracarboxylic compounds, arrows indicate the progress of the reduction. Spectra were recorded in dichloromethane containing [^{n}Bu$_4$N][BF$_4$] (0.4 M) as the supporting electrolyte at 273 K. A: PTE, B: PDE, C: PMIDE, D: PMI, E: PDI-(BDPA)$_2$.

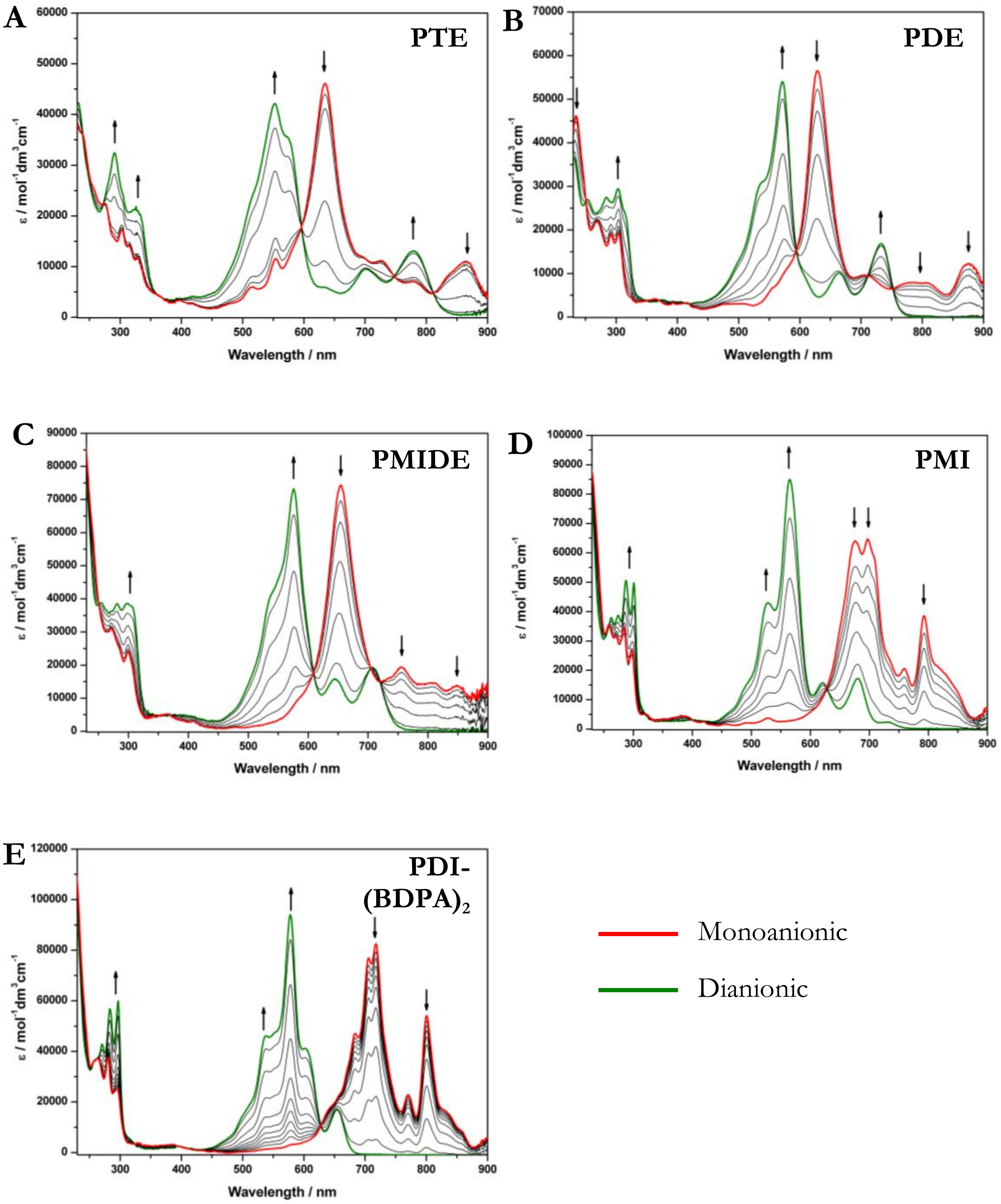

Figure 4.12: UV/vis absorption spectra showing the interconversion from monoanionic (red) to dianionic (green) species for a series of perylene tetracarboxylic compounds, arrows indicate the progress of the reduction. Spectra were recorded in dichloromethane containing [^{n}Bu$_4$N][BF$_4$] (0.4 M) as the supporting electrolyte at 273 K. A: PTE, B: PDE, C: PMIDE, D: PMI, E: PDI-(BDPA)$_2$.

The two compounds displaying oxidation processes within the solvent window of dichloromethane, **PTE** and **PMIDE** were also probed using spectroelectrochemical techniques (Figure 4.13). Both compounds' initial set of absorbance bands were largely (but not completely) diminished upon oxidation and a new, unstructured band emerged at a similar position to the compounds' dianionic counterparts. An additional, much weaker band an extra ~220 nm greater in wavelength than the principal band also formed in the near infrared spectral region. In the case of **PMIDE**, the spectrum corresponding to the neutral species was not completely regenerated following oxidation, likely due to the extreme potential of +1.15 V (vs Fc^+/Fc) required to oxidise the compound also leading to partial solvent decomposition.

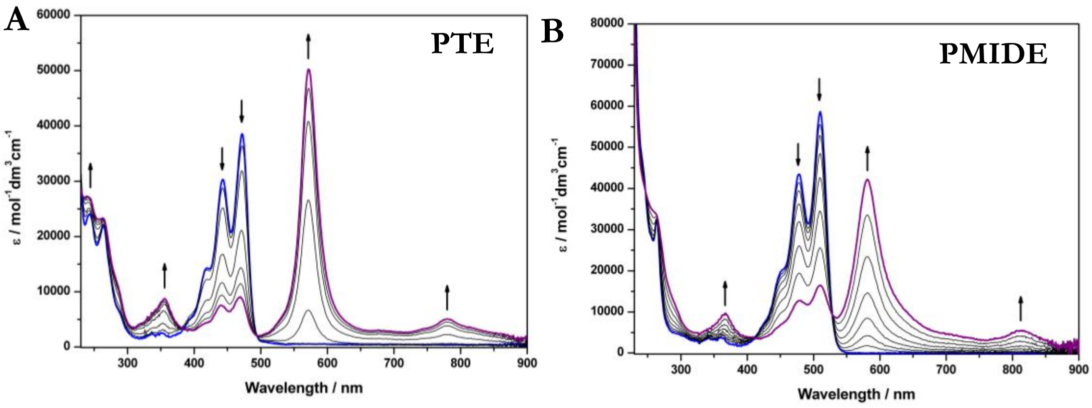

Figure 4.13: UV/vis absorption spectra showing the interconversion from neutral (blue) to monocationic (purple) species for A: PTE and B: PMIDE, arrows indicate the progress of the oxidation. Spectra were recorded in dichloromethane containing $[^nBu_4N][BF_4]$ (0.4 M) as the supporting electrolyte at 273 K.

The optical absorbance data recorded for the complete series of tetracarboxylic perylene compounds and **NDI-(BDPA)$_2$** are summarised below (Table 4.2).

Table 4.2: Summary of optical spectroscopy for the tetracarboxylic perylene compounds and NDI-(BDPA)$_2$.

Compound	λ_{max} / nm (ε / 10^3 mol^{-1}dm^{3}cm^{-1})			
	Neutral	**Monoanionic**	**Dianionic**	**Monocationic**
PTE	471 (38.6), 443 (30.3), 419 (14.3), 264 (21.9), 243 (24.1)	866 (11.1), 7.27 (11.2), 635 (46.1), 554 (11.5), 303 (17.3)	778 (13.1), 701 (9.5), 553 (42.2), 328 (21.5), 291 (32.4), 232 (42.3)	780 (5.0), 571 (50.3), 469 (9.1), 440 (7.6), 356 (8.8), 240 (27.3)
PDE	507 (37.8), 478 (31.1), 360 (4.2), 265 (22.2), 240 (34.6)	876 (12.5), 706 (9.7), 629 (57.3), 304 (19.4), 292 (19.0), 269 (21.8), 235 (46.2)	733 (16.9), 664 (10.1), 572 (54.0), 303 (29.5), 284 (27.5), 253 (27.0)	
PMIDE	509 (59.3), 477 (44.0), 263 (32.6)	847 (14.1), 755 (19.8), 655 (75.7), 300 (23.9), 272 (31.0)	707 (19.4), 645 (15.8), 576 (73.4), 298 (38.8), 281 (38.6), 256 (38.8)	811 (5.6), 581 (42.4), 510 (16.7), 478 (12.7), 367 (9.9)
PMI	527 (89.7), 491 (53.2), 460 (19.1), 369 (6.0)	793 (38.6), 759 (20.6), 697 (64.7), 676 (64.0), 284 (34.6), 258 (35.6)	680 (17.3), 621 (15.8), 565 (85.0), 528 (43.0), 301 (49.8), 288 (50.6)	
PDI-(BDPA)$_2$	533 (94.8), 496 (54.6), 463 (18.9), 261 (31.7)	800 (54.5), 770 (23.1), 717 (82.6), 705 (76.9), 684 (47.1), 280 (37.1), 263 (36.8)	654 (17.0), 578 (94.3), 537 (46.3), 297 (60.1), 283 (56.9), 270 (42.9)	
NDI-(BDPA)$_2$	386 (16.9), 366 (16.9)	783 (4.6), 703 (2.3), 612 (8.3), 537 (10.3), 484 (28.7), 271 (17.6)	623 (13.2), 573 (7.2), 530 (2.1), 427 (25.2), 249 (39.4)	

Obtained at an optically transparent electrode cell in dichloromethane, containing [^{n}Bu$_4$N][BF$_4$] (0.4 M) at 273 K, spectral range: 230 - 900 nm.

4.2.3.3. *Variable Temperature study of* ***PTE***

When recording the absorption spectrum for the spectroelectrochemical measurements of **PTE**, a significant change in the structure of the spectrum was noted upon cooling below 0 °C (Figure 4.14). The dominant 0→0 and 0→1 transitions are muted and a lower energy band emerges at 497 nm as the solution was cooled from 0 °C to -30 °C. This spectral change is consistent with aggregation of the molecules, and is very similar to results obtained for thin films of perylene-3,4,9,10-tetraesters investigated by Wang and co-workers.[46]

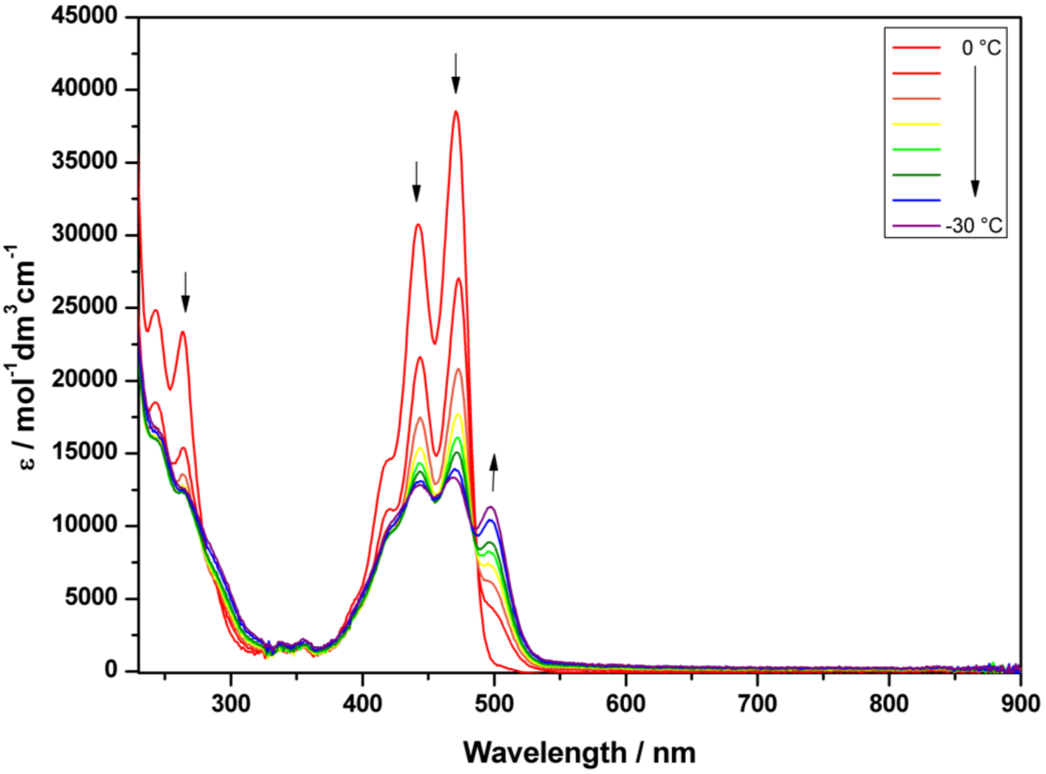

Figure 4.14: Variable temperature UV/vis absorption spectra of 222 µM PTE in dichloromethane. Arrows indicate the progress of the cooling.

PDIs tend to crystallise by π-π intermolecular stacking between neighbouring aromatic cores, accompanied by the development of a new absorption peak at ~570 nm.[47, 48] These data show that this new peak does not appear, implying that cooling does not promote π-π stacking, and instead the combination of aliphatic and aromatic fragments of **PTE** might cause microphase segregation instead.[49] Furthermore, Wang presented that films samples of perylene-3,4,9,10-tetraesters with ester chains four and eight carbons long could be cooled to form crystalline aggregates.[46] For a longer, twelve carbon ester chain, this did not occur; thin films were instead amorphous in structure. A cooled isotropic solution of their four-carbon perylene ester formed mesomorphic phase liquid crystals. **PTE** contains ten-carbon ester chains, midway between the crystalline octyl-ester perylene compound and the amorphous dodecyl-ester analogue. Careful tailoring of the alkylester chain can influence aggregate structure of perylene esters in thin films and help advance performance in optoelectronic devices.[46] Perhaps cooling the isotropic solution of **PTE** limits conformational freedom allowing otherwise supressed van der Waals interactions to govern molecular aggregation and packing.

4.2.4. Synthesis of a Multichromophoric PDI Dimer

To continue the synthesis of asymmetric PDIs, perylene monoimide monoanhydride **PMI** was furnished with a benzoic acid imide group, under the usual imidization conditions to produce **PDI-COOH** (Scheme 4.8). A carboxylic acid functional group was selected for its ability to form both strong covalent linkages as esters or amides, as well as its ability to form coordination bonds with many metal centres adopting interesting three-dimensional geometries, allowing for the possibility of studying soluble PDI coordination complexes. **PDI-COOH** could be readily purified by silica gel column chromatography; the polar carboxylic acid group adhered the molecules to the silica stationary phase, allowing impurities to be easily washed away with the mobile phase. The addition of a low concentration of trifluoroacetic acid to the mobile phase then allowed for elution of **PDI-COOH**.

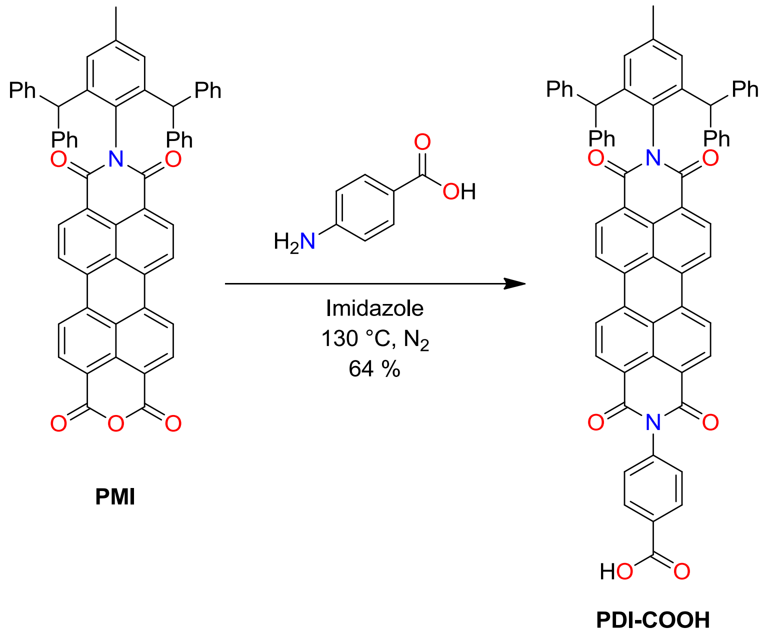

Scheme 4.8: Synthesis of PDI-COOH.

Single crystals of **PDI-COOH** were grown by vapour diffusion of hexane into a chloroform solution of the compound, and analysed by X-ray diffractometry, crystallising in the *P*-1 space group (Figure 4.15). Currently there are no crystal structures of *N*,*N*'-asymmetrically disubstituted PDIs in the literature: the majority of published asymmetric PDIs employ long, branched aliphatic chains that do not facilitate crystallisation.

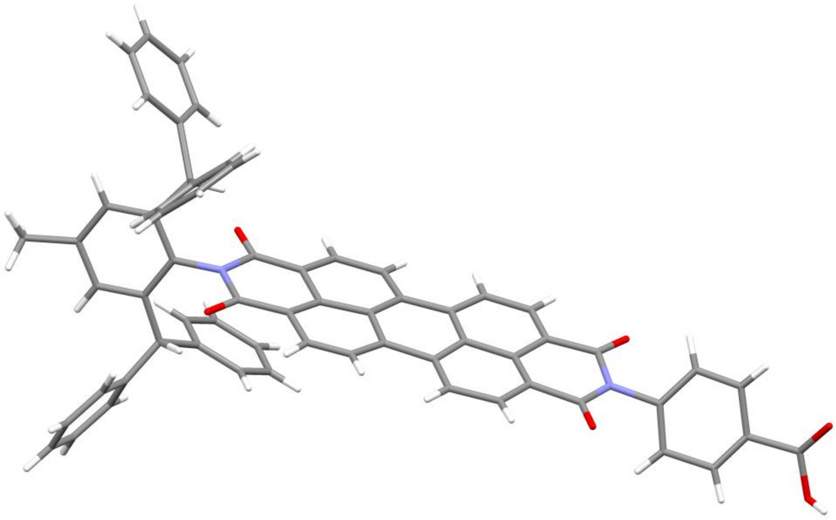

Figure 4.15: Single crystal structure of PDI-COOH. Atom colours - C: grey, O: red, N: blue and H: white.

Similarly to **PMI** (see above), the molecules of **PDI-COOH** pack in antiparallel pairs, with a separation between the perylene cores of 3.50 Å (Figure 4.16). Each pair of molecules is separated from their neighbours by the aromatic rings of the bis(diphenylmethyl-4-methylphenyl) imide group. The carboxylic acid groups at the other imide terminal form intermolecular hydrogen bonded dimers with other **PDI-COOH** molecules, at a typical hydrogen bond donor-acceptor distance of 2.62 Å, and donor-hydrogen-acceptor angle of 164°.

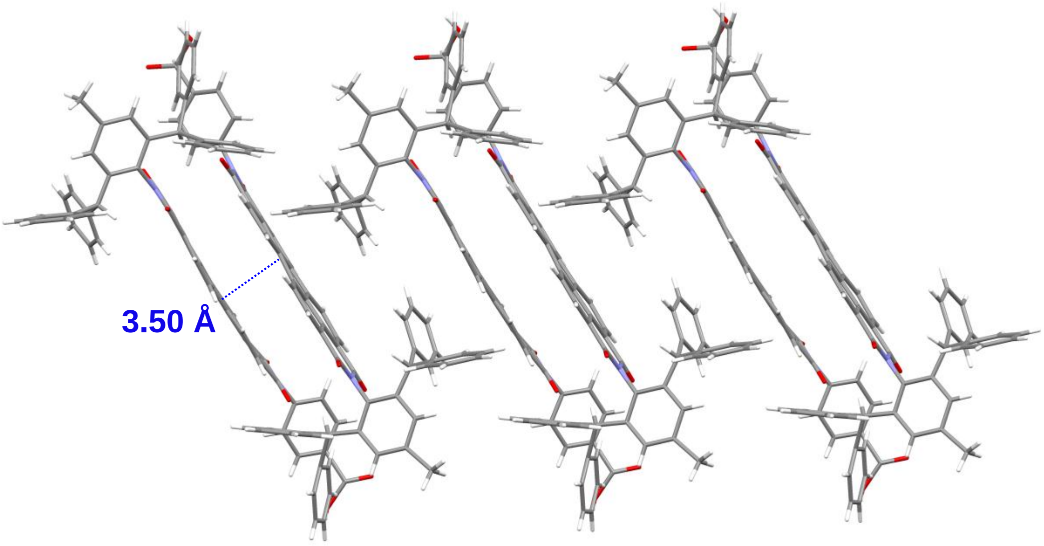

Figure 4.16: Packing motif of PDI-COOH molecules in a single crystal, displaying cofacial pairing. Atom colours - C: grey, O: red, N: blue and H: white. Distance between centres of perylene cores marked.

Two molecules of **PDI-COOH** were combined with a rigid 1,4-benzenedimethanol bridge employing the general method for an *N*,*N*-dicyclohexylcarbodiimide catalysed esterification published by Steglich[50] to produce one molecule of **PDI Dimer** (Figure 4.17). Normally the alcohol species should be present in excess, though this would favour production of a mono-esterified **PDI-COOH** rather than the dimer, hence a 1:1 acid: alcohol stoichiometry was chosen for the coupling reaction, affording the desired product in 25 % yield. **PDI Dimer** was sufficiently soluble for complete electrochemical characterisation.

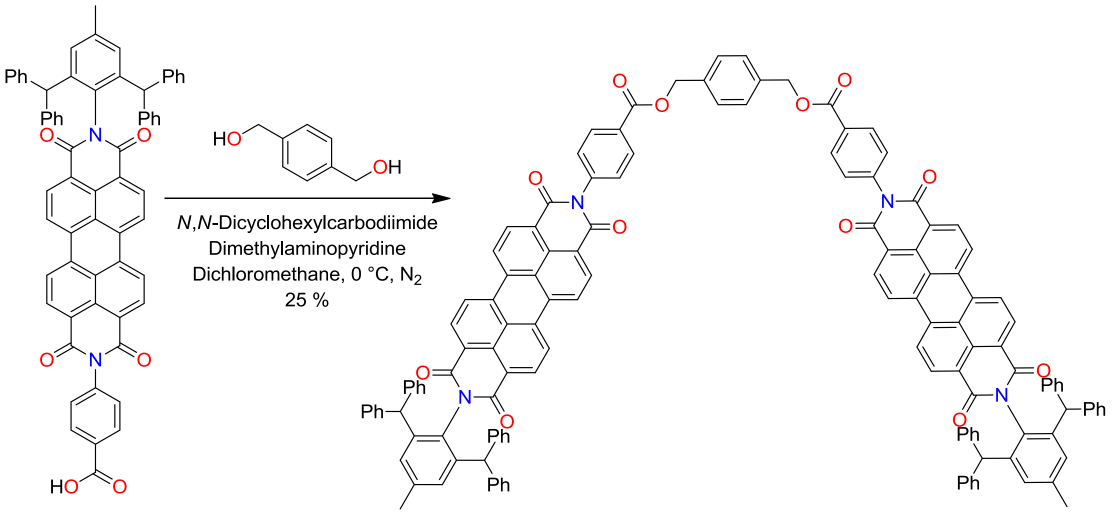

PDI-COOH **PDI Dimer**

Figure 4.17: Synthesis of PDI Dimer.

4.2.4.1. *Electrochemistry of **PDI Dimer***

Cyclic voltammograms of **PDI-COOH** and **PDI Dimer** both display two reversible reductions and no oxidation processes (Figure 4.18), typical for PDI compounds (see above). For both compounds the reductions occur at identical potentials of -0.95 V and -1.17 V (vs. Fc^+/Fc), though in the case of **PDI Dimer**, coulometry confirmed that these were two-electron reductions. Since only two reduction processes are detected for **PDI Dimer**, this would suggest that the two PDI chromophores do not communicate across their connected imide region: the electronic configuration of one PDI subunit does not affect the other.

EPR spectroscopy was used to investigate further, since the addition of two electrons to **PDI Dimer** has the potential to form spin s = 0, ½ or 1 systems. Communication between the radicals would form either the s = 0 singlet state, which would be EPR silent; or an s = 1 triplet state that would also be readily observable with EPR spectroscopy: an s = 1 state would be EPR silent in fluid solution, but detectable as a frozen solution. A lack of any communication between the radical electrons would form a 2 x s = ½ system, resembling that of monomeric PDIs.

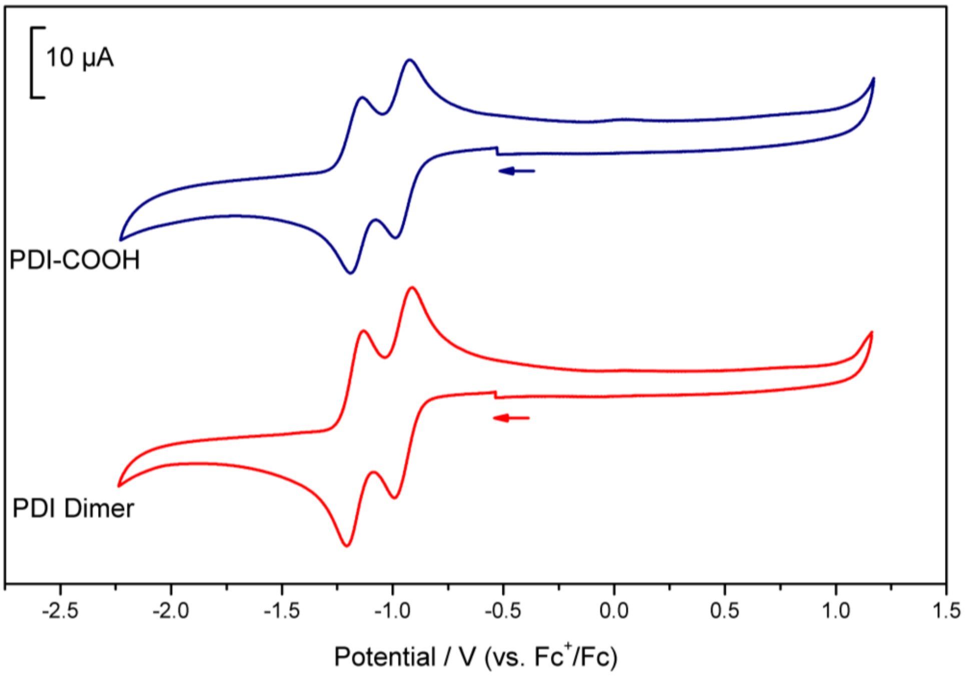

Figure 4.18: Cyclic voltammograms of PDI-COOH (blue) and PDI Dimer (red) in dichloromethane containing 0.4 M [^{n}Bu$_4$N][BF$_4$] as the supporting electrolyte, with a scan rate of 100 mVs^{-1}.

The dianion of **PDI Dimer** was electrogenerated in dichloromethane containing 0.4 M [^{n}Bu$_4$N][BF$_4$] as the supporting electrolyte and the EPR spectrum of [**PDI Dimer**]$^{2-}$ was recorded (Figure 4.19). The spectrum resembles that of an s = ½ system, exhibiting some hyperfine coupling that could not be fully resolved. A g_{iso} value of 2.0034 was measured. From this result it appears that the two perylene centres do not significantly interact with one another, most likely because the linker that separates them is rigid enough to prevent intramolecular stacking and connects the two subunits at an orbital node.

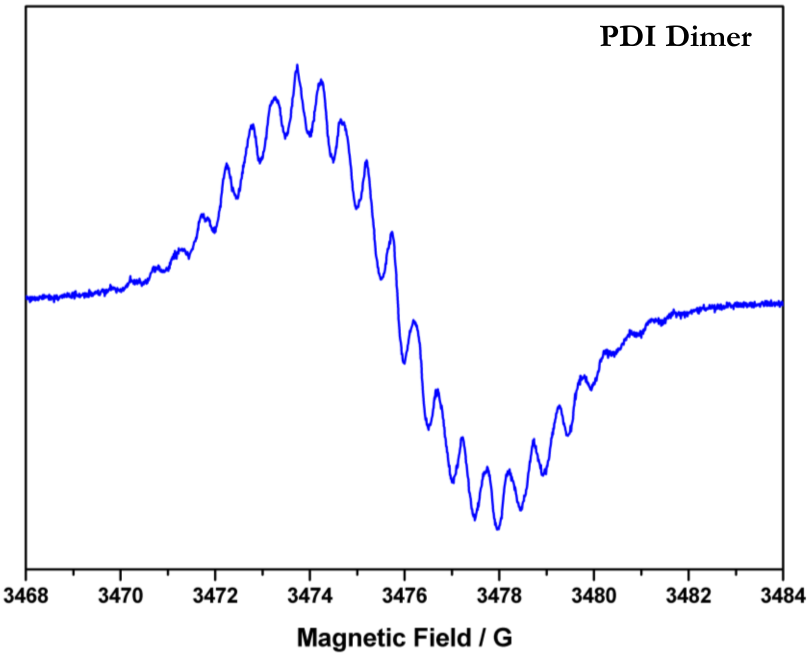

Figure 4.19: Experimentally measured EPR spectrum of [PDI Dimer]$^{2-}$.

The optical properties of the dimer arrangement are almost identical to that of the monomeric **PDI-(BDPA)$_2$**: a strong characteristic S_0 to S_1 electronic transition displaying 0→0, 0→1 and 0→2 vibronic progression is seen for the neutral molecule, becoming replaced with bands at lower energy upon reduction to [**PDI Dimer**]$^{2-}$. Further reduction to [**PDI Dimer**]$^{4-}$ also proceeds as for the symmetrical **PDI-(BDPA)$_2$** with an intense band forming at 576 nm (Figure 4.20). The molar extinction coefficient is twice as great for the **PDI Dimer** species as for the corresponding **PDI-(BDPA)$_2$** species. At λ_{max} for the neutral molecules ε = 179,800 mol^{-1}dm^{3}cm^{-1} for **PDI Dimer** and ε = 94,800 mol^{-1}dm^{3}cm^{-1} for **PDI-(BDPA)$_2$**. A comparable trend is seen for the first and second reduced species.

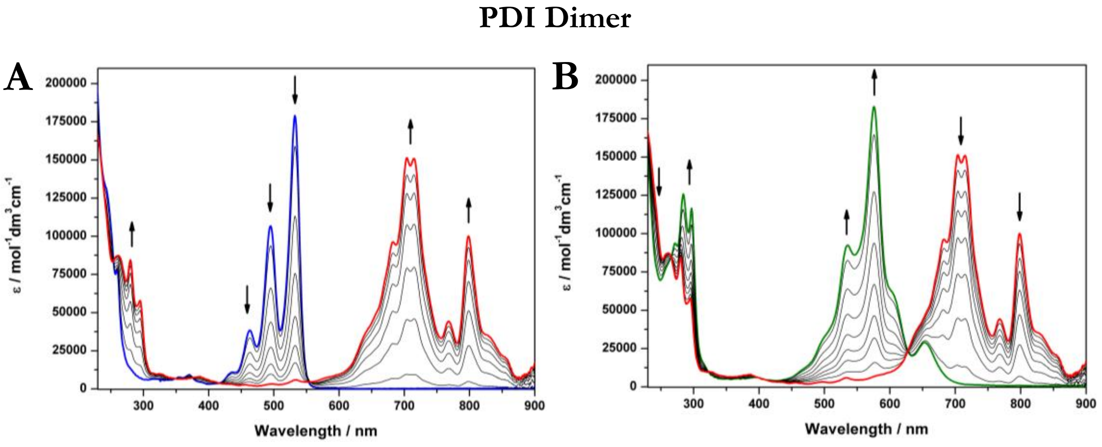

Figure 4.20: UV/vis absorption spectra showing the inter-conversion between the various charge states of PDI Dimer, arrows indicate the progress of the reductions. A: from neutral (blue) to dianionic (red), B: from dianionic (red) to tetranionic (green) species. Spectra were recorded in dichloromethane containing [^{n}Bu$_4$N][BF$_4$] (0.4 M) as the supporting electrolyte at 273 K.

Overall, despite the covalent linkage uniting two PDI chromophores, **PDI Dimer** performs analogously to monomeric PDIs, and no communication between the two subunits occurs. Whilst no great enhancement in physical properties was observed for **PDI Dimer**, the covalent linkage of the two PDI cores might augment the chemical properties: a rigid spacer was used to connect the two imide termini by ester bonds, placing 8 oxygen atoms in close proximity. This arrangement of electron-dense oxygen atoms could function as a binding pocket for metal complexes and hydrogen bond donors; allowing a purposely-engineered molecule to bind and occupy the space between the two tethered PDI cores, perhaps extracting the charge generated on each core following reduction.

4.2.5. PDI-Adenine Hydrogen Bonding

4.2.5.1. *Hydrogen Bonding in PDIs*

Substitution with just a hydrogen atom at the imide group forms a region on the PDI unit with a hydrogen bond acceptor-donor-acceptor pattern. Supramolecular chemists have taken advantage of imide-hydrogen bonding interactions to promote self-assembly along the imide axis of the PDI units, rather than utilising the π-aggregation properties of the molecules.[51, 52] Melamine and its derivatives are of particular importance to chemists studying hydrogen-bonding using PDIs because they have a complementary (donor-acceptor-donor) hydrogen-bonding pattern to PDIs, enabling the formation of three intermolecular hydrogen bonds between one imide terminus of PDI and a melamine molecule.

This multiple hydrogen bonding interaction was first investigated in 1995 for NDIs and amphiphilic melamines by Kimizuka et al.[53] who observed the formation of fibrous superstructures in nonpolar solvents. Shortly afterwards Würthner and co-workers explored the complexation between PDI derivatives and amphipathic and ditopic melamines, including investigations into the hierarchical organisation of these hydrogen bonded species (Figure 4.21).[54-56] The PDIs were substituted with large aromatic groups at the four bay positions to limit any π-aggregation, allowing the primary intermolecular bonding to be between the PDIs and the melamine derivatives. A mixture of NMR, UV/vis and fluorescence spectroscopy was used to measure the binding constants of the PDIs with melamine in a variety of solvents. In $CDCl_3$, the binding constant (*K*) for the interaction pictured below (Figure 4.21) was 240 M^{-1}, increasing to ~90,000 M^{-1} in n-hexane, the decrease in solvent polarity favouring hydrogen bond formation.[54, 55]

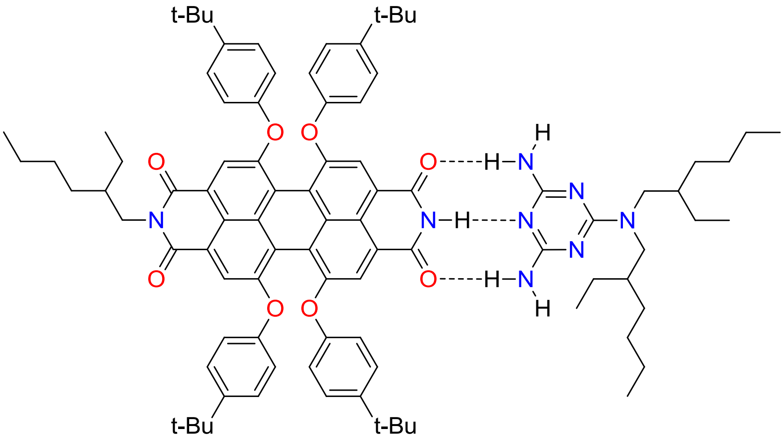

Figure 4.21: Complementary hydrogen bonding between a PDI molecule and a melamine derivative reported by Würthner et al.[54] Hydrogen bonds represented as dashed lines.

The use of ditopic melamine derivatives, able to form complementary hydrogen bonds with two PDI molecules leads to the formation of some interesting structures: on a highly-oriented pyrolytic graphite surface, Hoeben et al.[57] detected the formation of 12-membered rosettes, between 6 PDI and 6 ditopic melamines furnished with oligo(*p*-phenylenevinylene) chains. A similar, azobenzene-equipped ditopic melamine derivative formed tubular nanostructures in a 1:2 PDI: azobenzene-melamine ratio.[58] Unsubstituted PDI and melamine have also been co-adsorbed on an Ag/Si(111) surface, forming a two-dimensional honeycomb network, with a melamine molecule resting at the vertex of each hexagonal pore, triple hydrogen bonded to a PDI molecule forming the edge of each pore.[51] Each pore could accommodate a heptameric cluster of C_{60}, excellently demonstrating how controlled self-assembly can be used to organise a complex mixture of components in a precise manner. To overcome the need to mix components of these assemblies in an exact stoichiometry, Wasielewski and co-workers[59] designed a self-complementary PDI with a di(tridodecyloxyphenyl)-melamine imide group that self-aggregated into tubular nanostructures. Efficient electron transfer between the tridodecyloxyphenyl donor imide group and the PDI acceptor occurred as a direct consequence of these complementary hydrogen bonding interactions.

4.2.5.2. *Hydrogen Bonding Study of PDI to Adenine*

Given that imide-substitution with the BDPA tecton was able to solubilise **PMI**, a perylene monoimide monoanhydride, it was reasoned that solubility would be retained even if the anhydride group was converted to a simple imide, containing only a hydrogen atom. A soluble PDI capable of forming hydrogen bonds as described above would allow for solution phase analysis of the hydrogen bonding interactions and be useful in the construction of complicated supramolecular systems by providing a binding site that other molecular components can be specifically designed to target. Thus, **PMI** was used as a precursor to synthesise **PDI-NH**, by reacting **PMI** with aqueous ammonia under reflux (Scheme 4.9). The product could be readily separated by column chromatography, the imide ring of the product providing a different polarity to the anhydride precursor.

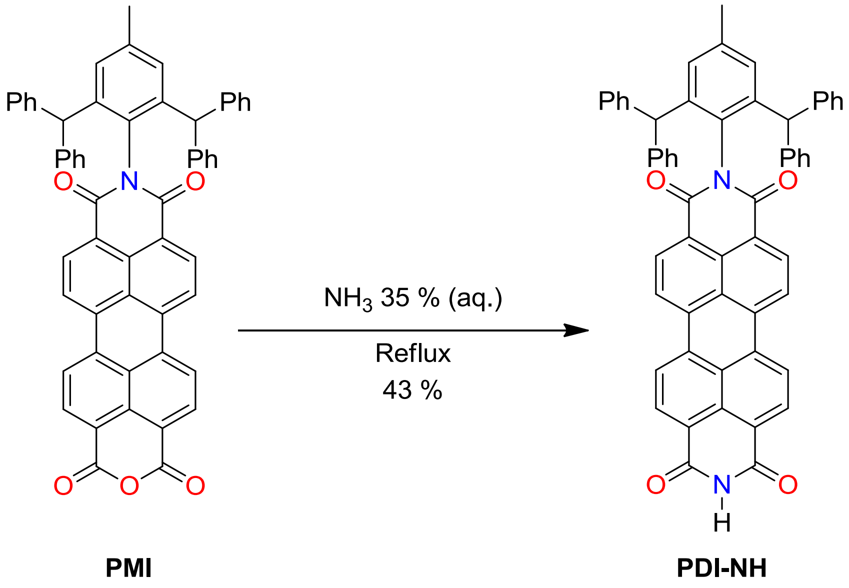

Scheme 4.9: Synthesis of PDI-NH.

As mentioned in Chapter 1, the imide region of PDIs resembles the nucleobases thymine and uracil found in the genetic material of many biological systems (Figure 4.22A), suggesting that hydrogen bonding should occur with adenine (the complementary nucleobase), mimicking the base-pairing found in DNA and RNA. Finding a biologically active molecule that would form specific interactions with a PDI dye would be interesting, and offers an advantage over the well-studied melamine interaction.

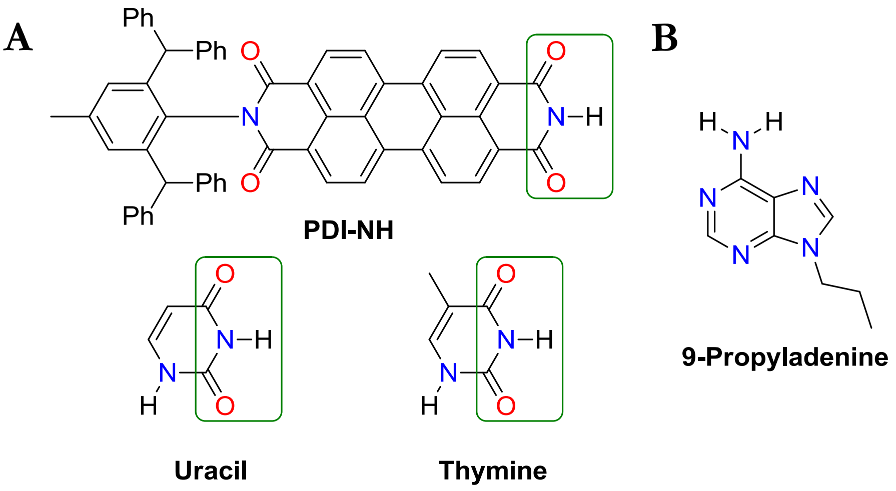

Figure 4.22: A: Structures of PDI-NH, Thymine and Uracil highlighting the analogous hydrogen bonding regions of each molecule. B: Structure of 9-propyladenine.

An NMR titration experiment was undertaken to assess the binding strength of the interaction between **PDI-NH** and a simple adenine derivative, 9-propyladenine (structure shown in Figure 4.22B) in deuterated chloroform solution.[60, 61] Initially, the possibility of self-association was considered; intermolecular hydrogen bonds between the imide region of PDI have been observed on a surface with scanning tunnelling microscopy.[62] The effect of concentration of **PDI-NH** on the position of the N-H chemical shift as measured by ^{1}H NMR spectroscopy was used to determine the self-dimerisation binding strength. The self-association binding constant for **PDI-NH** was measured at $K_{\mathrm{d}} = 3.3\ \mathrm{M}^{-1}$, following an NMR dilution experiment (Figure 4.23). The self-association constant for 9-propyladenine has been previously reported at $K_{\mathrm{d}} = 2.8 \pm 1.7\ \mathrm{M}^{-1}$.[63]

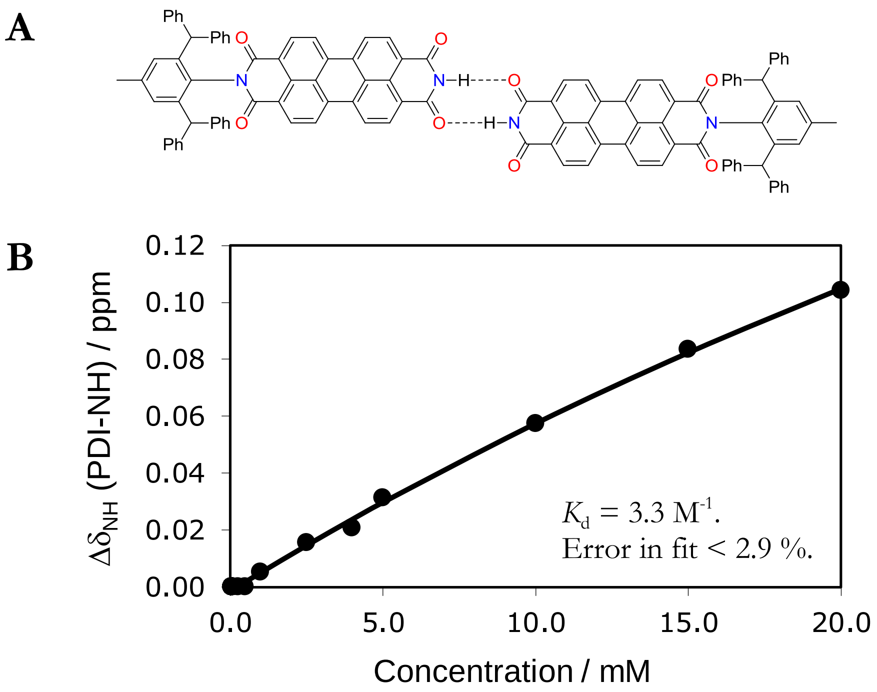

Figure 4.23: A: Structure of the self-associated dimer of PDI-NH. B: The effect of concentration on the N-H chemical shift (δ_{NH}) of PDI-NH.

In both instances, the self-association constants are small (< 5 M^{-1}). Whilst keeping the concentration of **PDI-NH** constant, the concentration of 9-propyladenine was gradually increased, recording the ^{1}H NMR spectrum after each addition of 9-propyladenine. The position of the N-H chemical shift of **PDI-NH** (δ_{NH}) was used to assess binding. Without any 9-propyladenine present, the position of this peak was at δ_{NH} = 8.53 ppm, shifting downfield in response to the addition of 9-propyladenine. At [9-propyladenine] = 51 mM, δ_{NH} = 12.44 ppm, representing a significant downfield shift as a consequence of the hydrogen bonding interaction (Figure 4.24).

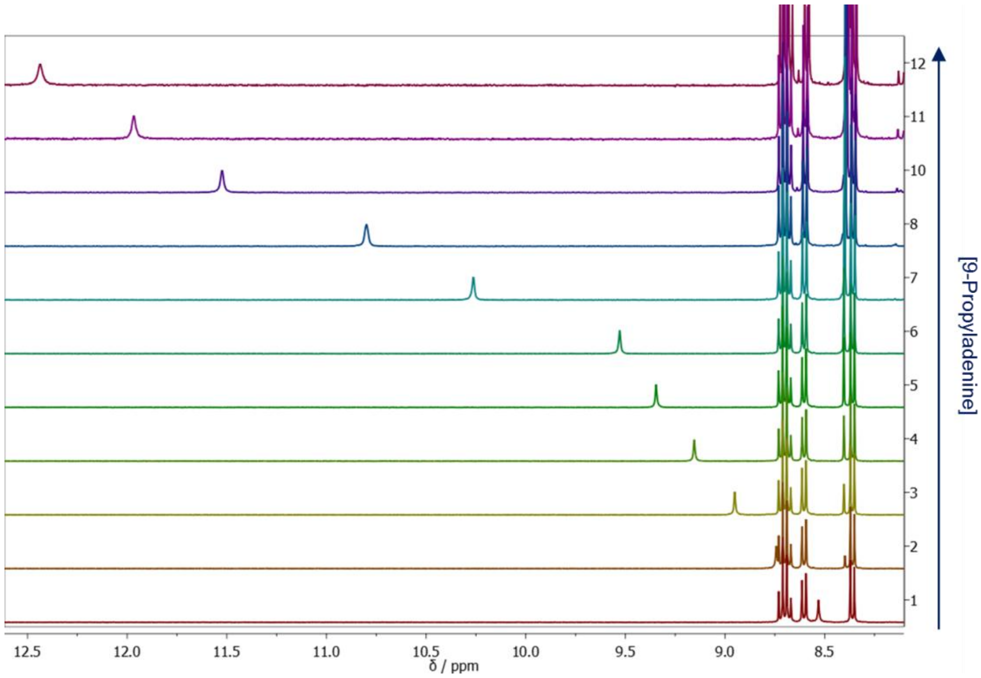

Figure 4.24: ^{1}H NMR spectra illustrating the change in δ_{NH} for PDI-NH during the titration of PDI-NH with 9-propyladenine. Spectrum 1 corresponds to pure PDI-NH, spectra 2 to 12 are recorded with [PDI-NH] = 4 mM and an increasing [9-propyladenine] from 1 to 51 mM.

The results of the NMR titration show the interaction between **PDI-NH** and 9-propyladenine is more favourable than self-association, with $K = 54.9$ M^{-1}, one order of magnitude greater than for each of the self-association constants (Figure 4.25). Although smaller than the PDI: melamine binding constant (240 M^{-1}),[55] only two hydrogen bonds are involved instead of the three for PDI: melamine, so the binding constant can be expected to be lower. An additional experiment was used to determine binding stoichiometry, whereby the concentrations of both **PDI-NH** and 9-propyladenine were varied. Following Job's method, a plot of mole fraction of **PDI-NH** against the product of the change in chemical shift of the N-H proton (relative to the shift in the absence of 9-propyladenine) and the mole fraction of **PDI-NH** show a peak at a mole fraction of 0.5, indicating that binding occurs in a 1:1 ratio (Figure 4.26).[64]

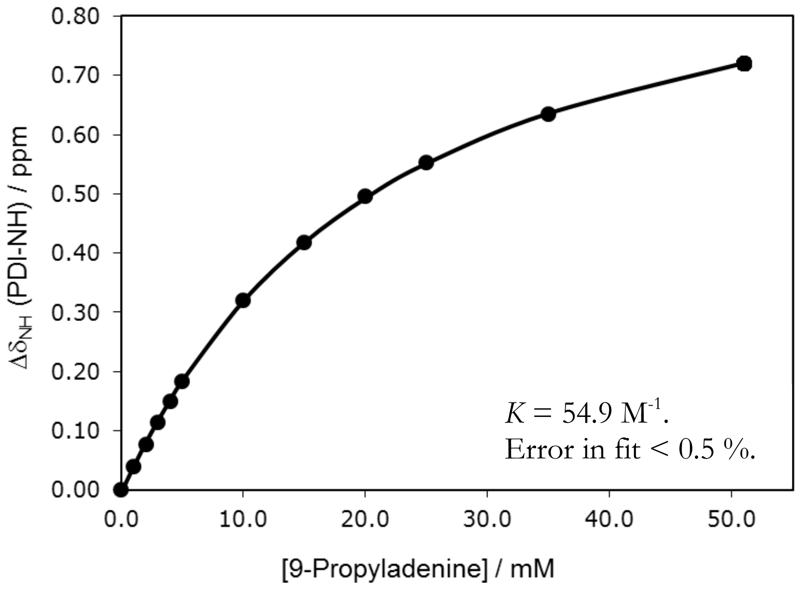

Figure 4.25: The effect of 9-propyladenine concentration on the position of δ_{NH} for PDI-NH at a constant concentration of PDI-NH.

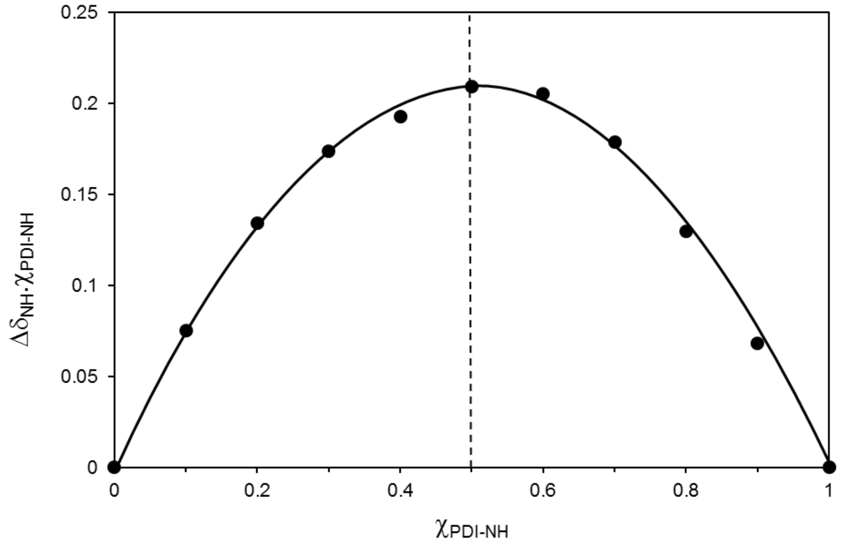

Figure 4.26: Job's Plot corresponding to the binary 1:1 combination of PDI-NH and 9-propyladenine.

Furthermore, the NMR studies indicate that the hydrogen bonding pattern between **PDI-NH** and 9-propyladenine adopts both Watson-Crick and Hoogsteen modes (Figure 4.27). 9-Propyladenine contains two aromatic hydrogen atoms: one located between the two nitrogen atoms on the six-membered ring (C2-H), and one between the two nitrogen atoms on the five-membered ring (C8-H). Watson-Crick binding requires the nitrogen atom hydrogen-bond acceptor on the six-membered ring, pulling electron density away from C2 (and C2-H) thus causing a downfield shift in the C2-H proton signal. Similarly, Hoogsteen binding requires the nitrogen atom adjacent to C8 as a hydrogen bond acceptor, so the C8-H signal will be shifted downfield in the presence of Hoogsteen bonding.

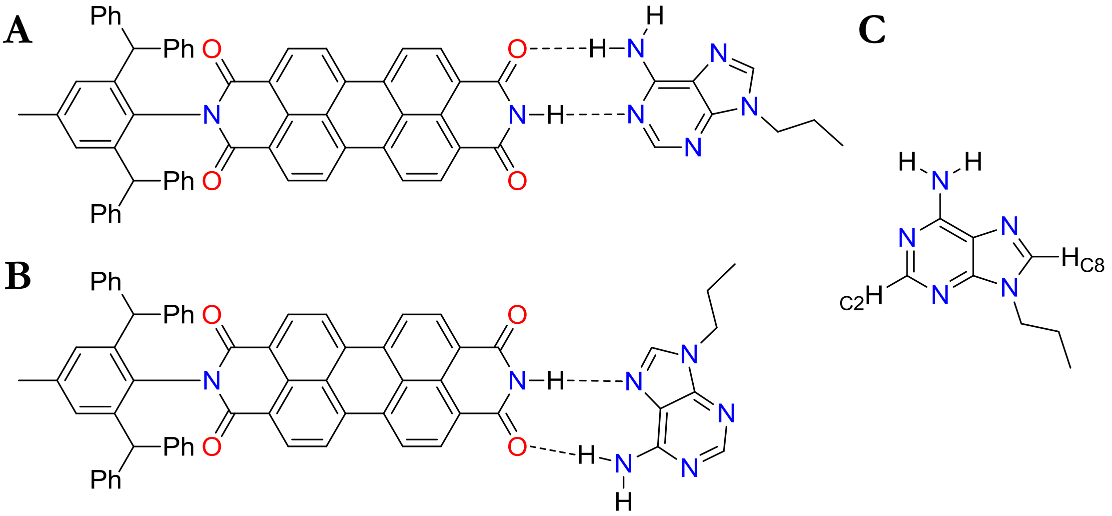

Figure 4.27: Structures of PDI-NH: 9-propyladenine binding modes. A: Watson-Crick, B: Hoogsteen. C: Numbering of 9-propyladenine aromatic protons.

A change in the position of both C2-H and C8-H protons is noted as the concentration of 9-propyladenine is increased, implying both Watson-Crick and Hoogsteen binding occur (Figure 4.28). This shift is upfield because as the concentration of 9-propyladenine increases, there are more free molecules not involved in binding to **PDI-NH**, so on average the protons become more shielded.

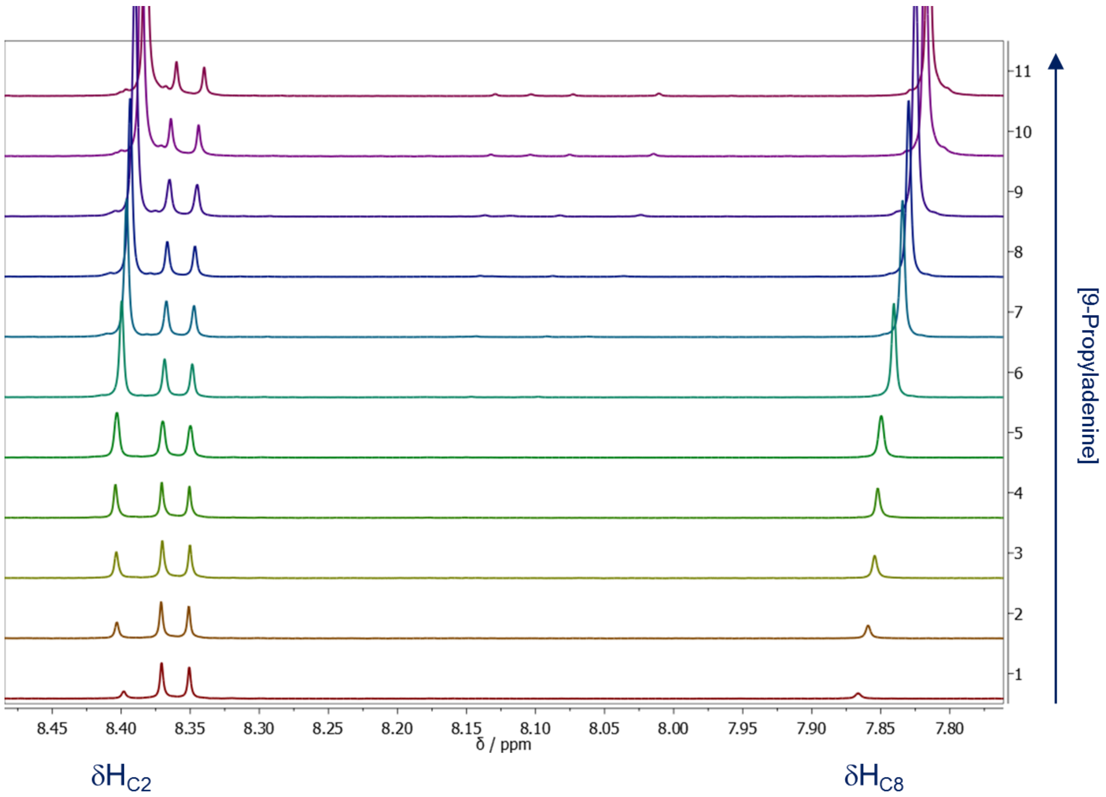

Figure 4.28: ^{1}H NMR spectra illustrating the shifts in the C2-H and C8-H proton signals of 9-propyladenine during the titration of PDI-NH and 9-propyladenine. Spectrum 1 contains 1 mM 9-propyladenine, increasing to 51 mM for spectrum 11. The concentration of PDI-NH was constant at 4 mM.

4.2.6. Thionated PDI Donor-Acceptor Systems

4.2.6.1. *Synthesis*

To supplement the results described for NDI donor-acceptor systems in Chapter 3, homologous phenothiazine-perylene diimide donor-acceptor systems were also fabricated, expanding the rylene core. Once again, **PMI** provided a suitable precursor to the PDI compound, affording **PDIS$_0$-PTZ** in good yield following the reaction with **PTZ-NH$_2$** (synthesis of **PTZ-NH$_2$** described in Chapter 3) (Scheme 4.10). Unlike for the NDI homologue **NDIS$_0$-PTZ**, which formed colourless solutions and blue solids, **PDIS$_0$-PTZ** does not noticeably change colour from solution to solid state and is the typically expected red-orange colour for PDI compounds. Unlike all PDIs so far described within this thesis, however, **PDIS$_0$-PTZ** is not fluorescent in solution, signifying that the presence of the phenothiazine chromophore is quenching this process (see below). Utilising the previously effective conditions, **PDIS$_0$-PTZ** was thionated with Lawesson's reagent to form a blue compound (Scheme 4.10), identified as **PDIS$_2$-PTZ** by a combination of mass spectrometry and NMR spectroscopy.

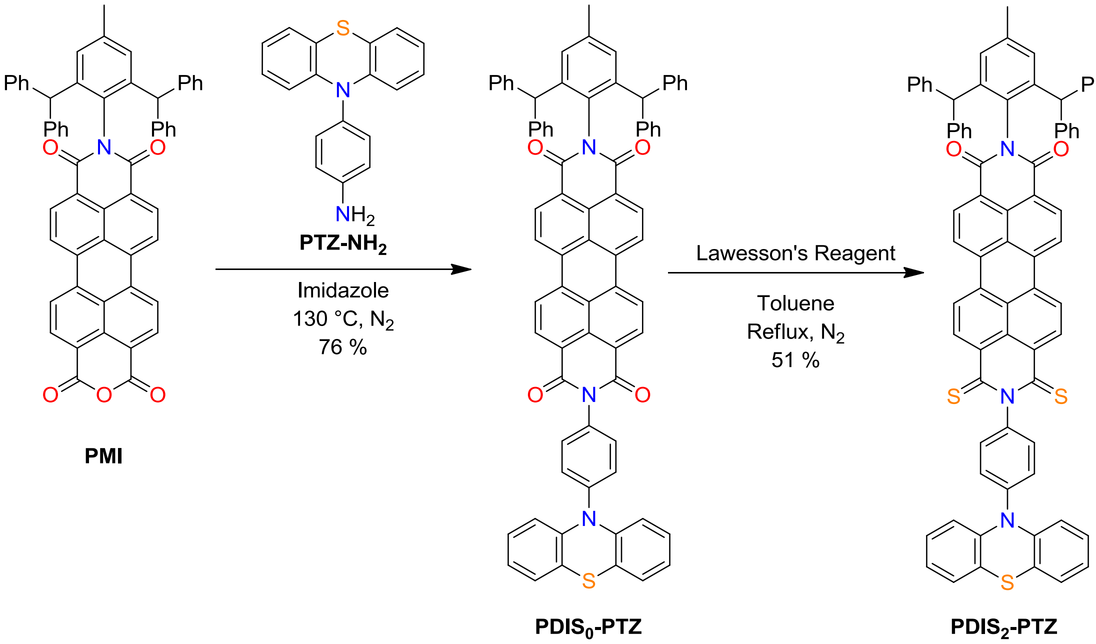

Scheme 4.10: Synthesis of PDI donor-acceptor systems PDIS$_0$-PTZ and PDIS$_2$-PTZ.

Mass spectrometry indicated the presence of two sulfur atoms, meaning the product could exist as one of four isomers. The ^{1}H NMR spectrum revealed four pairs of doublets for the aromatic protons of the perylene core (as was the case for the nonthionated **PDIS$_0$-PTZ**) and the ^{13}C NMR spectrum for **PDIS$_2$-PTZ** contained only one C=O and one C=S peak, discounting the possibility of cis- or trans- isomers. This means that both sulfur atoms on the isolated compound were contained within the same imide group, forming a perylene monoimide monothioimide compound. Although such geminate dithionated regioisomers have been reported in the literature for NDIs[65] and PDIs,[66] they were only formed in minuscule quantities and could not be isolated. Two geminately substituted isomers are possible, one with the thioimide located at the phenothiazine terminus, the other with the thioimide at the 2,6-bis(diphenylmethyl-4-

methylphenyl) end. The protons of the phenylene spacer between the perylene and phenothiazine chromophores are strongly affected by the thionation, splitting from a single peak corresponding to all four phenylene protons of **PDIS$_0$-PTZ** to two smaller multiplets for each pair of phenylene protons for **PDIS$_2$-PTZ**. No substantial shift was detected for protons of the 2,6-bis(diphenylmethyl-4-methylphenyl) group. Additionally the X-ray crystal structure (see below) of **PDIS$_2$-PTZ** confirms that the thionation occurs at the phenothiazine terminus. This is to be expected: the studies with NDIs and NIs in Chapter 3 indicate thionation can readily occur proximal to the phenothiazine-substituted imide region and steric effects from the large aromatic features at the other terminus would likely eradicate any chance of thionation occurring there. Moreover, only a single thionated product was obtained from the reaction, and in reasonable yield: the lower level of thionation, as well as regioselectivity greatly improve the viability of producing this thionated PDI when compared with the NDIs, where material was lost to different levels of thionation and structural isomerism.

4.2.6.2. *X-ray Crystallography*

Single crystals of both **PDIS$_0$-PTZ** and **PDIS$_2$-PTZ** were grown by vapour diffusion of pentane into a chloroform solution of the compound. Both molecules crystallised in the $P2_1/c$ space group with one molecule in the asymmetric unit (Figure 4.29).

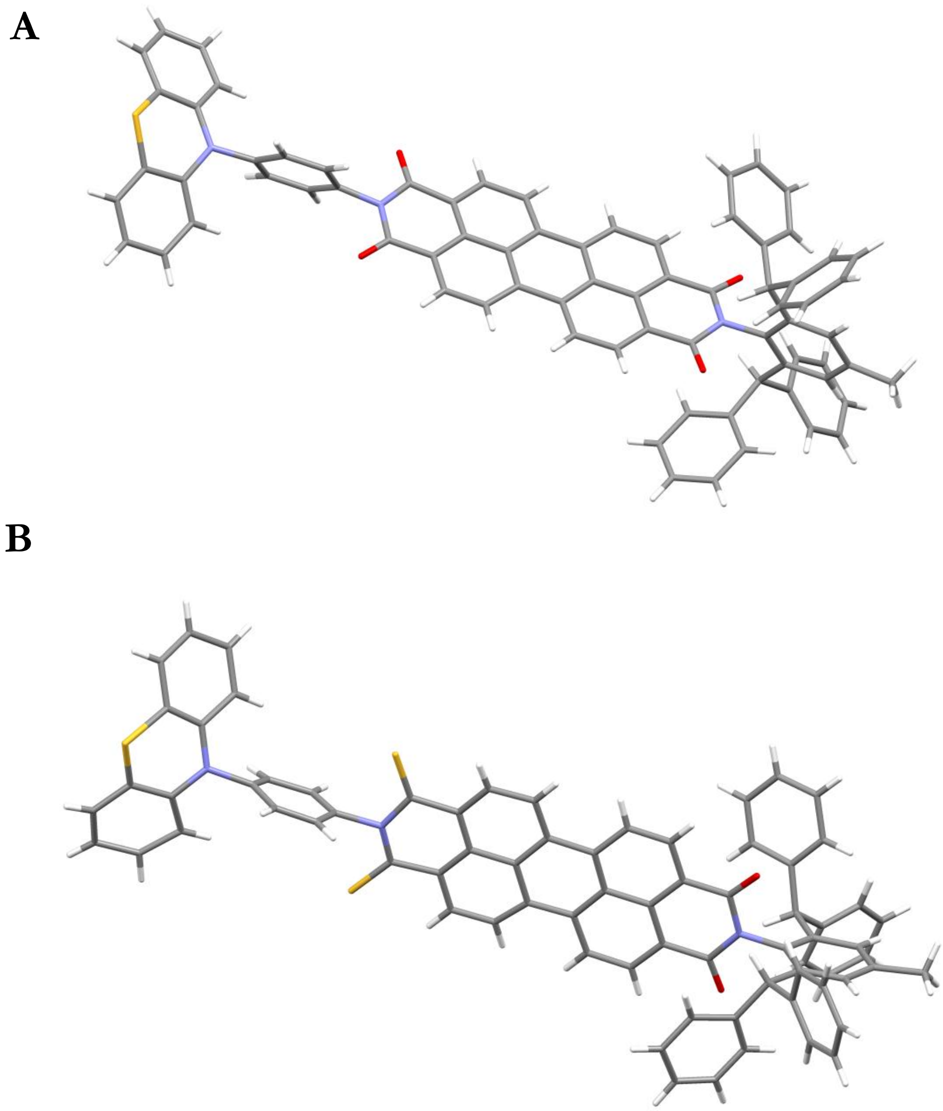

Figure 4.29: Single crystal structures of PDI-dyads. A: PDIS$_0$-PTZ, B: PDIS$_2$-PTZ. Atom colours - C: grey, O: red, N: blue, H: white and S: yellow.

The packing arrangement of both molecules is also similar. Along the screw axis, the molecules are organised such that the phenothiazine group of one molecule lies in close proximity to the perylene core of its neighbour (Figure 4.30). This proximity could perhaps facilitate electron transport in the solid state, allowing for electron or hole hopping between molecules.

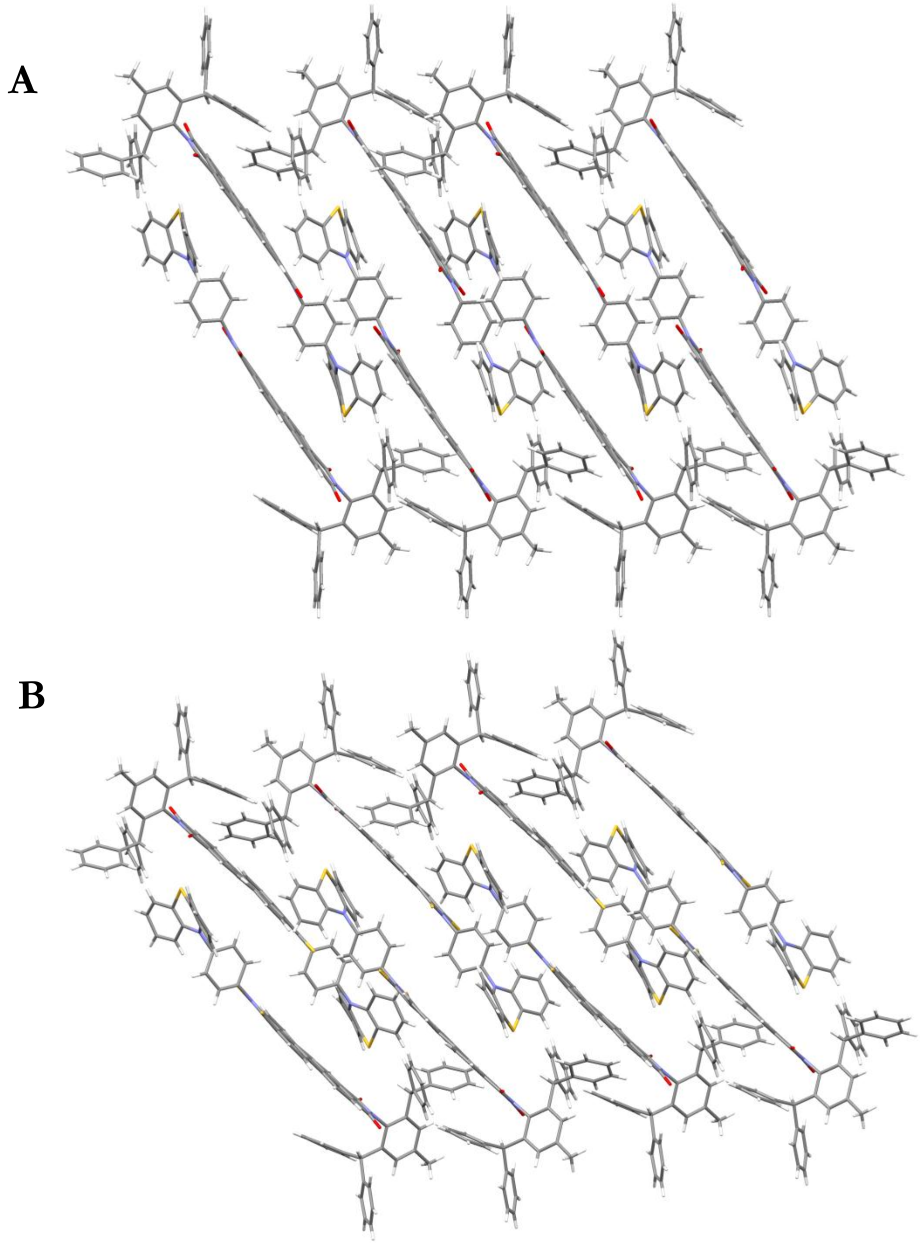

Figure 4.30: Single crystal structure packing motifs of PDI-dyads, viewed perpendicular to the crystallographic screw-axis. A: PDIS$_0$-PTZ, B: PDIS$_2$-PTZ. Atom colours - C: grey, O: red, N: blue, H: white and S: yellow.

4.2.6.3. *Cyclic Voltammetry*

Each PDI dyad was found to exhibit two reversible one electron reduction processes and one reversible one electron oxidation process, as was present for the NDI dyads. An additional oxidation process was also detected, but this was not found to be reversible under the experimental conditions (Figure 4.31). **PDIS$_0$-PTZ** was reduced at -0.94 and -1.16 V (vs. Fc^+/Fc), very similar potentials to **PDI-COOH**. As expected, an anodic shift in the reduction potentials occurred following thionation, with **PDIS$_2$-PTZ** becoming reduced at -0.68 and -0.93 V (vs. Fc$^+$/Fc). Although the thionation-induced increase in first reduction potential is a substantial 260 mV, the effect of thionation is less prominent for the PDI dyad systems than their NDI counterparts: the difference in first reduction potentials between **NDIS$_0$-PTZ** and the dithionated **NDIS$_2$ cis-PTZ** was 360 mV, almost 1.4 times greater than for the PDI dyads. As with the NDIs, thionation appears to lower the LUMO energy of the PDI moiety, improving its power as an electron acceptor.

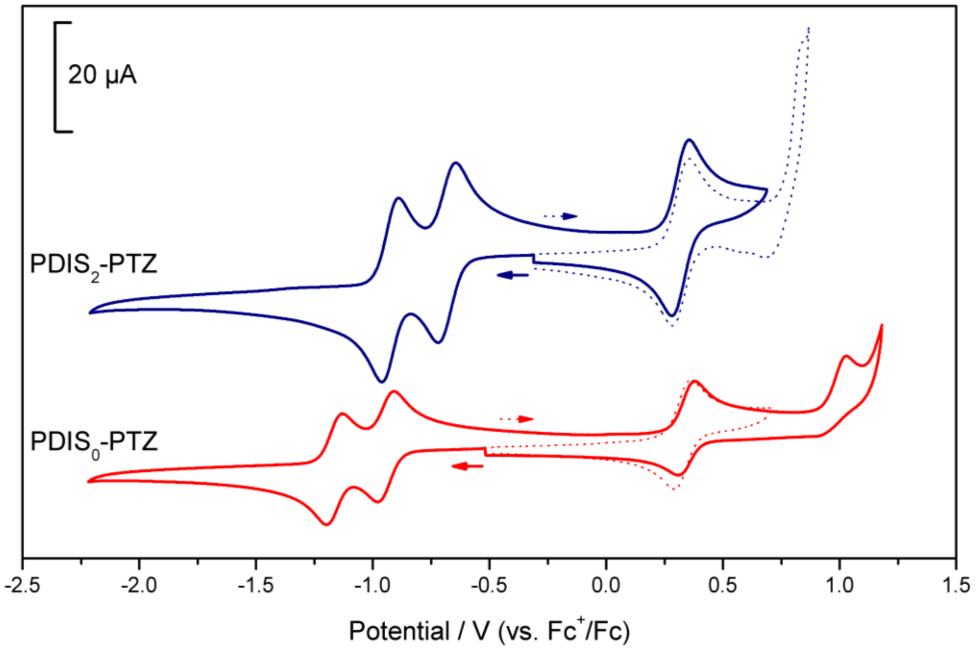

Figure 4.31: Cyclic voltammograms of PDI dyads in dichloromethane containing 0.4 M [^{n}Bu$_4$N][BF$_4$] as the supporting electrolyte, with a scan rate of 100 mVs^{-1}. Red: PDIS$_0$-PTZ, blue PDIS$_2$-PTZ.

The oxidation potentials for the PDI dyads are 0.33 and 0.32 V (vs. Fc$^+$/Fc) for **PDIS$_0$-PTZ** and **PDIS$_2$-PTZ** respectively, virtually identical to each other and to those of the NDI- and NI- dyads containing the same phenothiazine based electron donor.

4.2.6.4. *Spectroelectrochemistry and Optical Properties*

The optical absorbance properties of the two PDI dyads were probed using spectroelectrochemical techniques to investigate the change in absorbance profiles upon reduction and oxidation of the compounds. Both reduction processes as well as the first oxidation process were investigated in this manner for each dyad.

PDIS$_0$-PTZ displayed the distinctive absorbance profile PDI compounds, with a band in the visible region resulting from the S_0 to S_1 electronic transition showing $0 \rightarrow 0$, $0 \rightarrow 1$, $0 \rightarrow 2$ and even $0 \rightarrow 3$ vibrational structure. An extra band is noted at 259 nm, from the phenothiazine chromophore. Thionation bathochromically shifts the absorption maximum of **PDIS$_2$-PTZ** to 633 nm, a difference of just over 100 nm, compared with **PDIS$_0$-PTZ**. The hallmark PDI band structure is diminished in the UV/vis spectrum of **PDIS$_2$-PTZ**: only the $0 \rightarrow 0$ and $0 \rightarrow 1$ vibronic bands form clear peaks, the $0 \rightarrow 2$ and $0 \rightarrow 3$ bands are lost as shoulders to the other peaks. Coupled with the data obtained for the thionated NDI compounds and from cyclic voltammetry, it can be deduced that the HOMO-LUMO gap has decreased as a consequence of the thionation, allowing for control of the frontier orbital energy.

The absorbance spectrum of the monoanionic [**PDIS$_0$-PTZ**]$^{\cdot-}$ considerably resembled that of **PDI-(BDPA)$_2$**, the original bands becoming replaced by intense bands at lower energy (Figure 4.32). A similar transformation occurs upon reduction of **PDIS$_2$-PTZ**, though the emergent band at 768 nm is much less structured and a more intense ([**PDIS$_0$-PTZ**]$^{\cdot-}$ λ_{max} = 716 nm, ε = 72,800 mol^{-1}dm^{3}cm^{-1}; [**PDIS$_2$-PTZ**]$^{\cdot-}$ λ_{max} = 768 nm, ε = 142,100 mol^{-1}dm^{3}cm^{-1}).

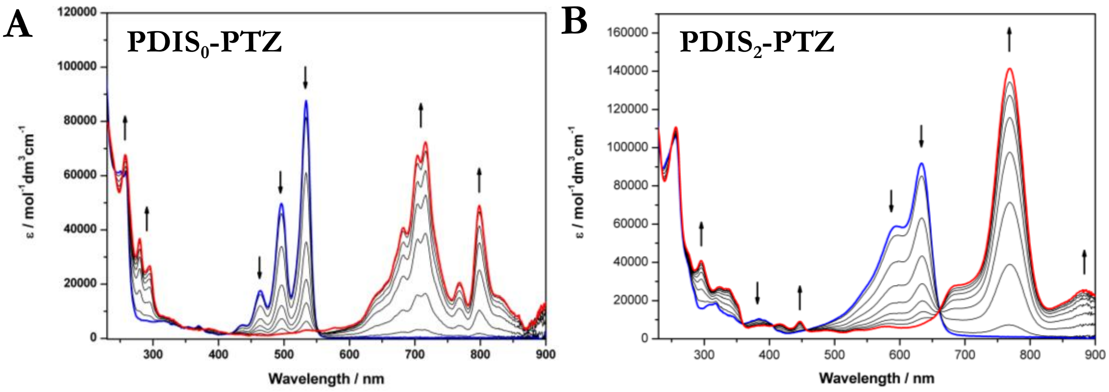

Figure 4.32: UV/vis absorption spectra showing the inter-conversion from neutral (blue) to monoanionic (red) species for PDI dyads, arrows indicate the progress of the reduction. Spectra were recorded in dichloromethane containing [^{n}BuN$_4$][BF$_4$] (0.4 M) as the supporting electrolyte at 243 K. A: PDIS$_0$-PTZ, B: PDIS$_2$-PTZ.

The dianionic form of **PDIS$_0$-PTZ** behaved identically to **PDI-(BDPA)$_2$** performing typically for a PDI. Further reduction of [**PDIS$_2$-PTZ**]$^-$ to [**PDIS$_2$-PTZ**]$^{2-}$ sees a return in appearance to the neutral species' spectrum: the peaks at 633 nm (ε = 92,300 mol^{-1}dm^{3}cm^{-1}) and 592 nm (ε = 59,500 mol^{-1}dm^{3}cm^{-1}) for the neutral **PDIS$_2$-PTZ** become peaks at 643 nm (ε = 146,000 mol^{-1}dm^{3}cm^{-1}) and 589 nm (ε = 69,800 mol^{-1}dm^{3}cm^{-1}) for [**PDIS$_2$-PTZ**]$^{2-}$ (Figure 4.33). Both compounds were fully spectroelectrochemically reversible.

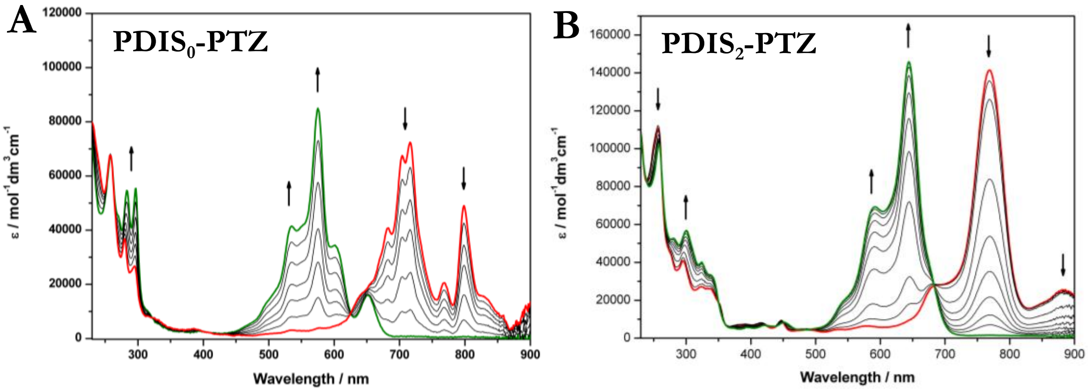

Figure 4.33: UV/vis absorption spectra showing the inter-conversion from monoanionic (red) to dianionic (green) species for PDI dyads, arrows indicate the progress of the reduction. Spectra were recorded in dichloromethane containing [^{n}BuN$_4$][BF$_4$] (0.4 M) as the supporting electrolyte at 243 K. A: PDIS$_0$-PTZ, B: PDIS$_2$-PTZ.

Oxidation of the two PDI dyad compounds proceeded similarly as for the various NDI and NI dyads: the emergent band at ~515 nm corresponding to the oxidised phenothiazine chromophore overlaps with the PDI spectrum, causing a slight rise in absorptivity of the two PDI species (Figure 4.34).

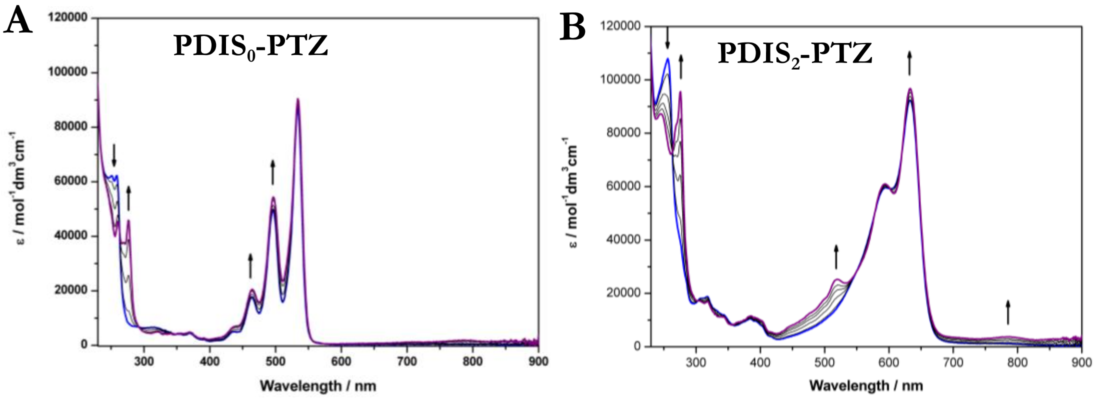

Figure 4.34: UV/vis absorption spectra showing the inter-conversion from neutral (blue) to monocationic (purple) species for PDI dyads, arrows indicate the progress of the oxidation. Spectra were recorded in dichloromethane containing [^{n}BuN$_4$][BF$_4$] (0.4 M) as the supporting electrolyte at 243 K. A: PDIS$_0$-PTZ, B: PDIS$_2$-PTZ.

The optical absorbance data for the PDI-phenothiazine dyads are summarised below (Table 4.3).

Table 4.3: Summary of optical spectroscopy for PDI-phenothiazine compounds.

Compound	λ_{max} / nm (ε / 10^3 mol^{-1}dm^{3}cm^{-1})			
	Neutral	**Monoanionic**	**Dianionic**	**Monocationic**
PDIS$_0$-PTZ	533 (88.0), 496 (50.1), 465 (17.7), 259 (61.4)	798 (49.1), 768 (20.8), 716 (72.8), 704 (67.4), 681 (40.9), 296 (26.6), 280 (36.8), 258 (67.9)	652 (16.0), 601 (34.5), 575 (85.1), 535 (41.8), 297 (55.6), 283 (54.7), 258 (67.1)	534 (90.9), 497 (54.7), 464 (20.6), 277 (46.2), 261 (45.5)
PDIS$_2$-PTZ	633 (92.3), 592 (59.5), 318 (18.9), 256 (106.1)	883 (25.4), 768 (142.1), 447 (9.0), 296 (40.8), 257 (110.9)	643 (146.0), 589 (69.8), 451 (8.7), 325 (40.4), 301 (57.1), 281 (52.7), 259 (102.9)	786 (3.7), 633 (96.9), 593 (61.3), 520 (25.6), 318 (16.9), 277 (95.3), 247 (87.6)

Obtained at an optically transparent electrode cell in dichloromethane, containing [^{n}Bu$_4$N][BF$_4$] (0.4 M) at 243 K, spectral range: 230 - 900 nm.

Initially mentioned above, **PDIS$_0$-PTZ** is not fluorescent in solution, in stark contrast to typical PDI compounds (such as **PDI-(BDPA)$_2$** which had a fluorescence quantum yield Φ_f = 1.00). The measured quantum yield for **PDIS$_0$-PTZ** was less than 0.01, indicating that the fluorescence process is completely quenched by the addition of the phenothiazine imide group. The emission process for a very similar phenothiazine-PDI system, recently reported by Shoer et al.[67] was also completely quenched; attributed to complete charge transfer and determined by femtosecond transient absorption spectroscopy. This charge separation occurred within 33.0 ps in dichloromethane and gave a charge separated lifetime of 174 ± 2 ps. It is highly likely that the emission of **PDIS$_0$-PTZ** is quenched by the same mechanism. **PDIS$_2$-PTZ** is also non-emissive: in addition to charge transfer induced quenching, intersystem crossing to a triplet state is also possible, as witnessed for thionated PDIs by Tilley et al.[66]

4.2.6.5. *Electron Paramagnetic Resonance Spectroscopy*

EPR measurements were taken for the reduced and oxidised dyad species. As expected, the LUMO of the dyads lies on the perylene core of the molecules, evidenced by the complex EPR spectrum for the reduced molecules (Figure 4.35). The molecules' HOMO is phenothiazine based, analogous EPR spectra were recorded for both PDI dyads (Figure 4.36) as for the NDI- and NI-phenothiazine compounds in Chapter 3.

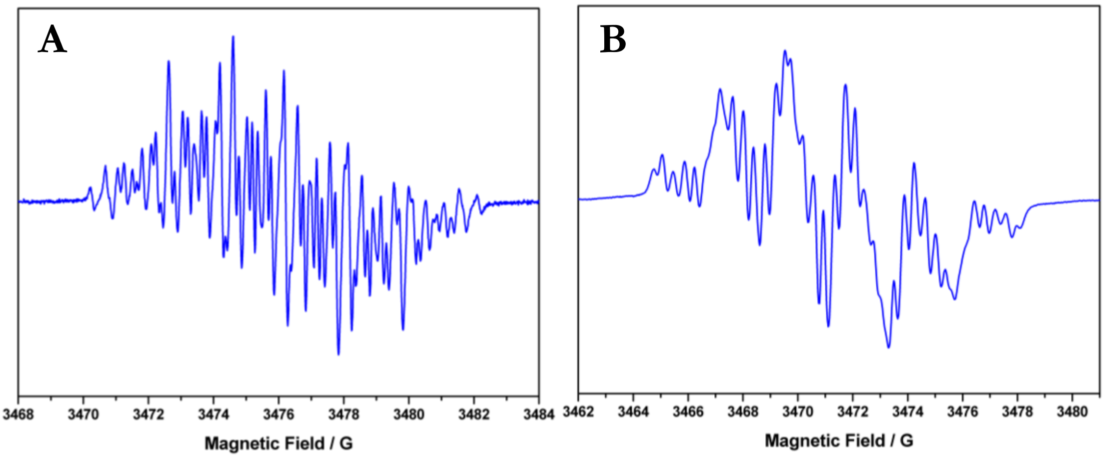

Figure 4.35: Experimentally measured EPR spectrum of reduced PDI-phenothiazine dyads. A: PDIS$_0$-PTZ, B: PDIS$_2$-PTZ.

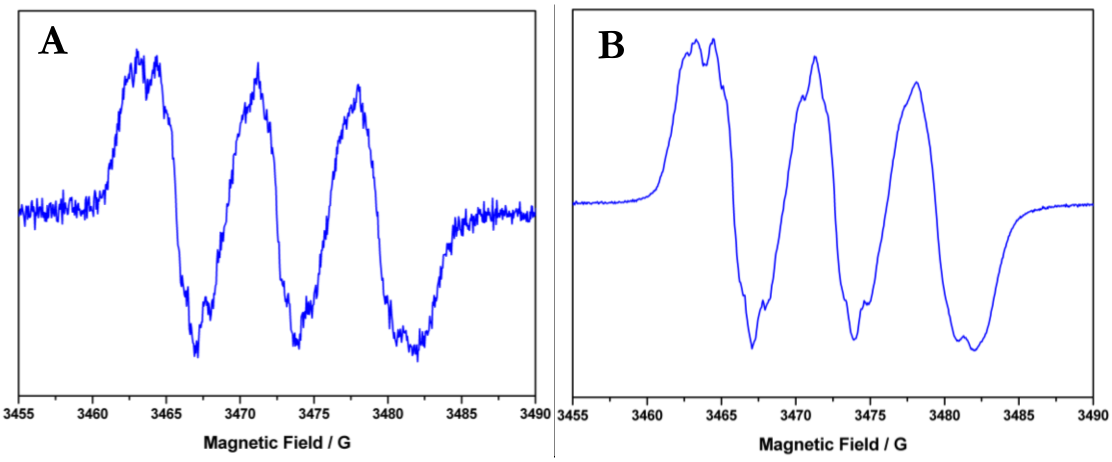

Figure 4.36: Experimentally measured EPR spectrum of oxidised PDI-phenothiazine dyads. A: PDIS$_0$-PTZ, B: PDIS$_2$-PTZ.

The experimentally determined g_{iso} values for the two oxidised PDI dyads are identical to each other and to those for the NDI- and NI- dyads at 2.0055. Such consistency across this range of molecules is further evidence that the phenothiazine HOMO is fully separated from the various acceptor orbitals. The g_{iso} values for **PDIS$_0$-PTZ** and **PDIS$_2$-PTZ** are 2.0033 and 2.0063 respectively. The increase in value can be attributed to the 'heavy atom effect' as seen for the other thionated molecules discussed. The overall difference in g_{iso} value is 0.0030; the same as the difference between **NIS$_0$-PTZ** and **NIS$_2$-PTZ** was reported in Chapter 3. The geminate substitution pattern (as seen for **PDIS$_2$-PTZ** and **NIS$_2$-PTZ**) appears to have a smaller effect on the g_{iso} value than a cis- or trans- substitution pattern.

4.3. Conclusions

A large aromatic tecton, 2,6-bis(diphenylmethyl-4-methylphenyl) has been employed as a solubilising group in the synthesis of non-core substituted perylene diimides to excellent effect. The steric bulk of this tecton is sufficient to eliminate aggregation between the aromatic cores of symmetric PDIs substituted with two of these groups: single crystal X-ray crystallography reveals that adjacent PDI molecules are separated by 11.5 Å, over three times the typical intermolecular separation of PDIs. Single crystal X-ray crystallography of a related perylene monoimide monoanhydride, functionalised with just one of these groups also show disruption of π-aggregation, with stacking limited to pairs of molecules.

An efficient route to non-core substituted asymmetric PDIs has also been confirmed expanding the potential use of more complicated PDI systems in nanotechnology and materials chemistry. In this study this innovative solubilising moiety has been used to produce several asymmetric PDI targets including a multichromophoric PDI dimer, a PDI capable of forming intermolecular hydrogen bonds, and a PDI donor-acceptor system.

Electrochemical investigations of the dimer indicated that no unusual properties resulted from the covalent association of two PDI units. Each chromophore was reduced at the same potential and no communication was detected between the two unpaired electrons of the reduced molecule. The molecular extinction coefficient was found to be double that of an individual PDI unit, with no synergistic effects boosting the absorptivity beyond the expected value.

The hydrogen bonding between a soluble PDI containing an unsubstituted (N-H) imide and complementary adenine was probed using NMR spectroscopy, determining the binding constant for the binary bonding interaction to be 54.9 M^{-1}. This value is one order of magnitude greater than either of the corresponding homodimers, implying formation of the hydrogen bonded heterodimer is significantly more favourable. This research reinforces the potential of PDIs (and other rylene diimides) as markers in biological systems: although it was known that these imides could form complementary hydrogen bonds with certain nucleobases, the strength of this binding has not been previously reported.

Lastly, a donor-acceptor system has been synthesised containing a phenothiazine donor and PDI acceptor. Furthermore, thionation was exercised as a means of controlling the HOMO-LUMO gap within these dimers, yielding results similar to the thionated NI and NDI systems described earlier in this thesis. Interestingly, the 2,6-bis(diphenylmethyl-4-methylphenyl) imide group is also suitably encumbering as to inhibit thionation at the nearby carbonyl positions, allowing access to an otherwise unattainable geminate dithionated rylene diimide. Crystallographic analysis of this compound confirms this thionation pattern as the first example of a perylene monoimide monothioimide, further expanding the synthetic scope of PDIs.

4.4. Materials and Methods

4.4.1. Synthesis

4.4.1.1. *Synthesis of 2,6-bis(diphenylmethyl)-4-methylaniline (**BDPA**)*

The synthesis of this compound was carried out by modifying a literature procedure.[68] Diphenylmethanol (15.00 g, 81.42 mmol) and *p*-toluidine (4.36 g, 40.69 mmol) were heated to melt the *p*-toluidine and a solution of zinc chloride (2.71 g, 19.88 mmol) in hydrochloric acid (3.4 mL, 36 %) was added dropwise. The mixture heated to 160 °C for 2 h with a condenser fitted. The reaction mixture was cooled to room temperature and extracted with dichloromethane (2 x 50 mL). The organic phase was washed with saturated ammonium chloride (100 mL) and brine, and then dried over magnesium sulfate. The solution was concentrated and the product precipitated by the gradual addition of cold methanol to afford 2,6-bis(diphenylmethyl)-4-methylaniline as small white crystals (10.48 g, 58.6 %). ^{1}H NMR (400 MHz, $CDCl_3$): δ ppm 7.29 (t, *J* = 6.9 Hz, 8 H), 7.24 (d, *J* = 6.8 Hz, 4 H), 7.11 (d, *J* = 7.1 Hz, 8 H), 6.40 (s, 2 H), 5.49 (s, 2 H), 2.03 (s, 3 H). ^{13}C NMR (100 MHz, $CDCl_3$): δ ppm 142.75, 139.62, 129.52, 129.23, 129.02, 128.45, 126.64, 126.56, 52.36, 20.99. HRMS $(ESI)^+$ m/z 440.2378 ($C_{33}H_{30}N$ $[M+H]^+$ requires 440.2373).

4.4.1.2. *Synthesis of 3,4,9,10-tetra(decyloxycarbonyl)perylene (**PTE**)*

The synthesis of this compound was carried out according to a literature procedure.[14] To a stirred solution of potassium hydroxide (6.00 g, 107 mmol) in deionised water (100 mL), perylene-3,4,9,10-tetracarboxylic dianhydride (7.84 g, 20 mmol) was added, and the mixture heated to 70 °C for 1 hour. The solution was filtered under gravity and hydrochloric acid (1 M) was added to adjust the pH to 8-9. To this, Aliquat-336 (2.70 g, 6.7 mmol) and potassium iodide (0.5 g, 3.0 mmol) were added and the mixture and stirred vigorously for 10 min. Decyl bromide (35.4 g, 160 mmol) was added and the mixture heated under reflux for 2 hours. The reaction product was extracted with chloroform (250 mL) and washed with an aqueous solution of sodium chloride (3 x 100 mL, 15 % (w/v)). Methanol was added to precipitate the title compound as an orange solid, which was collected by filtration (16.42 g, 83 %). λ_{max} (abs) = 471 nm. ^{1}H NMR (400 MHz, $CDCl_3$): δ ppm 8.31 (d, *J* = 8.0 Hz, 4 H), 8.06 (d, *J* = 7.9 Hz, 4 H), 4.33 (t, *J* = 6.9 Hz, 8 H), 1.80 (quin, *J* = 7.3 Hz, 8 H), 1.49 - 1.40 (m, 8 H), 1.40-1.22 (m, 56 H), 0.88 (t, *J* = 6.9 Hz, 12 H). ^{13}C NMR (100 MHz, $CDCl_3$): δ ppm 168.49, 133.10, 130.51, 130.44, 129.04, 128.85, 121.38, 65.65, 31.90, 29.56, 29.54, 29.34, 29.32, 28.58, 26.02, 22.68, 14.10. IR (ATR): 2954, 2918, 2850, 1731, 1719, 1271, 1169 cm^{-1}. MS (MALDI)$^-$ m/z 989.0 ($C_{64}H_{92}O_8$ [M]$^-$ requires 988.68). Elemental Analysis: 77.65 %C, 9.35 %H ($C_{64}H_{92}O_8$ requires 77.69 %C, 9.37 %H).

4.4.1.3. *Synthesis of Perylene-3,4-anhydride-9,10-di(decyloxycarbonyl)* (***PDE***)

The synthesis of this compound was carried out according to a literature procedure.[14] To a solution of 3,4,9,10-tetra(decyloxycarbonyl)perylene (3.28 g, 3.32 mmol) in toluene (0.87 mL) and n-dodecane (4.35 mL), heated to 95 °C, *p*-toluenesulfonic acid monohydrate (632 mg, 3.32 mmol) was added. The solution was stirred at 95 °C for 5 hours to produce a sticky red paste, which was dissolved in chloroform (100 mL) via a Soxhlet extractor and subsequently adsorbed on to silica gel. This was purified by column chromatography (silica, 40: 1 chloroform: acetone) to afford the title compound as a sticky red solid (1.86 g, 81 %). λ_{max} (abs) = 507 nm. ^{1}H NMR (400 MHz, $CDCl_3$): δ ppm 8.66 (d, *J* = 8.0 Hz, 2 H), 8.57 - 8.50 (m, 4 H), 8.15 (d, *J* = 7.9 Hz, 2 H), 4.35 (t, *J* = 6.9 Hz, 4 H), 1.81 (quin, *J* = 7.2 Hz, 4 H), 1.50 - 1.42 (m, 4 H), 1.38 - 1.25 (m, 24 H), 0.88 (t, *J* = 6.8 Hz, 6 H). ^{13}C NMR (125 MHz, $CDCl_3$): δ ppm 168.03, 160.27, 137.23, 133.56, 132.76, 131.83, 131.49, 130.38, 129.24, 129.21, 126.34, 123.45, 122.09, 117.96, 66.03, 31.89, 29.55, 29.54, 29.32, 29.31, 28.55, 25.99, 22.67, 14.10. IR (ATR): 2955, 2922, 2854, 1768, 1729, 1708, 1594, 1286, 1127 cm^{-1}. MS (MALDI)$^-$ m/z 690.5 ($C_{44}H_{50}O_7$: $[M]^-$ requires 690.36). Elemental Analysis: 75.88 %C, 7.33 %H ($C_{44}H_{50}O_7$ requires 76.49 %C, 7.29 %H).

4.4.1.4. *Synthesis of N-(2,6-bis(diphenylmethyl)-4-methylphenyl)-perylene-3,4-dicarboximide-9,10-di(decylcarbonyl) (**PMIDE**)*

Perylene-3,4-anhydride-9,10-di(decyloxycarbonyl) (200 mg, 290 μmol), 2,6-bis(diphenylmethyl)-4-methylaniline (382 mg, 0.87 mmol), zinc acetate (46 mg, 0.25 mmol) and imidazole (5.00 g, 73.4 mmol) were heated to 140 °C for 16 h under nitrogen. The reaction mixture was cooled to room temperature and dissolved in chloroform (100 mL), before washing with hydrochloric acid (2 x 100 mL, 2 M) and brine (100 mL). The organic layer was dried over magnesium sulfate and the solvent removed. The red product was purified by column chromatography (silica, chloroform) to yield the title compound as a red powder (95 mg, 30 %). λ_{max} (abs) = 509 nm. ^{1}H NMR (400 MHz, $CDCl_3$): δ ppm 8.47 (d, *J* = 8.2 Hz, 2 H), 8.43 (d, *J* = 8.2 Hz, 2 H), 8.29 (d, *J* = 8.0 Hz, 2 H), 8.1 (d, *J* = 7.9 Hz, 2 H), 7.09 - 7.17 (m, 12 H), 7.01 (dd, *J* = 7.2, 1.9 Hz, 8 H), 6.78 (s, 2 H), 5.36 (s, 2 H), 4.35 (t, *J* = 6.9 Hz, 4 H), 2.25 (s, 3 H), 1.82 (quin, 4 H), 1.38 - 1.25 (br, 28 H), 0.89 (t, *J* = 6.8 Hz, 6 H). ^{13}C NMR (100 MHz, $CDCl_3$): δ ppm 168.29, 162.54, 142.22, 137.87, 135.52, 132.41, 131.84, 131.57, 131.34, 130.39, 129.57, 129.46, 129.35, 128.08, 126.19, 122.58, 122.23, 121.75, 65.86, 52.52, 31.90, 29.56, 29.54, 29.32, 28.57, 26.01, 22.68, 21.77, 14.11. HRMS (MALDI)$^+$ m/z 1111.5756 ($C_{77}H_{77}N_1O_6$ $[M]^+$ requires 1111.5745).

4.4.1.5. *Synthesis of N-(2,6-bis(diphenylmethyl)-4-methylphenyl)-perylene-3,4-dicarboximide-9,10-anhydride (**PMI**)*

p-Toluenesulfonic acid monohydrate (47 mg, 0.25 mmol) was added to a stirred solution of *N*-(2,6-bis(diphenylmethyl)-4-methylphenyl)-perylene-3,4-dicarboximide-9,10-di(decylcarbonyl) (278 mg, 250 μmol) in toluene (25 mL) at 95 °C. After 5 h a red precipitate had formed. Methanol (25 mL) was added and the mixture filtered. The solid product was purified by column chromatography (silica, 49:1 chloroform: acetone) to yield the title compound as a red precipitate (185 mg, 91 %). Suitable crystals for X-ray diffractometry were grown by slow evaporation of a chloroform solution of the compound. λ_{max} (abs) = 527 nm. Fluorescence quantum yield $\Phi_f = 0.95$. ^{1}H NMR (400 MHz, $CDCl_3$): δ ppm 8.81 (q, *J* = 8.2 Hz, 4 H), 8.73 (m, *J* = 8.2 Hz, 2 H), 8.50 (m, *J* = 8.0 Hz, 2 H), 7.10 - 7.15 (m, 12 H), 6.92 - 6.97 (m, 8 H), 6.82 (s, 2 H), 5.24 (s, 2 H), 2.27 (s, 3 H). ^{13}C NMR (125 MHz, $CDCl_3$): δ ppm 162.08, 160.02, 142.17, 142.05, 138.18, 136.56, 133.83, 133.61, 131.89, 131.34, 131.16, 129.66, 129.53, 129.39, 128.14, 126.90, 126.57, 126.29, 123.97, 123.76, 123.23, 119.02, 52.61, 21.77. HRMS (MALDI)$^+$ m/z 813.2540 ($C_{57}H_{35}N_1O_5$ [M]$^+$ [M$^+$] requires 813.2510).

4.4.1.6. *Synthesis of N-(2,6-bis(diphenylmethyl)-4-methylphenyl)-N'-(4-carboxyphenyl)-perylene-3,4,9,10-tetracarboxylic diimide (**PDI-COOH**)*

N-(2,6-bis(diphenylmethyl)-4-methylphenyl)-perylene-3,4-dicarboximide-9,10-anhydride (107 mg, 132 μmol), 4-aminobenzoic acid (36 mg, 260 μmol) and imidazole (5.00 g, 73.4 mmol) were heated to 130 °C for 3.5 h. The reaction mixture was cooled to room temperature and hydrochloric acid (100 mL, 2 M) was added. The red precipitate was collected by centrifugation and washed twice more with hydrochloric acid and twice with water. The pellet was extracted into chloroform (50 mL) and washed once with water (50 mL) and once with brine (50 mL), then purified by column chromatography (silica, gradient elution 19:1 chloroform: acetone to 99:1 chloroform: trifluoroacetic acid) to yield the title compound as a red powder (78 mg, 64 %). Suitable crystals for X-ray diffraction were grown by vapour diffusion of hexane into a chloroform solution of the compound. ^{1}H NMR (400 MHz, $CDCl_3$): δ ppm 8.79 (d, *J* = 8.0 Hz, 2 H), 8.72 (d, *J* = 8.2 Hz, 2 H), 8.64 (d, *J* = 8.3 Hz, 2 H), 8.38 (d, *J* = 7.9 Hz, 2 H), 8.34 (d, *J* = 8.4 Hz, 2 H), 7.52 (d, *J* = 8.4 Hz, 2 H), 7.18 – 7.11 (m, 12 H), 7.00 (dd, *J* = 6.71, 2.45 Hz, 8 H), 6.78 (s, 2 H), 5.35 (s, 2 H), 2.25 (s, 3 H). ^{13}C NMR (100 MHz, $CDCl_3$): δ ppm 169.71, 163.39, 162.25, 142.20, 142.10, 139.99, 138.12, 135.59, 134.39, 132.08, 131.41, 131.36, 131.27, 129.91, 129.75, 129.65, 129.55, 129.46, 129.11, 128.14, 126.82, 126.46, 126.28, 123.55, 123.34, 123.17, 122.92, 52.59, 21.78. HRMS (FD)$+^-$ m/z 932.2854 ($C_{64}H_{40}N_2O_6$ $[M]^+$ requires 932.2881).

4.4.1.7. *Synthesis of* ***PDI Dimer***

The reaction conditions were adapted from a literature procedure.[50] A Schlenk flask was charged with *N*-(2,6-bis(diphenylmethyl)-4-methylphenyl)-*N*'-(4-carboxyphenyl)-perylene-3,4,9,10-tetracarboxylic diimide (27 mg, 29 μmol), benzene dimethanol (4.0 mg, 29 μmol), 4-dimethylaminopyridine (1 mg, 29 μmol) and anhydrous dichloromethane (10 mL) and cooled to 0 °C. *N*,*N*-Dicyclohexylcarbodiimide (6.6 mg, 31.8 μmol) was added and the reaction stirred for 3 h at room temperature. The reaction mixture was filtered to remove any urea and the solvent removed under reduced pressure. The crude product was taken up into dichloromethane (10 mL) and washed with hydrochloric acid (2 x 20 mL, 0.5 M) and sat. sodium hydrogen carbonate (20 mL), then dried over magnesium sulfate. The product was and purified by column chromatography (silica, 49:1 chloroform: acetone) to yield the title compound as a red powder (7 mg, 24.6 %). λ_{max} (abs) = 532 nm. ^{1}H NMR (400 MHz, $CDCl_3$): δ ppm 8.77 (d, *J* = 8.0 Hz, 4 H) 8.70 (d, *J* = 8.2 Hz, 4 H) 8.62 (d, *J* = 8.2 Hz, 4 H) 8.37 (d, *J* = 8.0 Hz, 4 H) 8.30 - 8.34 (m, 4 H)

7.54 (s, 4 H) 7.46 - 7.50 (m, 4 H) 7.10 - 7.16 (m, 24 H) 6.97 - 7.02 (m, 16 H) 6.78 (s, 4 H) 5.46 (s, 4 H) 5.35 (s, 4 H) 2.25 (s, 6 H). ^{13}C NMR (125 MHz, $CDCl_3$): δ ppm 165.66, 163.33, 162.22, 142.18, 142.10, 139.45, 138.11, 136.06, 135.49, 134.36, 131.99, 131.32, 131.27, 130.93, 130.51, 129.87, 129.64, 129.54, 129.44, 128.98, 128.49, 128.13, 126.77, 126.44, 126.27, 123.53, 123.28, 123.11, 122.95, 66.62, 52.57, 21.77. HRMS $(FD)^+$ m/z 1966.6287 ($C_{136}H_{86}N_4O_{12}$ $[M]^+$ requires 1966.6237).

4.4.1.8. *Synthesis of N,N'-di(2,6-bis(diphenylmethyl-4-methylphenyl)-perylene-3,4,9,10-tetracarboxylic diimide (**PDI-(BDPA)$_2$**)*

Perylene-3,4,9,10-tetracarboxylic dianhydride (392 mg, 1.00 mmol), 2,6-bis(diphenylmethyl)-4-methylaniline (1.54 g, 3.50 mmol), zinc acetate (50 mg, 0.27 mmol) and imidazole (10.0 g, 147 mmol) were heated to 140 °C for 16 h under nitrogen. The reaction mixture was cooled to room temperature and hydrochloric acid (50 mL, 2 M) was added. The red precipitate was collected by centrifugation and washed twice more with hydrochloric acid. The pellet was then taken up into chloroform (50 mL) and washed with water (100 mL) and brine, dried over magnesium sulfate and the solvent removed. The solid product was purified by column chromatography (silica, chloroform) to yield the title compound as an orange powder (105 mg, 8.5 %). Suitable crystals for X-ray diffractometry were grown by vapour diffusion of hexane into a chloroform solution of the compound. λ_{max} (abs) = 533 nm. Fluorescence quantum yield $\Phi_f = 1.00$. ^{1}H NMR (400 MHz, $CDCl_3$): δ ppm 8.60 (d, J = 8.0 Hz, 4 H), 8.35 (d, J = 8.0 Hz, 4 H), 7.14 (m, 24 H), 6.99 (m, 16 H), 6.78 (s, 4 H), 5.35 (s, 4 H), 2.25 (s, 6 H). ^{13}C NMR (125 MHz, $CDCl_3$): δ ppm 162.04, 141.98, 141.84, 137.79, 134.53, 131.12, 131.05, 129.34, 129.30, 129.25, 127.87, 126.29, 126.00, 122.95, 122.66, 52.34, 21.52. HRMS $(MALDI)^+$ m/z 1234.4703 ($C_{90}H_{62}N_2O_4$ $[M]^+$ requires 1234.4704).

4.4.1.9. *Synthesis of N,N'-di(2,6-bis(diphenylmethyl-4-methylphenyl)-naphthalene-1,4,5,8-tetracarboxylic diimide (**NDI-(BDPA)$_2$**)*

Naphthalene-1,4,5,8-tetracarboxylic dianhydride (268 mg, 1.00 mmol), 2,6-bis(diphenylmethyl)-4-methylaniline (527 mg, 1.20 mmol), zinc acetate (46 mg, 250 μmol) and imidazole (5.00 g, 73.4 mmol) were heated to 140 °C for 16 h under nitrogen. The reaction mixture was cooled to room temperature and dissolved in chloroform (100 mL), before washing with hydrochloric acid (2 x 100 mL, 2 M) and brine (100 mL). The organic layer was dried over magnesium sulfate and the solvent removed to afford a brown solid, which was purified by column chromatography (silica, chloroform) to yield the title compound as a beige powder (107 mg, 9.6 %). Suitable crystals for X-ray diffractometry were grown by vapour diffusion of hexane into a chloroform solution of the compound. λ_{max} (abs) = 386 nm. ^{1}H NMR (400 MHz, $CDCl_3$): δ ppm 8.31 (s, 4 H), 7.11 - 7.15 (m, 24 H), 6.96 - 7.01 (m, 16 H), 6.78 (s, 4 H), 5.32 (s, 4 H) 2.24 (s, 6 H). ^{13}C NMR (100 MHz, $CDCl_3$): δ ppm 161.75, 142.11, 141.92, 138.40, 130.87, 130.48, 129.79, 129.49, 128.18, 126.45, 126.41, 126.25, 52.71, 21.76. MS (MALDI)$^-$ m/z 1109.1 ($C_{80}H_{58}N_2O_4$ [M]$^-$ requires 1110.4).

4.4.1.10. *Synthesis of N-(2,6-bis(diphenylmethyl)-4-methylphenyl)-perylene-3,4-dicarboximide-9,10-imide (**PDI-NH**)*

N-(2,6-bis(diphenylmethyl)-4-methylphenyl)-perylene-3,4-dicarboximide-9,10-anhydride (30 mg, 37 μmol) was added to aqueous ammonia solution (35 %, 25 mL) and the resulting suspension heated to reflux for 16 h. After cooling to room temperature, the red product was extracted with chloroform (50 mL) and washed with water (2 x 100 mL) and brine (100 mL) and dried over $MgSO_4$. The solution was concentrated under reduced pressure and the crude product purified by column chromatography (silica, 19:1 chloroform: acetone) to give the product as a red solid (13 mg, 43 %). ^{1}H NMR (400

MHz, $CDCl_3$, 4 mM) δ ppm 8.76 - 8.64 (m, *J* = 8.1, 8.1, 8.1 Hz, 4 H), 8.60 (d, *J* = 7.5 Hz, 2 H), 8.53 (s, 1 H), 8.36 (d, *J* = 8.3 Hz, 2 H), 7.17 - 7.08 (m, 12 H), 7.03 - 6.96 (m, 8 H), 6.78 (s, 2 H), 5.35 (s, 2 H), 2.25 (s, 3 H). ^{13}C NMR (125 MHz, $CDCl_3$) δ = 163.05, 162.23, 142.18, 142.12, 138.10, 135.57, 134.32, 131.30, 131.28, 130.75, 129.65, 129.55, 129.41, 128.12, 126.99, 126.37, 126.26, 123.53, 123.25, 123.02, 122.90, 52.56, 21.77. HRMS $(MALDI)^+$ m/z 812.2665 ($C_{57}H_{36}N_2O_4$ $[M]^+$ requires 812.2670).

4.4.1.11. *Synthesis of N-(2,6-bis(diphenylmethyl)-4-methylphenyl)-N'-(10-phenyl-10H-phenothiazine)-perylene-3,4,9,10-tetracarboxylic diimide (**PDIS$_0$-PTZ**)*

A mixture of *N*-(2,6-bis(diphenylmethyl)-4-methylphenyl)-perylene-3,4-dicarboximide-9,10-anhydride (141 mg, 173 μmol), 10-(4-aminophenyl)-10H-phenothiazine (70 mg, 243 μmol) and imidazole (5.00 g, 73.4 mmol) were heated to 130 °C under nitrogen for 3 h. The reaction was then cooled to 100 °C and hydrochloric acid (50 mL, 2 M) was added. After 10 min, the reaction mixture was allowed to cool to room temperature and extracted with chloroform (2 x 100 mL). The combined organics were washed with hydrochloric acid (100 mL), water (100 mL) and brine (100 mL) and dried over $MgSO_4$. The orange solution was concentrated under reduced pressure and the crude product purified by column chromatography (silica, 99:1 chloroform: acetone) to give the product as a red solid (140 mg, 76 %, mp = 276 °C). λ_{max} (abs) = 530 nm. Fluorescence quantum yield $\Phi_f < 0.01$. ^1H NMR (400 MHz, $CDCl_3$) δ ppm 8.81 (d, *J* = 8.0 Hz, 2 H), 8.74 (d, *J* = 8.2 Hz, 2 H), 8.64 (d, *J* = 8.2 Hz, 2 H), 8.38 (d, *J* = 8.0 Hz, 2 H), 7.57 (s, 4 H), 7.17 - 7.09 (m, 14 H), 7.04 - 6.96 (m, 10 H), 6.91 (dt, *J* = 1.3, 7.4 Hz, 2 H), 6.79 (s, 2 H), 6.53 (dd, *J* = 1.1, 8.2 Hz, 2 H), 5.35 (s, 2 H), 2.25 (s, 3 H). ^{13}C NMR (125 MHz, $CDCl_3$) δ ppm 163.63, 162.24, 143.76, 142.20, 142.11, 141.89, 138.10, 135.53, 134.43, 133.90, 132.02, 131.35, 131.28, 130.98, 130.00, 129.93, 129.64, 129.55, 129.49, 128.14, 127.05, 127.01, 126.84, 126.49, 126.27, 123.55, 123.29, 123.20, 123.13, 123.07, 121.91, 117.58, 52.60, 21.78. IR (ATR): 3056, 3022, 1702, 1665, 1592, 1576, 1340 cm^{-1}. HRMS (MALDI)$^+$ m/z 1085.3298 ($C_{75}H_{47}N_3O_4S_1$ [M]$^+$ requires 1085.3282).

4.4.1.12. *Synthesis of N-(2,6-bis(diphenylmethyl)-4-methylphenyl)-N'-(10-phenyl-10H-phenothiazine)-perylene-3,4-imide-9,10-dithioimide (**PDIS$_2$-PTZ**)*

PDIS$_0$-PTZ (140 mg, 129 μmol) and Lawesson's reagent (261 mg, 645 μmol) were dissolved in anhydrous toluene (25 mL) and heated to reflux for 20 h. The solution was cooled to room temperature and washed with sat. aq. $NaHCO_3$ (100 mL), water (100 mL) and sat. aq. NaCl (100 mL), dried over $MgSO_4$, filtered and the soovent removed to give a blue solid. This was purified by column chromatography (silica, gradient elution from chloroform to 19:1 chloroform: acetone) to give **PDIS$_2$-PTZ** as a blue microcrystalline powder (73 mg, 51 %, mp = 277 °C). λ_{max} (abs) = 633 nm. ^{1}H NMR (400 MHz, $CDCl_3$) δ ppm 9.03 (d, *J* = 8.4 Hz, 2 H), 8.61 (d, *J* = 8.2 Hz, 2 H), 8.56 (d, *J* = 8.7 Hz, 2 H), 8.37 (d, *J* = 8.0 Hz, 2 H), 7.57 - 7.50 (m, 2 H), 7.43 - 7.37 (m, 2 H), 7.19 - 7.09 (m, 14 H), 7.06 - 6.98 (m, 10 H), 6.91 (dt, *J* = 1.1, 7.4 Hz, 2 H), 6.80 (s, 2 H), 6.58 (dd, *J* = 1.1, 8.2 Hz, 2 H), 5.37 (s, 2 H), 2.26 (s, 3 H). ^{13}C NMR (100 MHz, $CDCl_3$) δ ppm 190.18, 162.29, 144.43, 143.70, 142.19, 142.14, 141.18, 138.10, 137.46, 137.41, 134.72, 134.12, 131.42, 131.30, 130.68, 130.28, 129.66, 129.61, 129.57, 129.50, 128.15, 127.08, 127.01, 126.53, 126.29, 126.12, 124.95, 123.52, 123.48, 123.06, 121.93, 117.59, 52.59, 21.79. IR (ATR): 3056, 3021, 1706, 1665, 1588, 1567, 1220, 1163 cm^{-1}. HRMS (MALDI)$^+$ m/z 1117.2822 ($C_{75}H_{47}N_3O_2S_3$ [M]$^+$ requires 1117.2825).

4.5. References

1. F. Wurthner, *Chem. Commun.*, 2004, 1564-1579.
2. H. Langhals, R. Ismael and O. Yürük, *Tetrahedron*, 2000, **56**, 5435-5441.
3. N. Jouault, Y. Xiang, E. Moulin, G. Fuks, N. Giuseppone and E. Buhler, *Phys. Chem. Chem. Phys.*, 2012, **14**, 5718-5728.
4. H. Langhals, *Heterocycles*, 1995, **40**, 477-500.
5. H. Langhals, W. Jona, F. Einsiedl and S. Wohnlich, *Adv. Mater.*, 1998, **10**, 1022-1024.
6. R. Sun, C. Xue, M. Owak, R. M. Peetz and S. Jin, *Tetrahedron Lett.*, 2007, **48**, 6696-6699.
7. C. Huang, Ph.D, Georgia Institute of Technology Ph.D Thesis, 2010.
8. A. Wicklein, A. Lang, M. Muth and M. Thelakkat, *J. Am. Chem. Soc.*, 2009, **131**, 14442-14453.
9. H. Tröster, *Dyes Pigm.*, 1983, **4**, 171-177.
10. H. Langhals, *United States Patent 5693808*, 1997.
11. Y. Nagao and T. Misono, *Bull. Chem. Soc. Jpn.*, 1981, **54**, 1269-1270.
12. A. Wicklein, M.-A. Muth and M. Thelakkat, *J. Mater. Chem.*, 2010, **20**, 8646-8652.
13. Y. Nagao, *Prog. Org. Coat.*, 1997, **31**, 43-49.
14. C. Xue, R. Sun, R. Annab, D. Abadi and S. Jin, *Tetrahedron Lett.*, 2009, **50**, 853-856.
15. K. Balakrishnan, A. Datar, T. Naddo, J. Huang, R. Oitker, M. Yen, J. Zhao and L. Zang, *J. Am. Chem. Soc.*, 2006, **128**, 7390-7398.
16. Y. Che, A. Datar, K. Balakrishnan and L. Zang, *J. Am. Chem. Soc.*, 2007, **129**, 7234-7235.
17. Y. Che, X. Yang, G. Liu, C. Yu, H. Ji, J. Zuo, J. Zhao and L. Zang, *J. Am. Chem. Soc.*, 2010, **132**, 5743-5750.
18. Y. Zhang, C. Peng, X. Ma, Y. Che and J. Zhao, *Chem. Commun.*, 2015, **51**, 15004-15007.
19. X. Liu, Y. Zhang, X. Pang, Y. E, Y. Zhang, D. Yang, J. Tang, J. Li, Y. Che and J. Zhao, *J. Phys. Chem. C*, 2015, **119**, 6446-6452.
20. Y. E, X. Ma, Y. Zhang, Y. Zhang, R. Duan, H. Ji, J. Li, Y. Che and J. Zhao, *Chem. Commun.*, 2014, **50**, 13596-13599.
21. L. Y. Yang, M. M. Shi, M. Wang and H. Z. Chen, *Chin. Chem. Lett.*, 2008, **19**, 1260-1263.
22. S. Chen, P. Slattum, C. Wang and L. Zang, *Chem. Rev.*, 2015, **115**, 11967-11998.
23. H. Langhals and R. Ismael, *Eur. J. Org. Chem.*, 1998, **1998**, 1915-1917.
24. H. Liu, L. Shen, Z. Cao and X. Li, *Phys. Chem. Chem. Phys.*, 2014.
25. J. M. Giaimo, A. V. Gusev and M. R. Wasielewski, *J. Am. Chem. Soc.*, 2002, **124**, 8530-8531.
26. Y. Wang, Y. Chen, R. Li, S. Wang, W. Su, P. Ma, M. R. Wasielewski, X. Li and J. Jiang, *Langmuir*, 2007, **23**, 5836-5842.
27. J. Feng, Y. Zhang, C. Zhao, R. Li, W. Xu, X. Li and J. Jiang, *Chem. Eur. J.*, 2008, **14**, 7000-7010.
28. C. Hippius, F. Schlosser, M. O. Vysotsky, V. Böhmer and F. Würthner, *J. Am. Chem. Soc.*, 2006, **128**, 3870-3871.
29. T. van der Boom, R. T. Hayes, Y. Zhao, P. J. Bushard, E. A. Weiss and M. R. Wasielewski, *J. Am. Chem. Soc.*, 2002, **124**, 9582-9590.
30. G. Qi, L. Jiang, Y. Zhao, Y. Yang and X. Li, *Phys. Chem. Chem. Phys.*, 2013, **15**, 17342-17353.

31. T. Ishi-i, K.-i. Murakami, Y. Imai and S. Mataka, *J. Org. Chem.*, 2006, **71**, 5752-5760.
32. L. Xue, Y. Shi, L. Zhang and X. Li, *ChemPhysChem*, 2013, **14**, 3319-3326.
33. L. F. Dössel, V. Kamm, I. A. Howard, F. Laquai, W. Pisula, X. Feng, C. Li, M. Takase, T. Kudernac, S. De Feyter and K. Müllen, *J. Am. Chem. Soc.*, 2012, **134**, 5876-5886.
34. E. H. A. Beckers, S. C. J. Meskers, A. P. H. J. Schenning, Z. Chen, F. Würthner, P. Marsal, D. Beljonne, J. Cornil and R. A. J. Janssen, *J. Am. Chem. Soc.*, 2006, **128**, 649-657.
35. M. R. Wasielewski, *Acc. Chem. Res.*, 2009, **42**, 1910-1921.
36. F. Würthner, T. E. Kaiser and C. R. Saha-Möller, *Angew. Chem. Int. Ed.*, 2011, **50**, 3376-3410.
37. M. C. Baier, J. Huber and S. Mecking, *J. Am. Chem. Soc.*, 2009, **131**, 14267-14273.
38. F. Graser, *US Patent No. 4446324*, 1984.
39. P. D. Frischmann, K. Mahata and F. Wurthner, *Chem. Soc. Rev.*, 2013, **42**, 1847-1870.
40. C. Ramanan, A. L. Smeigh, J. E. Anthony, T. J. Marks and M. R. Wasielewski, *J. Am. Chem. Soc.*, 2012, **134**, 386-397.
41. F. Würthner, *Pure Appl. Chem.*, 2006, **78**, 2341-2349.
42. P. D. Frischmann and F. Würthner, *Org. Lett.*, 2013, **15**, 4674-4677.
43. H. Langhals, S. Demmig and H. Huber, *Spectrochim. Acta A*, 1988, **44**, 1189-1193.
44. F. Graser and E. Hädicke, *Liebigs Ann. Chem.*, 1980, **1980**, 1994-2011.
45. M. Lenes, G.-J. A. H. Wetzelaer, F. B. Kooistra, S. C. Veenstra, J. C. Hummelen and P. W. M. Blom, *Adv. Mater.*, 2008, **20**, 2116-2119.
46. X. Mo, H.-Z. Chen, M.-M. Shi and M. Wang, *Chem. Phys. Lett.*, 2006, **417**, 457-460.
47. R. A. Cormier and B. A. Gregg, *Chem. Mater.*, 1998, **10**, 1309-1319.
48. K. Y. Law, *Chem. Rev.*, 1993, **93**, 449-486.
49. F. Würthner, C. Thalacker, S. Diele and C. Tschierske, *Chem. Eur. J.*, 2001, **7**, 2245-2253.
50. B. Neises and W. Steglich, *Angew. Chem. Int. Ed.*, 1978, **17**, 522-524.
51. J. A. Theobald, N. S. Oxtoby, M. A. Phillips, N. R. Champness and P. H. Beton, *Nature*, 2003, **424**, 1029-1031.
52. T. Seki, X. Lin and S. Yagai, *Asian J. Org. Chem.*, 2013, **2**, 708-724.
53. N. Kimizuka, T. Kawasaki, K. Hirata and T. Kunitake, *J. Am. Chem. Soc.*, 1995, **117**, 6360-6361.
54. F. Würthner, C. Thalacker and A. Sautter, *Adv. Mater.*, 1999, **11**, 754-758.
55. F. Würthner, C. Thalacker, A. Sautter, W. Schärtl, W. Ibach and O. Hollricher, *Chem. Eur. J.*, 2000, **6**, 3871-3886.
56. C. Thalacker and F. Würthner, *Adv. Funct. Mater.*, 2002, **12**, 209-218.
57. F. J. M. Hoeben, J. Zhang, C. C. Lee, M. J. Pouderoijen, M. Wolffs, F. Würthner, A. P. H. J. Schenning, E. W. Meijer and S. De Feyter, *Chem. Eur. J.*, 2008, **14**, 8579-8589.
58. S. Yagai, S. Hamamura, H. Wang, V. Stepanenko, T. Seki, K. Unoike, Y. Kikkawa, T. Karatsu, A. Kitamura and F. Wurthner, *Org. Biomol. Chem.*, 2009, **7**, 3926-3929.
59. L. E. Sinks, B. Rybtchinski, M. Iimura, B. A. Jones, A. J. Goshe, X. Zuo, D. M. Tiede, X. Li and M. R. Wasielewski, *Chem. Mater.*, 2005, **17**, 6295-6303.
60. A. P. Bisson, C. A. Hunter, J. C. Morales and K. Young, *Chem. Eur. J.*, 1998, **4**, 845-851.

61. A. P. Bisson, F. J. Carver, D. S. Eggleston, R. C. Haltiwanger, C. A. Hunter, D. L. Livingstone, J. F. McCabe, C. Rotger and A. E. Rowan, *J. Am. Chem. Soc.*, 2000, **122**, 8856-8868.
62. C. Ludwig, B. Gompf, J. Petersen, R. Strohmaier and E. W., *Z. Phys. B: Condens. Matter*, 1994, **93**, 389-390.
63. A. G. Slater, Y. Hu, L. Yang, S. P. Argent, W. Lewis, M. O. Blunt and N. R. Champness, *Chem. Sci.*, 2015, **6**, 1562-1569.
64. J. S. Renny, L. L. Tomasevich, E. H. Tallmadge and D. B. Collum, *Angew. Chem. Int. Ed.*, 2013, **52**, 11998-12013.
65. L. M. Kozycz, C. Guo, J. G. Manion, A. J. Tilley, A. J. Lough, Y. Li and D. S. Seferos, *J. Mater. Chem. C*, 2015, **3**, 11505-11515.
66. A. J. Tilley, R. D. Pensack, T. S. Lee, B. Djukic, G. D. Scholes and D. S. Seferos, *J. Phys. Chem. C*, 2014, **118**, 9996-10004.
67. L. E. Shoer, S. W. Eaton, E. A. Margulies and M. R. Wasielewski, *J. Phys. Chem. B*, 2015, **119**, 7635-7643.
68. G. Berthon-Gelloz, M. A. Siegler, A. L. Spek, B. Tinant, J. N. H. Reek and I. E. Marko, *Dalton Trans.*, 2010, **39**, 1444-1446.

Chapter 5

Conclusions

5.1. Conclusions

Although research into the chemistry of the rylene diimide class of compounds has been a topic of interest for many decades now, the changes that occur upon thionation have only recently been brought to light. The results described within this thesis have gone some way towards exploring these changes, as well as describing some of the new properties that emerge following thionation. The electrochemical techniques of cyclic voltammetry, spectroelectrochemistry and electron paramagnetic resonance spectroscopy are of particular importance to this thesis, as these techniques are less common in the literature, despite providing a great deal of information about the molecules in their reduced forms. Understanding the nature of these species is important in order to fully utilise them in practical applications and devices.

Currently there have been three reports in the literature focussed on thionation of naphthalene diimides (NDIs); however these accounts only report the optical absorbance of the neutral molecules and provide rudimentary measurements of their reduction potentials. Here, a more complete investigation into the electrochemical properties of thionated NDI systems has revealed that in addition to the steady bathochromic shift in absorbance maximum of ~45 nm per sulfur atom substitution for the neutral NDIs, that this trend is preserved following electrochemical reduction to mono- and dianionic molecules. Furthermore, the cis and trans isomers of dithionated NDIs could be readily distinguished by the absorbance spectra of their reduced forms, which proved spectroelectrochemistry as a valuable tool for the characterisation of the more complex asymmetric systems later synthesised.

Cyclic voltammetric measurements of the thionated NDI series discovered a steady anodic shift in the reduction potential of the NDIs with the number of sulfur atoms by ~150 mV per substitution. Density functional theory calculations validated this trend, indicating the increase in electron affinity occurs as a result of decreasing LUMO energy. EPR spectroscopy has probed the nature of thionated NDI radicals for the first time finding that the location of the radical electron is within an orbital extending across the aromatic core of the NDIs. The isotropic g-factor increases with the sulfur content of the NDIs, a consequence of the 'heavy atom' effect. Interestingly though, the cis and trans dithionated isomers possess different g_{iso} values, despite each imide group containing one carbonyl and one thiocarbonyl bond. This result also assisted with characterisation of the cis isomer of the phenothiazine-NDI dyad later produced.

There has been some speculation in the literature as to why the more thionated NDI derivatives (with 3 and 4 sulfur atom substitutions) are less readily formed, with conjecture that the low LUMO of the trithionated NDI may prevent reactivity to Lawesson's reagent. Thionation reactions with a naphthalic imide (NI) homologue indicate that thionation of both sides of the imide (which is required to synthesise NDIs with 3 and 4 sulfur substitutions) does not easily occur, implying a largely steric effect prevents thionation of the adjacent carbonyls. A trithionated NDI with aliphatic imide groups was successfully synthesised, yet required use of dithionated NDIs as the reagent for the reaction, and decomposed quickly. Interestingly, the trithionated derivative of the asymmetric NDI-phenothiazine dyad, bearing an aromatic imide substituent, formed readily as a single isomer and did not quickly decompose. This unexpected result indicates that an aromatic imide substituent (e.g. of the phenothiazine linker) enables thionation at the adjacent carbonyls. Straightforward geminate dithionation of the related NI- and perylene diimide (PDI)-phenothiazine dyads, further supports the observation that aromatic imide groups assists double thionation of the same imide region, possibly even promoting the Lawesson's reagent chemistry to favour thionation close to an aromatic ring. Currently no reports exist in the literature of the thionation of aromatically (imide) substituted rylene diimides for comparison. Based off the findings described in this thesis, perhaps if a suitable solubilising aromatic group is employed at the imide region of an NDI, it would be possible to produce the tetrathionated product in good yield for study.

Supplementing the techniques of spectroelectrochemistry and EPR spectroscopy, the photochemistry of thionated NDIs has been measured for the first time, utilising transient absorption spectroscopy and time resolved infrared spectroscopy. Although the TA and TRIR data presented within this thesis seems to suggest that intersystem crossing from a singlet to a triplet excited state is favoured in thionated NDI systems (as was the case for thionated PDIs), further DFT calculations are required to augment these spectral assignments and to fully elucidate these findings.

Furnishing one imide terminus of NDI with an organic phenothiazine (PTZ) donor group and the other with a solubilising n-octyl chain produced a viable donor-acceptor candidate molecule for use in organic photovoltaic devices. This NDI-PTZ dyad was a blue colour in the solid state, dissolving to form colourless solutions; a possible indicator that charge separation was taking place. Transient absorption spectroscopy confirmed this, giving a charge separated lifetime of 130 ps. The same phenothiazine donor group was also equipped onto an NI acceptor in almost quantitative yield. This time the radical pair persisted for 260 ps before recombination occurred.

Both NDI- and NI-PTZ dyads then underwent thionation reactions. Two products were isolated from the NDI reaction: a single trithionated isomer and the cis dithionated isomer. Trans and geminate dithionated isomers were also formed, but could not be separated from each other, even creating a cocrystal. If reaction conditions and stoichiometry were carefully controlled, it should be possible to synthesise the trithionated NDI-PTZ compound in high yield, increasing practicability of such a system.

In contrast, the NI-PTZ dyad readily reacted with Lawesson's reagent to generate a fully thionated product in good overall yield. Moreover, there are six functionalisable positions on the aromatic core of naphthalic imides, allowing even more complicated systems to be fabricated from a dithionated NI centre, extending the viability of such systems.

Cyclic voltammetry of these dyads showed that the thionation had no effect on the oxidation potential of the phenothiazine moiety, which remained a constant 0.33 V (vs. Fc^+/Fc) across all dyads regardless of how many oxygen atoms had been replaced with sulfur. Consequently, the choice of electron donor partnered with the degree of thionation can be used to precisely control the HOMO-LUMO gap of rylene diimide based donor-acceptor structures. In this work, the experimentally determined separation between the HOMO and LUMO of the trithionated NDI-PTZ dyad is 0.87 eV, unprecedentedly low for an NDI. Full thionation of the NI-PTZ dyad saw an increase in reduction potential to -1.13 V (vs. Fc^+/Fc), making dithionated NIs competitive with nonthionated NDIs as n-type electron acceptor materials.

TA spectroscopy in tandem with TRIR spectroscopy was used to assess charge separation in the thionated NDI- and NI- dyads finding that the lifetime of the charge separated state increases by roughly one order of magnitude, over the nonthionated counterparts. Charge separated lifetimes greater than 2 ns were measured for the thionated NDI- and NI- dyad compounds, which is sufficiently long to allow for charge extraction to occur in an organic electronic device.

Through the use of the branched aromatic tecton 2,6-bis(diphenylmethyl)-4-methylphenyl (BDPA), a substantial increase in the solubility of perylene-3,4-imide-9,10-anhydrides (PMIs) was noted. Solubilising groups commonly deployed at the imide termini of PDIs include bifurcated aliphatics and 2,6-diisopropylphenyl, however this research found these groups insufficient to overcome π-π stacking in PMIs, necessitating the use of the larger group. This research required a highly soluble PMI, to provide complete freedom in the choice of functional group at the other imide terminus; to take part in the necessary chemistry to synthesise downstream products; and to allow for a thorough analysis and electrochemical characterisation of the product PDIs. Single crystal X-ray diffraction was able to determine that the steric bulk of the BDPA group vastly increases the intermolecular distance of *N*,*N*'-symmetric PDIs and limits π-stacking to dimers in the case of an asymmetric PMI, with a large separation between these dimers.

The BDPA-furnished PMI served as an excellent precursor for the synthesis of *N*,*N*'-asymmetric PDIs, including a PDI dimer, a PDI substituted at one end with just a hydrogen atom and a PDI-PTZ donor-acceptor system. Electrochemical analysis of the PDI dimer did not unearth any unusual properties: each chromophore within the dimer behaved equally, with no communication detected by cyclic voltammetry or EPR spectroscopy. The interaction between the imide region of PDIs and adenine was examined using NMR spectroscopy, establishing that favourable hydrogen-bonding occurs between these two complimentary units. The majority of literature focusses on the hydrogen bonding interactions between the PDI imide region and melamine, so this research provides a refreshing angle of biological importance.

Finally, the thionated phenothiazine-rylene diimide donor acceptor series was expanded to include PDIs. Addition of the phenothiazine chromophore to the imide terminal of PDI quenches fluorescence, likely a consequence of charge transfer, though TA spectroscopy is required to fully clarify this. Thionation of PDI-PTZ generated exclusively a geminately dithionated PDI-PTZ product. Isolation of this particular sulfur substitution pattern has not been reported before in the literature: current accounts imply the thionation reaction will occur more favourably on opposite imide termini (forming cis and trans isomers in equal yield) before a second sulfur substitution can occur on the same imide group. Steric effects of the BDPA tecton are likely the cause of this, preventing thionation at the BDPA-substituted imide terminus of the PDI, hence a unique perylene monoimide monothioimide has been created. Electrochemical analysis of these donor acceptor dyads found similar results to the NDI series: the sulfur substitution increases electron affinity by decreasing LUMO energy. The HOMO-LUMO gap for the dithionated PDI-PTZ was measured by cyclic voltammetry to be 1.00 eV.

Overall, the techniques of spectroelectrochemistry, electron paramagnetic resonance spectroscopy, density functional theory and transient absorption spectroscopy have provided a good understanding of the nature of thionated rylene diimides, particularly as singly and doubly reduced molecules and shown how the energies of the frontier orbitals can be tailored through simple sulfur substitution. Soluble, functional *N*,*N*'-asymmetric rylene diimide dyes have been synthesised in good yield for application as n-type semiconductors within organic photovoltaic devices. It is hoped that the findings presented within this thesis will prove valuable in expanding the field of rylene diimide research, especially the emerging area of chalcogen atom substitution.

Chapter 6

Materials and Methods

6.1. Reagents and Purification

All chemical reagents were used as-purchased from Alfa Aesar, Fisher Scientific, Sigma-Aldrich, or VWR International. Column chromatography was performed on Merck silica gel 60 (0.2 - 0.5 mm, 50 - 130 mesh). Preparative thin layer chromatography was also employed, using silica gel as the stationary phase on plates purchased from AnalTech. Anhydrous toluene was dried by passing through a column packed with 4 Å molecular sieves, degassed and stored over a potassium mirror in a nitrogen atmosphere. Anhydrous dichloromethane was purchased from Sigma-Aldrich (Fluka) and stored over 4 Å molecular sieves in a nitrogen atmosphere. Ferrocene was purchased from Aldrich and used as received. 9-Propyladenine was synthesised by Dr. Anna Slater according to a literature procedure.[1] $[^{n}Bu_4N][BF_4]$ was prepared by the reaction of a 14 % aqueous solution of sodium tetrafluoroborate with a 13 % aqueous solution of tetrabutylammonium hydrogen sulfate and crystallised by dropwise addition of a dichloromethane solution of the compound into diethyl ether.

Reactions sensitive to air and moisture were performed using a standard Schlenk line, with nitrogen as the inert atmosphere. Glassware used was flame dried under vacuum and backfilled with nitrogen.

6.2. General Equipment

6.2.1. NMR Spectroscopy

^{1}H and ^{13}C NMR spectra were recorded using either a Bruker AV(III)400, AV(III)500, AV400 or DPX400 machines at room temperature. Chemical shifts are reported with respect to the $CDCl_3$ residual peak at 7.27 ppm (^{1}H) and 77.00 ppm (^{13}C). For ^{1}H NMR spectroscopy, splitting patterns are described in brackets after the shift as splitting pattern (s = singlet, d = doublet, t = triplet, q = quartet, m = multiplet, br = broad); coupling constant (*J* in Hz) and the number of atoms in that environment.

6.2.2. Mass Spectrometry

EI M/S spectra were taken using a Bruker Apex IV 4.7 T mass spectrometer. ESI M/S spectra were recorded with a Bruker MicroTOF using methanol or acetonitrile as the solvent. FD M/S spectra were measured with a JOEL AccuTOF GCX spectrometer. MALDI-TOF M/S spectra were recorded with a Bruker Ultraflex III mass spectrometer using trans-2-[3-(4-tert-butylphenyl)-2-methyl-2-propenylidene]-malononitrile as the matrix. HRMS MALDI spectra were obtained by cross-calibrating the recorded spectrum against that of a polyethylene glycol standard.

6.2.3. Elemental Analysis

Elemental analysis was performed using an automated CE-440 Elemental Analyser.

6.2.4. Infrared Spectroscopy

ATR IR spectra were obtained in the 400-4000 cm^{-1} range using a Bruker Tensor 27 spectrometer with an ATR attachment.

6.2.5. Fluorescence Spectroscopy

Fluorescence spectra were recorded on a Horiba FluoroMax-3 using a quartz fluorescence cuvette, with a 1 cm path length. Samples were prepared in clean solvent and solution concentrations were selected such that the absorbance in a 10 cm path length cuvette was less than 1.0 at wavelengths greater than the excitation wavelength to reduce inner filter effects. Quantum yields were measured using a comprehensive method published by Williams et al.[2] Briefly, the optical absorbance was measured against the integrated emission intensity for five different concentrations for both the sample to determine and a reference sample.

A cuvette with side length 10 cm was filled with a solution of the fluorescent compound and its UV/vis absorption spectrum was recorded, such that the maximum absorbance was less than 1.0. The fluorescence cuvette was then filled from the solution in the larger cuvette and measured. This was repeated using solution concentrations 0.8, 0.6, 0.4 and 0.2 times that of the initial measurement to give a total of five concentrations. The UV/vis absorbance at the excitation wavelength was then plotted against the integrated emission intensity. These measurements were then repeated in a similar manner for the reference sample. The ratio of the gradients of the plots for these two samples is equal to the ratio of the quantum yields. To minimise error, data for both samples were recorded in the same solvent (chloroform) and samples excited at the same wavelength. Absorbances were corrected for the solvent background and taken at a constant wavelength of 471 nm. *N*,*N*'-bis(diisopropylphenyl)-3,4,9,10-perylene tetracarboxylic diimide (Perylene Orange) was synthesised and crystallised from chloroform/hexane and employed as the reference for PDI samples with a literature quantum yield Φ_F of 1.00 under the experimental parameters.[3]

6.3. X-ray Crystallography

6.3.1. Equipment and Software

Single crystal X-ray diffraction experiments were performed on an Oxford Diffraction SuperNova CCD area detector diffractometer at 120 K using monochromated Cu Kα radiation (λ = 1.54184 Å); on Agilent GV1000 AtlasS2 or TitanS2 CCD area detector diffractometers at 120 K using monochromated CuKα radiation (λ = 1.54184 Å); or at the UK Diamond Light Source I19-1 3-circle diffractometer[4] (λ = 0.6889 Å). Absorption corrections were applied using analytical numerical methods using CrysAlisPro software.[5] The structures were solved by direct methods using either ShelXS[6] or ShelXT[7] and refined with ShelXL[8] using a least squares method. In all instances, Olex2 software was used as the solution, refinement and analysis program.[9] All hydrogen atoms were placed in geometrically calculated positions; non-hydrogen atoms were refined with anisotropic displacement parameters. CIF checks were performed by Dr. William Lewis. In specific cases, geometric restraints were applied.

6.3.2. Crystal Data

Single crystals of $\mathbf{NDIS_0}$ were grown by evaporation of a chloroform solution of the compound. The structure was collected on a GV1000 AtlasS2 diffractometer (120 K, CuKα radiation).

Crystal Data for $\mathbf{NDIS_0}$: $C_{24}H_{26}N_2O_4$ (M =406.47 g/mol): monoclinic, space group $P2_1/n$ (no. 14), a = 13.4100(3) Å, b = 8.3348(2) Å, c = 18.3351(4) Å, β = 101.022(2)°, V = 2011.50(9) Å^3, Z = 4, T = 120(2) K, μ(CuKα) = 0.743 mm^{-1}, $Dcalc$ = 1.342 g/cm^3, 7787 reflections measured ($7.524° \leq 2\theta \leq 148.798°$), 3963 unique ($R_{int}$ = 0.0157, R_{sigma} = 0.0211) which were used in all calculations. The final R_1 was 0.0371 ($I > 2\sigma(I)$) and wR_2 was 0.1062 with GOF = 1.032.

Single crystals of $\mathbf{NDIS_1}$ were grown by evaporation of an acetonitrile solution of the compound. The structure was collected on a GV1000 AtlasS2 diffractometer (120 K, CuKα radiation).

Crystal Data for $\mathbf{NDIS_1}$: $C_{24}H_{26}N_2O_3S$ (M =422.53 g/mol): monoclinic, space group $P2_1/c$ (no. 14), a = 9.1049(7) Å, b = 8.6592(7) Å, c = 13.7163(8) Å, β = 100.773(7)°, V = 1062.35(13) Å^3, Z = 2, T = 120.01(10) K, μ(CuKα) = 1.582 mm^{-1}, $Dcalc$ = 1.321 g/cm^3, 3983 reflections measured ($9.888° \leq 2\theta \leq 148.168°$), 2080 unique ($R_{int} = 0.0171$, $R_{sigma} = 0.0208$) which were used in all calculations. The final R_1 was 0.0715 ($I > 2\sigma(I)$) and wR_2 was 0.2373 with GOF = 1.044.

O11 and S14 are disordered over two positions and their respective occupancies were fixed at a ratio of 0.75: 0.25. O14A and S11A are disordered over two positions and their respective occupancies were fixed at a ratio of 0.75: 0.25.

Single crystals of **$NDIS_2$ trans** were grown by slow evaporation of a chloroform/hexane solution of the compound. The structure was collected on a GV1000 AtlasS2 diffractometer (120 K, CuKα radiation).

Crystal Data for **$NDIS_2$ trans**: $C_{24}H_{26}N_2O_2S_2$ (M =438.59 g/mol): monoclinic, space group $P2_1/c$ (no. 14), $a = 8.7955(3)$ Å, $b = 9.4770(4)$ Å, $c = 12.8838(5)$ Å, $\beta = 92.537(3)°$, $V = 1072.87(7)$ Å^3, $Z = 2$, $T = 120.00(10)$ K, $\mu(CuK\alpha) = 2.436$ mm^{-1}, $Dcalc = 1.358$ g/cm^3, 4286 reflections measured ($10.066° \leq 2\theta \leq 148.75°$), 2105 unique ($R_{int} = 0.0244$, $R_{sigma} = 0.0363$) which were used in all calculations. The final R_1 was 0.0398 ($I > 2\sigma(I)$) and wR_2 was 0.1066 with GOF = 1.035.

Single crystals of **$NDIS_0$-PTZ** were grown by vapour diffusion of pentane into a chloroform solution of the compound. The structure was collected on a SuperNova diffractometer (120 K, CuKα radiation).

Crystal Data for **$NDIS_0$-PTZ**: $C_{41}H_{34}Cl_3N_3O_4S$ (M + $CHCl_3$) (M =771.12 g/mol): triclinic, space group P-1 (no. 2), $a = 8.7193(3)$ Å, $b = 11.6007(4)$ Å, $c = 18.7861(9)$ Å, $\alpha = 87.754(3)°$, $\beta = 87.804(3)°$, $\gamma = 78.925(3)°$, $V = 1862.48(13)$ Å^3, $Z = 2$, $T = 120(2)$ K, $\mu(CuK\alpha) = 3.128$ mm^{-1}, $Dcalc = 1.375$ g/cm^3, 13098 reflections measured ($9.22° \leq 2\theta \leq 148.178°$), 7319 unique ($R_{int} = 0.0391$, $R_{sigma} = 0.0377$) which were used in all calculations. The final R_1 was 0.1021 ($I > 2\sigma(I)$) and wR_2 was 0.3289 with GOF = 1.409.

One alkyl chain, containing atoms 41 to 48 is disordered over two positions. The chloroform molecule is disordered over the same two positions as the alkyl chain. The respective occupancies were refined competitively. The alkyl chain converged to ratios of 0.37: 0.63 and the chloroform also converged to a ratio of 0.37: 0.63. Chemically equivalent bonds of the disordered atoms were restrained to be approximately equal to each other and those of the ordered equivalent. Enhanced rigid bond and similarity restraints were applied to the thermal parameters of the disordered atoms.

Single crystals of **NDIS$_3$-PTZ** were grown by vapour diffusion of hexane into a chloroform solution of the compound. The structure was collected on a Kappa Rigaku Saturn724+ diffractometer with a CrystalLogic Kappa (4 circle) goniometer (150 K, Synchrotron).

Crystal Data for **NDIS$_3$-PTZ**: $C_{40}H_{33}N_3OS_4$ (M =699.93 g/mol): monoclinic, space group Pc (no. 7), a = 27.4330(9) Å, b = 14.3097(4) Å, c = 8.5187(3) Å, β = 93.320(3)°, V = 3338.45(19) Å^3, Z = 4, T = 150(2) K, μ(Synchrotron) = 0.299 mm^{-1}, $Dcalc$ = 1.393 g/cm^3, 11575 reflections measured ($5.13° \leq 2\theta \leq 48.414°$), 9537 unique ($R_{int}$ = 0.0314, R_{sigma} = 0.0376) which were used in all calculations. The final R_1 was 0.0357 ($I > 2\sigma(I)$) and wR_2 was 0.0940 with GOF = 1.031.

Single crystals of **NDIS$_2$-PTZ** were crystallised by slow evaporation of a chloroform solution of the compound. The structure was collected on a GV1000 AtlasS2 diffractometer (120 K, CuKα radiation).

Crystal Data for **NDIS$_2$-PTZ**: $C_{40}H_{33}N_3O_2S_3$ (M =683.87 g/mol): monoclinic, space group Pc (no. 7), a = 27.3800(4) Å, b = 14.16026(18) Å, c = 8.42558(12) Å, β =

93.5537(14)°, V = 3260.38(8) Å^3, Z = 4, T = 120(2) K, μ(CuKα) = 2.411 mm^{-1}, *Dcalc* = 1.393 g/cm^3, 45316 reflections measured (8.994° ≤ 2θ ≤ 147.97°), 12123 unique (R_{int} = 0.0640, R_{sigma} = 0.0432) which were used in all calculations. The final R_1 was 0.0564 (I > 2σ(I)) and wR_2 was 0.1467 with GOF = 1.039.

Two of the carbonyl groups (cis carbonyls) on both molecules are disordered over two positions with sulfur atoms (S22B and O21B, S13B and O12B, S22A and O21A, and S12A and O13A). Their respective occupancies were refined competitively. S22B and S21B along with S13B and O12B both converged to a ratio of 0.47: 0.53. S22A and O21A along with S12A and O13A both converged to a ratio of 0.38: 0.62. Chemically equivalent bonds of the disordered atoms were restrained to be approximately equal to each other and those of the ordered equivalent. Restraints were applied to allow for the disordered molecules to lie in the common plane to the rest of the molecule. Enhanced rigid bond restraints were applied to the thermal parameters of the whole molecule.

Single crystals of **NIS$_0$-PTZ** were grown by vapour diffusion of pentane into a chloroform solution of the compound. The structure was collected on a Kappa Rigaku Saturn724+ diffractometer with a CrystalLogic Kappa (4 circle) goniometer (100 K, Synchrotron).

Crystal Data for **NIS$_0$-PTZ**: $C_{31}H_{19}Cl_3N_2O_2S$ (M + $CHCl_3$) (M =589.89 g/mol): orthorhombic, space group Pbca (no. 61), a = 9.07634(15) Å, b = 18.5416(5) Å, c = 31.2516(5) Å, V = 5259.31(18) Å^3, Z = 8, T = 100(2) K, μ(Synchrotron) = 0.427 mm^{-1}, *Dcalc* = 1.490 g/cm^3, 64180 reflections measured (4.442° ≤ 2θ ≤ 63.568°), 9248 unique (R_{int} = 0.0318, R_{sigma} = 0.0158) which were used in all calculations. The final R_1 was 0.0387 (I > 2σ(I)) and wR_2 was 0.1052 with GOF = 1.053.

Single crystals of **NIS_2-PTZ** were grown by vapour diffusion of pentane into a chloroform solution of the compound. The structure was collected on a GV1000 TitanS2 diffractometer (120 K, CuKα radiation).

Crystal Data for **NIS_2-PTZ**: $C_{30}H_{18}N_2S_3$ (M =502.64 g/mol): monoclinic, space group Pc (no. 7), a = 12.36487(18) Å, b = 9.88933(14) Å, c = 9.81295(15) Å, β = 104.3620(15)°, V = 1162.43(3) $Å^3$, Z = 2, T = 120(2) K, μ(CuKα) = 3.091 mm^{-1}, $Dcalc$ = 1.436 g/cm^3, 4526 reflections measured (8.942° ≤ 2θ ≤ 147.822°), 3017 unique (R_{int} = 0.0322, R_{sigma} = 0.0322) which were used in all calculations. The final R_1 was 0.0356 (I > 2σ(I)) and wR_2 was 0.0958 with GOF = 0.992.

Single crystals of **PDI-$(BDPA)_2$** were grown by vapour diffusion of hexane into a chloroform solution of compound. The structure was collected on a GV1000 AtlasS2 diffractometer (120 K, CuKα radiation).

Crystal Data for of **PDI-$(BDPA)_2$**: $C_{94}H_{66}Cl_{12}N_2O_4$ (+ 4 x $CHCl_3$) (M =1712.88 g/mol): monoclinic, space group I2/a (no. 15), a = 18.2761(17) Å, b = 13.8702(14) Å, c = 32.394(3) Å, β = 97.314(9)°, V = 8145.0(14) $Å^3$, Z = 4, T = 120(2) K, μ(CuKα) = 4.171 mm^{-1}, $Dcalc$ = 1.397 g/cm^3, 16957 reflections measured (5.5° ≤ 2θ ≤ 150.778°), 8099 unique (R_{int} = 0.1551, R_{sigma} = 0.2028) which were used in all calculations. The final R_1 was 0.1887 (I > 2σ(I)) and wR_2 was 0.5503 with GOF = 1.176.

Enhanced rigid bond and similarity restraints were applied to the thermal parameters of all molecules. Chemically equivalent bonds of the chloroform molecules were restrained to be approximately equal to each other.

Single crystals of **NDI-(BDPA)$_2$** were grown by vapour diffusion of hexane into a chloroform solution of the compound. The structure was collected on SuperNova diffractometer (120 K, CuKα radiation).

Crystal Data for **NDI-(BDPA)$_2$**: $C_{81}H_{59}Cl_3N_2O_4$ (M + $CHCl_3$) (M =1230.65 g/mol): triclinic, space group P-1 (no. 2), a = 14.2993(12) Å, b = 15.5105(12) Å, c = 16.1638(10) Å, α = 61.874(7)°, β = 80.223(7)°, γ = 82.031(7)°, V = 3108.6(5) Å^3, Z = 2, T = 120(2) K, μ(CuKα) = 1.776 mm^{-1}, $Dcalc$ = 1.315 g/cm^3, 23088 reflections measured (6.286° ≤ 2θ ≤ 149.678°), 12261 unique (R_{int} = 0.0275, R_{sigma} = 0.0333) which were used in all calculations. The final R_1 was 0.0663 (I > 2σ(I)) and wR_2 was 0.1912 with GOF = 1.021.

On one molecule, the aromatic ring containing atoms 58A to 62A is disordered over two positions. The respective occupancies were refined competitively. The atoms of the ring converged to a ratio of 0.67: 0.33. Additionally the resolved chloroform molecule was disordered over two positions. The respective occupancies were fixed at a ratio of 0.7: 0.3. Chemically equivalent bonds of the disordered atoms were restrained to be approximately equal to each other and those of the ordered equivalent. Enhanced rigid bond and similarity restraints were applied to the thermal parameters of the disordered atoms.

Single crystals of **PMI** were grown by evaporation of a chloroform solution of the compound. The structure was collected on a GV1000 AtlasS2 diffractometer (120 K, CuKα radiation).

Crystal Data for **PMI**: $C_{58}H_{36}Cl_3NO_5$ (M + $CHCl_3$) (M =933.23 g/mol): triclinic, space group P-1 (no. 2), a = 10.9926(4) Å, b = 11.9491(3) Å, c = 18.2926(6) Å, α = 79.310(3)°, β = 85.055(3)°, γ = 69.185(3)°, V = 2206.42(13) Å^3, Z = 2, T = 120(2) K,

$\mu(\mathrm{CuK}\alpha) = 2.325\ \mathrm{mm}^{-1}$, $Dcalc = 1.405\ \mathrm{g/cm}^3$, 16588 reflections measured ($4.918° \leq 2\theta \leq 148.416°$), 8695 unique ($R_{\mathrm{int}} = 0.0186$, $\mathrm{R}_{\mathrm{sigma}} = 0.0216$) which were used in all calculations. The final R_1 was 0.0574 ($I > 2\sigma(I)$) and wR_2 was 0.1634 with GOF = 1.043.

The chloroform molecule is disordered over two positions and the occupancies of the two parts were refined competitively. They converged to a ratio of 0.32: 0.68. Chemically equivalent bonds of the disordered atoms were restrained to be approximately equal to each other. Enhanced rigid bond and similarity restraints were applied to the thermal parameters of the disordered atoms. Similarity restraints were applied to the thermal parameters of atoms C67-C72. Enhanced rigid bond and similarity restraints were applied to the thermal parameters of the phenyl groups containing the atoms C41-C46 and C67-C72.

Single crystals of **PDI-COOH** were grown by slow evaporation of a chloroform solution of the compound. The structure was collected on a Kappa Rigaku Saturn724+ diffractometer with a CrystalLogic Kappa (4 circle) goniometer (120 K, Synchrotron). The crystal was kept at 120(2) K during data collection.

Crystal Data for **PDI-COOH**: $C_{66}H_{42}N_2O_6Cl_6$ (+2 $CHCl_3$) (M =932.98 g/mol): triclinic, space group P-1 (no. 2), a = 12.0991(5) Å, b = 22.5225(9) Å, c = 23.4989(11) Å, α = 110.836(4)°, β = 97.775(4)°, γ = 98.568(3)°, V = 5793.8(5) Å^3, Z = 4, T = 120(2) K, $\mu(\mathrm{Synchrotron}) = 0.347\ \mathrm{mm}^{-1}$, $Dcalc = 1.343\ \mathrm{g/cm}^3$, 20564 reflections measured ($3.124° \leq 2\theta \leq 48.662°$), 20564 unique ($\mathrm{R}_{\mathrm{sigma}} = 0.0569$) which were used in all calculations. The final R_1 was 0.1948 ($I > 2\sigma(I)$) and wR_2 was 0.5690 with GOF = 1.995.

Disordered solvent chloroform could not be sensibly modelled so the structure was treated with PLATON SQUEEZE.[10] This gave an estimate of 465 electrons per cell, corresponding to approximately 4 molecules of chloroform per asymmetric unit. These molecules were included in the sum formula. Atom O22A is disordered over two positions (O22A and O22B) and the respective occupancies of the two atoms was refined competitively, converging to a ratio of 0.74: 0.26. The benzoic acid ring of one molecule conatining atoms C80 to C88 is disordered over two positions (C80 to C88 and C80B to C88B) and their respective occupancies refined competitively, converging to a ratio of 0.68: 0.32. The chemically identical bonds of these two components were restrained to be geometrically similar. Enhanced rigid bond restraints were applied to the thermal parameters of the whole molecule.

Single crystals of **PDIS$_0$-PTZ** were grown by vapour diffusion of pentane into a chloroform solution of the compound. The structure was collected on a GV1000 AtlasS2 diffractometer (120 K, CuKα radiation).

Crystal Data for **PDIS$_0$-PTZ**: $C_{75}H_{47}N_3O_4S$ (M =1086.21 g/mol): monoclinic, space group P2$_1$/c (no. 14), a = 26.5322(11) Å, b = 12.9232(5) Å, c = 17.8678(6) Å, β = 91.725(3)°, V = 6123.8(4) Å^3, Z = 4, T = 120(2) K, μ(CuKα) = 0.880 mm^{-1}, $Dcalc$ = 1.178 g/cm^3, 25016 reflections measured ($6.666° \leq 2\theta \leq 147.124°$), 11975 unique ($R_{int}$ = 0.0272, R_{sigma} = 0.0308) which were used in all calculations. The final R_1 was 0.0893 ($I > 2\sigma(I)$) and wR_2 was 0.2668 with GOF = 1.069.

Disordered solvent pentane could not be sensibly modelled to give convergence and the data was treated with PLATON SQUEEZE,[10] which gave an estimate of 360 electrons per cell, corresponding to approximately 2 molecules of pentane per asymmetric unit. These molecules were added to the sum formula.

Single crystals of **PDIS$_2$-PTZ** were grown by slow addition of pentane into a chloroform solution of the compound. The structure was collected on a GV1000 TitanS2 diffractometer (120 K, CuKα radiation).

Crystal Data for **PDIS$_2$-PTZ**: $C_{85}H_{71}N_3O_2S_3$ (M + 2 C_5H_{12}) (M =1118.39 g/mol): monoclinic, space group P2$_1$/c (no. 14), a = 25.854(4) Å, b = 13.2446(11) Å, c = 18.207(2) Å, β = 90.303(15)°, V = 6234.4(13) Å^3, Z = 4, T = 120(2) K, μ(CuKα) = 1.522 mm^{-1}, $Dcalc$ = 1.345 g/cm^3, 16493 reflections measured (6.838° ≤ 2θ ≤ 147.432°), 10611 unique (R_{int} = 0.1025, R_{sigma} = 0.1746) which were used in all calculations. The final R_1 was 0.1166 (I > 2σ(I)) and wR_2 was 0.3942 with GOF = 0.9470.

Disordered solvent pentane could not be sensibly modelled so the structure was treated using PLATON SQUEEZE,[10] which gave an estimate of 332 electrons per unit cell, corresponding to 2 molecules of pentane per asymmetric unit. These molecules were included in the sum formula. Enhanced rigid bond restraints were applied to the thermal parameters of the whole molecule.

6.4. Electrochemistry

6.4.1. Cyclic Voltammetry

Cyclic voltammetry was carried out using an Autolab PGSTAT20 potentiostat under an argon atmosphere using a three-electrode arrangement in a single compartment cell. Glassy carbon was used as the working electrode, platinum wire as the secondary electrode and a silver/silver chloride reference electrode, chemically isolated from the test solution via a fritted bridge tube containing electrolyte solution, in the cell. An analyte concentration of 1 mM was used with [^{n}Bu$_4$N][BF$_4$] (400 mM) as a supporting electrolyte. Redox potentials are referenced to the ferrocenium/ferrocene couple, which was implemented as an internal reference.[11] In one instance, the decamethylferrocenium/decamethylferrocene couple was used instead, to avoid signal overlap and calibrated to ferrocenium/ferrocene. No compensation was applied for internal resistance.

6.4.2. Spectroelectrochemistry

UV/vis spectroelectrochemical measurements were performed using an optically transparent quartz electrochemical cell, with a 0.5 mm path length. A three-electrode configuration of a platinum/rhodium gauze working electrode, platinum wire secondary electrode and a silver/silver chloride reference electrode (chemically isolated via a fritted bridge tube) were used in the cell. The potential at the working electrode was regulated with a Sycopel Scientific Ltd DD10M potentiostat and the spectra recorded with a Perkin Elmer 16 spectrophotometer. Temperature control was achieved with a stream of chilled nitrogen gas (cooled by passing through a tube submerged in liquid nitrogen) across the surface of the cell, adjusting the flow rate as necessary in response to a temperature sensor (±0.1 °C). [^{n}Bu$_4$N][BF$_4$] (400 mM) was used as the supporting electrolyte for the experiments.

6.4.3. Bulk Electrolysis and Electron Paramagnetic Resonance Spectroscopy

Bulk electrolysis was performed under an argon atmosphere at 0 °C in a two-component cell: a platinum/rhodium gauze working electrode and secondary electrode are separated by a glass frit. A silver/silver chloride reference electrode was bridged to the test solution through a vycor frit, oriented at the centre of the working electrode. The working electrode compartment, containing analyte (1 mM), was stirred rapidly with a magnetic stirrer bar during electrolysis. [^{n}Bu$_4$N][BF$_4$] (400 mM) was used as the supporting electrolyte for the experiments.

After electrolysis was completed, the prepared solution was transferred by cannula to a quartz EPR tube for analysis on a Bruker EMX spectrometer. Solution phase (fluid) spectra were recorded at room temperature and frozen (glass) spectra were recorded by freezing the electrogenerated radical solution in liquid nitrogen within an additional quartz dewar. Spectra were simulated when possible using WIN EPR SimFonia software.

6.4.4. Infrared Spectroscopy of Electrogenerated Species

Samples of oxidised or reduced compound were electrogenerated using the bulk electrolysis technique described above, with a working electrode compartment containing the analyte at (1 mM) and $[^{n}Bu_4N][BF_4]$ (200 mM) as the supporting electrolyte at 0 °C. After electrolysis, the prepared solution was transferred by cannula to an argon-purged adjustable path-length IR cell with KBr windows for analysis on a Nicolet Avatar 360 FT-IR spectrometer. The spectra were recorded at ambient temperature.

6.5. NMR Binding Studies

6.5.1. Self-association study for PDI-NH

A 20 mM concentration sample of PDI-NH was prepared by dissolving in deuterated chloroform and 500 μL of this sample was transferred to a capped NMR tube and the ^{1}H NMR spectrum recorded for this sample. A determined quantity of deuterated chloroform was added to this NMR tube to dilute the sample to a known concentration and the ^{1}H NMR spectrum recorded again for this new concentration. This process was repeated, such that the ^{1}H NMR spectra were obtained for PDI-NH concentrations at 20, 15, 10, 5, 4, 2.5, 1.0, 0.5, 0.25, 0.10 and 0.05 mM. The N-H chemical shift was used for fitting the following equations, following the non-linear curve procedure for a dimerisation model.[12] Where $[A]_0$ is the total concentration of PDI-NH, [A] is the concentration of the unbound free PDI-NH species, [AA] is the concentration of the hydrogen bonded PDI-NH dimer, K_d is the dimerisation constant, δ_f is the free chemical shift (for the N-H proton of PDI-NH), δ_d is the limiting bound shift of the dimer and δ_{obs} is the observed chemical shift (for the N-H proton of PDI-NH).

$$\mathrm{A} + \mathrm{A} \leftrightarrow \mathrm{AA}$$

$$[\mathrm{AA}] = \frac{1 + 4K_d[\mathrm{A}]_0 - \sqrt{1 + 8K_d[\mathrm{A}]_0}}{8K_d}$$

$$[\mathrm{A}] = [\mathrm{A}]_0 - 2[\mathrm{AA}]$$

$$\delta_{\mathrm{obs}} = \frac{2[\mathrm{AA}]}{[\mathrm{A}]_0}\delta_{\mathrm{d}} + \frac{[\mathrm{A}]}{[\mathrm{A}]_0}\delta_{\mathrm{f}}$$

6.5.2. PDI-NH: 9-Propyladenine Titration

A 4 mM solution of PDI-NH in deuterated chloroform was prepared and 500 μL of this sample was transferred to an NMR tube and the ^{1}H NMR spectrum recorded. To the remaining 4 mM PDI-NH solution, 9-propyladenine was added to produce a stock solution containing 4 mM PDI-NH and 51.01 mM 9-propyladenine in deuterated chloroform. This stock solution was titrated into the original NMR tube and the ^{1}H NMR spectrum recorded after the addition of each titre for a range of 9-propyladenine concentrations between 0 and 51.01 mM. The N-H chemical shift of PDI-NH was used for fitting to the following equations, using the non-linear curve procedure for a dimerisation binding model.[13] Where $[\mathrm{H}]_0$ is the total concentration of PDI-NH, [H] is the concentration of unbound free PDI-NH, $[\mathrm{G}]_0$ is the total concentration of 9-propyladenine, [G] is the concentration on unbound free 9-propyladenine, [HG] is the concentration of the hydrogen bonded PDI-NH: 9-propyladenine dimer, K is the dimerisation binding constant, δ_f is the free chemical shift (for the N-H proton of PDI-NH) and δ_d is the limiting bound shift of the dimer and δ_{obs} is the observed chemical shift (for the N-H proton of PDI-NH).

$$\mathrm{H} + \mathrm{G} \leftrightarrow \mathrm{HG}$$

$$[\mathrm{HG}] = \frac{1 + K[\mathrm{H}]_0[\mathrm{G}]_0 - \sqrt{(1 + \ [\mathrm{H}]_0[\mathrm{G}]_0)^2 - 4K^2[\mathrm{H}]_0[\mathrm{G}]_0}}{2K}$$

$$[\mathrm{H}] = \ [\mathrm{H}]_0 - [\mathrm{HG}]$$

$$\delta_{\mathrm{obs}} = \frac{[\mathrm{HG}]}{[\mathrm{H}]_0}\delta_{\mathrm{b}} + \frac{[\mathrm{H}]}{[\mathrm{H}]_0}\delta_{\mathrm{f}}$$

6.6. Density Functional Theory

Density Functional Theory calculations were performed using Gaussian 03 software with the B3LYP exchange-correlation function.[14, 15] Geometry optimisations were performed for all molecules in the gas phase without solvent effects, with geometry optimisations recognised as local minima by frequency calculations. Molecular orbital diagrams were generated using Molekel 4.2 software.[16, 17] All calculations were carried out on the University of Nottingham's High Performance Computer.

6.7. Photochemistry

6.7.1. Time-Resolved Infrared Spectroscopy

Ultrafast TRIR spectra in dichloromthane solution were collected using the Nottingham ultrafast TRIR apparatus and measurements performed by Dr. Raphael Horvath. Briefly, this comprises of a Spectra Physics MaiTai titanium:sapphire oscillator and regenerative Spectra Physics Spitfire Pro amplifier system to generate 800 nm laser pulses (full width at half maximum (fwhm) = 150 fs) at a frequency of 1 kHz. This output is split into two parts; the first of which pumps an optical parametric amplifier (OPA) to generate pump pulses at 355 nm. The second part is used to pump a computer controlled Light Conversion OPA with a frequency generator unit to generate tuneable IR probe pulses (fwhm = 150 fs) with a spectral bandwidth of ~180 cm^{-1} and pulse energy of ~2 μJ (both at 2000 cm^{-1}). A delay between the pump and probe beams, ranging from 0.5 ps up to 2 ns, is achieved using an optical delay line, before the pump beam is focused onto the sample using a quartz lens. The IR pulses generated are split by a germanium beam splitter into a reference and probe beam. The reference beam is detected by a separate single element Kolmar Technology mercury-cadmium-telluride (MCT) detector. At the sample the overlap of the pump and probe is such that the pump beam is slightly larger in diameter (~400 μm) than that of the probe (~200 μm). After passing through the sample, the probe is split into its component frequencies by a 250 mm Spectral Products DK240IR monochromator containing either 150 or 300 $grooves.mm^{-1}$ diffraction gratings (giving spectral resolutions of either 4 or 2 cm^{-1} respectively). The intensities of these component frequencies are measured by a 128 element Infrared Associates MCT array detector and both these signals and that of the single element detector are amplified by an Infrared Systems Development Corp 144-channel amplifier and digitized by a 16-bit analogue to digital converter.

6.7.2. Transient Absorption Spectroscopy

Fast Transient Absorption Spectroscopic measurements were performed using a pump-probe method. In brief, the probe beam of white light continuum is generated by focusing a small amount of 800 nm (∼400 nJ) laser beam into a 4 mm thick Sapphire disk. The picosecond 400 nm pump beam is obtained from a Spectra Physics Ti: sapphire oscillator/regenerative amplifier system and a Minioptic Technology TimePlate Tripler TP-1 harmonic generator and the time difference (up to 3 ns) between the pump and probe pulses is controlled by an optical delay line. The nanosecond 355 nm pump beam is produced with an Advanced Optical Technology ACE-25QSPXHP/MOPA Q-switched Nd:YVO laser which is electronically synchronised to the Spitfire Pro amplifier.

The delay between pump and probe pulses can be controlled with a Stanford Research System DG535 pulse generator from 0.5 ns to 100 μs. The white light beam is split into two parts. One part passes through the sample spatially overlapped with the pump beam. Another part serves as a reference to the probe beam fluctuations. The polarization of the pump pulse is set an angle of 54.7° relative to the probe pulse to recover the isotropic absorption spectrum. Both parts of the probe beam are monitored by a Spectronic Device Ltd Cronin Camera duel array detector (512 pixels). The detector is mounted in the focal plane of a 303 mm Acton spectrograph with a 150 g mm^{-1} grating. The pump beam size (~400 μm diameter) is larger than the probe spot (~200 μm diameter). A Harrick solution cell with 2 mm CaF_2 windows is mounted on a motorized cell mount, which moves the cell in plane rapidly and continuously.

6.8. References

1. L. Zhang, J. Fan, K. Vu, K. Hong, J.-Y. Le Brazidec, J. Shi, M. Biamonte, D. J. Busch, R. E. Lough, R. Grecko, Y. Ran, J. L. Sensintaffar, A. Kamal, K. Lundgren, F. J. Burrows, R. Mansfield, G. A. Timony, E. H. Ulm, S. R. Kasibhatla and M. F. Boehm, *J. Med. Chem.*, 2006, **49**, 5352-5362.
2. A. T. R. Williams, S. A. Winfield and J. N. Miller, *Analyst*, 1983, **108**, 1067-1071.
3. A. M. Brouwer, *Pure Appl. Chem.*, 2011, **83**, 2213-2228.
4. H. Nowell, S. A. Barnett, K. E. Christensen, S. J. Teat and D. R. Allan, *J. Synch. Rad.*, 2012, **19**, 435-441.
5. CrysAlisPro, 2013, Agilent Technologies UK Ltd. Oxford, UK.
6. G. Sheldrick, *Acta Crystallographica Section A*, 2008, **64**, 112-122.
7. G. Sheldrick, *Acta Cryst. A*, 2015, **71**, 3-8.
8. G. Sheldrick, *Acta Cryst. C*, 2015, **71**, 3-8.
9. O. V. Dolomanov, L. J. Bourhis, R. J. Gildea, J. A. K. Howard and H. Puschmann, *J. Appl. Cryst.*, 2009, **42**, 339-341.
10. P. van der Sluis and A. L. Spek, *Acta Cryst. C*, 2015, **71**, 9-18.
11. R. R. Gagne, C. A. Koval and G. C. Lisensky, *Inorg. Chem.*, 1980, **19**, 2854-2855.
12. A. P. Bisson, F. J. Carver, D. S. Eggleston, R. C. Haltiwanger, C. A. Hunter, D. L. Livingstone, J. F. McCabe, C. Rotger and A. E. Rowan, *J. Am. Chem. Soc.*, 2000, **122**, 8856-8868.
13. A. P. Bisson, C. A. Hunter, J. C. Morales and K. Young, *Chem. Eur. J.*, 1998, **4**, 845-851.
14. M. J. Frisch, G. W. Trucks, H. B. Schlegel, G. E. Scuseria, M. A. Robb, J. R. Cheeseman, J. A. Montgomery, T. Vreven, K. N. Kudin, J. C. Burant, J. M. Millam, S. S. Iyengar, J. Tomasi, V. Barone, B. Mennucci, M. Cossi, G. Scalmani, N. Rega, G. A. Petersson, H. Nakatsuji, M. Hada, M. Ehara, K. Toyota, R. Fukuda, J. Hasegawa, M. Ishida, T. Nakajima, Y. Honda, O. Kitao, H. Nakai, M. Klene, X. Li, J. E. Knox, H. P. Hratchian, J. B. Cross, V. Bakken, C. Adamo, J. Jaramillo, R. Gomperts, R. E. Stratmann, O. Yazyev, A. J. Austin, R. Cammi, C. Pomelli, J. W. Ochterski, P. Y. Ayala, K. Morokuma, G. A. Voth, P. Salvador, J. J. Dannenberg, V. G. Zakrzewski, S. Dapprich, A. D. Daniels, M. C. Strain, O. Farkas, D. K. Malick, A. D. Rabuck, K. Raghavachari, J. B. Foresman, J. V. Ortiz, Q. Cui, A. G. Baboul, S. Clifford, J. Cioslowski, B. B. Stefanov, G. Liu, A. Liashenko, P. Piskorz, I. Komaromi, R. L. Martin, D. J. Fox, T. Keith, A. Laham, C. Y. Peng, A. Nanayakkara, M. Challacombe, P. M. W. Gill, B. Johnson, W. Chen, M. W. Wong, C. Gonzalez and J. A. Pople, *Gaussian 03, Revision D.01*, 2004, Wallingford CT
15. C. Lee, W. Yang and R. G. Parr, *Phys. Rev. B*, 1988, **37**, 785-789.
16. P. Flükiger, H. P. Lüthi, S. Portmann and J. Weber, *MOLEKEL 4.2*, 2000, Swiss Center for Scientific Computing, Manno (Switzerland).
17. S. Portmann and H. P. Lüthi, *Chimia Int. J. Chem.*, 2000, **54**, 766-770.